GREEN SYNTHESIS OF CAPPED SILVER NANOPARTICLES AND THEIR HYBRIDS: ANTIMICROBIAL AND OPTICAL PROPERTIES

By

AKINSIKU Anuoluwa Abimbola
(CUGP100229)

January, 2017

GREEN SYNTHESIS OF CAPPED SILVER NANOPARTICLES AND THEIR HYBRIDS: ANTIMICROBIAL AND OPTICAL PROPERTIES

By

AKINSIKU Anuoluwa Abimbola
(Matric Number: CUGP100229)
B. Sc (Chemistry), M. Sc (Industrial Chemistry) (Abeokuta)

A THESIS SUBMITTED TO THE SCHOOL OF POSTGRADUATE STUDIES OF COVENANT UNIVERSITY, OTA, OGUN STATE, NIGERIA

IN PARTIAL FULFILMENT OF THE REQUIREMENTS FOR THE AWARD OF DOCTOR OF PHILOSOPHY (Ph.D) DEGREE IN CHEMISTRY, IN THE DEPARTMENT OF CHEMISTRY, COLLEGE OF SCIENCE AND TECHNOLOGY, COVENANT UNIVERSITY, OTA.

ACCEPTANCE

This is to attest that this thesis is accepted in partial fulfilment of the requirement for the award of the degree of **Doctor of Philosophy in Chemistry** in the Department of **Chemistry,** College of Science and Technology, Covenant University, Ota.

Philip John Ainwokhai …….
Secretary, School of Postgraduate Studies Signature & Date

Professor Samuel Wara ……
Dean, School of Postgraduate Studies Signature & Date

DECLARATION

I, **AKINSIKU, Anuoluwa Abimbola (CUGP100229)**, declare that this research was carried out by me under the supervision of Professor E. O. Dare of the Department of Chemistry, Federal University of Agriculture, Abeokuta and Professor K. O. Ajanaku of the Department of Chemistry, Covenant University, Ota. I attest that the thesis has not been presented either wholly or partly for the award of any degree elsewhere. All sources of scholarly information used in this thesis were duly acknowledged.

AKINSIKU Anuoluwa Abimbola …….

Signature & Date

CERTIFICATION

We certify that the thesis titled "Green Synthesis of Capped Silver Nanoparticles and their Hybrids: Antimicrobial and Optical Properties" is an original research work carried out by **AKINSIKU Anuoluwa Abimbola (CUGP100229),** in the Department of Chemistry, College of Science and Technology, Covenant University, Ota, Ogun State, Nigeria, under the supervision of Professor E. O. Dare and Professor K. O. Ajanaku. We have examined and found the research work acceptable for the award of the degree of Doctor of Philosophy in Chemistry.

Professor E. O. Dare ……
Supervisor Signature & Date

Professor K. O. Ajanaku ……
Co-Supervisor Signature & Date

Dr. A. B. Williams ……
Head of Department Signature & Date

Professor R. A. Oderinde ……
External Examiner Signature &Date

Professor S. Wara ……
Dean, School of Postgraduate Studies Signature & Date

DEDICATION

This thesis is dedicated to God Almighty, my help, shield and the lifter of my head. I return all glory to Him alone.

AKNOWLEDGEMENTS

My profound gratitude goes to God Almighty, for the strength, wisdom, provisions and guidance for the success of this work. To Him alone I ascribe all the glory. I sincerely appreciate the Chancellor of this great university, Dr. D. O. Oyedepo and all members of the Board of Regent of Covenant University. I acknowledge Vice-Chancellor, Professor A.A.A Atayero and members of their Management team, for their drive towards achieving excellence.

I deeply acknowledge my amiable Supervisor, Professor E. O. Dare for his mentorship, good heart and relentless effort in achieving quality research. Sir, I appreciate the time you devoted to this work; financial contribution and your understanding. Moreover, my heart-felt appreciation goes to my Co-Supervisor, Professor K. O. Ajanaku, for his passionate heart and the thorough reading of this thesis. Big thanks to the Head of Department of Chemistry, Dr. A.B. Williams. I am indebted to Mr. Olusola Rotimi, Mr. Olufemi Olaofe of the University of Western Cape, Bellvillle campus, Cape-Town and Mr. Shitole Joseph of iThemba Labs, South Africa for the characterization of the nanoparticles. My special thanks to Mr. Seun Ejilude for the antimicrobial analysis of this work.

I am also grateful to the Dean, School of Post-graduate Studies, Professor Samuel Wara and the Dean of College of Science and Technology, Professor Nicholas Omoregbe, for their immense efforts in driving the vision 10: 2022 in terms of quality research. I recognize Professor M. A. Mesubi and Professor K. Odusami for their love and fatherly hearts. I cannot but mention the tremendous efforts of Dr. O. O. Ajani and Dr. J. A. Adekoya during and after the bench work. To other senior colleagues in the Department, Dr. J. A. O. Olugbuyiro, Dr. K. O. Ogunniran, Dr. T. O. Siyanbola, I say thank you for encouraging me. “Mama Atan”, thanks a lot for the help rendered in locating the plants used in this work. To all my teachers, God bless you all!

I appreciate other members of Faculty and Staff of the Department for their love and support. God bless you all. Dr. S. Rotimi, Mrs. Akinyele (Chief Technologist, Biological Sciences Department), Mr. A. Adeyemi and other Technologists in the Department of Biochemistry, thank you all. To my wonderful friends, Dr. Elizabeth Olowookere, Dr. J. O. Popoola, Miss Justina Achuka, Miss Olusola Kayode, Mrs Joan Ayo-Ajayi and family, thank you. I acknowledge Pastor and Pastor Mrs. Joshua Olaleye of RCCG, Strong Tower, Akoka, Lagos, for their prayers

and encouragement. Mr. A. A. Akinsiku (My father-in-law), I appreciate you for your understanding during the bench work.

To my wonderful siblings, Pastor Tosin Sotomi and wife, Pastor Segun Sotomi, Engineer Dele and Mrs. Folasade Ayeni, Mr. Ope Sotomi and the wife, thank you all for your prayers and love. Baby of the house, Pastor Tolu Sotomi who allowed God to use him for the success of this work, from the beginning to the end; Tolu, God bless you and crown all your efforts with good success. I cannot forget my late parents, Apostle A. T. Sotomi (JP) and Mrs. F. A. Amope Sotomi; you greatly motivated me to start Ph.D programme immediately after my M.Sc programme. Your lives were beautiful memories, God bless you; continue to rest in the bosom of God.

To our son, Master Ayodeji Oluwatise, my joy, thank you for your endurance during my bench work. Ololade Michelle, welcome to the world at a time like this. My sincere appreciation goes to the love of my life, Builder Emmanuel Akinsiku. Thank you for your understanding and allowing God to use you for the success of this Ph.D research work. You stood by me prayerfully, financially; you even sacrificed your time for me. “Ife mi”, God bless you, and reward your labour of love.

AKINSIKU Anuoluwa Abimbola, 2017

TABLE OF CONTENTS

CHAPTER TWO: LITERATURE REVIEW

CHAPTER THREE: MATERIALS AND METHODS

CHAPTER FOUR: RESULTS AND DISCUSSION

LIST OF TABLES

LIST OF FIGURES

LIST OF PLATES

LIST OF SCHEMES

LIST OF ACRONYMS AND ABBREVIATIONS

0D	Zero dimension
1D	One dimension
2D	Two dimensions
3D	Three dimensions
Abs	Absorbance
Ag NPs	Silver nanoparticles
Ag-Ni NPs	Silver-nickel nanoparticles
Ag-Co NPs	Silver-cobalt nanoparticles
EDS/EDX	Energy Dispersive Spectrometry/X-ray
FTIR	Fourier Transmission Infra-red
Hrs	Hours
nm	Nanometer
NPs	Nanoparticles
PL	Photoluminescence
SAED	Selected Area Electron Diffraction
SEM	Scanning Electron Microscopy
SPB	Surface Plasmon Band
SPR	Surface Plasmon Resonance
SEM	Scanning Electron Microscope
TEM	Transmission electron microscopy
UV-Vis	Ultraviolet-Visible
XRD	X-Ray Diffraction

ABSTRACT

Unique properties of silver (Ag) and its allied nanoparticles are of great interest in the fields of chemistry and technology. However, the widespread applications of nanoparticles call for synthesis routes involving eco-friendly procedures. Silver nanoparticles (Ag NPs) and their hybrids nanoparticles (Ag-Ni and Ag-Co) were synthesized using locally available biodiversity plants as alternative method to the expensive and toxic chemicals previously used. Fresh plants were collected and extracted in water by cold extraction. Phytochemical screening was carried out on the plant extracts and green plant-mediated reduction method was employed. Nanoparticles formation and growth were monitored with UV-Vis spectrophotometer at time intervals. The nanoclusters were further characterized using photoluminescence (PL), scanning electron microscope (SEM), transmission electron microscope (TEM), fourier transmission infra-red (FTIR), x-ray diffraction (XRD) and selected electron area diffraction (SAED). Antimicrobial activity of the nanoparticles was investigated on clinically isolated pathogens. Formation of nanoparticles was indicated by colour change in the reaction medium when nucleation and growth commenced as early as 2 minutes in the reaction at 70°C, compared to the syntheses carried out at room temperature. Optical properties were displayed with surface plasmon resonance bands (SPR) above 400 nm in Ag NPs and their hybrids. The high intensities of absorption were characterized with red-shifted wavelengths, except the Ag NPs and the corresponding nanohybrids formed using the extract of *S. occidentalis* (327-350 nm). However, near uniform emission of fluorophores was exhibited by Ag NPs (438-466 nm) and Ag allied nanoparticles (581-778 nm) irrespective of the excitation wavelengths. The morphological characterization of Ag-Co nanohybrid using SEM and TEM revealed novel alloy structure in which Ag atoms were attached to the vertices of cobalt in a planar arrangement. Other morphologies obtained using *C. indica* leaf extract were cluster-in-cluster spherical arrangement, nanorod, nanocube with truncated edges, rectangle and quasi-spheres; all caged, thereby providing stability for the newly formed nanoparticles. Cubic structures with truncated/irregular edges and quasi-spherical morphologies were formed by monometallic Ag NPs using other plant extracts. However, the corresponding Ag-Ni and Ag-Co nanobimetallic derived from these plant extracts resulted in nanohybrid with Ag core and Ni shell arrangement, nanocubes with truncated edges and multiply-twinned nanoparticles. Evidence of capping of the newly formed nanoparticles by the biomolecules was demonstrated by the diagonal orientation of Ag

nanoparticles through mapping. Hexagonal shaped nanoparticles with truncated edges were observed in the Ag NPs obtained from *L. inermis* leaf extract. The formation of highly crystalline Ag dominated by face-centre cubic (FCC) was supported by *p*-XRD. SAED also supported formation of hybrid nanoparticles as crystallinity decreased when compared with the equivalent Ag monometallic nanoparticles. The antimicrobial activity of nanoparticles against clinical isolates was highly significant (6.25 mg/mL MIC, and 12.5 mg/mL MBC) in the hybrid nanoparticles which demonstrated higher growth inhibition of the test organisms as revealed in one-way analysis of variance (ANOVA) using SPSS statistical tool ($p < 0.05$). The outcome of these findings suggests the application of *Canna indica*-influenced Ag NPs as antibacterial against *E. coli, S. pyogenes* and antifungus against *C. albicans*. Ag-Co nanoparticles formed using the extract of *C. indica* is a potential material in optical devices. The use of Ag NPs with narrow size distribution can serve as conductive fillers in electronically conductive adhesives (ECA).

CHAPTER ONE
INTRODUCTION

1.1 Background to the Study

The quest for environmental remediation has led to the synthetic routes involving eco-friendly protocols. Green synthesis methods are gaining more awareness in the field of chemistry and chemical technologies; these cancel out high production cost, and high energy involved in the usual methods of synthesizing nanoparticles via the conventional techniques of using hazardous chemicals like sodium borohydride or hydrazine (Anastas & Warner, 1998). The green synthesis also involves elimination of complex synthesis routes, choice of water as solvent, replacement of toxic reducing agent and stabilizing agent with renewable and sustainable materials. All these are environmentally friendly and are considered as alternative methods for the synthesis of nanomaterials for various applications (Raveendran, Fu & Wallen, 2003). From survey, biological syntheses of nanomaterials make use of bacteria, yeasts, fungi and algae (microorganisms). The use of plants or plant extracts for metal and metal hybrid nanoparticles synthesis is currently a new research focus that has gained wide acceptance (Rauwel, Küünal, Ferdov & Rauwel, 2015).

Materials on nanometer scale are of special interest because of the novel characteristics they possess; applications of such materials are in the chip-technology, when material is reduced to the smallest confines (Brynjolfsson & McAfee, 2012; Koole, Groeneveld, Vanmaekelbergh, Meijerink & Donegá, 2014). Catalysis also takes advantage of the huge efficient surface area obtained in nanomaterials. Furthermore, the ability to tune the properties of nanomaterials offers application in lighting, opto-electronics, photovoltaic, biomedical and thermoelectric (Donega, 2011).

In recent time, noble metal nanoparticles have been the area of focus of researches as they show improved physical and chemical properties in the fields of electronic, optical, mechanical, magnetic and chemical processing. This could be as a result of their small size with large specific surface, quantum size effect and electronic structures. Hence, metallic nanoparticles have found relevance in the fields of electronics, photochemical, biomedicine, chemistry, catalysis and photonics (Mazur, 2004; Guglielmo, Lopez, Lapuente, Mallafre, & Suarez, 2010).

Over the years, Creighton method had been in use for the synthesis of silver nanoparticles (AgNPs), i.e. the reduction of silver nitrate (precursor) with sodium borohydride ($NaBH_4$). This procedure often yields 10 nm of narrow size distribution (Creighton, Blatchford & Albrecht, 1979). This method had also been used for metals like Pt, Ni, Cu, Pd, etc. Suspensions of Cu and Ni were not very stable due to the oxidation of the metal particles, as this requires strong capping ligands to prevent the oxidation. Hence, reduction potentials of the source ions need to be taken into consideration (Scott, Ye, Henriquez & Crooks, 2003).

Silver metals were discovered to have the highest efficiency out of the three metals (Ag, Au and Cu) that show plasmon resonance in the visible spectrum (Kreibig & Vollmer, 1995). Also, the optical excitation of plasmon resonance in nanosized silver nanoparticles, exhibit the most efficient mechanism in terms of light interaction with matter. A single silver nanoparticle (Ag NP) displays utmost interaction with light than any other particle of the same dimension from other known organics or inorganic chromophores. This was estimated to be ten times more than that of the geometric cross-section, as Ag particles capture more light that is physically incident on them. Moreover, Ag is one of the materials with tuneable plasmon resonance to any wavelength in the visible spectrum (Evanoff & Chumanov, 2003).

1.2 Metals

About 70 % of elements in the periodic table are considered as metals, 5 are metalloids with both metallic and non-metallic properties. A metal is any material with high conductivity and reflectivity that can be deformed plastically. They are usually malleable, ductile and shiny. Different characteristics are displayed by metals when exposed to many conditions (Hillert, 1997). Metals such as nickel, vanadium, molybdenum, cobalt and the platinum group metals enable the catalytic reactions for the synthesis of many organic chemicals from petroleum. Gold, silver and platinium (noble metals) have found applications in biomedical- drug delivery, imaging, photothermal therapy and immunochromatography (Philip, 2010).

1.3 Noble Metal Nanomaterials

Noble metals possess distinctive feature of non-interaction with other elements. The common ones are silver (Ag), gold (Au), platinium (Pt) and palladium (Pd), but the case is different at nanometric scale length. The transitions to nanoscale length change both their physical and chemical properties, which can be tuned by controlling parameters like size, shape, building composition, etc. Unique size-dependent properties (optical, electrical, magnetic and

chemical) emerge, which turn them to the building units of nanostructures for many technological uses (Guo & Wang**,** 2011).

Gold nanoparticles display size-dependent and visible surface plasmon resonance (SPR), whereas its nanorods, nanocages and hollow nanosphere show absorption near-infrared (Murphy *et al.,* 2005; Skrabalak *et al*., 2008; Cobley, Chen, Cho, Wang & Xia, 2011). Platinium nanomaterials dendritic structure had been studied to show higher electrocatalytic properties in small molecule oxidation and oxygen reduction reactions than the commercial catalysts in fuel cells (Tian, Zhou, Sun, Ding & Wang, 2007; Wang & Yamauchi, 2009; Mazumder, Lee & Sun, 2010). However, higher surface-enhanced Raman scattering activity had been confirmed in Ag nanostructures with more edges and corners possessing proper size complex than silver nanoparticles with the spherical ones (Mulvihill, Ling, Henzie & Yang, 2009). Hence, molecular-like properties and strong size-dependent fluorescent emission were predicted for nanoclusters of Ag, Au and Pt that possess several atoms comparable to Fermi wavelength of electrons (Xu & Suslick, 2010). The ability to control key parameters of noble metal nanoparticles make them applicable for many purposes like catalysis, photography, electronics, photonics, sensing, imaging and information storage devices (Wang & Yamauchi, 2009; Mazumder *et al.,* 2010).

1.4 Optical Properties of Noble Metal Nanoparticles

The optical properties of nanoparticles are based on surface plasmon polaritons (SPP) and the localized surface plasmon resonance (LSPR). These properties are known as the two plasmonic effects on metal surfaces (Maier, 2007). The charge density wave propagation on the interface of metal and dielectric are the SPP, while LSPR is the collective oscillation of the conduction electrons in the metal nanostructures joint with electromagnetic field. According to Willets and Duyne (2007), there is energy confinement within the metal interface and the dielectric as it propagates in the other two dimensions. Electron confinement of the excited electron in nanoparticles is also revealed in their optical characterizations in terms of absorption and photoluminescence (PL) spectra (Dong, 2012).

Strong interaction of closely packed atoms of metal nanoparticles results in optical properties (Solid-State Physics, 2015). The optical property of metal nanoparticles is due to their interaction with light; as shown in their intense colours. A unique optical property of noble metal nanoparticles is the light scattering effect, as a result of surface plasmon oscillation

decay by its energy radiation, when the absorbed light is converted into heat (Jain, Huang, El-Sayed & El-Sayed, 2008). Noble metal nanocrystals experience shift in the surface plasmon resonance (SPR) as an optical effect when combined or coated with other materials. This effect may also cause change in the photoluminescence intensity as the case were in semiconductor nanocystals.

1.4.1 Surface Plasmon Resonance (SPR) in Noble Metal Nanostructures

Surface plasmon resonance is termed as the collective oscillation in the resonant motion of free conduction electrons of the metal nanoparticles in the presence of electromagnetic field. An intense bright colour is a major attribute of metal nanoparticles, as a result of their unique interaction with light. The electron oscillation is imagined as a photon restrained to the size of the nanostructure that contains strong electric field around the particle (Kreibig & Vollmer, 1995).

For gold, silver and copper nanoparticles in the visible regions, there is a strong improvement in the electric field intensity, scattering and absorption at the localized surface plasmon resonance (LSPR) frequency (Eustis & El-Sayed, 2006). The absorption frequency of metal plasmon in the visible region for silver, copper and gold nanoparticles are 390-400 nm, 565-570 nm and 500-550 nm respectively (Tauran, Brioude, Coleman, Beonjoom & Kim, 2013). The wavelength of the LSPR can be fine-tuned to a desired position by controlling the dielectric constant of the surrounding medium. The biological application of LSPR is the ability to change the nanostructure shape, size, composition or medium (Tuning) (Oldenburg, Averitt, Westcott, Halas, 1998; Link & El-Sayeed, 2000; Kelly, Coronado, Zhao & Schatz, 2003; Jain, Eustis & El-Sayed 2006).

1.5 Size Effect

Size effect results in change of physico-chemical properties. The classical size effects are very obvious in variation of physical properties like lattice parameters, thermal conductivity, diffusion, hardness, plasticity etc. There are two types of size effects: the classical (internal and external ones) and quantum effects. The internal also called intrinsic size effects are the changes observed in particles like lattice paremeters, hardness, band gap, luminescence, melting point, diffusion coefficients, sorption, chemical activities, etc. regardless of external disorder (Pokropivny, Lohmus, Hussainova, Pokropivny & Vlassov, 2007). Consequently, the

external size effects which are unavoidable are the results of interference between various physical fields and matter interaction. These lead to the decrease of building units: the particles, domain and grains to a critical value. However, the size is comparable with a length of the physical phenomenon- the phonons (Pokropivny *et al*., 2007).

1.5.1 Quantum Size Effect

The experimental extraordinary properties observed (extremely small crystals) when electrons are confined to a small region of space in one, two or three dimensions is known as the quantum size effect (McGraw-Hill Dictionary, 2003). It is the response to change in the particle size by energy adjustment in the electrons as a result of 'geometrical' constraints by the particle boundaries (Takagahara & Takeda 1992; Wise, 2000; Zhao, Zhang, Dang & Liu, 2004). The uniqueness of nanomaterials is as a result of surface to volume ratio and quantum size effect (John, Balaguru & Jeyaprakash, 2012). Particles in nanometer scale (1-100 nm) are size-dependent compared with their bulk amount of matter. Furthermore, properties like electrical conductivity, ionization potential and electron affinity, colour, melting point and magnetism in nanoscale become size dependent; and can be tuned by altering the size of nanoparticles. Nanosize effect is now gaining applications in catalysis for solar cells, fuel cells, batteries and hydrogen storage (energy-related materials), nanomagnets and transistors (electronics); quantum dots for quantum computing (Roduner, 2006).

However, size effect in new nanostructured materials brings about novel discoveries and development in nanotechnology (Pokropivny *et al*., 2007). It is worth mentioning that nanostructures (any agglomeration of matter at nanomeric level) and nanomaterials (nanoscale particles) are of distinctive feature of a large fraction of surface atoms per unit volume; there is an increase in surface atoms to interior atoms ratio, as this explains the dramatic changes in their physical and chemical properties. They are also considered to possess increased total surface energy with the overall surface area that is stoutly dependent on the dimension of material. The large surface area in nanostructured materials results in thermodynamic unstability, as this must be overcome to prevent overall surface area reduction which leads to growth size in the nanomaterials (Cao & Wang, 2004).

Nanomaterials are built-up based on the fact that an atom at the surface of small catalyst particle is of different properties when compared with those of the same atom at the surface of a larger particle. In addition, an atom entrenched at different positions of a crystal face has

different unique property at each particular location. Hence, these effects could be concluded to initiate from either surface effects or quantum confinement effects (Roduner, 2006).

However, another quantum size effect is the blue shift of luminescence observed in the increase of low dimensional quantum states as experienced in the physical properties-electroconductivity in magnetic field, oscillation of the superconductivity critical temperature, magnetoresistance and hypersound generation (Pokropivny *et al*., 2007).

1.6 Quantum Confinement Effects

The spatial confinement effect and properties depend on the feature length scales of a given property i.e. composition and structure of the materials are the determinant factors. This differs from one material to another. The spatial confinement of excitons in semiconductor nanostructures results in quantum confinement (Rossetti & Brus, 1982). The direct influence of ultra-small length scale on the energy band structure which results in the changes of atomic structure is known as the quantum confinement effect (Takagahara & Takeda 1992, Wise, 2000; Zhao *et al*. 2004). Groups IV, III-IV and II-VI (semiconductors) are in quantum confinement ranges between 1 and 25 nm length scale with a comparable spatial extent of the electronic wave function and the particle size. Nanomaterials appear to be quantized because of the movement confinement of electrons. This effect results in discrete energy levels based on the size of the structure from simple potential. Dimension control and structural compositions of the materials determine its precise purpose; quantum size effects of metal nanostructures have been applied in electronic and optoelectronic components (Pedersen, 2006). Quantization effect is significant as the particle dimension of a semiconductor is near to; or below the bulk semiconductor Bohr radius. This effect leads to material properties size dependent. As the particle size approaches Bohr exciton radius, the quantum confinement results in:

i. transition energy
ii. increasing excito
iii. luminescence band gap energy
iv. blue shift in the absorption
v. collapse of the continuous energy bands of a bulk material into discrete atomic-like energy levels (Yoffe, 1993).

In quantum confined structure, the electron and hole (motion carriers) are restricted in one or more directions by potential barriers (Miller, Prakash & Prakash, 1984), as illustrated in Table 1.1.

Table 1.1: Quantum confined Structures (Source: Miller *et al*. 1984)

Structure	Quantum Confinement	Number of Free Dimension
Bulk	0	3
Quantum well/superlattices	1	2
Quantum wire	2	1
Quantum dot/nanocrystals	3	0

1.7 Classification of Nanoparticles

1.7.1 Composition

Single or composite of materials are classified by composition. They can be found in nature as agglomerations of materials with various compositions. However, pure single-composition materials can be easily synthesized today by a variety of methods (Buzea, Blandino & Robbie, 2007).

1.7.2 Morphology

The following classifications are based on morphological characteristics of nanoparticles: flatness, sphericity and classification between high-and-low aspect ratio particles (aspect ratio). Nanotubes and nanowires, containing shapes like helices, zigzags, belts, or possibly nanowires with diameter that varies with length are examples of high aspect ratio nanoparticles. On the other hand, spherical, oval, cubic, prism, helical or pillar, collections of many particles existing as powders, suspension, or colloids are classified under small-aspect ratio morphologies (Buzea *et al*., 2007).

1.7.3 Dimensionality

Dimension-based classification within the nanometer range was developed to accommodate 0D dimensional structures (nanopores and nanoparticles), 1D system confined in a direction

(layered or laminate structures), usually thin films or surface coatings used in circuitry of computer chips and coatings on eyeglasses, 2D system restricted in two dimensions (filamentary structures of greater length compared with the cross-sectional dimensions); it includes 2D nanostructured films, having nanostructures firmly attached to a substrate and nanopore filters used for small particle separation and filtration. Moreover, free particles with large aspect ratio to dimensions in the nanoscale range are also considered. However, in 3D system, the three dimensions are confined (structures consisting of consolidated equiaxed crystallites). These include thin deposited films under conditions that generate atomic-scale porosity, colloids, and free nanoparticles consisting of various morphologies (Buzea *et al*., 2007; Pokropivny *et al.,* 2007).

Table 1.2: Dimensionality classification and properties

Dimensionality	**Criteria**	**Examples**
Zero-dimensional (0D)	The nanostructure has all dimensions in the nanometre size range.	Nanoparticles, quantum dots, nanodots
One-dimensional (1D)	One dimension of the nanostructure is outside the nanometric size range	Nanowires, nanorods, nanotubes, nanoneedles, typically thin films or surface coatings
Two-dimensional (2D)	Two dimensions of the nanostructure are outside the nanometric size range. 2D nanostructures display plane-like structures	Nano-coatings, thin films and nanolayers and asbestos fibres
Three-dimensional (3D)	Three dimensions of the nanostructure are outside the nanometer size range. Consists of nanocrystalline units with properties on nanoscale as a result of size effect	Bulk different distributions of nanoparticles and nanocrystallites

Source: Buzea *et al.,* 2007; Pliofkhazraei & Rouhaghdam, 2010

1.7.4 Nanoparticle Uniformity and Agglomeration

Nanoparticles in form of aerosols, suspensions/colloids are in this category, based on their chemistry and electromagnetic properties, as magnetic nanoparties tend to cluster. Behaviour of nanoparticles as larger particles depends on the size of agglomerate formed, unless their surfaces are coated with non-magnetic materials. Figure 1.1 is the summary of classification of nanomaterials from the point of view of nanostructure dimensions, morphology, composition, uniformity and agglomeration state.

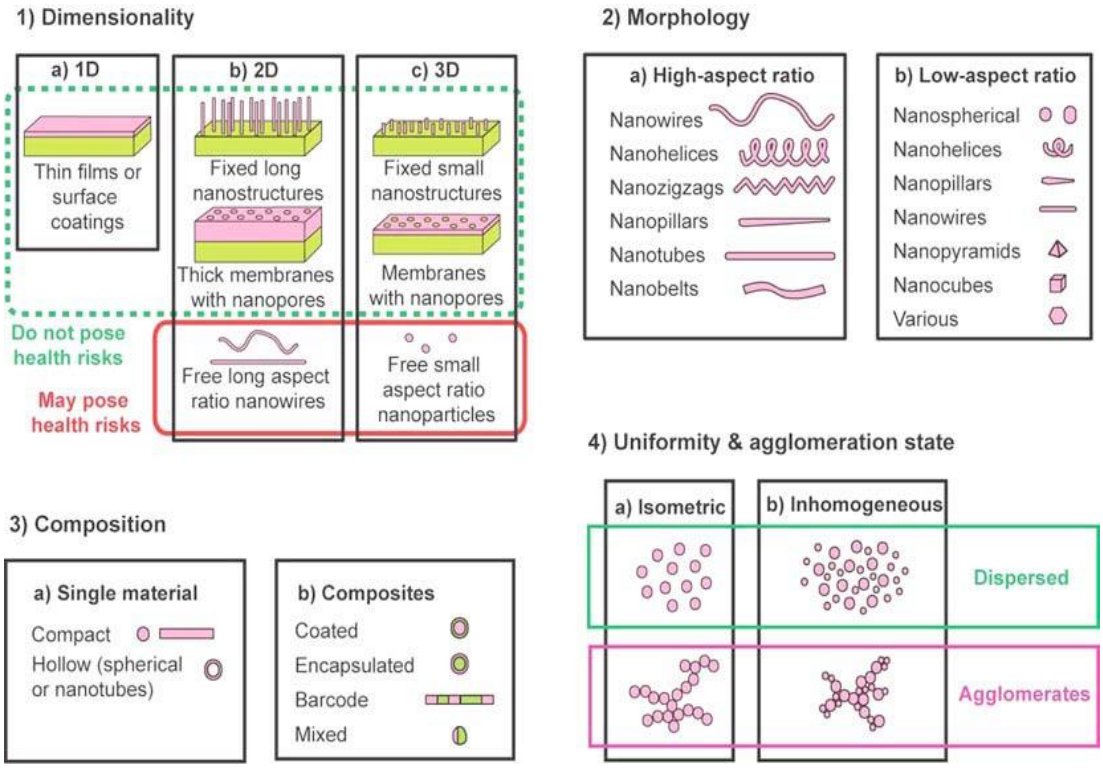

Figure 1.1: Classification of nanostructured materials (Buzea *et al.*, 2007)

1.8 Statement of the Research Problem

Nanoparticles and nanomaterials are products of a rapidly growing technology (Ju-Nam & Lead, 2008). They are widely applied in many fields - catalysis, electronics, biology and biomedical material science, cosmetics, renewable energies, physics and environmental remediation due to their distinctive properties. Unfortunately, the use of toxic organic solvents and strong reducing agents result in producing hazardous wastes which pose a great threat on the environment (Walker, Bethell, Schiffrin & Whyman, 1994; Wu & Lai, 2004; Herrera, Resto, Briano & Rinaldi, 2005; Kitchens, McLeod & Roberts, 2005; Liu *et al.,* 2006; Liu *et al.,* 2007). Furthermore, conventional synthesis of metallic nanoparticles is often time consuming unlike green method in which nucleation, onset growth and reaction completion could take place within 30 minutes (Akinsiku, Ajanaku, Adekoya, & Dare, 2015).

In addition, the development of eco-friendly and cost effective nanomaterials is a necessity, as the synthess of nanoparticles is still expensive (Kim *et al*., 2003; Parak *et al*., 2003; Schultz, 2003; Wei, Zhou & Liu, 2005; Smith, Duan, Rhyner, Ruan, & Nie, 2006; González & Noguezm, 2007; Gross, Winnacker & Wellmann, 2007; Wang, Li & Hua, 2007). It is noteworthy that Nigeria is endowed with natural biodiversity whose bioreducing potential in a green environment has been under-utilized.

1.9 Justification for the Study

As the demands for commercial nanoparticles are on the increase due to their wider applications in many fields, plant mediated green synthesis provides a cost-effective facile step as an additional method, that is eco-friendly and sustainable (Kulkarni, Srivastava, Harpale & Zunjarrao, 2011). The technique provides stable nanoparticles dispersions that resist aggregation in biological media, and have high oxidation resistance that are of significant importance (Boca & Astilean, 2010).

Nucleation is rapid, and the onset of growth can commence as early as 5 minutes in green synthesis of metal nanoparticles. The reaction is very fast unlike other chemical syntheses whose nucleation can commence up to 2 hours. Other chemical syntheses produce large quantities of hazardous wastes (Wu & Lai, 2004; Liu *et al.,* 2006; Liu *et al.,* 2007) due to the strong organic chemicals like sodium borohrdride or hydrazine (surfactants and reducing agents) employed (Walker *et al.,* 1994; Herrera *et al.,* 2005; Kitchens *et al*., 2005). The

methods may still lead to the presence of some toxic chemical species adsorbed on the surface of the product that may have adverse effects in medical applications. Consequently, to solve the public health problem of drug resistance by the disease causing microbes, new drug procedure needs to be adopted. Hence, the aforementioned challenges may be overcome by using plants or microorganisns instead of hazardous chemicals, high-energy and wasteful purification. It has also been suggested that elaborate synthesis processes are eliminated when green synthesis is employed (Anastas & Warner, 1998). Furthermore, this work is targeted at exploiting locally available biomaterials for silver nanostructuring, as this creates ground for screening active components of our bioresource to create value-added products.

1.10 Aim and Objectives of the Study

The aim of this research is to synthesize and evaluate some properties of novel Ag nanoparticles, Ag-Ni and Ag-Co hybrid nanoparticles using locally available biodiversity.

The set objectives of the study are to:

i. utilize locally based eco-friendly plant extracts as reducing agents/capping agents for the syntheses of silver and its hybrid nanoparticles, this hopefully will replace expensive chemicals previously used.
ii. engage synthesized nanoparticles with optical properties for enhanced optical materials using UV-Vis spectrophotometer and photoluminescence (PL).
iii. determine the optimum time, absorption wavelength of the synthesized nanoparticles at room temperature and 70℃, using UV-Vis spectrophotometer.
iv. study the morphological features of the particles using SEM and TEM; further characterize the particles with XRD, EDX and FTIR.
v. evaluate the antimicrobial properties of the synthesized nanoparticles against selected bacteria and fungi.

1.11 Research Questions

i. Can all available locally sourced plant extracts serve as reducing/capping agent in the synthesis of nanoparticles instead of costly chemicals?
ii. What purpose can the biosynthesized nanoparticles serve?
iii. Can public health problem of drug resistance by the disease causing microbes be tackled through green route of nanoparticles synthesis?

1.12 Hypothesis

The hypotheses of this research are:

i. If organic chemicals act as reducing agents, then plants rich in phytochemicals can be used as bioreducing agents.
ii. If nanoparticles prepared from chemical method possess antibacterial activities, then green route synthesized nanoparticles should serve the same purpose.
iii. The optical properties of hybrid nanoparticles should be enhanced than the monometallic nanoparticles.

1.13 Scope of Work

Seven different plants were collected in Atan-Iju, Ota, south west of Ogun State in Nigeria. The plants were identified and authenticated at Forest Research Institute of Nigeria (FRIN) at Ibadan. The plant extracts served as reducing/capping agents in the synthesis of nanoparticles. The plant-mediated nanoparticles were characterized. The antimicrobial activity of the nanoparticles was tested on clinical isolates.

CHAPTER TWO

LITERATURE REVIEW

2.1 Nucleation and Growth Mechanisms of Nanoparticles in Solution

Kashchiev (2000) described nucleation and growth of crystalline materials from solution as the phenomenon involving assembling of atoms or molecules straight from solution. During nucleation, there is a rapid formation of nuclei and growth when the critical size is exceeded, as a function of the ratio of surface to bulk energy.

2.2 Theory of Nucleation and Growth

2.2.1 LaMer Mechanism

LaMer mechanism was the first mechanism to separate the nucleation and growth (LaMer & Dinegar, 1950). The mechanism further divided the processes of nucleation and growth into three parts:

i. Quick increase in the concentration of free monomers in solution.
ii. Decrease in the concentration of free monomer in solution as a result of "Burst nucleation", whose rate was described as "effectively infinite". After this stage, no nucleation took place due to decrease in the concentration of monomers.
iii. Growth under the control of monomer diffusion through the solution.

The growth of silver halide had been studied to follow classical nucleation and growth pattern (Sugimoto, Shiba, Sekiguchi & Itoh, 2000; Sugimoto & Shiba, 2000). LaMer and Dinegar (1950) carried out experiment on the nucleation and growth of sulphur solution formation. Particles larger in size than the critical radius grew in a short time period of nucleation; as the growth process was proposed to be either diffusion or surface reaction. Thereafter, the mechanism of formation of nanocrystals or colloids from a homogeneous supersaturated aqueous medium was developed. The plot of concentration of monomer against time as proposed by LaMer mechanism is shown in the Figure 2.1.

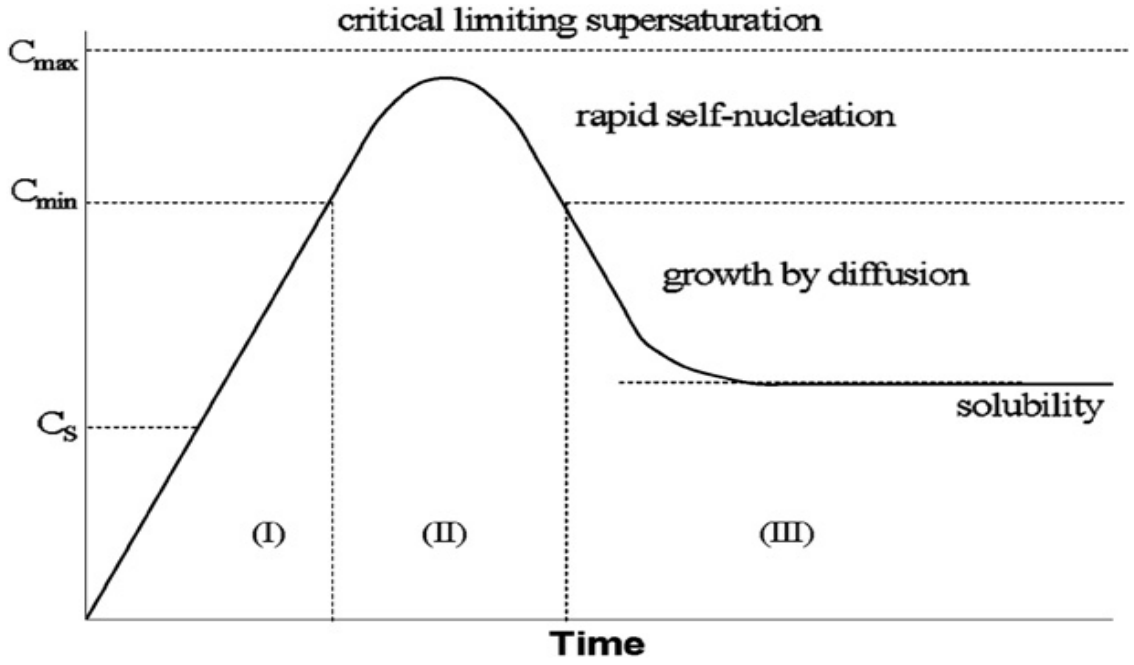

Figure 2.1: LaMer Mechanism of Nucleation (LaMer & Dinegar, 1950)

2.3 Ostwald Ripening and Digestive Ripening

The growth mechanism in Ostwald ripening, by the change in solubility of nanoparticles was considered to be size dependent, as described by Gibbs− Thomson relation:

$$C_r = C_b \exp\left(\frac{2\gamma v}{r k_b T}\right) \text{ ---------- (1)}$$

Chemical potential $\Delta\mu = 2\gamma v/r$. Then C_r is expressed as a function of r where v is the molar volume of the bulk crystal and C_b is the concentration of the bulk solution.

Re-dissolution took place as a result of high solubility and surface energy of smaller particles in the solution as the growth of larger particles continued the more. Lifshitz and Slyozov (1961), Wagner (1961) theories best described Ostwald ripening within a close system. However, surface energy of the particle within solution controlled the formation process. Conversely, smaller molecules may grow at the expense of the bigger ones as depicted by Lee *et al.* (2005). The phenomenon is known as "digestive ripening", opposite of Ostwald ripening.

Moreover, Finke-Watzky two step mechanisms resulted in the nucleation step followed by critical size, and not a classical nucleation. In the process, nucleation and growth took place simultaneously:

$A \rightarrow B$	Slow continuous nucleation (Finney & Finke, 2008)
$A + B \rightarrow 2B$	Auto catalytic surface growth which is not diffusion controlled (Zhang, Khalizov, Wang, Hu & Xu, 2012)

Ostwald (1879) described crystal formation processes as the best mechanism that explained particle coarsening in anisotropic growth systems (Ostwald, 1879; Wagner, 1961; Kukushkin & Osipov, 1998). The features of this mechanism included crystal solubility in the liquid medium as the pathway for surface dissolution that led to spherical particles. The limitation of Ostwald ripening mechanism was its inability to fostering anisotropic growth in some systems with higher solute concentration than the equilibrium concentrations (Jun *et al*., 2003). Growth by precipitation was explained by Peng and co-workers as dissolved ions in high-energy facets instead of coarsening, as observed in the supersaturated solutions which prevent dissolution of smaller particles according to literature (Peng, Wickham & Alivisatos, 1998).

Hence, a new route for the synthesis of complex-shaped nanostructures as the building units for crystal growth mechanism was discovered to be "oriented attachment". The attachment of primary particles in an irrepressible and highly oriented pattern in order to achieve secondary mono-crystalline particles (Penn & Banfield, 1998, 1999; Banfield, Welch, Zhang, Ebert & Penn, 2000; Penn, Oskam, Strathmann, Searson, Stone & Veblen, 2001). The mechanism involved self-assembly of adjacent nanoparticles, as they shared a common crystallographic orientation and docking of particles at a planar interface. Bigger particles took an oriented attachment manner. In the process, pairs of high energy surfaces are removed, thereby leading to reduction in the surface free energy (Peng *et al*., 1998; Murray, Kagan & Bawendi, 2000).

2.4 Classical Nucleation

Classically, nucleation is defined as the process of growing crystal, where nuclei (seeds) serves as the template for growth. Mullin (1997) came up with the findings that primary nucleation was usually void of other crystalline matter. Crystallization in solution, as it applied to chemical syntheses followed classical route, except the formation of porous solids (Puntes, Zanchet, Erdonmez & Alivisatos, 2002; Robinson, Zacchini, Tung, Maenosono &

Thanh, 2009). Nucleation was deliberated to be the first step of any new thermodynamic phase, or formation of structures. It may either be heterogeneous (nucleation at nucleation sites on the surfaces in the system) or homogeneous (Pruppacher & Klett, 1997).

Ostwald proposed meta-stable intermediates to precede thermodynamically stable crystalline phase, which then transform into the final product. Ostwald's step rule explained that "phases that are structurally more similar to the solution form more readily" (Ostwald, 1897); but classical theory failed to explain this. Consequently, in a lot of methods, formations of amorphous precursors preceded crystallization of the final products. Nucleation and growth may occur either by the addition of single atoms or molecules or by the aggregation of nano-size building blocks like pre-nucleation clusters or nanoparticles (Banfield *et al*., 2000; Navrotsky, 2004; Gebauer, Volkel & C'lfen, 2008; Pouget, 2009). Non-classical mechanisms (mechanisms involving such precursors) are outside the scope of classical nucleation and growth theory (Colfen & Antonietti, 2005).

2.4.1 Classical Crystal Growth

The classical crystal growth mode was considered to occur via adding up of atom-by-atom, monomer-by-monomer, to an inorganic or organic model. It was achieved by precipitating a solid phase out from solution, i.e. dissolution of small particles/metastable (unstable phase), and re-precipitation of the more stable phase (Dirksen & Ring, 1991). For nanocrystal growth, this could be achieved by the addition of excess solute, resulting in precipitation and formation, while nanoparticles formation involves supersaturation of the solution for nucleation to take place. The dissolution of solute usually occur at higher concentration followed by cooling to lower temperature, or by reaction mixture leading to supersaturated solution (Peng *et al*., 1998; Murray *et al*., 2000). Thus, precipitation process involved nucleation step and growth phases (Pamplin, 1975).

According to reports in literature, the growth of nanoparticles depended on two mechanisms: surface reaction and monomer's diffusion (Sugimoto, 2001). Nucleation stopped as the concentration of growing species decreased below the minimum concentration; then, growth continued until equilibrium (Cao, 2004). Particles generation within short nucleation period was encouraged, as uniform size distribution would be obtained, as reaction would proceed to self-sharpening growth stage when the smaller particles grew quickly at the expense of larger ones due to larger free energy of the smaller particles. A prominent monodispersed size

particle was proposed at this stage, if nucleation and growth can be stopped. Conversely, depletion in the reactants as a result of particle growth led to Ostwald ripening, i.e. growth of larger molecules, at the expense of smaller ones, which got smaller and finally dissolved. Surface energy reduction was considered to be the driving force in Ostwald ripening (Zhang, Liu & Yu 2009).

However, in the experiment carried out by Zhang *et al*. (2009), broad size distribution as characterized by two size regimes (a bigger and a smaller particle with critical size in-between) was attained at growth stage when saturation ratio (S) reduced, and the corresponding critical nuclei size (r*) increased leading to the dissolution of particles lower than the new critical size. At this stage, monodisperse particles were considered difficult, and the particle sizes grew larger even up to micrometer size range. Exhaust of reactants resulted in reduction in saturation ratio, and increase in the critical nuclei size. Hence, for short burst of nucleation, high saturation ratio (S) is the requirement (Zhang *et al*., 2009). Thus, classical growth theory entailed bonding and dissolution of atoms or molecules. There may be occasional attachment to the surface of a large crystal seeds, which may occur in one way or various ways. The atoms or molecules join together by growing and spreading in layers while the molecules on the surface of the growing seed were weakly adsorbed.

2.4.2 Aggregation Growth Modes

Colfen and co-worker described another classical crystal growth mechanism as the deposition of soluble species (atom/molecule) on the solid surface. Aggregation is common to particles with mesoscopic conversion process (Colfen & Mann, 2003). Reviewed literature also accounted growth by aggregation to be larger than those of atom or molecule addition. As particles grew to stable sizes, growth continued by combining with the smaller unstable nuclei instead of colliding with other stable particles.

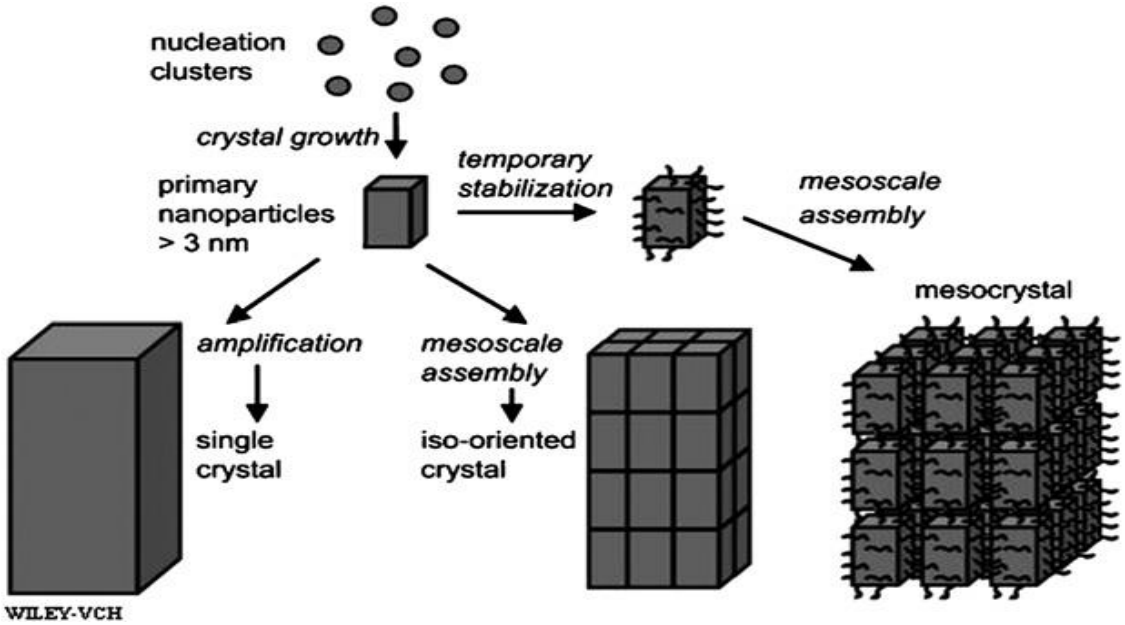

Figure 2.2: Schematic representation of classical and aggregation-based crystallization (Zhang *et al.*, 2009)

Figure 2.2 is the schematic representation of classical growth model and arrangement of primary nanoparticles by oriented attachment. Organic coated nanoparticles formed mesocrystal or mesoscale assembly that form three-dimensional and well-alligned crystals (Colfen & Antonietti, 2005; Kulak *et al*., 2007; Chen, Qiao, Xie, Fan, Zhou & He, 2007). For thermodynamically stable crystal growth kinetics of nanoparticles, Ge *et al*. (2007) proposed addition of surface protective agents like organic ligands or inorganic capping materials or an inert environment for the reaction. However, oriented-attachment growth was reported by Colfen and Antonietti (2005) to be of better advantage, as it produced defect-free one dimensional single crystal; unlike classical crystallization that causes defect structures during fibre growth.

2.5 Coalescence and Orientated Attachment Growth

The difference between coalescence and oriented attachment is the direction of lattice at grain boundary. Coalescence has no preference for attachment, unlike the oriented attachment which has common crystallographic alignment (Zheng *et al*., 2009).

Traditionally, solution synthesis of colloidal nanoparticles was by crystal coarsening via Ostwald ripening mechanism, in which larger particles were grown from small primary nanoparticles, and oriented attachment was considered to be the mechanism of formation. The

sharing of familiar crystallographic orientation and docking of these particles at a planar interface made the adjacent nanoparticles to be self-assembled. In oriented attachment mechanism, pairs of high energy surfaces were removed, resulting in a large reduction in the surface free energy thermodynamically (Mullin, 1997).

"Contact epitaxy" was reported in a research involving deposition of Ag nanoparticles on Cu substrates. The reaction was considered a spontaneous self-assembly. An epitaxial alignment with the substrate was observed in the initial random orientation of Ag nanocrystals; as a result of nanoparticles rotation within the aggregates at short range interaction took place between adjacent surfaces (Averback & Zhu, 1996; Yeadon, Ghaly, Yang, Averback & Gibson, 1998). Many systems were reported to grow either by direct particle aggregation or undirected particle aggregation. These growth modes then resulted in faceted or anisotropic particles growth as it occurred near equilibrium. Oriented attachment was observed in the growth of anatase TiO_2 (Penn & Banfield, 1999).

2.6 Methods for the Synthesis of Nanoparticles

Apart from the naturally occurring nanomaterial, the existing approaches to the synthesis of nanoparticles have been: *the bottom-up approach and the top down approach*. These approaches were originated from Feynman in an American Physical Society lecture in 1959. In his lecture, he suggested that materials and devices could be made-up to atomic specifications (Feynman, 1959). His suggestion, of course, has materialized beyond wildest imagination in our time.

2.6.1 Top-Down Approach

This method is about grinding down of components to achieve nanostructures. Nanoparticles are synthesized from larger components. Examples of techniques involved in this approach are nanolithography, nanomanipulation, mechanical attrition and laser ablation. Filipponi and Sutherland (2010) considered bulk substrate as the starting material, which is then gradually removed step-by-step to build up nanometric size range materials. An easy illustration of top-down approach is the carving of statue from a large marble block. The approach is considered to be economical and support production on a large scale. The challenge of using top-down approach in nanoparticles synthesis is the imperfection of surface structures, which has effect on physical and chemical surface chemistry of the nanostructures. However, introduction of

impurities as it were in nanowires via lithography, internal stress, surface defects and contaminations are inevitable in the approach (Pokropivny *et al*., 2007). An example of this approach is the laser ablation method.

2.6.1.1 Laser Ablation Method/Mechanical Attrition

Laser ablation process proves to be more efficient method of synthesizing nanoparticles with narrow size distribution. The process is further divided into evaporation of the target material and hydrodynamic expansion of the ablated plume into the ambient gas. Routes to nanoparticles formation in laser ablation are:

i. Homogeneous nucleation: Supersaturation of vapour atoms produced by laser ablation takes place.
ii. Particle growth stage: Critical nuclei grow and capture atoms on their surfaces; thereby change into larger particles.

Research proved that aluminium nanoparticles via laser ablation can be doped with carbon using ethylene and argon quench flow. Also, nanoparticles sizes vary in different media of ambient air and gas (Dudoitis, Uleviėius, Raèiukaitis, Ðpirkauskaitë, Plauðkaitë & Lithuanian, 2011; Manikam, Cheong & Razak, 2011; Guoqiang & Wenying, 2012).

2.6.2 Bottom-Up Approach

The bottom-up approach, or self-assembly, is all about manipulating matter from the atomic level to the nanomeric size scale. It involves the miniaturization of components (Feynman, 1959). The technique entails colloidal dispersion approach for nanoparticles synthesis. Again, basic units are built up into larger structures in nanometric size range by use of either chemical or physical forces. In other words, there is an arrangement of minute components to form more complex assemblies (Pokropivny *et al*., 2007).

The synthesis can be related to a brick building arranged on top of each other: the method uses atoms or molecules instead of bricks for self-assembly of atoms into required nanostructures (nanostructures with fewer defects and long range ordering). The method is based on the reduction of Gibb's free energy to achieve nanostructures and nanomaterials close to thermodynamic equilibrium. Unfortunately, the bottom-up approach consumes time and the routes are complex (Poole-Jr. & Owens, 2003).

Bottom-up approach is further divided into gas-phase and liquid-phase methods. Both methods are routed through single atom or molecule as the starting material. Gas-phase method includes plasma arching, chemical vapour deposition etc.; sol-gel method is an example of liquid-phase technique (Yongqi, Fengzhou & Zongwei, 2011). Production of ultra-fine particles/nanoparticles (building block for nanostructured materials) involves chemical reactions and physical routes.

Commercial and industrial productions of nanoparticles are mainly by:

i. Gas phase methods: Methods involving nanoparticles synthesis through gas phase process are vapour deposition, flame pyrolysis, high temperature evaporation and plasma synthesis.
ii. Liquid phase methods: This method involves chemical reactions involving solvents that result in the formation of colloids, aerosols etc.
iii. Sol-gel methods.
iv. Solid phase mechanical methods: This includes grinding, milling and alloying. Different techniques can be used for the optimumzation of nanoparticles properties (Pokropivny *et al*., 2007).

2.6.2.1 Gas Phase Process

2.6.2.1.1 Vapour-Phase Deposition Method

Nanostructures like thin films, nanotubes, multilayers, nanofilaments or nanometric size range particles are usually produce by vapour-phase deposition. Nanoparticles synthesized by gas-phase typically follow the mechanism of homogeneous nucleation of a supersaturated vapour (initiated by small nucleus formation from the molecules), and particle growth (surface growth mechanism) by condensation, coagulation and capture. Oxygen and oxides are the commonly used reactive gases for direct supersaturation when solid is evaporated into a background gas (Pokropivny *et al*., 2007). Common heating methods include flame pyrolysis, furnace flow reactors, laser induced pyrolysis, laser vaporization, thermal plasma, microwave plasma, sputtering and laser ablation. Vapour-phase deposition method can be further divided into two.

Physical vapour deposition (PVD): Thermal evaporation like electron beam heating or flame synthesis, laser ablation/ pulse laser deposition, spark erosion and sputtering are employed in

bombardment of atoms or ions to remove target material in PVD conversion techniques (Pokropivny *et al*., 2007).

Chemical vapour deposition/ Gas-vapour deposition): Chemical vapour deposition (CVD) uses a chemical route for the synthesis of high purity and high performance solid materials. Thin films had been developed through this process in semiconductor industry. However; nano-sulphur was also prepared through this method. Moreover, carbon nanotubes can be synthesized using CVD. Unlike the PVD, substrates are only exposed to more volatile precursors; which in-turn decomposes on the substrate surface to generate the desire nanostructured materials. There is growth control (areas) by photolithography/photomasking: etching of deposition pattern on the surface layer of the wafers (Yang *et al*., 2010).

2.6.2.1.2 Plasma-Assisted Vapour Deposition Synthesis

Protective coatings are obtained using plasma-assisted vapour deposition method. Ionized gas used in both the physical and chemical methods results in materials of high purity. Both the PVD and CVD can be plasma aided. Magnetron sputtering (modified form) a static magnetic field is used around the sputtering target in order to restrict the plasma to the target area. Of course, this method achieves high deposition. Vapourization of material from the solid surface takes place as ions of inert gas bombardment takes place. In plasma-assisted PVD, the vapour is from a solid target; plasma-aided CVD uses gas phase precursors which later condense into thin films or nanoparticles. Plasma enhanced CVD consumes more dissociation temperature as a result of the high energy of the plasma compared with the conventional CVD. Semiconductors and polymers can be deposited through this route. Figure 2.2 is the schematic diagram of vapour condensation process.

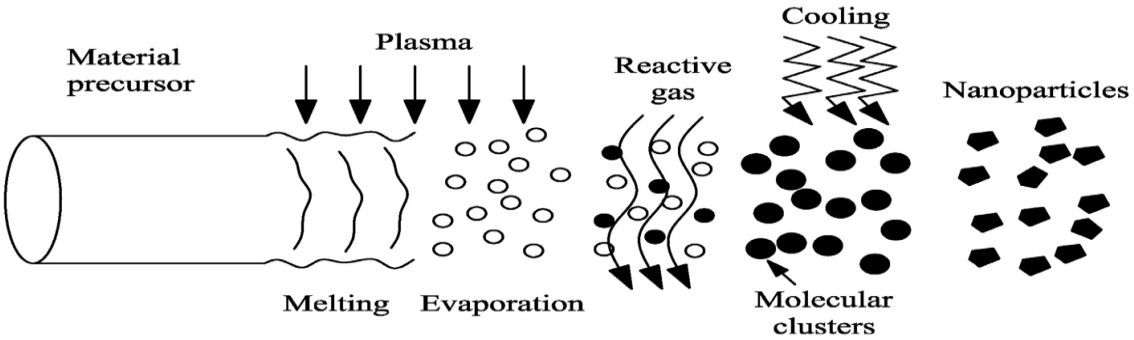

Figure 2.3: Vapour condensation process (Pokropivny *et al*., 2007)

2.6.2.2 Molecular Beam Epitaxy (MBE)

A molecular beam epitaxy (MBE) is a multi-functional machine for nanoparticles synthesis. It is an "ultra-high-precision, ultra clean evaporator, combined with a set of *in-situ* tools such as Auger electron spectroscopy (AES) and/or reflection high-energy electron diffraction (RHEED), for characterization of the deposited layers during growth. Nanostructures that can be synthesized through MBE are the semiconductor quantum wells, superlattices and quantum wires and metallic or magnetic multilayers for spin valve structures. There is also chemical beam epitaxy (Figure 2.4), as the machine uses gaseous sources like metal-organic compounds (metallorganic MBE) (Pokropivny *et al*., 2007).

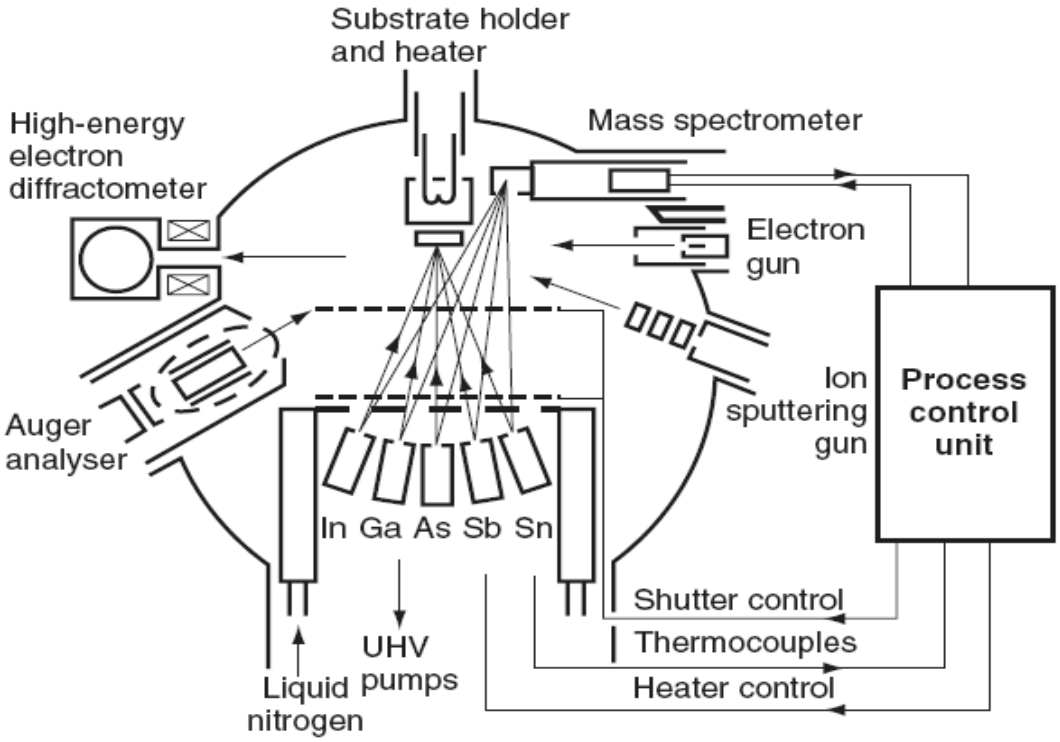

Figure 2.4: Schematic diagram of a molecular beam epitaxy thin film deposition system (Kelsall, Hamley & Geoghegan, 2005)

2.6.2.3 Inert Gas Condensation

Gas condensation method involves the condensation of atoms and molecules in the vapour phase. This condensation method is widely used in nanopowders synthesis. The technique entails the evaporation of metal into a pre-evacuated chamber of about 10^{-7} torr containing low-pressure inert gas. Cooling of metal vapour is by collisions with the inert gas atoms (Figure 2.5). Reaction mechanism includes supersaturation, nucleation and homogeneity. The

outcome of the process is particle size in the range of 1-100 nm. Inert gas variation is the size control measure (Pokropivny *et al*., 2007).

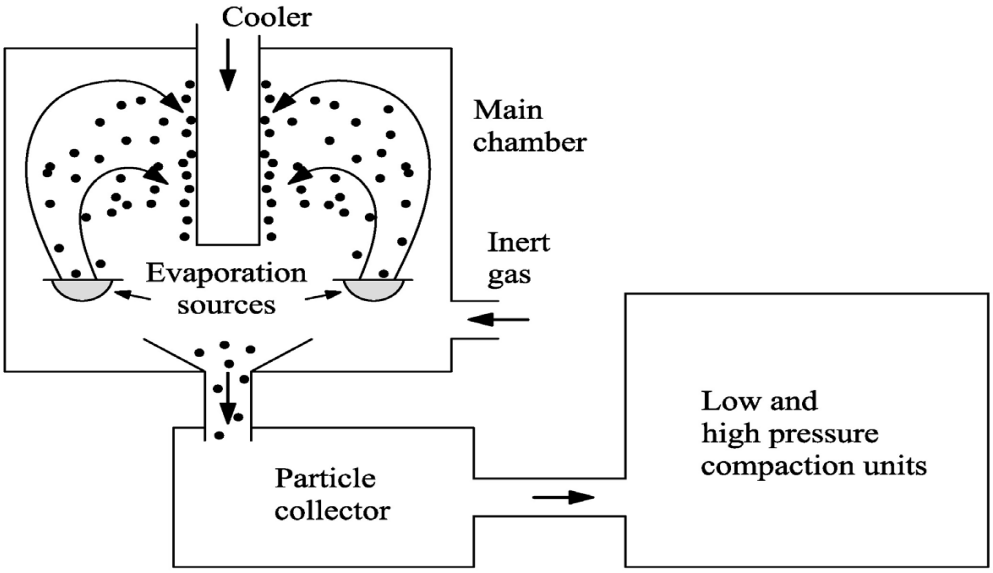

Figure 2.5: Schematic diagram of an inert gas condensation apparatus (Pokropivny *et al*., 2007)

2.6.2.4 Flame Pyrolysis

Flame pyrolysis is another route to nanoparticles synthesis. In this case, heat is the chemical reaction initiator. The starting material is positioned in the heat flow of inert carrier gas, and then the appropriate precursors (materials with low pressure) are fed in. Nanomaterials developed through this method are fumed silica (SiO_2), carbon black, ultra-fine TiO_2 among others. Agglomeration in particles is the only challenge in this method.

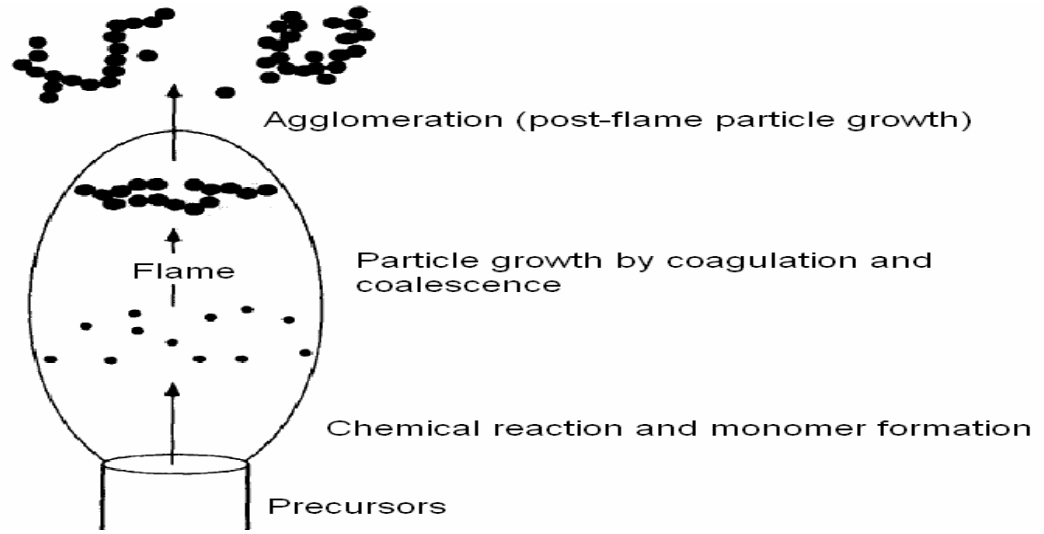

Figure 2.6: Schematic diagram of a flame pyrolysis (Pokropivny *et al*., 2007)

2.6.2.5 Laser Pyrolysis

In this method, infra-red laser is the source of heat for the flowing reacting gas. The absorbed laser energy by the source molecules is also their source of heat. Heating of the precursors results in the supersaturations which invariably yield nanoparticles.

2.7 Liquid Phase Methods

2.7.1 Colloidal Method

This is a wet chemistry method of getting insoluble precipitates. Solution mixtures of different ions are precipitated under controlled temperature and pressure. This method has been the basic principle of metal nanoparticles formation. Faraday, in 1857 was the first scientist to introduce colloidal precipitation by reducing $HAuCl_4$ with phosphorus to produce gold colloids. However, the ancient temple glass stain of red and purple was achieved through gold colloids; the products obtained were of very high quality. Nowadays, nanomaterials of organics, metal, metal oxide and pharmaceuticals are produced by colloidal processes.

Sonochemistry (a sub-set of colloidal method) methods use ultrasonic radiation with precursor solution to initiate chemical reaction. This results in creation, growth and rapid collapse of small bubbles. Acoustic cavitation is used as the control measure. Nanoparticles from colloidal method can also be converted to dry powder by filtering or spray drying (Pokropivny *et al*., 2007).

2.7.1.1 Solution Precipitation

Solution precipitation is used to fabricate single and multi-component oxide nanopowders under optimal reaction conditions. Nanometer-size particles are precipitated inside an incessant fluid solvent. Quantum dots by deposition on substrate, nanocomposites by self-assembly on substrates as ordered 2D and even 3D arrays, which are in the end implanted in other media are also produced. Aging (increase in particle size with time) is the only challenge in many colloidal methods (Pokropivny *et al*., 2007). However, advancement in nanotechnology can still provide solution to this challenge.

2.7.1.2 Mechanochemical Synthesis

The mechanochemical synthesis of nanoparticles involves the combination of mechanical force and chemical treatment. However, the process reaction is about solid-state displacement reaction during ball milling; as well as by-product of larger phase particle. Metal nanoparticles synthesized by this process include Ag, Co, Cr, Cu, etc. as well as oxides and sulphide (Paskevicius *et al.,* 2009). In an experiment carried out during milling, it was found that there was a continuous regeneration of nanometer-sized grain as chemical reactions took place at the interfaces. The reactions were considered to have taken place either by a steady state approach or self-propagating combustion approach (Takacs, 1996). Micron-size particles, as an effect of high temperature and nanosize particles are formed by self-propagating combustion and steady state approach of mechanochemical synthesis respectively (Ding, Miao, McCormick & Street, 1995).

Nanocrystalline particles spread in a soluble salt matrix are the products of mechanochemical synthesis. Nanoparticles as small as 5 nm can be obtained if matrix phase of the resulting powder are removed with suitable solvents. According to McCormick and co-worker, nanoparticles of the desired phase as small as 5 nm could be obtained through selective removal of the matrix phase by washing the resulting powder with appropriate solvents (McCormick *et al*., 2001). The two major types of synthesis involving mechanochemical processing of nanoparticles are sonochemical and electrodepostion.

Sonochemical synthesis: Nanoparticles with special structures and different morphologies are often produced through sonochemical method. Metal and metal oxide nanoparticles are mostly prepared via this method. Iron(iii)oxide nanopowder was successfully synthesized, in which pentacarbonyl $Fe(CO)_5$ served as the precursor (Kataby, Prozorov &Gedanken, 1999;

Pinkas *et al.*, 2008). Other precursors used in sonochemical method included $FeCl_3$, $Fe(NO_3)_3$, $Fe(OAc)_2$, and $Fe(OEt)_3$ (Srivastava, Perkas, Zaban, & Gedanken, 2002). The method is faster, and allows integration of nanoparticles into porous structures (Rajaram *et al.*, 1995; 1998; Schmidt, 2001).

The ultrasonic sound (chemical effect) had been proven from acoustic cavity; as chemical reactions were as a result of formation, growth and implosive collapse of bubbles in liquid (Dierking, Koshbar, Afzali-Ardakani, Lowe & Held, 1997). Hassanjani-Roshan *et al*., (2011) synthesized spherical nanocrystalline iron oxide (Fe_2O_3 nanoparticles), an average size of 19 nm, sonochemically using suspension containing $FeCl_3.6H_2O$ as the starting material which reacted with aqueous NaOH solution as the source of oxygen. The reaction was carried out under ultrasonic irradiation (Hassanjani-Roshana, Vaezib, Shokuhfarc & Rajabalic, 2011).

Electrodeposition: This is a cheap method of nanoparticles synthesis. It is about coating an electrically conductive object of a relatively thin metal layer with electrical current: induction of chemical reactions in an aqueous electrolyte solution when voltage is applied. Metal oxide and chalcogenides nanostructured materials are usually deposited by this technique. Electrodeposition may be anodic (electrochemical oxidation of metal anode in the presence of other ions in solution which react together and deposit on the anode) or cathodic (deposition on the cathode from solution precursors). The reaction may be carried out at low temperatures. Inter-diffusion of materials is reduced when multilayer thin film is fabricated. However, the amount of delivered qantity of charges delivered is used to monitor the thin-film thickness. Current is used to control the deposition rate, magnitude of the applied potential to control composition and defect chemistry. Conversely, there may be a periodic transfer from one electrolytic cell to another. The deposited final film can range in thickness from a few nanomaters to tens of microns.

Furthermore, the reactions may also be carried out inside a nanoporous membrane for growth. Nanocylinders were produced by anodized alumina with cylindrical nanopores of regular dimensions. Limitation in the nanocrystal was observed when deposition took place on planar substrate. However, arrays of defect for nucleation sites for electrodeposition of nanocrystals may be achieved by substrate surface modification using atomic force microscope (AFM) or scanning tunneling microscope (STM). Bio and micro technologies engage electrodeposition technique because:

i. functional materials can be developed via complex 3-D masks
ii. the reaction may take place near room temperature using water-based electrolytes.
iii. few atoms or large dimensions deposition can be obtained (Pokropivny *et al.*, 2007).

2.8 Sol-Gel Method

Sol-gel chemistry is a colloidal chemistry technology that involves transformation of liquid (the sol), chemically into a gel state. The method is common in the fabrication of oxide nanoparticles; solid oxide materials turn up after successive post treatment. Novel materials are the outcome. The method is not expensive. In addition, the process is about colloidal solution of solid particles (*the sol*): a few hundred nm in diameter, which is suspended in a liquid phase. Organic dyes and rare earth (Dopants) of small measure can be incorporated in the sol for products of uniform dispersity; applicable in ceramics and thin-film oxide production (Klein, 1994; Corriu &Trong, 2009).

The sol-gel process is primordial, and it is still relevant in nanotechnology. Products like ultra-fine powders, monolithic ceramics and glasses, ceramic fibres, inorganic membranes, aerogels, etc. had been fabricated via sol-gel method. In the process, a homogeneous solution containing molecular reactant precursors-sol is transformed into a 3D polymer-gel; leading to an elastic equal-volume solid (Brinker & Scherer, 1990). The sol-gel process involves hydrolysis of metal alkoxide with water (nucleophilic), as shown in the mechanisn below:

$$\boldsymbol{M(OR)_y + xH_2O \rightarrow M(OR)_{y-x}(OH) + x\,ROH}$$

According to Pokropivny (2007), sol-gel method results in condensation reaction which releases water molecule and alcohol respectively. The gel formed later dried to get rid of the solvent. Xerogels/aerogels (microporous solid matrices formed at 25-100℃ drying treatment) are used as filters in microfiltration, ultrafiltration, nanofiltration, pervaporation and reverse osmosis. Other products fabricated with this process include various ceramic membranes which are formed by casting and moulding the gels. Silica fibre used in light transmission can also be drawn from gel. Advantages of sol-gel technology are:

i. control of precursor solution to yield excellent stoichiometry.
ii. easy compositional conversions.

iii. low annealing temperature.
iv. coating deposition on large-area substrates
v. low cost and simple equipment
vi. ease of introducing different functional groups
vii. synthesis of choice microstructure

Applications of materials obtained from sol-gel are in optics, space, biosensor, medicine, electronics and separation technology (Klein, 1994; Corriu & Trong, 2009). Other relevance is in protective coatings: optical coatings, anti-reflective coatings, zeolite synthesis, dental and biomedical use of ultra-fine and uniform ceramic powders etc. (Pokropivny *et al*., 2007.

2.9 Microemulsion Method

Microemulsion entails precise particle size control. Xie, Zheng, Bai & Liu (2009) applied this principle in nanosulphur synthesis of size range 50-100 nm from sublimed sulphur, as the reagents in aqueous phase initiated nucleation and nanoparticles growth. However, particle size and morphology control were achieved by altering the water to surfactant molar ratio.

Reverse microemulsion synthesis of rhombic nanosulphur of an average particle size of 10 nm was also produced from biodegradable iron chelate in the work of Deshpande *et al.* in 2008. From sodium polysulphide, Wang, & Yamauchi (2009) obtained nanosulphur using acid catalysis in reverse microemulsion, which resulted in monoclinic sulphur of an average particle size of 20 nm (Deshpande, Khomane, Vaidya, Joshi, Harle, & Kulkarni 2008; Xie *et al*., 2009). From the aforementioned syntheses, the shortcoming of polysulphide as the source of sulphur can be overcome by using green method because polysulphide is needed for nanosulphur.

2.10 Green Synthesis of Nanoparticles

Green synthesis of nanoparticles is, at present, a new research focus among sundry techniques of synthesizing nanoparticles. The method is gaining acceptance due to its eco-friendly nature. It is a bottom-up approach method; the synthesis route includes use of microorganisms (bacteria, yeast, fungi, algae and viruses), plants or plant extracts (Mohanpuria, Rana & Yadav, 2008; Rauwel *et al.*, 2015).

2.10.1 Green Synthesis using Microorganisms

The development of noble metal nanoparticles was initially developed by taking the advantage of either intra or extracelluar inorganic materials by bacteria. Prokaryotic bacteria *e.g Pseudomonas stutzeri* AG259 cultured in high concentrations of $AgNO_3$, *Proteus mirabilis* PTCC 1710, were used to develop silver and gold nanoparticles (Klaus, Joerger, Olsson & Granqvist, 1999). Bacteria-mediated green synthesis has the shortcoming of slow synthesis rate and limited number of sizes and shapes compared with chemical methods of synthesis.

Another green method route of synthesizing metallic nanoparticles is the use of fungi. Microbiology study of fungi is not common because of the difficulty in characterizing them in terms of their microscopic structures and mechanistic studies for nanoparticles characterization (Xu, Jahic, Blomsten & Enfors, 1999). Conversely, fungi-mediated green synthesis was reported to be a better choice in nanoparticles formation compared to bacteria-routed method. The fungi can secrete large quantity of extracellular proteins which played a role as metal reducing agent, capping of newly formed nanoparticles, aggregation reducer and stabilizer (Kitching, Ramani & Marsili, 2014).

Murali *et al*. (2003) engaged the tolerance and metal bioaccumulation ability of eukaryiotics in biosynthesis of nanoparticles. The synthesis mechanism involves the secretion of enzymes (reducing agent) in a large quantity to reduce metal ion (Murali, Absar, Khan & Rajiv, 2003; Mandal, Bolander, Mukhopadhyay, Sarkar & Mukherjee, 2006). However, nanoparticles are considered to be formed on the surface of the mycelia unlike chemical methods where nanoparticles are formed in the solution. Fungus – *Verticillium* reduced Ag^+ to Ag^0 when exposed to $AgNO_3$ solution in the study carried out by Mukherjee *et al.* (2001). Monodispersed and spherical nanoparticles of 25 nm average size diameter were formed. Mechanism in fungi-based method is by adsorption of Ag^+ on the surface of fungi cell. As reported, there was an electrostatic interaction between carboxylate groups in enzymes present in the cell wall of mycelia and Ag ions. This reduced the Ag ions, in return formed silver nuclei (Mukherjee, Ahmad, & Mandal, 2001a).

Different morphologies of nanoparticles arose from varied green synthesis routes; spherical, triangular up to hexagonal morphologies were developed by Klaus *et al.* (1999) via bacteria-mediated method. Ahmad *et al.*, (2011) were the first to account for the fungi mediated green nanoparticles synthesis using *Fusarium oxysporum*, which had better advantage of non-

binding to the biomass over intracellular method (Dur´an, Marcato, Alves, de Souza & Esposito, 2005; Balaji *et al*., 2009; Ahmad *et al.*, 2011). Extracellular yeast green method was also studied by researchers for nanoparticles synthesis (Mandal *et al.*, 2006; Mourato, Gadanho, Lino & Tenreiro, 2011; Apte, Sambre & Gaikawad, 2013). The use of algae (eukaryotic autotrophs) was successful in the production of nanoparticles. In 2007, Singaravelu reported highly stable nanoparticles from marine algae - *Sargassum wightii*. The characteristics of the synthesized nanoparticles through algae were shown to be more stable compare to other green routes (Singaravelu, Arockiamary, Kumar & Govindaraju, 2007). Table 2.1 is the compilled table showing size dependence of some nanoparticles.

Table 2.1: Size dependent synthesis of silver nanoparticles using micro-organisms

Type	Diameter (nm)	Reference
Bacteria		
Pseudomonas stutzeri AG259	200	Klaus *et al.*, 1999
Proteus mirabilis PTCC 1710	10-20	Samadi *et al*., 2009
Fungi		
Verticillium	25 ± 12	Mukherjee *et al.*, 2001a, 2001b
Fusarium oxysporum	5-15	Ahmad *et al.*, 2003
Cladosporium cladosporioides	20-50	Balaji *et al*., 2009
Fusarium oxysporum	20-50	Vigneshwaran, Kathe, Varadarajan, Nachane & Balasubramanya , 2006
Aspergillus fumigatus	5-25	Bhainsa and D'Souza, 2006
A. flavus	5-30	Naqvi, Kiran & Ali, 2013
Yeast		
MKY3	2-5	Kowshik, Ashtaputre & Kharrazi, 2003
Baker's yeast, *Saccharomyces cerevisiae*	60-80	Saravanan, Amelash, & Negash, 2014

2.10.2 Plant-Mediated Green Synthesis of Nanoparticles

The exploration of biodiversity plants, or plant extracts for metal ions reduction is considered a widespread protocol in recent years for the development of nanoparticles and nanostructured materials. Many reviewed literature reported phytochemicals present in the plants as the sources of reducing, stabilizing and capping agents, unlike the chemical method of nanoparticles synthesis that engage the use of harsh and toxic chemicals, which are often adsorbed on nanoparticles surface; consequently, this renders the synthesized nanoparticles inadequate for medical applications (Parashar & Srivastava, 2009).

Furthermore, biomolecules in plants and spices include polyphenols, carbohydrates, essential oils (terpenes, eugenols); they are found to contain active functional groups like the aldehyde, amine and carboxyl entities. There is no doubt that these functional groups are the sources of reducing, stabilizing and capping agents for the newly developed particles as expounded during growth processes (Harekrishna *et al*., 2009).

In addition, plant mediated route of green synthesis using plants with adequate phytochemicals have been confirmed to be faster (nucleation and onset growth commenced within few minutes) sustainable and cheaper than the microbes-routed method and the conventional methods (Rai, Yadav & Gade, 2008). Thus, many challenges encountered in other nanoparticles techniques are predicted to be overcome when plant-mediated procedure is employed in this research. Table 2.2 is the list of some research carried out on green plant-mediated synthesis of nanoparticles as compilled for this study.

Table 2.2: Biodiversity plants for the synthesis of particles with various sizes, shapes and structures

Plant	Part(s) used	Metal/Alloy	Size (nm)/ Shape	Reference
Azadirachta indica	leaves	Ag^{+}	20 nearly spherical shape	Tripathy, Raichur, Chandrasekaran, Prathna and Mukherjee (2010)
Cinnammum camphora	leaves	Ag^{+}, Au^{3+}	55 to 80 triangular or spherical	Huang *et al.* (2007)
Cinnamon zeylanicum	bark	Ag^{+}	31 and 40 Quasi-spherical and small, rod-shaped	Sathishkumar *et al.*(2009)
Aloe vera	Leaves	Au^{3+}	Spherical	Chandran, Chaudhary, Pasricha, Ahmad & Sastry (2006)
Aloe vera	Pulp	Ag^{+}	25 spherical	Zhang *et al*. (2010)
Aloe vera	Leaves	In_2O_3	5-50 nm	Maensiria *et al.*, 2008)
Ipomoea aquatica, Enhydra fluctuans Ludwigia adscendens	Leaves		100 – 400 spherical and cubic	Roy & Barik (2010)
Azadirachta indica	Leaves	Ag core–Au shell	Polydisperse, flat, plate-like, spherical, peculiar core–shell structure	Shankar *et al.* (2004)
Brassica juncea	Leaves	Ag^{+}, Au^{3+}, Cu^{2+}	5–35 50–100	Haverkamp, Marshall & Agterveld (2007)
Medicago sativa fcc	Leaves	Au^{3+}	4–10 twinned, crystal	Gardea-Torresdey *et al.*, (2002)

			and icosahedral	
Desmodium triflorum		Ag^{+}	5–20	Ahmad *et al.* (2011)
			Spherical	
Diopyros kaki	Leaves	Pt^{2+}	2 to 12	Song, Kwon & Kim (2010)
Gliricidia sepium	Leaves	Ag^{+}	27	
			spherical	
Afronomum	Seed	Ag^{+}	27	Dare *et al*. (2014)
melegueta	Leaves	Ag^{+}	13.1	
	Leaves	Ag^{+}	14	
Anacardium	Leaves	Ag^{+}	19	
occidentale Linn.				
	Leaves	Ag^{+}	8	
Pisidium guajava	Leaves	Ag^{+}	17	
	Leaves	Ag^{+}	33	
	Leaves	Ag^{+}	9	
Ocimum gratissimum				
	Leaves	Ag^{+}	43	
Newbouldia laevis	peels	Ag^{+}		
Gangironema	Stalk	Ag^{+}		
latifolium				
Piper guineense	Leaves	Ag^{+}		
Citrus aurantifolia				
Xylopia aethiopica				
Capsicum chinense				
Vernonia amygladina				

Shankar and co-workers fabricated hybrid nanoparticles via plant mediated synthesis. In the experiment, *Azadiracta indica* (Neem) leaf broth was used to develop Au, Ag and bimetallic Au core-Ag shell nanoparticles. Equal volume of silver and gold ion mixture was reduced using the phytochemicals like flavanone and terpenoids present in the leaves. In the experiment, the reaction was possible due to the presence of reducing sugars and terpenoids that acted as the reducing/capping agent. UV-Vis spectrophotometer was used to monitor the reaction rate. In their findings, reaction rate was faster in the reaction mixture of bimetallic (1:1 of Ag^{+}:$AuCl^{4-}$). The synthesis was characterized by an increase in the intensity of gold surface plasmon band (λ_{max} = 557 nm) than in the case of the pure $AuCl^{4-}$ ions nanoparticles synthesis. It was also noted that there was no intensity band corresponding to silver nanoparticles; as silver ions were assumed to be inadequate to form a uniform layer around the gold nanoparticles. Reaction times in Au/Ag hybrid nanoparticles formation and single Ag nanoparticles formations were 30 minutes and 2 hours respectively. Acceleration in the reduction of gold ions took place in the competitive process of silver and gold. A very few Ag NPs was noticed in the TEM result of the bimetallic mixture, as larger Au NPs were formed. The FT-IR spectrum of the hybrid nanoparticles indicated 1615 cm^{-1} (conjugated C=C or C=C of aromatic ring), 1400 (germinal methyls), and 1077 (ether linkages) cm^{-1}. All these were the same for the FT-IR spectrum in those of pure silver and gold nanoparticles (Shankar, Rai, Ahmad & Sastry, 2004).

The bimetallic Au/Ag hybrid nanoparticles of spherical morphology were of the average size between 50-100 nm, as confirmed by TEM. EDAX spectrum also indicated the presence of silver and gold in one of the core-shell particles in the experiment. In the metal hybrid formation, Ag NPs were formed after the equilibration of Au NPs as reported; hence, Ag NPs assembled onto the surface of the large AuNPs, indicating Au/Ag core–shell nanoparticles size and shape (Shankar *et al.,* 2004). From this experiment, another research can consider other metal and metal hybrid bimetallic nanoparticles formation by using plant extracts rich in phytochemicals to replace the harsh and toxic organic solvents.

The influence of parameter variation (temperature, metal ion concentration and leaf extract ratio) on the size of gold nanoparticles synthesis was studied by Kumar & Yadav (2013) using *Syzygium cumini* leaf extract. The results of his findings showed a mass increase in gold nanoparticles formation at 1, 3 and 5 mM metal ion concentrations. This was attributed to the presence of adequate substrate ions compared with the amount of reducing/stabilizing agents

in the reaction mixture before attaining critical level (Mohanpuria, Rana & Yadav, 2008). Aggregation was noticed at concentrations above 5 mM as concentrations below or above critical level resulted in none formation of nanoparticles (Dubeya, Lahtinenb, Sarkkaa & Sillanpaa, 2010). Nanoparticles diameter size range between 43 and 70 nm was achieved in their result.

Moreover, there was increase in intensity peak of absorbance of nanoparticles formed as compared to gold nanoparticles produced at room temperature. The influence of incubation temperature resulted in the varying particle sizes- 32 $\pm$ 3 nm, 53$\pm$ 4nm at 0°C and 80°C respectively. Uniformity was observed in the experiment due to enough stabilizers inside the plant extract to balance the metal ion reduction with the increase incubation temperature but little aggregation was noticed in the gold nanoparticles formed at 80°C.

Furthermore, increase in the leaf extract ratio increased the quantity of gold nanoparticles synthesized in the experiment from 5% to 40% with particle sizes around 38$\pm$ 7 nm and peak intensity at 550 nm. Reduction in gold nanoparticles size was observed in the experiment at an increased leaf extract ratio, due to the effect of adequate capping agents in the leaf extracts used (Kumar & Yadav, 2013).

Dare *et al*. (2014) reported the synthesis and kinetics of growth of nanosilver under bio-diversified plant influence. Coarsening and particle growth mechanism model were applied in the experiments. The following were the utilized plant extracts: *Afromomum melegueta, Anacardium occidentale, Capsicum chinense, Citrus aurantifolia, Ocimum gratissimum, Newbouldia laevis, Piper guineense, Pisidum guajava, Gangronema latifolium, Telfairia occidentalis, Xylopia aethiopica and Vernonia amygdalina*; these plants are all available in Nigeria. In their study, growth kinetics of bionanoparticles was elucidated as this aspect of plant-mediated green synthesis is not well attended to compare with chemical methods.

Nanoparticles formation took place in all the biodiversity plants engaged, with the evidence of colour change and plasmonic band resonance (PBR) in the reaction mixtures; except in the plant extracts of *Telfairia occidentalis* and *Citrus aurantifolia*. High acidity level and deficient biomolecules for Ag^+ reduction was explained to be responsible for such failure. Reaction completion was noted within 15th to 30th minutes of the reaction commencement with the evidence of spectra overlap in the successful plants for Ag^+ reduction. Very fast reactions observed in some plant extracts considered were attributed to adequate biomolecules

(Usman & Osuji, 2007; Tanko, Kamba, Saleh, Musa & Mohammed, 2008), as the slow reaction rate in others could be as a result of interaction between biomolecules and the growing silver nanoparticles-isotropic time dependent. In the nanoparticles characterization, nanoparticles of average sizes in all the plant extract used for the experiment ranged between 9 and 53 nm as confirmed by TEM. Bragg reflections with 2θ values 38.13°, 46.19°, 63.42° *and* 77.17° matching (111), (200), (220) and (311) plane lattice which indexed for face-centred cubic structure of silver were obtained from XRD as the Crystallinity nature of the Ag NPs produced (Huang *et al.*, 2007). Lifshitz–Slyozov–Wagner model (LSW) of growth mechanism for coarsening showed time-dependence of the particle size and size distribution (Lifshitz & Slyozov, 1961). The first step was through Ostwald Ripening (OR). Thompson–Freundlich model was considered as diffusion controlled, which decreased as particles grew to its maximum. The mechanism is dominated by diffusion-limited coarsening. Variation in the particle average sizes was explained as the effect of physicochemical, phytochemical and toxicity in individual plant used (Usman & Osuji, 2007; Aboua, Seri-Kouassi & Oua, 2010).

The research also predicted the coarsening of silver nanostructure using green method by OR, or OR → OA mechanism. Dual mechanism (OR → OA) was proposed to be responsible for the swift direction to coarsening (assembly) rather than the hypothetical nucleation-growth process. They also reported competition between coarsening and aggregation process (solution phase synthesis) with nucleation and growth process that is often produced big nanoparticles size (Arunasish *et al.*, 2012).

Many researches were carried out on plant-mediated routes to nanoparticles synthesis. Tripathy *et al.* (2010) engaged *Azadirachta indica* (Neem) leaves to develop silver nanoparticles. Silver and gold nanoparticles of triangular and spherical shapes were fabricated from *Cinnamomum camphora* extract (Haung *et al.*, 2007). Sathishkumar and co-workers used the bark extract of *Cznamon zeylanicum* to synthesize crystalline nanosilver (Sathishkumar *et al*., 2009). Chandran *et al*. (2006), Maensiria and co-workers (2008) and Zhang (2010) used *Aloe vera* plant; all in different experiments to synthesize gold and silver nanoparticles, indium oxide nanoparticles and silver nanoparticles respectively (Maensiria *et al*., 2008; Zhang *et al*., 2010). Weed resources- P*omoea aquatica*, *Enhydra fluctuans* and *Ludwigia adscendens* were explored by Roy and Barik (2010) to produce silver nanoparticles of average size range of 100-400 nm and different shapes. Gold, silver and copper alloy

nanoparticles were also synthesized in-vivo from *Brassica juncea* leaves (Haverkamp *et al*., 2007). Gold nanoparticles formation and growth inside live 'alfafa' plants was developed (Gardea-Torresdey *et al*., 2002), just to mention few. Researchers are still exploiting plant-mediated green synthesis for the development of nanoparticles and nanomaterials nowadays.

2.11 Pathogenicity of Microorganisms

Microorganisms capable of causing disease in plants, animals or insects are known as pathogen: biological agent that can damage its host during interaction. The damage on the host may be by toxins or virulence factor. The first damage is inflicted directly by the organism, while the latter is indirect via the activity of the host immunity responses. Pathogenicity can then be defined as the ability of microorganisms to transmit a disease or turn out into disease in a host organism (Casadevall & Pirofski, 1999). The extent of pathogenicity of the microbe is known as virulence, which is determined by the genetic, biochemical or structural characteristics that allows microbes to produce disease in a host. According to Sousa (2003), virulence is established by mechanisms of gaining access to environment and to the nutrients appropriated within them. These nutrients are then released in an exploitable form, and then move to new host after the nutrients are exhausted (Sousa, 2003; Todar, 2002).

Disease causing pathogens may be opportunistic, obligatory or facultative. Obligatory are pathogens that require living host for reproduction and survival; however, it can infect healthy immunocompetent individuals of susceptible host species, e.g. *Mycobacterium tuberculosis* (Cohen & Murray, 2004). Opportunistic pathogens are of low virulence to living hosts; and flourish on organic substrates. They powerfully and progressively attack potential host with compromised immune responses (Scheffer, 1991). Sufficient 'key-and-lock' depends on the interaction between hosts and pathogens. Molecular interaction is facilitated by the genetic make-up of both the hosts and the pathogens. Genetic variations, selection of the best-fitting mutants, and retention (or progression into disease) are the fundamental processes for alterating the interactions (Lynch & Conery, 2003).

Many pathogenic microorganisms attach themselves to their hosts through adhesins or specialized adherence factors (Hahn, 1997). However, they either physically penetrate or enter the host. Infection can be intracellular; as occurs in *Salmonella*, *Mycoplasma*, *Mycobacterium* spp., *Legionella* spp., *Shigella* and *Chlamydia*, or extracellular as occurred in *Pseudomonas*

aeruginosa. Intracellular bacterial pathogens are known to enter the host cell by an active invasion process that is made possible by surface-exposed proteins (Isberg, Voorhis & Falkow, 1987). Plant-pathogenic bacteria are mainly extracellular microorganisms that enter and multiply in host tissues through wounds or natural openings like stomata and microscopic pores in the leaf. Most mammalian fungal pathogens are also considered to be extracellular, in which some attack the host cytoplast (Tsarfaty, Sandovsky-Losica, Mittelman, Berdicevsky & Segal, 2000; Wasylnka & Moore, 2002).

2.11.1 Pathogenicity of *Staphylococcus aureus*

Staphylococcus aureus is a spherical bacterium (Gram-positive) of about 1 μm diameter. Its cell division takes place in more than one plane, and forms grape-like clusters. It is a hazardous human pathogen. It is a common infection of healthy skin, skin glands and mucous membranes (Crossley & Archer, 1997). According to Heyman (2004), about 20-30 % of the general population are carriers of *S. aureus*. Liu *et al*. (2006) reported the golden pigmentation of *S. aureus* colonies as a result of the presence of carotenoids: a virulence factor protecting the pathogen against oxidants produced by the immune system.

Staphyloccoci are also known to be facultative anaerobes – they produce energy by aerobic respiration and through fermentation, resulting in lactic acid. *Staphylococcus* sp. is catalase-positive and oxidase-negative; these characteristics differentiate it from *Streptococcus* sp. S. *aureus* can survive on complex nutrients like amino acids and vitamins. It possesses *peptidoglycan* structure cell wall (Crossley & Archer, 1997).

The manifestations of *S. aureus* infection include 'central venous catheter-associated bacteremia with ventilator- assisted pneumonia, endocarditis, osteomyelitis, toxic shock syndrome, staphylococcal foodborne diseases (SFD) and scalded skin syndrome (Schito, 2006). Infection through *S. aureus* can also be contacted via frequent catheter insertions and injections in hospitalized patients (Lindsay & Holden, 2004). Diekema and co-workers also reported lower respiratory track, bloodstream, skin and soft tissues infection by *S. aureus*. In addition, the pathogen was discovered to develop antimicrobial resistance aside other severe infections caused by it (Diekema *et al.*, 2001). The degree of pathogenicity of *S. aureus* (virulence factor) is as a result of many combined virulence determinants (Lowy, 1998). This comprises structural and further infection through its secreted products like '*α*-hemolysin, *β*-hemolysin, *γ*-hemolysin, leukocidin, and Panton-Valentine leukocidin (PVL)' which causes

osmotic cytolysis (Kaneko & Kamio, 2004; Plata, Rosato & Węgrzyn, 2009), colonization process by many adhesions, covalently attached to the cell peptidoglycans: adherence factors (Speziale, Pietrocola & Rindi, 2009).

2.11.2 Pathogenicity of *Streptococcus pyogenes*

Streptococcus pyogenes is a facultative, anaerobic Gram positive bacterium that grows in chains - extracellular. The pathogen is commonly known as beta-hemolytic group A streptococcus, or GAS because it showed antigen A on its cell wall; hence, it was classified by Lancefield serotyping as group A (Todar, 2002). It is known to cause soft infection of the skin and throat. Lately, the pathogen has been observed to cause severe infection in human (Canningham, 2000). Alarming death cases from *S. pyrogenes* have been reported (Carapetis, Steer, Mulholland & Weber, 2005). The pathogen infects by ahhesion of the bacteria onto human, and then spread to many organs (Terao, Kawabata, Kunitomo, Nakagawa & Hamada, 2002). It has β-hemolytic pattern of growth on blood agar (Collins & Kennedy, 1983; Cunningham, 2008; Bessen, 2009).

Fever, enlarged nostrils, pneumonia, cervical lymph nodes and malaise are caused by *S. pyogenes* infection. Streptococcal toxic shock syndrome, joint inflammation, carditis and CNS complications, hypertension, abnormalities of the urinary sediment, acute kidney pains, etc. are the complications of *S. pyogenes* (Carapetis *et al*., 2005; Cunningham, 2008).

S. pyogenes is a human pathogen that can be transmitted through hand contact with nasal discharge, respiratory droplet and skin contact with impetigo lesions. Contact with the surfaces of the pathogen found in its carrier state (in the anus, pharynx, skin, and vagina) can also spread the infection. The infection can spread to cattle, which can then be recontacted by human through raw milk and contaminated food sources (Bessen, 2009; Rasi & Pour-Heidari, 2009; Mead & Winn, 2000; ICMSF, 1996; Katzenell, Shemer & Bar-Dayan, 2001).

2.11.3 Pathogenicity of *Escherichia coli*

E. coli is a rod-shaped, Gram-negative and oxidative-negative pathogenic bacterium. It belongs to the family of Enterobacteriaceae. Aerobic and anaerobic at human body temperature (37°C) are its growth modes. It possesses peritrichous flagella which make the bacterium to be motile, it can also be non-motile. Plating of faecal samples on selective media is the method of isolating *E. coli*. Lactose-fermenting and non-lactose-fermenting strains can

be distinguished from each other by pH change in lactose fermentation. Red or pink colouration on medium (e.g. MacConkey agar) is the positive test result for the presence of *E. coli* colonies. This method is used to isolate *E. coli* from Gram-positive bacteria and other members of the family. All *E.coli* stains ferments lactose except most EIEC and Shigella strains. Thus, molecular techniques are more relevant in detecting and identifying the pathogen (Croxen, Scholz, Keeney, Wlodarska & Finlay, 2013).

Escherichia coli are opportunistic bacteria found in human gastrointestinal tract. They become pathogenic when certain genetic materials are acquired by them. It is one of the diarrhea causing agents. Other infections caused by the bacteria are septicemia, peritonitis, abscesses, meningitis, and urinary tract infections (UTI) in humans. The virulene factor is its ability to generate a hemolysin (Cavalieri, Bohach & Snyder1984; Wanke, 2013). *Escherichia coli* are also responsible for the postweaning diarrhea in pigs; causing mortality, morbidity, decreased growth rate, among others (Fairbrother, Nadeau & Gyles, 2005). *E. coli* is found to be sensitive to pH, temperature and some other stimulants. Example of its temperature and osmolarity (environmental) sensitivity is its ability to change its outer pore membrane diameter in order to get nutrients, or to prohibit inhibitory substances. It can also sense the presence of chemicals thereby responding by turning away from them. The presence of *E. coli* in the human intestine and faeces serves as an analytical tool to sense water contamination and faecal pollution; hence, wherever *E. coli* is found, there may be contamination by human intestinal parasites (Hooper & Gordon, 2001).

2.11.4 Pathogenicity of *Pseudomonas aeruginosa*

The pathogen *Pseudomonas aeruginosa* is an opportunistic bacterium. It can be found in the soil and aqueous surface in the environment. It can survive many sites, even medical facilities due to its very strong antibiotic resistance. The microorganism emerges and spread as this effect causes high mortality and morbidity; as a result, prevention and alternative treatment call for attention. The infections caused by *P. aeruginosa* are nosocomical, related with compromised host defense. It can be seen in the case of brutal burns, neutropenia, or cystic fibrosis (Lyczak, Cannon & Pier 2000; Hidron *et al.*, 2008). Airway infections–acute or chronic is an infection caused by *P. aeruginosa,* commonly found in hospitalized patients, which can be hospital or community acquired by defect in immunity (Arancibia *et al*., 2002).

Literature shows that the phenotype of *P. aeruginosa* isolated from acute infections exhibit many virulence factors different to those separated from chronic CF lung infections; which lack flagella, pili, downregulation in virlence mechanism (Smith, Buckley and Wu, 2006; Hogardt & Heesemann, 2010). Other virulence factor includes initiation of inflammatory response by flagella and pili (adhesins and maens of motility). T3SS (means of injecting toxins directly into host cells by pathogenic Gram-negative bacteria) is a virulence determinant that leads to acute invasive infection; resulting in enhanced mortality in infected patients (Sadikot, Blackwell, Christman & Prince, 2005; Hauser, 2009).

P. aeruginosa secret other virulence factors which contribute to pathogenicity. For example, exotoxin - an ADPRT, hinders host elongation factor; resulting in inhibition of protein synthesis, that lead to suppression of host immune response and death of cell (Schultz *et al*., 2000). However, the infections are extremely difficult to treat, as they resist antibiotics by different mechanisms of antibiotic resistance: intrinsic, acquired and adaptive (Moore & Flaws, 2011). There are few drugs to combat infections caused by *P. aeruginosa*; old drugs with many reported side effects are been considered again (Livermore, 2002). Hence, protein secretion systems, virulence factor, intrinsic drug resistance and efflux systems were reported to give insight to pathogenicity and persistence of *P. aeruginosa*. Nevertheless, the antimicrobial activities of the synthesized nanoparticles in this work may give support to the available antibiotics; targeting flagella or type 4 pili antigens of the stubborn pathogen.

2.11.5 Pathogenicity of *Candida albicans*

Candida albicans is a pathogenic and opportunist fungus (opportunist in patients with compromised immunity, immunologically weak persons or even healthy individuals). It is found to be a harmless commensal living in the genito-urinary tracts and gastrointestinal of about 70 % person. Studies showed that three out of four women are victims of infection caused by this microorganism once in their lifetime (Sobel, 1997; Meiller, Hube & Schild, 2009; Ruhnke & Maschmeyer, 2002; Schulze & Sonnenborn, 2009).

Candidiasis is the familiar infection caused by *C. albicans*; ranging from thrush (mucosal infections) that affects the vaginal, gastrointestinal epithelial cells, or oropharyngeal Mucosa. Vulvo Vaginal Candidiasis (VVC) with reoccurrences as Recurrent Vulvo Vaginal Candidiasis (RVVC) is common in women. The infection could be life-threatening in HIV

patients, low-birth weight infants and chemotherapy patients (Pfaller & Diekema, 2007; Schelenz, 2008).

C. albicans is a highly infectious fungus unlike other non-*albicans* genus- *Candida glabrata, Candida krusei, Candida dubliniensis, Candida parapsilosis* and *Candida tropicalis* that are recovered from infected persons (Gozalbo, Roig, Villam & Gil, 2004). Mortality rate as a result of *C. albicans* infection is as high as 50 % through bloodstream infections (Wey, Mori, Pfaller, Woolson & Wenzel, 1988; Gudlaugsson, Gillespie & Lee 2003; Eggimann, Garbino & Pittet, 2003). Formation of biofilm results in high-level drug resistance to many antifungal drugs (Douglas, 2003; Donlan & Costerton, 2002; Kumamoto, 2002); dislocated cells from biofilms resist the available drugs more than the free-living planktonic (Baillie & Douglas, 1998a,1998b; Ramage, Bachmann, Patterson, Wickes & Opez-Ribot, 2002).

Literature has shown that low drug infiltration through biofilms, mutants with defective biofilm are reasons for high drug resistance in fungi (Al-Fattani and Douglas, 2004; Ramage, VandeWalle, Opez-Ribot & Wickes, 2002). The two determinant factors of C. *albicans* pathogenicity are: (1) its virulent factors and (2) immune level of the host. From the microbial status, pathogenicty factors include host cell adhesion to array of surfaces for colonization and infection, hydrolytic enzymes secretion (e.g, SAPs - secreted aspartyl proteinases, phospholipases A, B, and C- the virulence factor) and biofilm formation on surfaces- biotic and abiotic (Cutler, 1991; Ghannoum, 2000; Calderone, 2002; Naglik, Challacombe & Hube, 2003; Ganguly & Mitchell, 2011). Virulent determinant in *C. albicans* includes Phenotypic Switching (Slutsky, Staebell, Anderson, Pfaller & Soll, 1987).

2.11.6 Pathogenicity of *Trichophyton rubrum*

Trichophyton rubrum is a mould fungus. It belongs to the dermatophytes group. *T. rubrum* causes skin infection (Dermatophytosis), which results in long and expensive treatment. Its ecological distribution determines their epidemiology; classified in anthropophilic, geophilic and zoophilic fungus. Villanueva (2010) reported the characteristics of *T. rubrum* as an etiologic agent of dermatophytosis which includes resistance structure, inhibition of host immune response via proteolitic enzymes and compounds, resistance system to antifungals. Infections caused by this pathogen are ringworm or tinea. The sites of the wound determine the names of the clinical forms, e.g. *Tinea capitis, Tinea facie, Tinea corporis, Tinea manum, Tinea cruris, Tinea pedis,* and *Tinea unguium* (feet infection) or *onychomycosis* (fungal

infection of fingernails or toenails resulting in thickening, roughness, and splitting of the nails)" (Infections caused by *T. rubrum*). Dermatophyte enters the host body via wound on the skin, scars and burns (Weirzman & Summerbell, 1995).

The pathogenicity factors determine the sites for *T. rubrum* infection, as it can exist in more than one clinical form. Other infection caused by the microorganism includes discolouration, loss of nails, scaly and thickening. Immunocompetent and immunocompromised people are at the risk of *T. rubrum* infection. Age, weather, anatomic sites, geographical locations, are the known factors that constitute occurrence of dermatophytosis. *T. rubrum* is common in tropical areas, and it often affects the feet. Good hygiene and avoidance of sharing infected objects can prevent the transmittance of *T. rubrum* infection. The dermatophyte infection of the pathogen can be tested through culture of the clinical samples or by fungus isolation in a cultured medium, also via molecular techniques (Villanueva, 2010).

2.12 Plant Description and Ethnobotanical Use

Canna indica (Linn.) belongs to the family Cannaceae. It is a medicinal plant of diverse uses. It is commonly known as Indian shot. Its ethnobotanical names in Nigeria include *idoro, Aberekanwo* (Yoruba), *Gwangwama* (Hausa), *Idodo, ido* (Ibo). It is a perennial plant growing up to to 1.5 m (5ft) by 0.6 m (2 ft). The leaves are fleshy with thin margins, usually not more than 1 foot long, and half as broad, lanceolate to sub-orbicular. Flower of *C. indica* is considered to possess both male and female organs-hermaphrodite (Lamaeswari & Ananthi, 2012). It is an herb with rhizomatous root stocks; reddish or yellowish showy flowers. It encompasses a variable number of rounds, shiny black seeds. In folkloric medicine, root decoction is used for the treatment of fever, dropsy, and dyspepsia. Seed juice is used to relieve earaches. The flowers are also used to cure eye diseases (Kirtikar and Basu, 1987; Nadkarni, 1991). Many varieties of *C. indica* are grown in the gardens and around houses for beautification. Its flowers were found to contain anthocyanins and methylated anthocyanidin glycosides (Lehn & Ourisson, 1962; Lin, Chung, Gan & Chiang, 1987).

The ethnomedical use of *C. indica* leaves include antimicrobial (Abdullah, Raus & Jamal, 2012), analgesic and anthelmintic activities. The flowers are known to cure eye diseases (Nirmal, Shelke, Gagare, Jadhav & Dethe, 2007) and shows antibacterial activity (Lamaeswari & Ananthi, 2012). Luteins, ß – carotene, violxanthin are the antioxidants in the flower of *C. indica* (Joshi, Kadam and.Kaldhone, 2008). Chemical components in the leaves

include lignin, furfural, hemicelluloses, and the rhizomes contain 5, 8- henicosdine, tetracosane, tricosane (Deming & Tinoi, 2006; Kolhe, Nirmal & Pal, 2008). Research also proved that extraction of *C. indica* rhizomes using water was effective for HIV-1 reverse transcriptase inhibitory activity (Woradulayapinij, Soonthornchareonnon & Wiwat, 2005). Extraction of the aerial parts using methanol confirmed antioxidant activity (Indrayan, Bhojakb, Kumara & Gaur, 2011). Phytochemicals - anthocyanins and methylated anthocyanidin glycosides were also contained in *C. indica* flowers (Srivastava & Vankar, 2010).

Senna occidentalis (Linn.) belongs to the family of Caesalpiniodea. It is commonly known as coffee senna. Vernacular names include *Akidi agbara (Igbo,)* Abo rere (Yoruba) and *Dora rai* (Hausa). In Western part of Nigeria, it is used for 'fekun' treatment, also concoction for 7th month pregnancy. The Yoruba tribe in Nigeria also uses *S. occidentalis* in the treatment of convulsion in children, when homogenized with palm oil. It is also used as blood cleanser and body cleanser after parturition for Trinidad citizens (Burkill, 1995). Ethnomedically, *S. occidentalis* is used in Africa for the treatment of abscesses, pile complaints, birth control, bronchitis, bruises, cataracts, childbirth, constipation, dysentery, edema, erysipelas, eye infections, fainting, fever, gonorrhoea, guinea worms, headache, hematuria, haemorrhages (pregnancy), hernia, increasing perspiration, inflammation, itch, jaundice, kidney infections, leprosy, malaria, pain (kidney), menstrual disorders, rheumatism, ringworms, scabies, skin diseases, skin parasites, sore throat, stomach ulcers, stomach ache, swelling, syphilis, tetanus, worms, water retention and wounds (Egharevba, Odigwe, Abdullahi, Okwute & Okogun, 2013).

Coffee senna species are typically shrubs or subshrubs that contain yellowish flowers. They have extrafloral nectarines. The leaves are paripinnately compound, the leaflets opposite, often with globose to clavate or cylindrical glands on the petiole and/or the rachis. Flowers are in few too many flowered racemes, pedicels without bracteoles. The fruit is a legume (Egziabher *et al*., 1989; Boulos, 1999 & Marazzi *et al*., 2006). The plants are also used for landscape gardening.

Nicotiana tabacum (tobacco) is a family member of solanaceae; an annual cultivated herbaceous plant. The leaves are commercially processed into tobacco. The plant can grow to up to 2.5 metres height (Ren, Nan, Timko & Michael, 2001). *N. tabacuum* possesses green leaves with pinkish flower; the leaves (ovate to lanceolate) are alternative, spiraling around

the stem. The plant parts contain sticky, short viscid (gummy) glandular hairs that exude secretion containing nicotine. It also serves as ornament due to its attractive and aromatic flower. Its tribal names in Nigeria are *ewe taba, ewe lapalapa, otaba and taba*, used in the treatment of ringworm, cold, ulcers, nausea, and anthelmintic. The large amount of toxin present in tobacco finds application in insecticides. The medicinal use of *N. tabacum* developed to routine smoking and chewing, as this habit of smoking, and additive effects of nicotine present in tobacco are dangerous to health (Flora of China, 1994).

Momordica charantia (Linn.), a member of Cucurbitaceae family is a climber with tendrids, leaves glabrous and lobed, palmate leaves. It is commonly known as African cucumba. Some tribes in Nigeria name it *Ejinrin were* (Yoruba), *Alo-ose* (Ibo), *Kakayi* (Hausa). It is used to treat diabetes, piles, convulsions, jaundice, sore, nervous disorders, diabetic recipe, emetic, night blindness, aphrodisiac and dysmenorrhoea in traditional medicine. The plant also possesses anthelmintic and antimicrobials properties. *Cassytha filiformis*is (Linn.), a family member of Lauraceae, is a parasitic, leafless plant. It is a perennial vine which sticks to the host. It spreads through the top of bushes and trees. The stem of *C. filiformis* is about 1 to 3 mm in diameter with maximum length of 10 to 20 feet. Single seed of *C. filiformis* contains a membranous testa with undefined separation from the cotyledons (Mythili, Gajalakshmi & Sathiavelu (2011). The plant has trivial use in the rural areas. The fruit serves as food both for birds and human beings. It is a love vine in the Caribbean region due to its aphrodisiac ability. Some *Cassytha* species are valuable as source of cord in the rural area, used to bind materials (Esbaugh, McClure & Bolyard, 1985).

The ethnomedicinal application of *Cassytha filiformis* in pacific region includes the treatment of cancer; traditionally used to treat some birthing issues by taking the juice from the crushed vine for a month before delivery, in order to ease labour pains. It was also reported in the treatment of gonorrhoea, kidney ailments and the diuretic in Taiwan. However, *C. filiformis* also find application in the treatment of cancer in Africa. In Kiribati, the plant is used for sorcery; fishing magic in Ulithi, head garlands for picnics in Hawai (Nelson, 2008).

Hibiscus sabdariffa also known as roselle is indigenous to tropical Africa. It belongs to Malvaceae family. *H. sabdariffa* is an erect or branched annual herb that produces red flowers (calyx and bract). The stem is about 3.5 m high. It has green to dark red leaves, alternate, glabrous and long petiolate. In Nigeria and Sudan, it is used in the preparation of red tea, karkade and zobo drink. Other drinks from the calyces are red sorrel, rosella and sour tea. The

fresh or dried calyces of *H. sabdariffa* are also used for making herbal tea, cold and hot beverages, wine chocolate, flavouring agents, pudding and cakes (Esselen & Sammy, 1975; Rao, 1996; Tsai, McIntosh, Pearce, Camden, & Jordan 2002; Plotto, 2004; Okoro, 2007; Bako, Ismail, Ikram, & Nazri, 2008; Mabrouk & Abubakar, 2009).

Calyces of roselle have been used in African folk medicine due to its spasmolytic, antibacterial, cholagogic, diuretic and anthelmintic properties. North Africa medicine uses it to treat cough and sore throat; the leaf pulp is utilized in topical application for external wounds and abscesses (Neuwinger, 2000). In Iran, the cardiovascular application of roselle includes treatment of high blood pressure by lowering cholesterol. In Africa, India and Mexico, concoction of *H. sabdariffa* are traditionally used for diuretic, cholerectic, febrifugal and hypotensive effects, decreasing the viscosity of the blood and stimulating intestinal peristalsis (Morton, 1987). Traditionally, in Nigeria, the decoction of the seeds is used to induce or enhance poor lactation (Gaya, Mohammad, Suleiman, Maje, & Adekunle, 2009).

Lawsonia inermis (Linn.) belongs to the family of Lythraceae. It is a much branched glabrous shrub or tree; 2 to 6 m in height. The arrangement of the small leaves are opposite along the branches. It is indigenous to East of Africa, North Africa and South-West Asia; a biennial dicotyledonous herb. *L. inermis* is an ornamental and dye plant (Sastri, 1962; Vasudevan & Laddha, 2003; Chauhan & Pillai, 2007). Traditionally, the orange-red dye and leaf paste of *L. inermis* is used in beautifying hands, nails and feet. It is also used as a hair dye. In India, it is used in the hot Indian summer due to its cooling effect. In traditional medicine, the leaves, flowers stem bark and roots of Henna are used to treat diseases such as rheumatoid arthritis, headache, ulcers, diarrheoa, leprosy, fever, leucorrhoea, diabetes, cardiac disease, malaria, skin diseases and small pox. It has been used to ease jaundice, skin diseases, venereal diseases, smallpox and spermatorrhoea. Mixture of the flowers is used to heal bruises hepatoprotective and colouring agent. The root part may be pulped to treat sore eyes, hysteria and nervous disorders (Chopra, Nayer & Chopra, 1956; Chakrabortty, Podder & Deshmukh, 1977; Bhardwaj, Seshadri & Singh, 1977; Bhardwaj, Bisht, & Jain, 1980; Shikhiev, Safarova, & Nurieva, 1987; Reddy, 1988; Chetty, 2008). The compilation of the plants used is shown in Table 2.3.

Table 2.3: Compendium of the biodiversified plants used

No	Species name	Family name	Local names	Common names	Part(s) used	Medicinal Uses
A	*Canna indica* (Linn.)	Cannaceae	Idodo, ido, idoro Gwangwama, Aberekanwo	Indian shot	Leaves	Asthma, Malaria, eye infection, clear vision
B	*Senna occidentalis* (Linn.)	Caesalpiniodea	Rere	Septic weed Coffee weeds	Leaves	'fekun' treatment, concoction for 7th month pregnancy
C	*Nicotiana tabacuum* (Linn.)	Solanaceae	Ewe taba, Otaba, taba	Tobacco	Leaves	Ringworm, cold, convulsions, ulcers, nausea, anthelmintic.
D	*Momordica charantia* (Linn.)	Cucurbitaceae	Ejinrin were, Alo-ose, Kakayi	African Cucumber, bitter gourd, balsam pear	Leaves, stems	Diabetes, piles, convulsions, jaundice, sore, nervous disorders, diabetic recipe, emetic, night blindness, aphrodisiac, dysmenorrhoea Anthelmintic, antimicrobials
E	*Cassytha filiformis* (Linn.)	Lauraceae	Omoniginigini, omonigelegele, sulunwahi	Devil's gut, parasitic vine	Stem twigs	Anthelmintics, antimicrobials, antifungal
F	*Hibiscus sabdariffa*	Malvaceae	Sobo, Gurguzuu	Zobo, Jamaican sorre, roselle	Calyces	Diuretic, coughs, dressing wounds, beverage blood enricher
G	*Lawsonia inermis* (Linn.)	Lythraceae	Lali , Laali, Lallee	Henna plant	Leaves	Spermatorrhoea, jaundice, gonorrhoea leucorrhoea, ulcers, menorrhagia, astringent, skin diseases

CHAPTER THREE
MATERIALS AND METHODS

3.1 Materials

3.1.1 Reagents and Apparatus

The following reagents were used in this work: silver nitrate ($AgNO_3$), nickel nitrate hexahydrate $Ni(NO_3)_2.6H_2O$ and cobalt chloride hexahydrate ($CoCl_2.6H_2O$). Whatman no.1 filter paper, watch glasses, measuring cylinders, standard flasks, mortar and pestle, refrigerator, beakers, distilled- deionized water. All the chemicals used were of analytical grade and were purchased from Sigma–Aldrich Chemical Limited. They were used as obtained.

3.1.2 Equipment

The following pieces of equipment were used: UV-Vis spectrophotometer, Scanning Electron Microscope (SEM), Transmission Electron Microscope (TEM) coupled with energy dispertive X-ray spectrometer, Fourier Transform Infra-Red (FTIR), X-ray Diffraction (XRD), photoluminescence spectrophotometer.

3.1.3 Plant Materials

Fresh leaves of *Canna indica* Linn., *Senna occidentalis* Linn., *Nicotianna tobaccum* Linn., *Momordica charantia* Linn., *Cassytha filiformis* Linn., *Lawsonia inermis* Linn., and *Hibiscus sabdariffa* (calyces) were the utilized biomass for this research. The plants were collected from open spaces and gardens at Atan-Iju, Ogun State, Nigeria. The collection site is located in moderately hot, humid tropical zone of Southwest Nigeria (Figure 3.1). The area has two distict seasons: rainy (March/April to October) and dry season (October/November to March/April) (Community portal of Nigeria, 2003).

3.1.4 Plant Identification and Authentication

The whole parts (flower, leaf, seed, stem and root) of each plant sample were collected. The plants were processed for identification. Plants whose images are shown in Figure 3.2 were identified and authenticated at the herbarium section of Forest Research Institute of Nigeria (FRIN). Voucher specimen of each plant was deposited at FRIN herbarium headquarters, Ibadan, Nigeria.

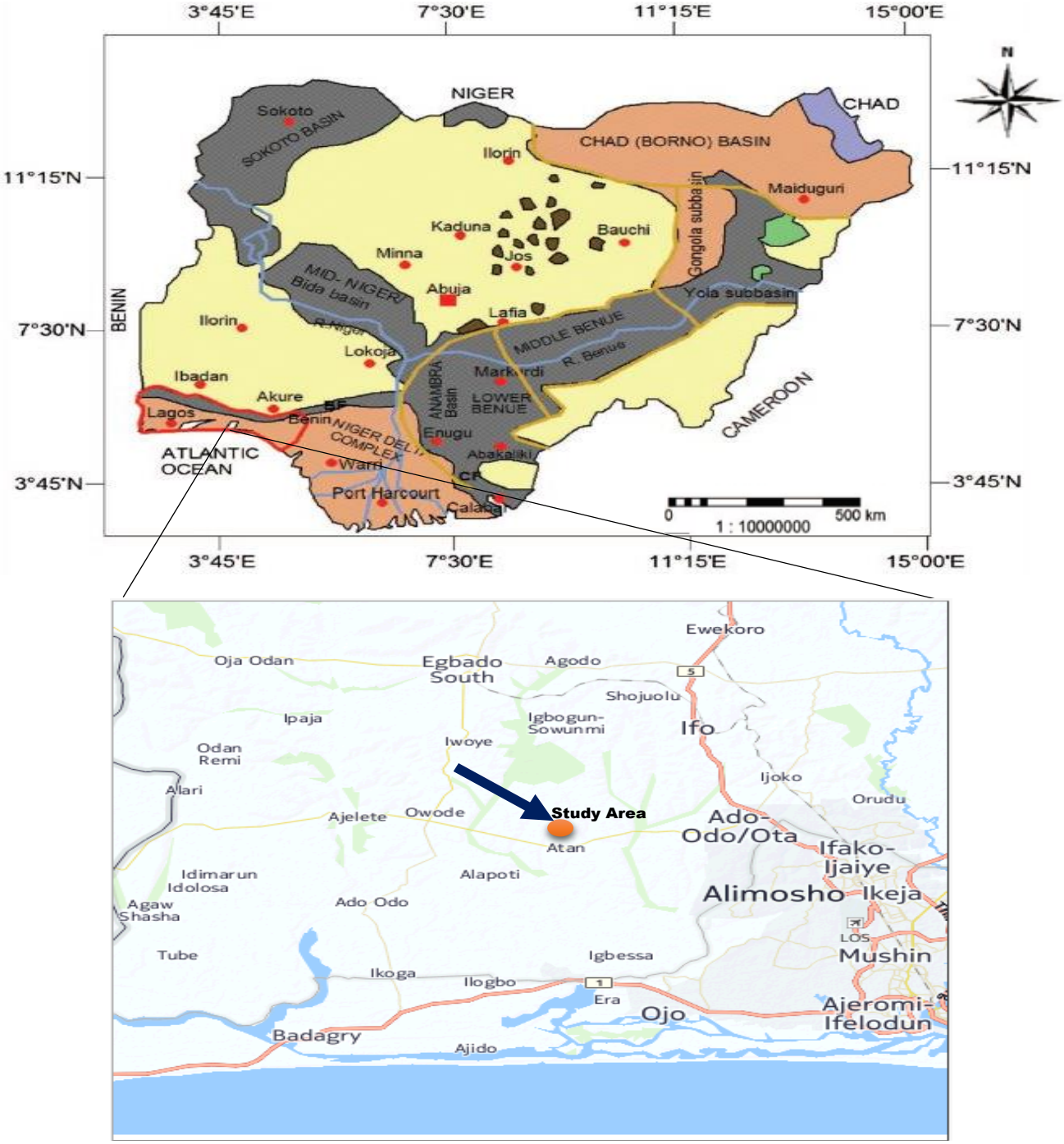

Figure 3.1: Map of Nigeria with arrow showing plant collection site

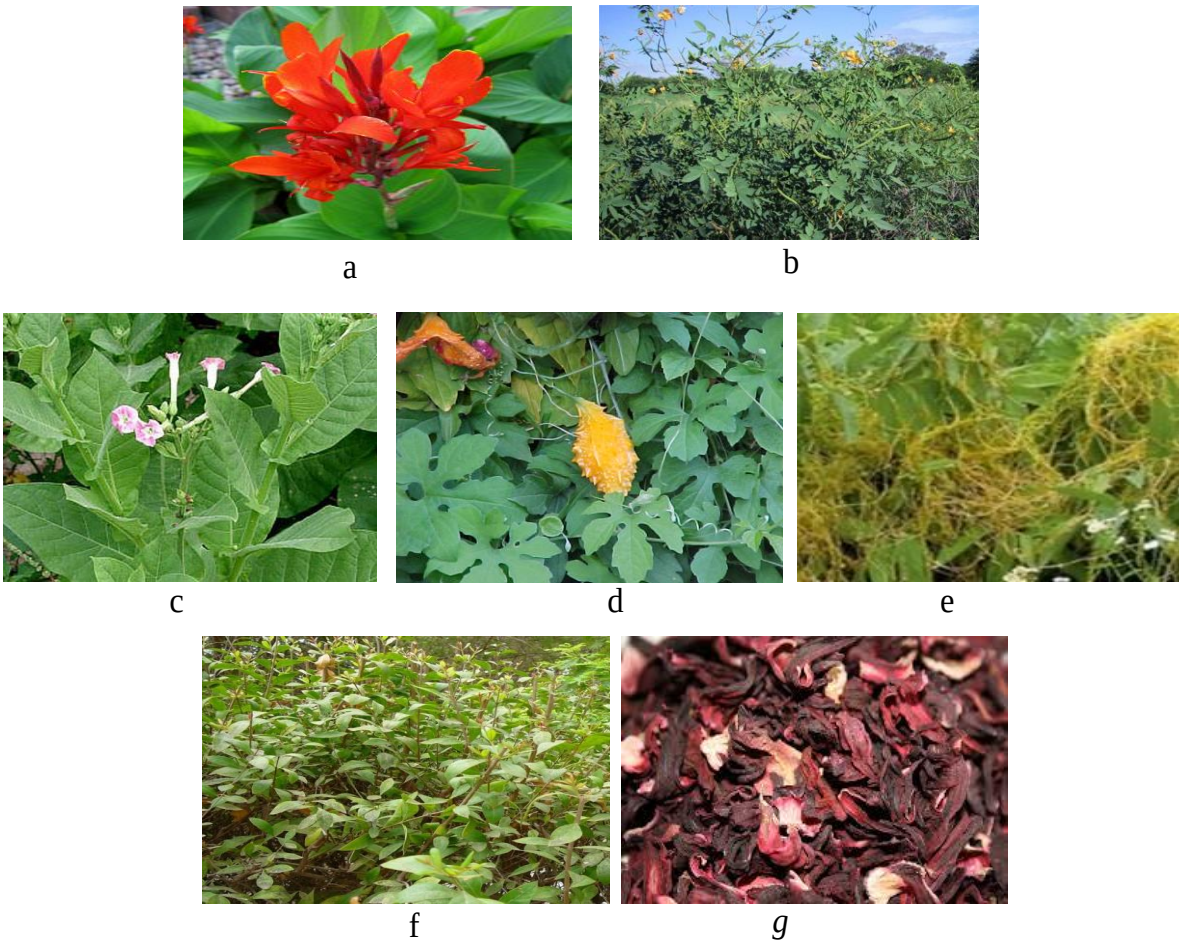

Figure 3.2: Images of the utilized biodiversity plants: (a) *Canna indica* Linn. (FHI No. 109928), (b) *Senna occidentalis* Linn. (FHI No.109927), (c*) Nicotiana tobaccunm* Linn. (FHI No.109929), (d) *Momordica charantia* Linn. (FHI No. 109926), (e) *Cassytha filformis* Linn. (FHI No.110017), (f) *Lawsonia inermis* Linn. (FHI No.110241) (g) *Hibiscus sabdariffai* Linn. (FHI No.110013)

3.1.5 Test Microorganisms

Freshly cultured clinical isolates were collected from the Department of Medical Microbiology and Parasitology, Sacred Heart Hospital, Lantoro, Abeokuta in Nigeria. The organisms used were: Gram–negative bacteria (*Escherichia coli* and *Pseudomonas aeuruginosa*), Gram–positive bacteria (*Staphylococcus aureus* and *Streptococcus pyogenes*) and fungi – (*Candida albicans* and *Trichophyton rubrum*).

3.2 Experimental Procedure/Methods

3.2.1 Preparation of Leaf Extract

The plants selected for the nanoparticles syntheses; *Canna indica* Linn., *Senna occidentalis* Linn., *Nicotiana tabaccunm* (Linn.), *Momordica charantia* Linn., *Cassytha filformis* Linn., *Lawsonia inermis* Linn. and *Hibiscus sabdariffai* Linn. were thoroughly rinsed with distilled water. Parts of the plant used for each plant were finely cut, and homogenized using mortar and pestle. Extraction was carried out at a ratio of 1:5 (w/v) using distilled-deionized water at room temperature. The mixture was then filtered with Whatman no. 1 filter paper. The filtrate was collected and kept at $4^{\circ}C$ for nanosilver and hybrid syntheses according to Ahmad and Sharma (2012). Part of the extract was also used for phytochemical screening. The procedure was implemented for every individual plant utilized.

3.2.2 Phytochemical Screening

The extract from each plant was screened for the presence of naturally occurring biologically active compounds (phytochemicals) like alkaloids, carbohydrates, proteins, tannins, phenols, saponins, flavonoids, terpenoids, steroids and glycosides. The screening was carried out using the following standard procedures (Yadav & Agarwala, 2011; Adetunji, Olaniyi & Ogunkunle, 2013).

3.2.2.1 Test for saponins

Distilled water (5 mL) was added to crude extract in a test tube. The mixture was shaken vigorously for two minutes. Persistent foaming on shaking indicated the presence of saponins.

3.2.2.2 Test for alkaloids

Crude extract (3 mL) was mixed with 1% HCl (2 mL), and then heated for 20 minutes on a steam bath. The mixture was filtered after cooling. Few drops of Mayer's and Wagner's reagents were added. The existence of alkaloids was indicated by the turbidity of the resulting precipitate.

3.2.2.3 Test for phenols

To the mixture of ethanolic (5 mL) and aqueous extract in a test tube, 2 drops of 5% $FeCl_3$ were added. A greenish precipitate showed the presence of phenols.

3.2.2.4 Test for tannins

The appearance of dirty white precipitate when 10% of freshly prepared KOH (1 mL) was added to the aqaueos extract (1 mL) connoted the presence of tannins.

3.2.2.5 Test for steroids

To 1 mL crude extract, 5 drops of H_2SO_4 was added. Red colouration showed the presence of steroids. Another test was carried out by mixing chloroform (2 mL) with crude extract (2 mL), and then 2 mL equal volume of concentrated H_2SO_4 and acetic acid were poured to the mixture separately. Green colouration confirmed the presence of steroids.

3.2.2.6 Test for flavonoids (Alkaline reagent test)

To 2 mL extract, 2 mL of 2% NaOH solution was added. Deep yellowish colouration which turned colourless when a few drops of diluted acid added signified the presence of flavonoids.

3.2.2.7 Test for glycosides

Crude extract (1 mL) was mixed with chloroform (2 mL). Then, 2 mL of concentrated H_2SO_4 was carefully poured to the mixture and shaken gently. Reddish brown colouration showed the presence of glycone part of glycoside (Salkowski's test).

Another test to confirm the presence of glycoside was carried out by mixing the crude extract (2 mL) with glacial acetic acid (2 mL) containing 1-2 drops of 2% $FeCl_3$ solution. The mixture was then transferred into another test tube already containing 2 mL concentrated H_2SO_4. Appearance of brown ring at the interphase confirmed the presence of cardiac glycosides (Keller-kilani test).

3.2.2.8 Test for terpenoids

Crude extract (2 mL) was dissolved in chloroform (2 mL) and then evaporated to dryness. Concentrated H_2SO_4 (2 mL) was added to the resulting solid and heated for 2 minutes. The appearance of greyish colouration indicated the presence of terpenoids.

3.2.2.9 Test for proteins

The appearance of white precipitate which turned red upon gentle heating when crude extract was mixed with Millon's reagent (2 mL) confirmed the presence of protein.(Millon's test). Another test was done to confirm the presence of proteins. Extract (2 mL) was bolied with 2% solution of Ninhydrin. Purple colouration signified the presence of amino acids and proteins (Ninhydrin, test).

3.2.2.10 Test for carbohydrate

The mixture of equal volume of Fehling A and Fehling B reagents (2 mL) were mixed with crude extract (2 mL) and gently bolied. Brick red precipitate indicated the presence of reducing sugars (Fehling's test).

Benedict's reagent (2 mL) was addd to the crude extract and boiled. A reddish brown precipitate indicated the presence of carbohydrates (Benedict's test).

Iodine solution (2 mL) was added to the crude extract. A blue or purple colouration showed the presence of carbohydrates (Iodine test).

Molisch's reagent was mixed with crude extract (2 mL) and shaken vigorously. Then concentrated H_2SO_4 (2 mL) was carefully added along the side of the test tube. Purple ring at the interphase of the test tube confirmed the presence of carbohydrates (Molisch's test).

3.2.3 Synthesis of Silver Nanoparticles (Ag NPs) using the Plant Extracts at 70℃

10 mL of the each plant extract was added to 100 mL of the varied concentrations of aqueous silver nitrate solution (0.5 - 2.0 mM) at a ratio of 1: 10 (v/v). The resulting mixture was continuously stirred and gradually heated to $70°C$ until reaction solution changed in colour. The bioreduction of Ag^+ ions to Ag^0 was monitored by taking samples at 5, 10, 15, 20, 30, 45, 60 minutes intervals of reaction time using UV-Vis spectrophotometer (double beam thermo scientific GENESYS 10S model). Sample was placed in quartz cuvette, operated at a resolution of 1 nm so as to determine the absorbance peak. The plant extracts acted as the reducing, capping and stabilizing agents (Ahmad &Sharma, 2012).

3.2.4 Synthesis of Ag NPs using the Plant Extracts at Room Temperature

The method used for the synthesis of Ag NPs at room temperature is similar to that of the bionanoparticles synthesis at $70°C$ temperature; nevertheless, this synthesis was without external application of heat. The experiment was carried out at room temperature; samples were taken at 5 minutes, 18 hours, 24 hours, 60 hours and 84 hourss time intervals. The experiment was repeated for all the plant extracts considered in this study.

3.2.5 Synthesis of Silver-Nickel Bimetallic Nanoparticles at 70℃

For the synthesis of Ag-Ni bimetallic nanoparticles, 20 mL of the plant extract was added to equal molar concentration mixture of 100 mL $AgNO_3$ and 100 mL $Ni(NO_3)_2.6H_2O$ in a beaker. The precursor concentrations were varied between 0.5 – 3.0 mM. The initial colour of the mixture was noted. The reaction mixture was continuously stirred, and gradually heated to 70℃ on a hotplate. The bioreductions of Ag^+ ions to Ag^0, and Ni^{2+} ions to Ni^0 were monitored spectrometrically by taking samples at varied time intervals, starting from the 5th minutes of commencing the reaction until noticeable colour change and the appearance of surface plasmon resonance (SPR). This procedure was used for each plant extract considered in this work for Ag-Ni bimetallic nanoparticle synthesis at $70°C$ temperature (Shankar *et al*., 2004).

3.2.6 Synthesis of Silver-Cobalt Bimetallic Nanoparticles at 70℃

20 mL of the plant extract was added to 200 mL of the varied equal molar concentrations (0.5 – 3.0 mM) of precursor mixture solution (100 mL $AgNO_3$ and 100 mL $CoCl_2.6H_2O$) in a beaker. The reaction mixture was continuously stirred with gradual heating to 70℃ on a hotplate. However, the bioreduction of 1:1 Ag^+ and Co^{2+} was monitored by UV-Vis spectrophotometer for a period of 4 hours. The reaction was observed for a noticeable colour change, and the appearance of absorption peak. The method was applied for Ag-Co bimetallic nanoparticles synthesis using all the plant extracts considered (Shankar *et al*., 2004).

3.2.7 Synthesis of Silver-Cobalt Bimetallic Nanoparticles at Room Temperature

At room temperature reaction condition, Ag-Co bimetallic nanoparticles were also synthesized. Plant extract was added to varied equal molar concentrations (0.5-3.0 mM) of precursor mixture solutions. The reaction was carried out at 1:10 v/v plant extract to precursor ratio. 50 mL of the plant extract was added to 500 mL of 1:1 Ag^+: Co^{2+} solution mixture.

Change in the reaction colour was monitored closely. The appearance of excitation was also monitored with UV-Vis spectrophotometer by taking aliquot measurements which ranged between minutes and days. This procedure was repeated for all plant extracts.

3.2.8 Isolation of the Biosynthesized Silver /Silver Hybrid Nanoparticles

Nanoparticles were separated from the reaction mixture by centrifugation and numerous washing using distilled deionized water. The biosynthsized nanoparticles were collected by centrifugation using centrifuge model 0508-1; operated at 5000 rpm for 30 minutes. For purification, the nanoparticles suspension was redispersed in distilled deionized water so as to remove the unbounded organics, and finally centrifuged at 5,000 rpm for 10 minutes. The suspension was oven dried and kept for further characterizations. In addition, the supernatant was kept in a refrigerator at 4℃ for toxicity analysis and nanoparticles recovery. This procedure was used for the isolation of silver and silver hybrid nanoparticles obtained from other plant extracts (Shankar *et al*. 2004).

3.2.9 Characterization of Nanoparticles

A double beam thermo scientific Genesys 10S UV-Vis spectrophotometer was used to determine the sizes, shapes and optical measurements, carried out between 200-800 nm wavelength ranges (Wiley, McLellan, Siekkinen & Xia, 2006; Swarnalathan, Christina & Payas, 2012). Maximum absorption wavelength was determined by placing each aliquot sample taken at time intervals in quartz cuvette operated at a resolution of 1 nm, distilled-deionized water was used as reference solvent. The photoluminescence of the biosynthesized nanoparticles was measured by Perkin-Elmer 55, spectrophotometer. The samples were placed in 1 x 1 cm quartz cell.

The surface morphology of the nanocluster images were recorded by scanning electron microscope (SEM) of model NOVA NanoSEM, operating at a working distance 6-13 mm, 5-20 keV accelerating voltage and 75-80 A emission current. The detailed structural and morphological characteristics, particle size determination were verified with Technai G2 transmission electron microscope (TEM) coupled with an energy-dispersive X-ray spectrometer (EDX) operated at an accelerating voltage of 200 KeV and 20 μA current. Samples for TEM analysis were prepared by drop-coating Ag, Ag-Ni, Ag-Co nanoparticles suspensions onto carbon-coated copper TEM grids. The films on the TEM grids were allowed

to stand for 2 min, after which the extra solution was removed using a blotting paper and the grid allowed drying prior to measurement.

The X-ray diffraction (XRD) measurements to determine the crystalline phase of the bioreduced Ag, Ag-Ni and Ag-Co nanoparticles were carried out on the films of the respective solutions drop-coated onto glass substrates on a Bruker AXS D8 diffractometer equipped with nickel filtered Cu Ka radiation (k = 1.5418 Å) at 40 kV, 40 mA, and at room temperature, at scanning rate of $0.05^{o}\ min^{-1}$ in a 2 hrs range from 20^{0} to 80^{0}.

The purified and dried nanopowders were subjected to FT-IR analysis to identify possible functional groups which may support existence of capping and stabilization by the plant extracts. Perkin-Elmer 100 series FT-IR which functioned at 4 ms^{-1} scan rate over the range of 4000-500 cm^{-1} wavenumber, in the diffuse reflectance mode at a resolution of 4 cm^{-1} in KBr pellets was used.

The photoluminescence study, XRD, SEM, TEM, FT-IR analyses were carried out at iThemba Labs, South Africa.

3.2.10 Antimicrobial Activity

3.2.10.1 Turbidity Standard for Inocula Preparation

The McFarland standard on laboratory guidance was used for the standardization of organisms for susceptibility testing. The standardization of the inocula density for susceptibility test was carried out using a modified method by British Society for Antimicrobial Chemotherapy (BSAC, 1990). $BaSO_4$ turbidity standard equivalent to 0.5 McFarland standards or its optical equivalent was used.

The 0.5 McFarland standard was prepared by adding 0.5 mL of 0.048 M $BaCl_2$ of (1.175% w/v) $BaCl_2$ in $2H_2O$) to 99.5 mL of 0.18 M H_2SO_4 with constant stirring to maintain a suspension. The correct density of the turbidity standard was verified by a pg instrument UV-Vis spectrophotometer model T90+, with 1 cm light path, and matched cuvette to determine the optical density at a wavelength of 625 nm. The acceptable range for the standard is 0.08 – 0.13 for 0.5 McFarland standard which is equivalent to 1.5 x 10^{8} bacterial cell per mL. The standard was distributed into screw cap tubes of the same size and volume; similar to method of growing, or diluting the bacterial inocula. The tubes were tightly sealed to prevent loss by

evaporation. They were then stored in the dark at room temperature. The turbidity standard was vigorously agitated on a vortex mixer before use. The standard remains potent for six months; appearance of large particles in the standard is an indication of expiration (BSAC, 1990).

3.2.10.2 Preparation of Inocula

The test organisms were obtained by clinical isolation. The strains were propagated in Mueller Hinton broth, prepared by dispersing 5 mL of the prepared broth medium into each screw capped test-tube; sterilized by autoclaving at 121℃ for 15 minutes. The test-tubes were cooled, and kept in an incubator for 24 hrs at 37℃, in order to determine the sterility. The isolates were inoculated into the sterilized test-tubes containing the medium, and placed in an incubator overnight at 37℃. Appearance of turbidity in broth culture was adjusted equivalent to 0.5 McFarland standards. This was done to obtain standardized suspension. Sterile normal saline was added in order to obtain turbidity optically comparable to that of the 0.5 McFarland standards or against a white background with contrasting black line. The McFarland 0.5 standard provided turbidity comparable to bacterial suspension containing 1.5 x 10^8 cfu/mL. The inocula gave semi confluent growth of colonies after overnight incubation as the denser inoculums use to result in reduced zone of inhibition, and lighter inoculums will have opposite effect (NCCLS, 1993).

Note: The suspension was used within 5 minutes so as to avoid population increase.

3.2.11 Determination of Antimicrobial Activity of the Synthesized Nanoparticles

3.2.11.1 Sensitivity of Test Organisms

The antimicrobial properties of the biosynthesized nanoparticles were investigated in the form of sensitivity testing, using the modified version of the method described by Aida. (Aida, Rosa, Blamea, Thomas & Salvador, 2001). The test organisms were collected on sterile agar slant and incubated at 37℃ for 24 hours. The following biochemical analyses were carried out on the bacteria test organisms: sugar fermentation, citrate utilization, oxidase reaction, vogue - proskauer, methyl red, capsule staining, spore staining, motility, indole test, urease test, hydrogen sulphide test, gelatin liquidification and gram staining. Conversely, the fungus *Candida albicans* was identified by Gram staining, germ tube test, sugar fermentation and assimilation tests. *Trichophyton rubrum* (fungus) was identified macroscopically and

microscopically using lactophenol cotton blue stains. These were then kept as stock culture on slant in the refrigerator at 4℃. The procedure was in agreement with recommended standards of National Committee for Clinical Laboratory Standards (NCCLS).

3.2.11.2 Agar Well Diffusion Method

Antibacterial activity of synthesized nanoparticles were evaluated by the well plate agar diffusion method as described in the Aida modified method (Aida *et al*., 2001). The microbial cultures were adjusted to 0.5 McFarland turbidity standards; and inoculated on Mueller hinton agar plate of diameter 9 cm. The plate was flooded with each of the standardized test organism (1 mL), and then swirled. Excess inoculum was carefully decanted. A sterile cork borer was used to make wells (6 mm in diameter) on the agar plates. Aliquots of the nanoparticle dilutions (0.1 mL) was reconstituted in 50% DMSO at concentrations of 100 mg/mL and applied on each of the well in the culture plates previously inoculated with the test organisms. However, each extract was tested in duplicate with 0.1 mL of 5 µg/mL ciprofloxacin as positive control for bacteria and fluconazole for fungi. These were then left on the bench for 1 hour for proper diffusion of the nanoparticles, (NCCLS, 1993). Thereafter, the plates were incubated at 37°C for 24 hours for bacteria and yeast; 28°C, 72 hours for *T. rubrum*. Antimicrobial activity was determined by measuring the zone of inhibition around each well (excluding the diameter of the well) for each nanoparticles obtained from the plant extract. Duplicate tests were conducted against each organism.

3.2.11.3 Determination of Minimum Inhibitory Concentration (MIC) by Tube Dilution Method

Sterile test tubes (12) were arranged in a rack. 1 mL of sterile nutrient broth was added to tube labelled 2 to 10. 1 mL of known nutrients broth concentration was added to tubes 1 and 2. Afterwards, serial doubling dilution from tube 2 to tube 10 was made, while the remaining 1 mL was discarded. 1 mL of ciprofloxacin was added to tube 11 (positive control); and water to tube 12 (negative control). 1 mL of 0.5 McFarland was added overnight and broth culture to all the tubes and then covered. The experiment was incubated overnight at 37°C and observed for the highest dilution showing no turbidity. The zone of inhibition was then verified and interpreted according to CLSI guidelines (2006) and the MIC was determined.

3.2.11.4 Determination of Minimum Bactericidal Concentration (MBC)

The MBC is the lowest concentration of antibiotic agent that kills at least 99.9% of the organisms. To determine MBC, using Doughari *et al*. (2007) method, 0.5 mL of the sample was removed from those tubes from MIC which did not show any visible sign of growth and inoculated on sterile Mueller Hinton agar by streaking. The plates were then incubated at 37^{o}C for 24 hours. The concentration at which no visible growth was seen was recorded as the minimum bactericidal concentration (MBC).

3.2.11.5 Determination of Minimum Fungicidal Concentration (MFC)

The method described by Doughari *et al*. (2007) was used to determine MFC. 0.5 mL of the sample which showed no visible sign of growth during MIC screening was taken from the test tubes, and then inoculated on sterile potato dextrose agar by streaking. The plates were then incubated at 37℃ for 24 hrs. The concentration at which no visible growth was seen was recorded as the minimum fungicidal concentration (MFC) (Doughari *et al*., 2007).

CHAPTER FOUR

RESULTS AND DISCUSSION

4.1 Phytochemical Analysis of the Plant Extracts

Phytochemicals present in the plants used are presented in Table 4.1.

Table 4.1: Phytochemical analysis of the plant extracts

		Phytochemical									
Sample	Plant	Proteins	Carbohydrates	Phenols	Tannins	Flavonoids	Saponins	Glycoside	Steroids	Terpenoids	Alkaloids
A	*Canna indica* Linn. (Leaves)	-	-	-	-	-	-	+	-	+	+
B	*Senna occidentalis* Linn. (Leaves)	-	+	-	-	-	-	+	-	-	-
C	*Nicotiana tobacuum* Linn. (Leaves)	-	+	-	-	-	-	+	-	-	+
D	*Momordica charantia* Linn. (Leaves)	-	-	-	-	-	+	+	-	-	-
Ds	*Momordica charantia* Linn. (Stem)	-	-	-	-	-	+	-	-	-	+
E	*Cassyth filiformis* Linn (whole part)	-	-	-	-	-	+	-	-	-	+
F	*Hibiscus sabdariffa* (Calyces)	+	+	+	+	-	-	-	+	-	-
G	*Lawsonia inermis* Linn.(Leaves)	-	+	-	-	-	+	+	-		-

+ Present - Absent

The phytochemical screening carried out on the plant extracts used in this study indicated the presence of one or more of alkaloids, carbohydrates, proteins, tannins, phenols, saponins, flavanoids, terpenoids, steroids and glycosides which were responsible for the reduction of metal ions and capping of the newly formed nanoparticles. The choice of water as the extraction solvent limited the amount of phytochemical observed in each plant compared with the screening carried out by Lamaeswari and Ananthi when alcohol was the solvent medium (Lamaeswari & Ananthi, 2012).

4.2 Optical (UV-Vis) Properties of Ag Nanoparticles (Ag NPs) under *Canna indica*-Influenced Synthesis at 70^{o}C

Table 4.2 shows the maximum intensity of absorbance by Ag NPs at varied precursor concentrations.

Table 4.2: Bioreduction parameters for the syntheses of silver and its hybrid nanoparticles using the extract of *Canna indica* leave at 70℃

	Maximum intensity (0.5 mM)		Maximum intensity (1.0 mM)		Maximum intensity (2.0 mM)		Maximum intensity (3.0 mM)	
NPs	Abs	λ_{max} (nm)	Abs	λ_{max} (nm)	Abs	λ_{max} (nm)	Abs	λ_{max} (nm)
Ag	0.118	Broad peak	0.312	416	0.222	Broad peak		
Ag-Ni	0.086	Broad peak	0.108	Broad peak	0.395	421	0.232	400-420 Broad peak
Ag-Co			0.251	427	0.223	504		

(a)

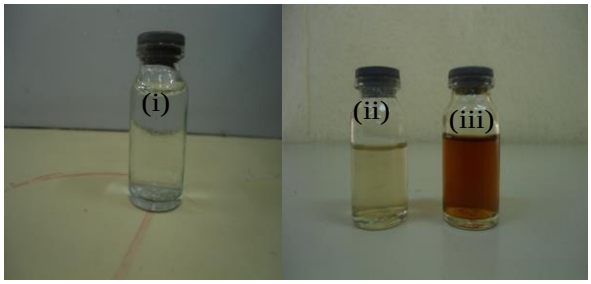

(i) $AgNO_3$ solution
(ii) $AgNO_3$ solution with extract before reduction
(iii) Final silver dispersion formed after reduction

(b)

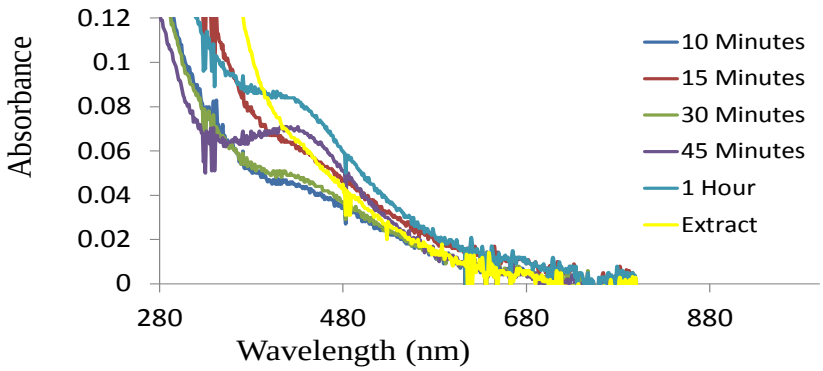

(c)

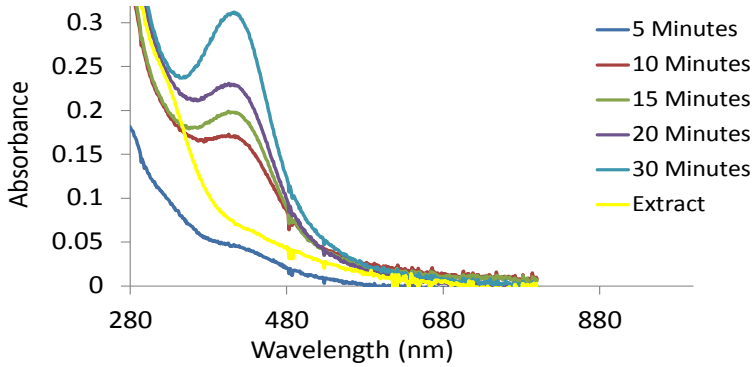

(d)

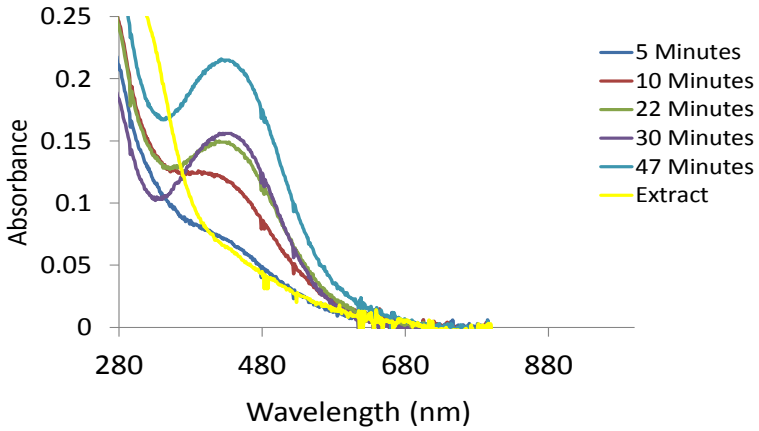

Figure 4.1: (a) Colour dispersion before and after nanoparticles formation, UV-Vis spectra of Ag NPs prepared by reducing (b) 0.5 mM (c) 1.0 mM (d) 2.0 mM precursor solutions using the extract of *C. indica* at 70℃

The UV-Vis spectra illustrating optical properties of the biosynthesized silver nanoparticles (Ag NPs), using the extract of *C. indica* leaves at 70℃ and varied precursor solution concentrations are represented in Figure 4.1(b-d). Evidence of reactivity between *C. indica* leaf extract and $AgNO_3$ solution (precursor) was physically indicated by a change in colour from light brown to reddish brown, which reflected bioreduction of Ag^+ to Ag^0 (Figure 4.1a). The observed colour change, with the corresponding single peak absorbance spectra was due to characteristic vibrations as a result of changes in the electronic energy levels of metal nanoparticles (Daisy, 2009).

The reactions were relatively fast, showing that the phytochemicals in *C. indica*: alkaloids, glycosides and terpenoids were adequate for Ag NPs formation (Kim *et al.*, 2003). The biomolecules acted as both the reducing and capping agents for the newly formed silver nanoparticles (Harekrishna *et al.*, 2009). The reactions were relatively faster for Ag NPs formed at higher precursor solution concentrations (1.0 and 2.0 mM), where nucleation and onset growth started as early as 5 minutes. The onset growth in 0.5 mM precursor was belated; leading to slow growth rate, as this suggested diverse mechanistic character in the formation of nanoparticles (Velicov, Zegers & Blaaderem, 2003; Smith, Duan, Rhyner, Ruan, & Nie, 2006).

The appearance of surface plasmon resonance (SPR) band with increased peak intensity confirmed the formation of Ag NPs. The SPR band was localized around 420 nm, similar to the wavelength absorption band of monometallic silver nanoparticles (Daisy, 2009). In Figure 4.1(c), the absorbance spectra show a wavelength of 416 nm with highest intensity of absorption (0.312 a.u.) in 1.0 mM precursor solution and a broad band around 450 nm with a shoulder at 380 nm in Ag NPs prepared from 2.0 and 3.0 mM precursor solutions (Table 4.2). The observed broad band suggested formation of polydispersed nanoparticles (Link & El-Sayed, 2000). Figure 4.2 illustrates optimum concentration and the growth comparison of Ag NPs prepared from varied precursor solution concentrations. The blue shift wavelength around 416 nm for 1.0 mM solution suggested the occurrence of quantum size confinement according to Dong (2012). The shape of the spectra (Figure 4.2) suggested formation of monodispersed spherical nanoparticles (Link, Wang & El-Sayed, 1999). Moreover, the red shift absorbance peak signified complete reduction and increase in the size of nanoparticles due to the biomolecular-capping of the silver cluster. Hence, signalled a potential application of the as-synthesized Ag NPs in optical materials (Lifshitz & Slyozov, 1961).

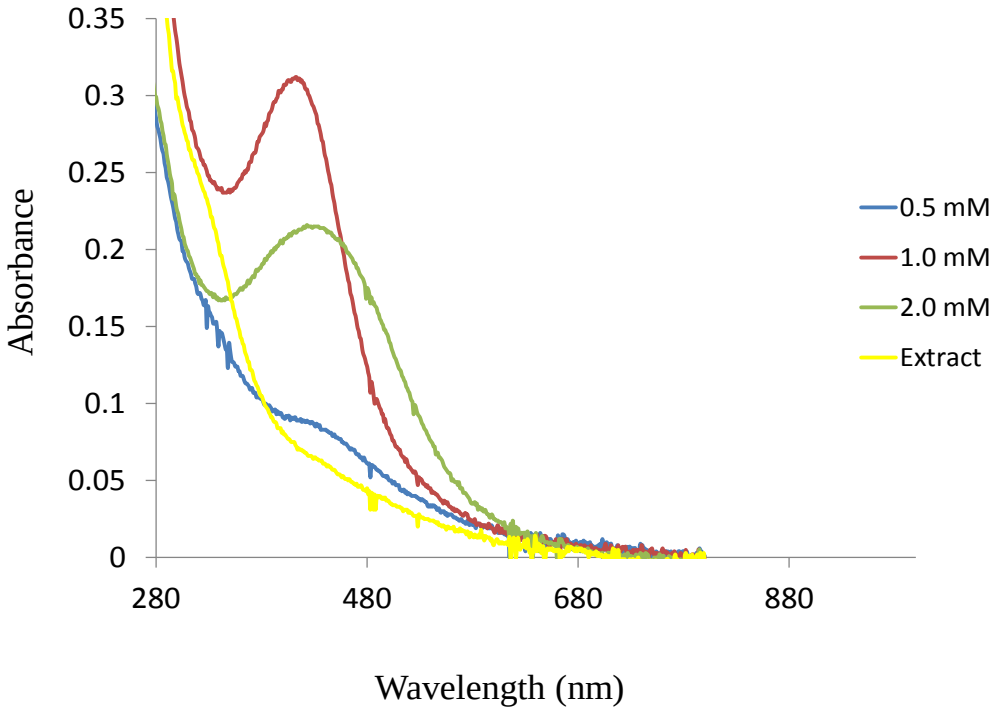

Figure 4.2: Growth comparison in *C. indica*–influenced Ag NPs prepared using varied precursor solution concentrations at 70 ℃, 30 minutes

4.2.1 TEM and Size Distribution of Ag Nanoparticles under *C. indica*-Influenced Synthesis at 70℃

Figure 4.3 (a, b) shows the particle size distribution histogram and TEM micrograph of Ag NPs formed using *C. indica* leaf extract.

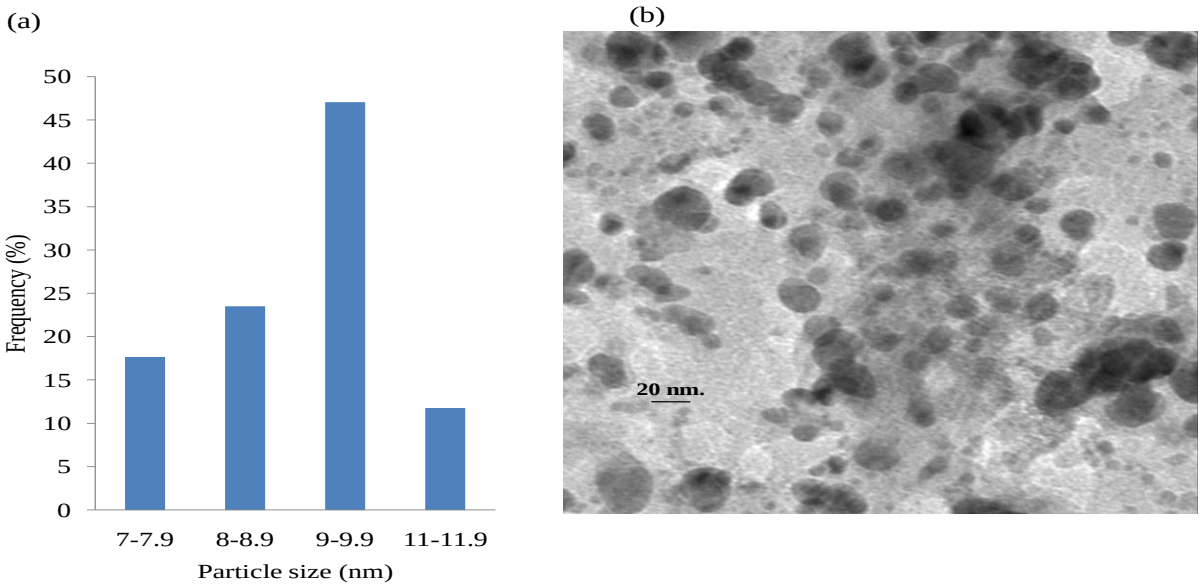

Figure 4.3: (a) Particle size distribution histogram of *C. indica* nanosilver determined from TEM image (b) Representative TEM image of Ag NPs under *C. indica*-influenced synthesis using 2.0 mM $AgNO_3$ precursor

The TEM image revealed monodispersed nanoparticles as a result of quantum confinement effect. Moreover, the observed quasi-spherical shape corroborated the shape of the SPR band in the UV-Vis spectra (Figure 4.1). The nanocluster shown in Figure 4.3(b), ranged from 7.54 to 11.52 nm in size, with a mean diameter of 9.10 ± 1.12 nm. This agrees with the histogram of the measured particles, showing highest frequency of particle distribution between the ranges of 9 - 9.9 nm similar to the findings by Dare *et al.*, (2014) in the green synthesis of Ag and Au NPs.

Table 4.3: The EDX result of Ag nanoparticles prepared from 2.0 mM $AgNO_3$

Element	Series	[wt.%]	[norm. wt.%]	[norm. at.%]	Error in %
Silver	L-series	55.44	87.58	89.25	0.77
Oxygen	K-series	1.35	3.99	6.13	1.11
Carbon	K-series	1.14	5.25	3.38	0.36
Nickel	K-series	0.96	1.60	0.62	0.09
Cobalt	K-series	0.93	1.56	0.60	0.09
Phosphorus	K-series	0.01	0.02	0.01	0.00
Sulphur	K-series	0.00	0.00	0.00	0.00
	Sum:	59.83	100.00	100.00	

The EDX analysis verified that the nanoparticles contained a large amount of silver- 89.25 atomic %. Carbon (3.38 atomic %) and oxygen (6.13 atomic %) which originated from the plant extract (Table 4.3). Hence, it can be deduced that high conversion of Ag^+ to Ag^0 was achieved in the reduction of 2.0 mM $AgNO_3$ precursor by *C. indica.*

4.2.2 XRD Patterns of *C. indica*-Influenced Ag Nanoparticles

The crystalline nature of the Ag monometallic nanocluster prepared under *C.indica*-influenced production is presented in Figure 4.4.

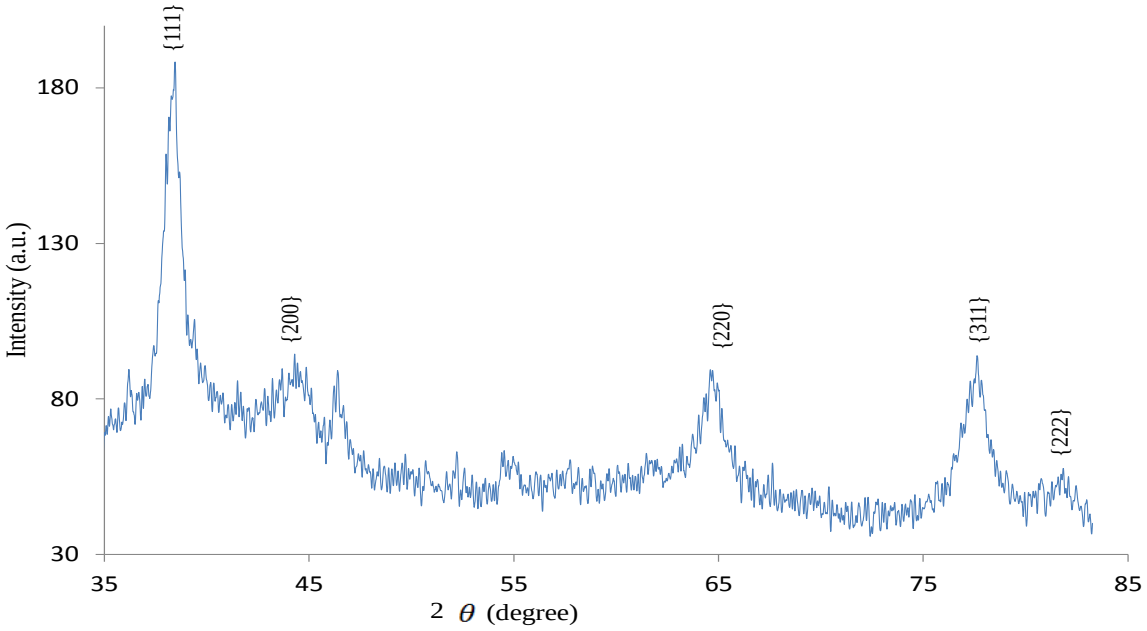

Figure 4.4: XRD patterns of Ag NPs synthesized using the extract of *C. indica* leaves and 2.0 mM precursor at 70℃

The sharp peak observed is an indication of crystallinity. The XRD patterns showed major characteristics reflections which appeared at 2θ = 38.48°, 44.30°, 64.75°, 77.68° and 81.82°. They were indexed to {111}, {200}, {220}, {311} and {222} Ag crystallographic planes of the face centred cubic (fcc) structure (JCPDS data no.04-0783).

4.2.3 FTIR Analysis of the Ag Nanoparticles

The spectrum indicating functional groups present in capped Ag nanoparticles synthesized using *C. indica* leaf extra is elucidated in Figure 4.5.

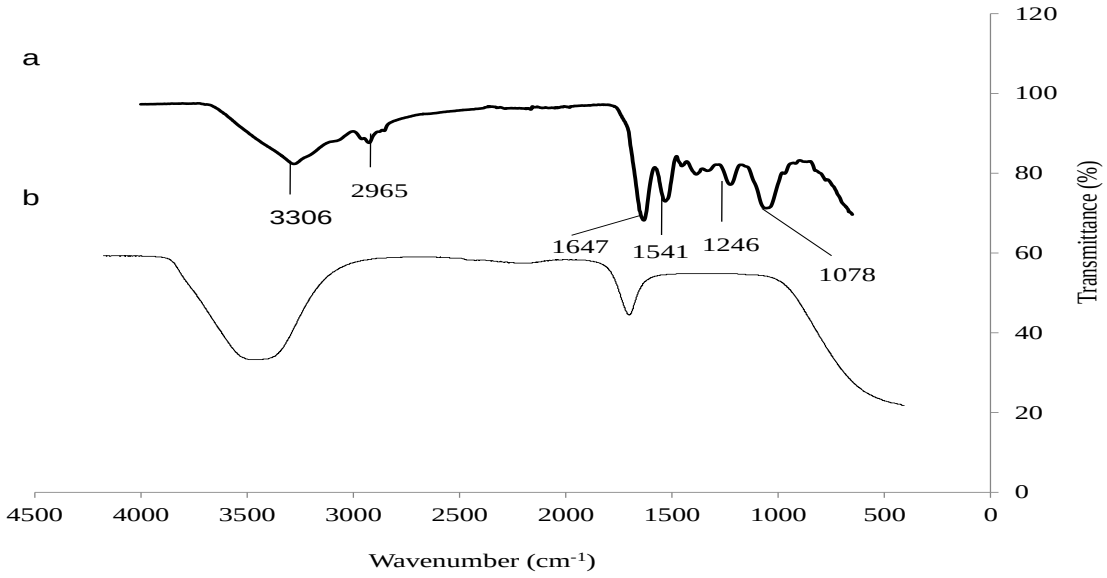

Figure 4.5: FTIR spectrum of Ag nanoparticles obtained using (a) green method (b) chemical method (Reproduced with permission from reference: Dare *et al*., 2014)

The possible biomolecules identified in the capped silver nanoparticles shows characteristic peaks at 3306, 2965, 1647, 1541, 1246 and 1078 cm^{-1}. The absorption bands were assigned to O-H stretching in glycosides, terpenoids or alkaloids), C-H stretching vibrations, -C=C in the aromatic rings of the three biomolecules, C=N, C-O stretching respectively. The observed peaks suggested capping of the nanoparticles by alkaloids, terpenoids and glycosides in the extract of Indian shot leaves.

In addition, the existence of the presence of C−O and ether linkage further corroborated the presence of glycosides in the *C. indica* plant; similar to previous work (Shankar *et al.*, 2004). Most plant-mediated nanoparticles synthesis were characterized by multiple peaks, due to the presence of organics in the plant used; illustrated in Figure 4.5(a), unlike the chemical method which normally display few and strong peaks (Figure 4.5b). This indeed proved an evidence of cappings provided by the bioreducing agents (plant extracts) which further stabilized the nanoparticles.

4.2.4 Optical (UV-Vis) Properties of Ag NPs under *C. indica*-Influenced Synthesis at Room Temperature

Figures 4.6 is the collective UV-Vis spectra of Ag NPs synthesized at room temperature.

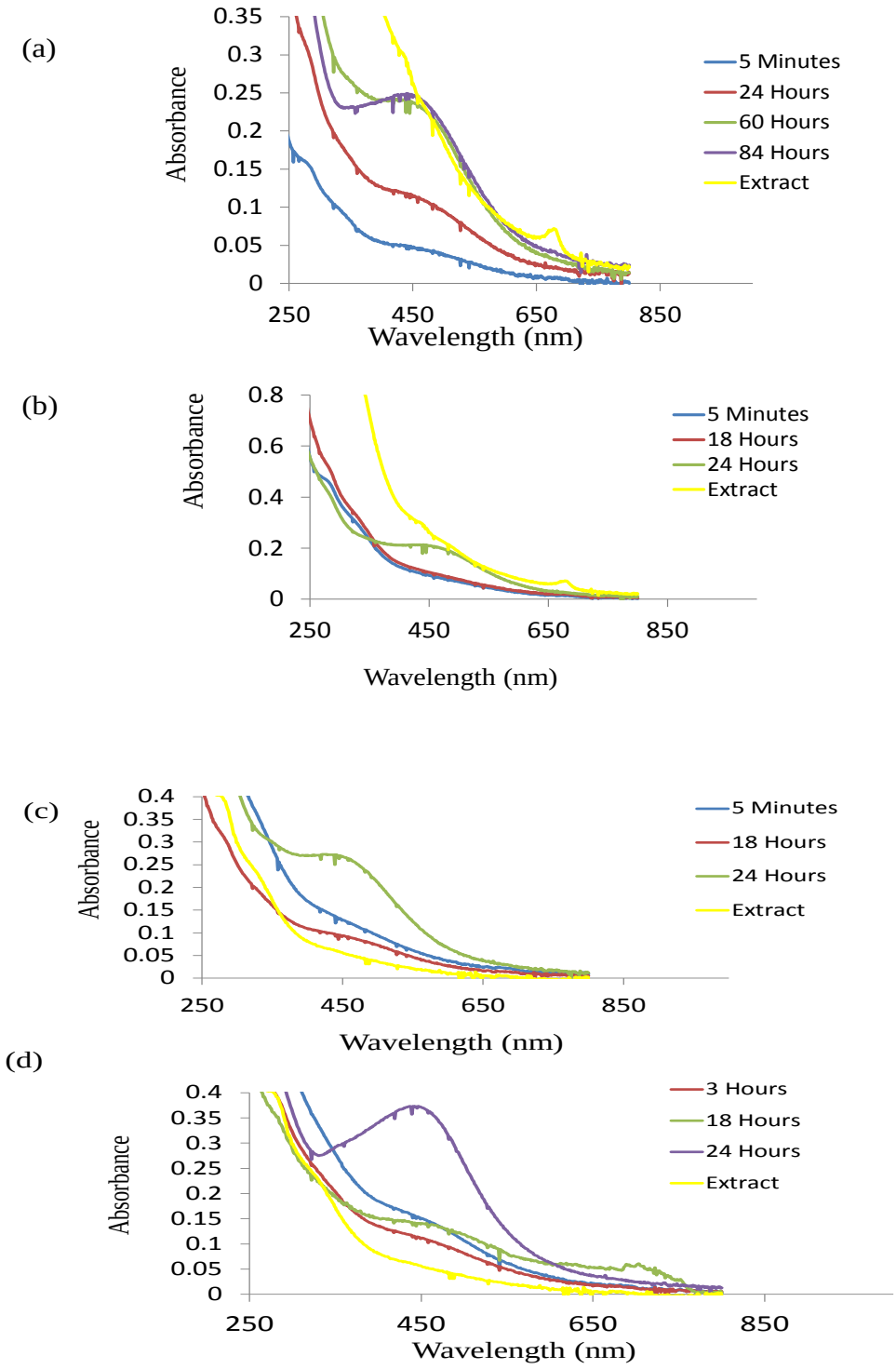

Figure 4.6: Room temperature time-resolved UV-Vis spectra of Ag NPs prepared by reducing (a) 0.5 mM (b) 1.0 mM (c) 2.0 mM (d) 3.0 mM $AgNO_3$ solution using the extract of *C. indica* leaves

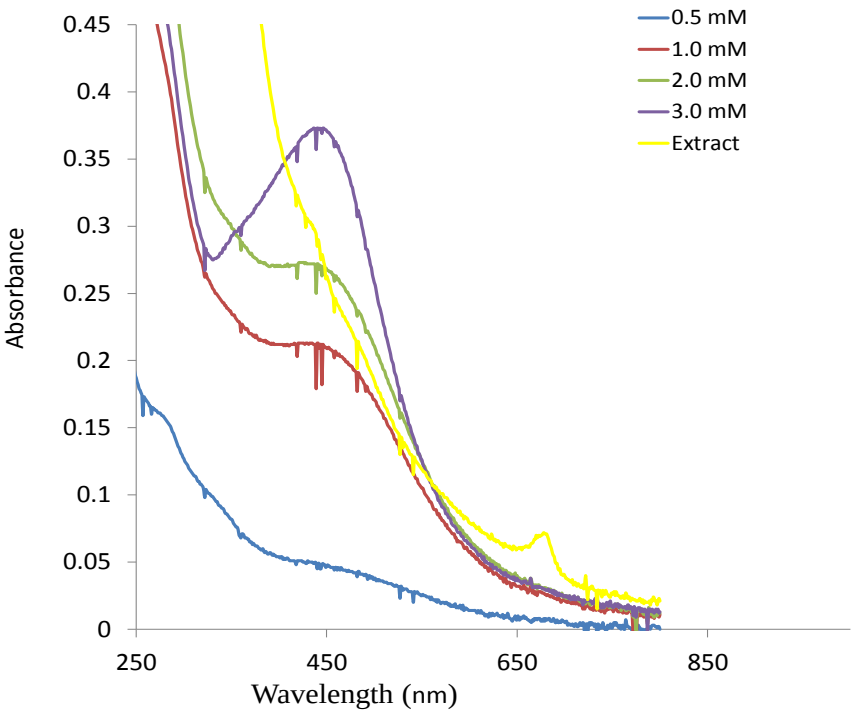

Figure 4.7: Growth comparison in Ag NPs prepared from varied precursor solution concentrations using the extract of *C. indica* leaves at room temperature, 24 hours

The nucleation and onset growth were very slow (24 hours) compared to the same reaction carried out at 70℃ (5-10 minutes). Hence, the improved rate of Ag NPs formation at 70℃ could be explained as the effect of temperature which increased kinetic energy of the reaction, leading to higher rate of Ag NPs formation.

Noticeable change in colour from light brown to reddish brown was also observed. This implied occurrence of vibration in the electronic energy levels of metal nanoparticles, which led to emergence of SPR that confirmed Ag NPs formation (Daisy, 2009). A characteristic broad wavelength band between 420-450 nm, and a shoulder around 400 nm in the Ag NPs obtained from 0.5, 1.0 and 2.0 mM metal solutions further proved the formation of nanoparticles. There was an increase in the peak intensity as a function of reaction time from the 18th - 24th hour (Figure 4.6). The red shifting in the maximum wavelength of Ag NPs connoted large particle size. Nonetheless, it is expected because the longer the reaction time, the larger the sizes of nanoparticles (Velicov *et al*., 2003; Smith *et al.,* 2006). In addition, the interaction of biomolecules with the growing silver particles could be explained to be isotropic because it was time dependent (Huang *et al*., 2007). The particles were polydispersed due to the peak broadening and absorption band above 420 nm (Link *et al.*, 1999).

The comparison of growth kinetics at the 24th hour of growth is revealed in Figure 4.7. Nucleation and formation of Ag NPs with maximum peak intensities of absorption were observed at the 84th hour in 0.5 mM precursor solution, 24th hour in 1.0, 2.0 and 3.0 mM metal solutions. The phytochemicals in *C. indica* leaves were sufficient for the biosynthesis, despite the slow rate of reaction. Different shapes and average sizes could also be explained as the effect of phytochemicals, physicochemical and toxicity in the plant (Usman & Osuji, 2007; Aboua *et al*., 2010).

4.2.5 Optical (UV-Vis) Properties of Ag-Ni Bimetallic Nanoparticles under *C. indica*-Influenced Synthesis at 70℃

The UV-Vis characterization of the as-prepared Ag-Ni bimetallic cluster in the presence of *C. indica* plant is presented in Figure 4.8.

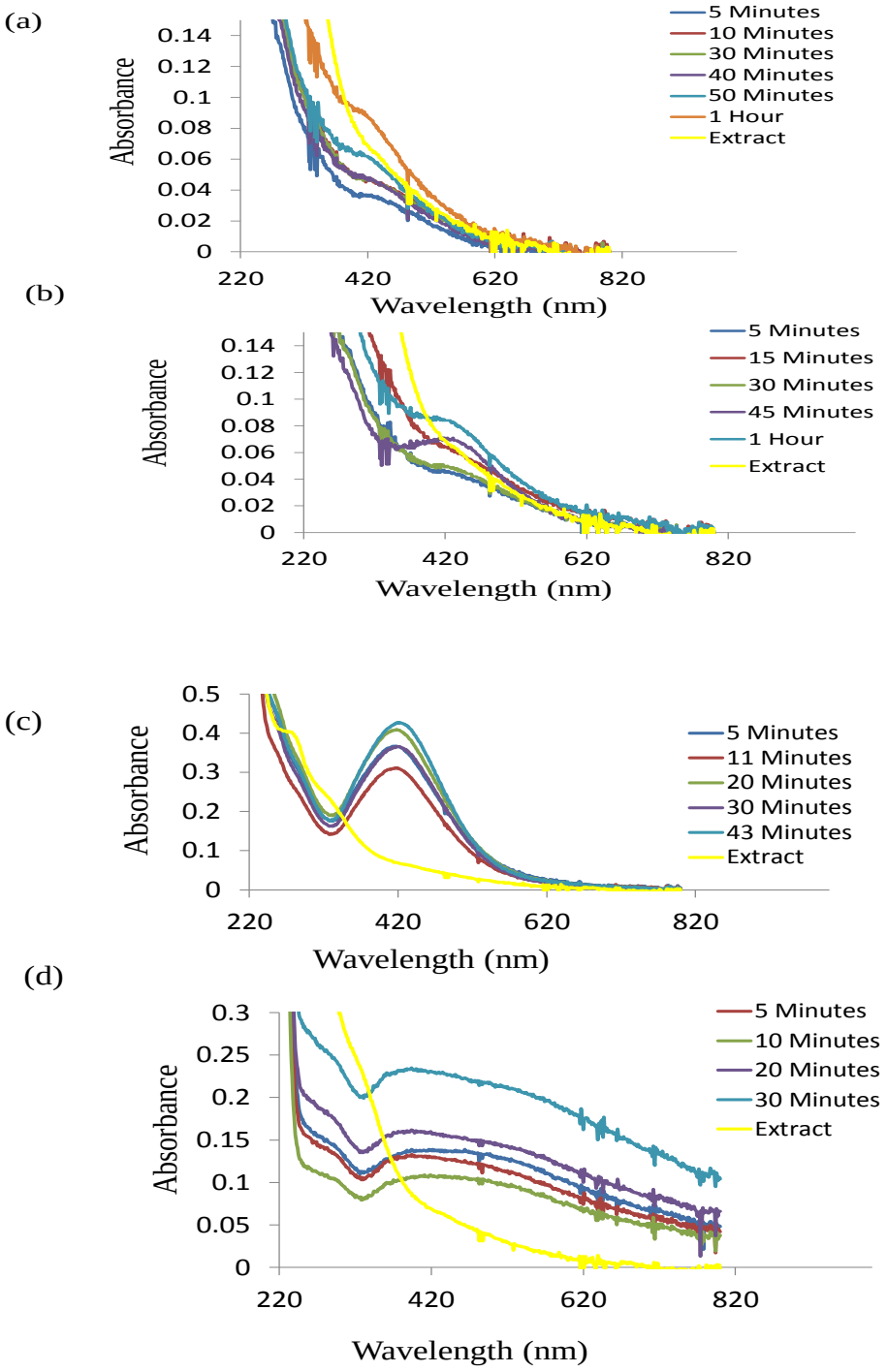

Figure 4.8: UV-Vis spectra of Ag-Ni bimetallic nanoparticles prepared by reducing (a) 0.5 mM (b) 1.0 mM (c) 2.0 mM (d) 3.0 mM solutions using the extract of *C. indica* leaves at 70℃

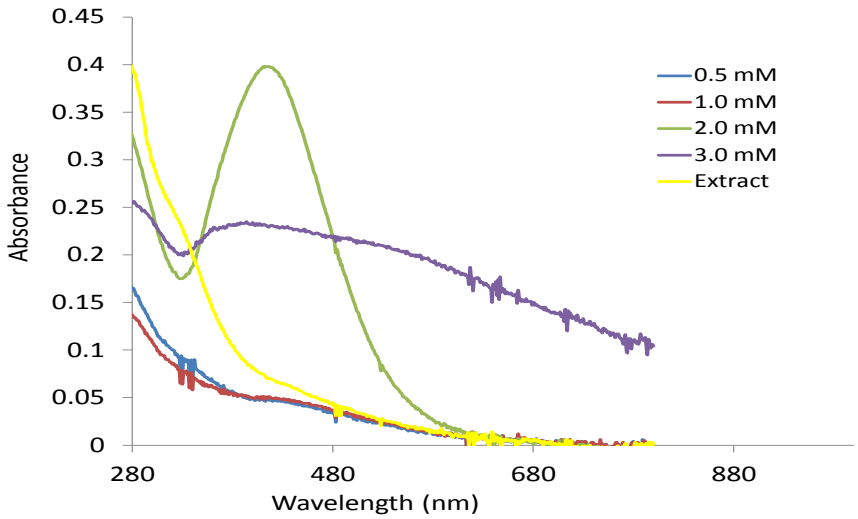

Figure 4.9: Growth comparison in Ag-Ni bimetallic nanoparticles using the extract of *C. indica* at 70℃, 30 minutes

Electron excitation and changes in the electronic energy levels occurred during the reduction process, leading to a change in colour of the reaction medium (brown to dark brown) within 30 minutes. An unprecedented bioreduction feature was observed in the reduction by *C. indica* leaf extract. This affected the nucleation and growth of hybrid nanoparticles within 5 minutes of the reaction in all the concentrations. This observation was different from the case of monometallic Ag NPs in which nucleation and formation were delayed till 20 minutes in 0.5 mM metal precursor. The appearance of SPR band in the hybrid nanoparticles prepared from 2.0 mM precursor solution was in contrast to the maximum intensity of absorption noticed in the corresponding monometallic Ag NPs, synthesized using the same plant extract as a reducing/capping agent. There were narrow absorption spectra which increased in peak intensity without any shift in the peak wavelength (421 nm); hence, these signified the presence of spherically shaped nanoparticles and an alloy formation. The result was corroborated by TEM results. An enrichment of the hybrid nanoparticles surface with silver was also proposed (Xia *et al*., 2010; Kishore *et al*., 2013). The observed narrow peak as well depicted the confinement of excited electron in the nanoparticles as shown in Figure 4.8 (Dong, 2012). The broad band between 400-450 nm in other nanobimetallic solutions of 0.5,

1.0 and 3.0 mM precursor suggested polydispersed structures (Ponarulselvam *et al*., 2012). Optimum reaction condition was portrayed in Ag-Ni hybrid prepared from 2.0 mM precursor solution with absorbance intensity of 0.312. Moreover, in this concentration, spectra overlap was observed at the 20th and 30th minute with no further changes in intensity and sizes. This indicated reaction completion. Figure 4.9 shows the growth comparison and optimum concentration for Ag-Ni bimetallic synthesis in different precursor solution concentrations at 70℃.

Furthermore, the presence of nickel (Ni) in the hybrid synthesis of course, led to a red shift in the wavelength absorption of Ag NPs from 416.0 nm to 421 nm, as observed in 2.0 mM precursor solution of Ag-Ni NPs (Table 4.3). Moreover, there was a noticeable increase in intensity of absorption when compared with single metal nanoparticles synthesis. The size increase due to red shifting was noted for application in optical materials (Kvítek, Siegel Hnatowicz & ŠvorIík, 2013).

4.2.6 TEM and Size Distribution of Ag-Ni Bimetallic Nanoparticles under *C. indica*-Influenced Synthesis at 70℃

The particle size distribution histogram and TEM image of the biosynthesized Ag-Ni bimetallic nanoparticles prepared from 2.0 and 3.0 mM metal precursor mixture are depicted in Figures 4.10 and 4.11 respectively.

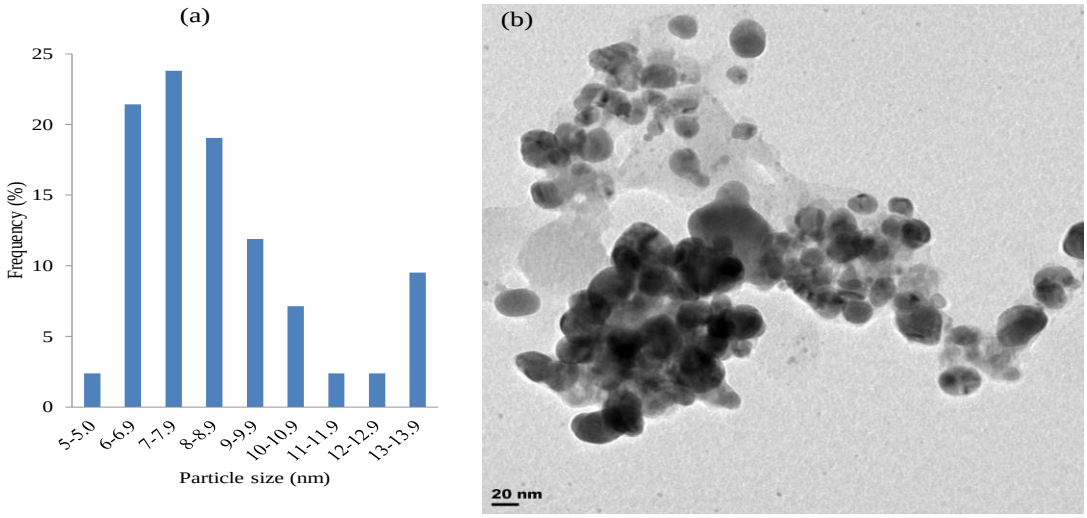

Figure 4.10: (a) Particle size distribution histogram of Ag-Ni NPs determined from TEM image (b) Representative TEM image of the bimetallic Ag-Ni NPs under *C. indica*-influenced synthesis using 2.0 mM precursor

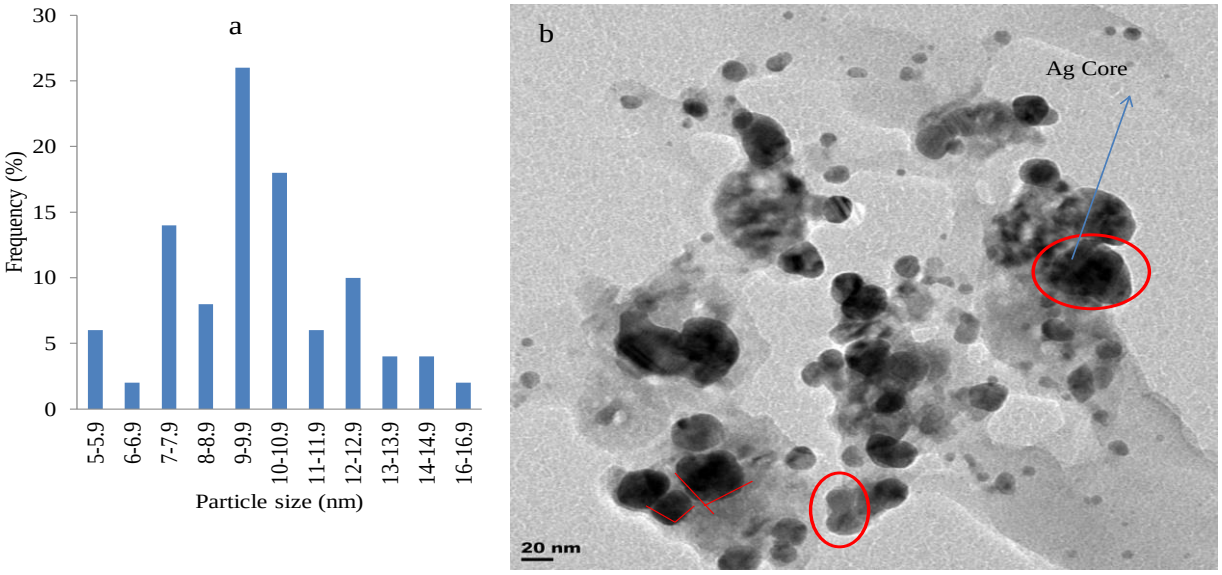

Figure 4.11:(a) Particle size distribution histogram of Ag-Ni NPs determined from TEM image (b) Representative TEM images of the bimetallic Ag-Ni NPs under *C. indica*-influenced synthesis using 3.0 mM metal precursor

The TEM designated particles with varying sizes. The image of hybrid nanoparticles for 2.0 mM metal precursor with an average size of 10.19 nm showed cluster structural arrangement (Figure 4.10). More of the particles were close in size range, which is an advantage of green synthesis. Capping of nanoparticles by the plant extract was noticed, as this provided stability for the nanocluster (Shankar *et al*., 2004).

However, the TEM micrograph of the hybrid nanoparticles prepared from 3.0 mM metal precursor showed different shapes: cube with truncated/irregular edges plausibly due to the effect of Ostwald ripening (Yang *et al*., 2010) and multiply twinned hybrid after 30 minutes of the reaction. The structural elucidation from the TEM image revealed formation of core-shell Ag-Ni nanoparticles. The denser silver particles were distinctly visible in the TEM image. The Ag nanoparticles appeared as a dark core with Ni particles appearing less dark on the surface (Figure 4.11b). This finding is unique in biosynthesis of nanoparticles. Similar report was carried out by Mntungwa and co-workers; nevertheless, chemical method was applied to obtain core-shell structural elucidation (Mntungwa, Pullabhotla & Revaprasadu, 2012). Morphology of the bimetallic Ag-Ni cluster demonstrated a mean particle size of 9.86 ± 2.37 nm. The highest number of the particles was in the range 9.0-9.99 nm as shown in Figure 4.11(a).

Table 4.4: The EDX result of Ag-Ni bimetallic nanoparticles from 2.0 mM precursor mixture

Element	Series	[wt.%]	[norm. wt.%]	[norm. at.%]	Error in %
Silver	L-series	33.33	49.90	69.22	0.80
Oxygen	K-series	10.11	12.11	8.12	5.85
Carbon	K-series	14.21	16.20	9.96	0.38
Nickel	K-series	14.45	19.46	11.11	0.60
Cobalt	K-series	0.55	0.32	0.46	0.06
Phosphorus	K-series	1.12	1.11	0.01	0.09
Sulphur	K-series	0.02	0.90	1.12	0.04
	Sum:	73.79	100.00	100.00	

The EDX showed the predominating quality of silver (69.22 atomic %) and nickel (11.11 atomic %), as an evidence of nanobiometallic formation. However, nanohybrid was silver enriched type with organic capping as revealed in the carbon content of 9.96 atomic % (Table 4.4).

4.2.7 Optical (UV-Vis) Properties of Ag-Co Bimetallic Nanoparticles under *C. indica*-Influenced Synthesis at 70℃

Figure 4.12(a) shows the combined UV-Vis spectra of Ag-Co bimetallic nanoparticles at 70℃ using the extract of *C. indica* leaves as a reducing agent.

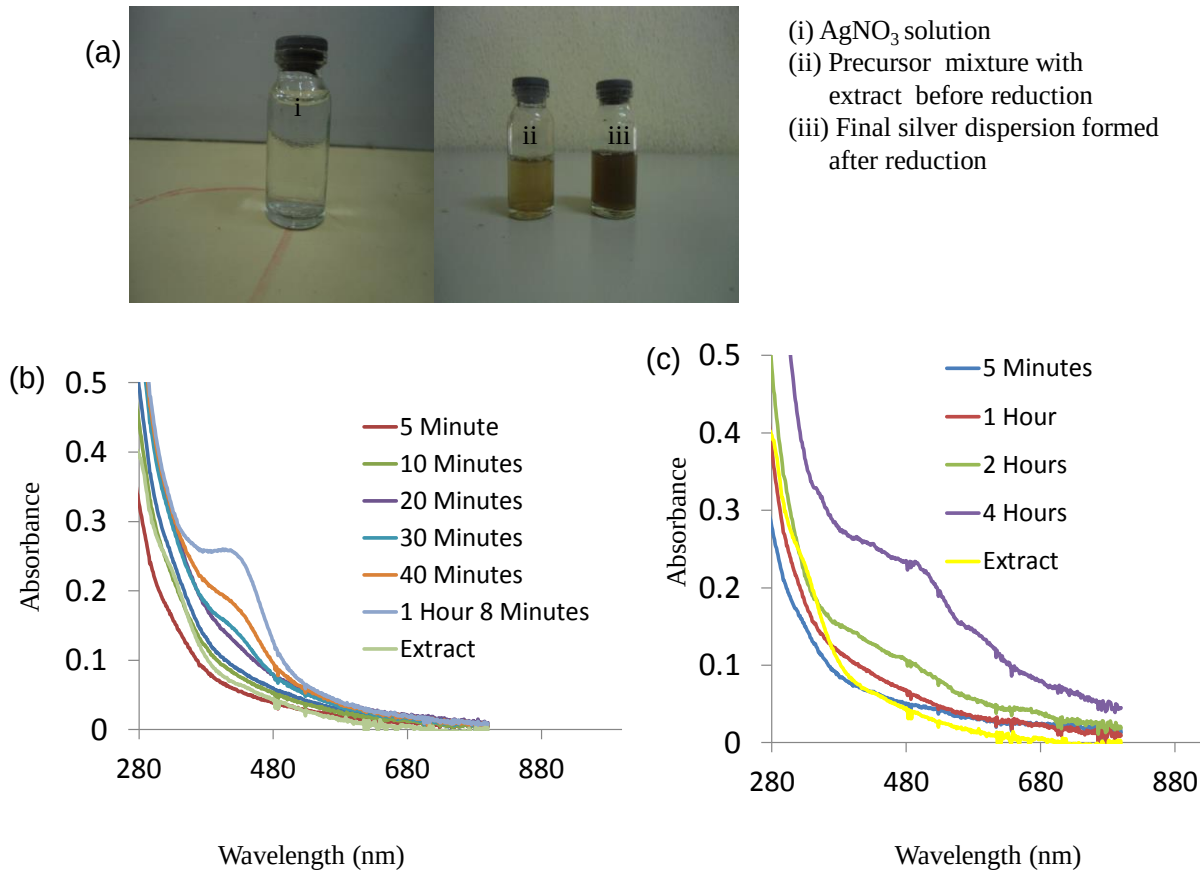

Figure 4.12: (a) Silver dispersion before and after nanoparticles formation, UV-Vis spectra of Ag-Co bimetallic NPs prepared from (b) 1.0 mM (c) 2.0 mM precursor solution concentrations using the extract of *C. indica* leaves as a reducing agent at 70℃

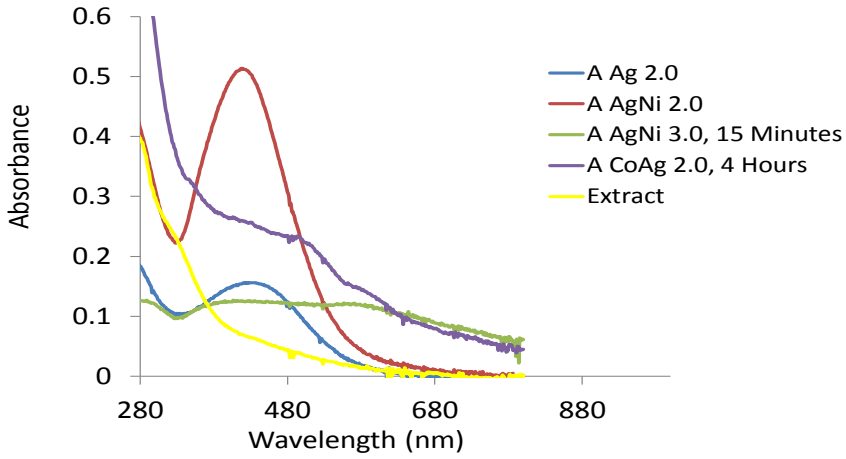

Figure 4.13: Growth of Ag NPs, Ag-Ni NPs and Co- Ag NPs at 2.0 mM concentrations, 40 minutes and 70 ˚C

Formation of nanoparticles was suggested by a change of colour in the reaction from light brown to deep brown as reported in the previous syntheses (Daisy, 2009) (Figure 4.12a). However, C. *indica* did not support Ag-Co hybrid NPs synthesis until the 40th minute and 4 hours of the reaction time as recorded in 1.0 and 2.0 mM precursor solutions respectively. The appearance of plasmon band was observed. The comparison of growth rate among Ag NPs, Ag-Ni and Ag-Co bimetallic nanoparticles is presented in Figure 4.13.

The presence of Co in the bimetallic Ag-Co nanoparticles caused a red shift in the surface plasmon absorbance to 427 nm and 504 nm in 1.0 and 2.0 mM metal solutions respectively. The shape of the spectra indicated core-shell structure formation (Figure 4.12). Large particle sizes are inevitable due to the longer time of the bioreduction process. The slow growing rate suggested different peculiar growth mechanisms of particle formation (Dare *et al*., 2014). However, this could also be attributed to strong interaction between the biomolecules present in the *C. indica* leaf extract and the growing particles, which was time dependent (Huang *et al*., 2007).

4.2.8 TEM and Size Distribution of Ag-Co Bimetallic Nanoparticles under *C. indica*-Influenced Synthesis

The particle size distribution histogram, TEM micrograph and the selected area electron diffraction (SAED) pattern of the fully hybridized novel Ag-Co clusters are shown in Figure 4.14.

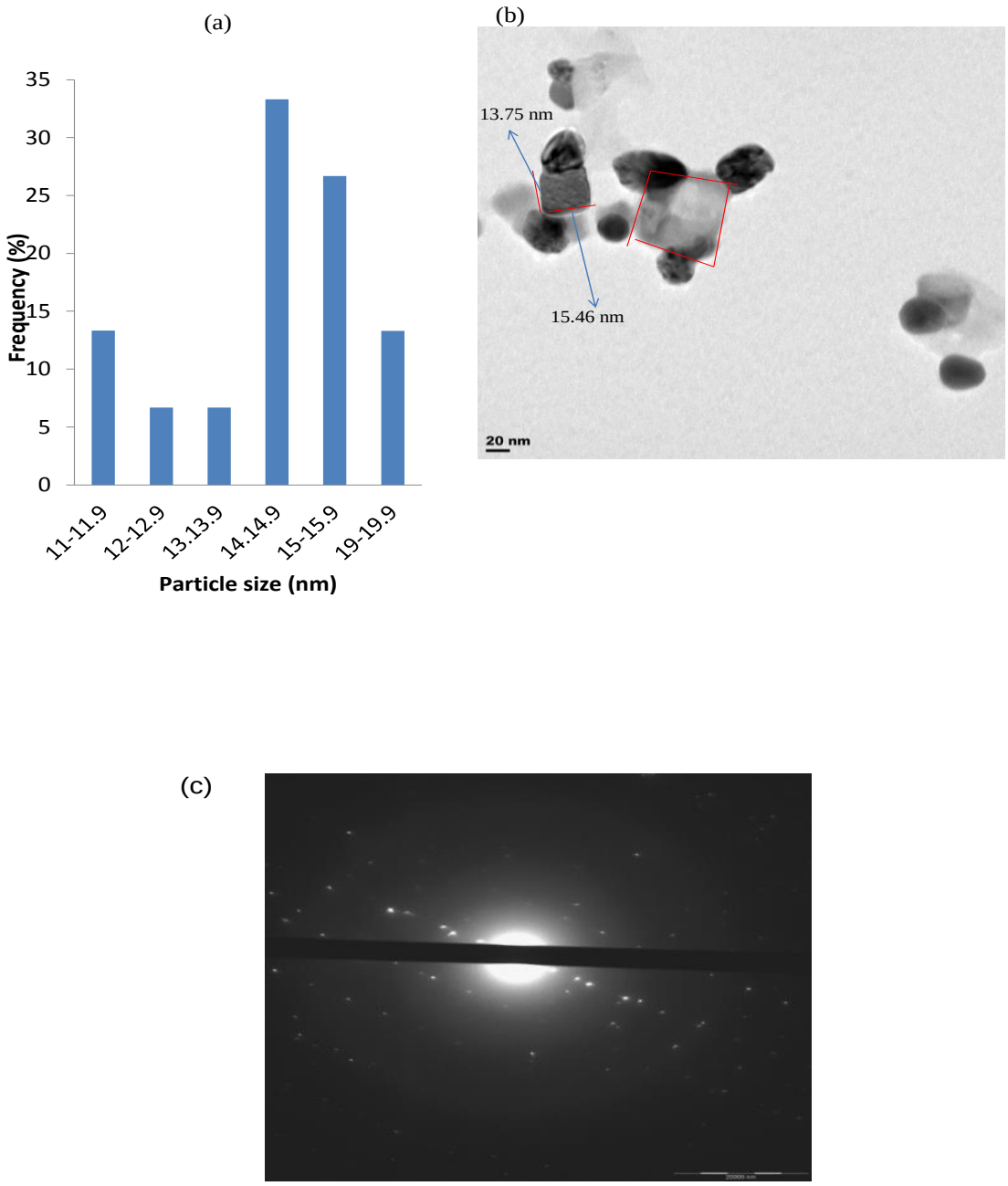

Figure 4.14: (a) Particle size distribution histogram of Ag-Co NPs determined from TEM image (b) Representative TEM images of the bimetallic Ag-Co NPs under *C. indica*-influenced synthesis using 1.0 mM metal precursor mixture (c) Selected area electron diffraction (SAED) pattern of the Ag-Co nanoparticles

Table 4.5: The EDX result of Ag-Co bimetallic nanoparticles prepared from 1.0 mM precursor mixture

Element	Series	[wt.%]	[norm. wt.%]	[norm. at.%]	Error in %
Silver	L-series	32.49	53.99	52.48	1.40
Oxygen	K-series	9.43	6.61	6.47	6.12
Carbon	K-series	9.21	2.80	9.52	0.40
Nickel	K-series	0.10	0.81	1.34	0.12
Cobalt	K-series	20.10	32.13	30.06	0.04
Phosphorus	K-series	0.47	1.68	0.57	0.05
Sulphur	K-series	0.11	1.60	0.13	0.04
	Sum:	71.91	100.00	100.00	

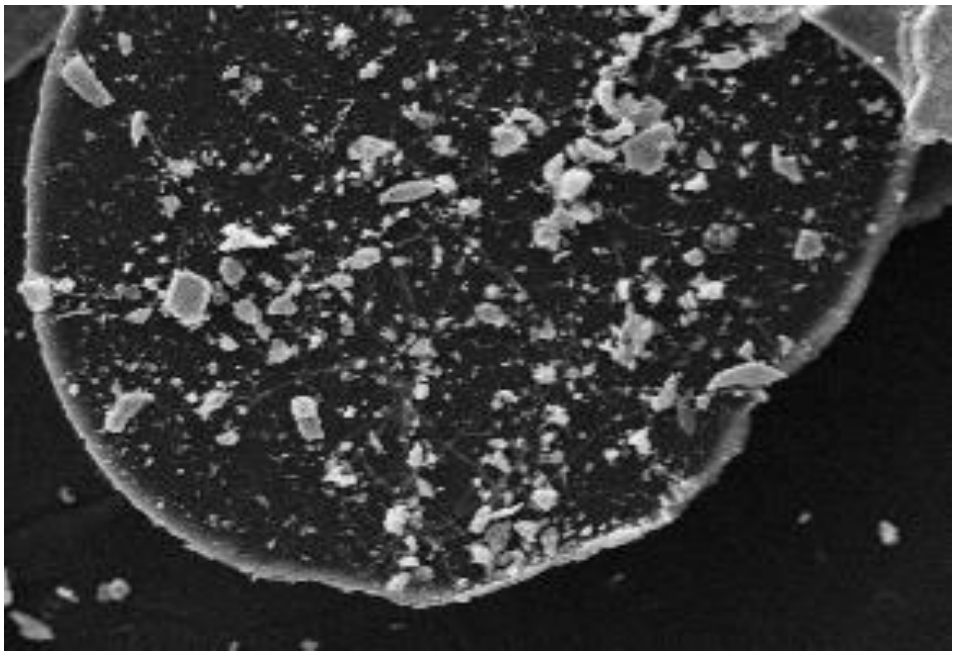

Figure 4.15: SEM image of highly capped Ag-Co bimetallic nanoparticles using the extract of *C. indica* leaves as a reducing agent

The morphology of the nanobimetallics showed novel alloy structure in which Ag atoms were attached to the vertices of cobalt in a planar arrangement in Ag-Co hybrid NPs. The cubic shape was not fully formed as a result of incomplete reduction and weak capping ability of *C.indica* leaf extract during the synthesis. An evidence of hybridization was observed in the novel morphology depicted in Figure 4.14(b). The nanoparticles showing an average diameter of 14.83 $\pm$ 2.37 nm comprised of cubic cobalt core, being capped by the metal alloy. Consequently, the SAED pattern also confirmed the formation of Ag-Co hybrid nanoparticles. Loss of crystallinity, an evidence of hybridization was depicted in the SAED pattern (Figure 4.14 b) as Ag and Co were fully incorporated.

Figure 4.15 is the SEM image of the hybrid Ag-Co nanocluster. The morphology showed a unique caging of several hybrid nanoparticles by the plant extract. The observed shapes included rod, cube, rectangle and spheres; all caged, thereby providing stability of the nanoparticles formed. The hybrid formation was supported by EDX, which showed more silver (52.48 atomic %) than cobalt (30.06 atomic %) in the elemental composition (Table 4.5).

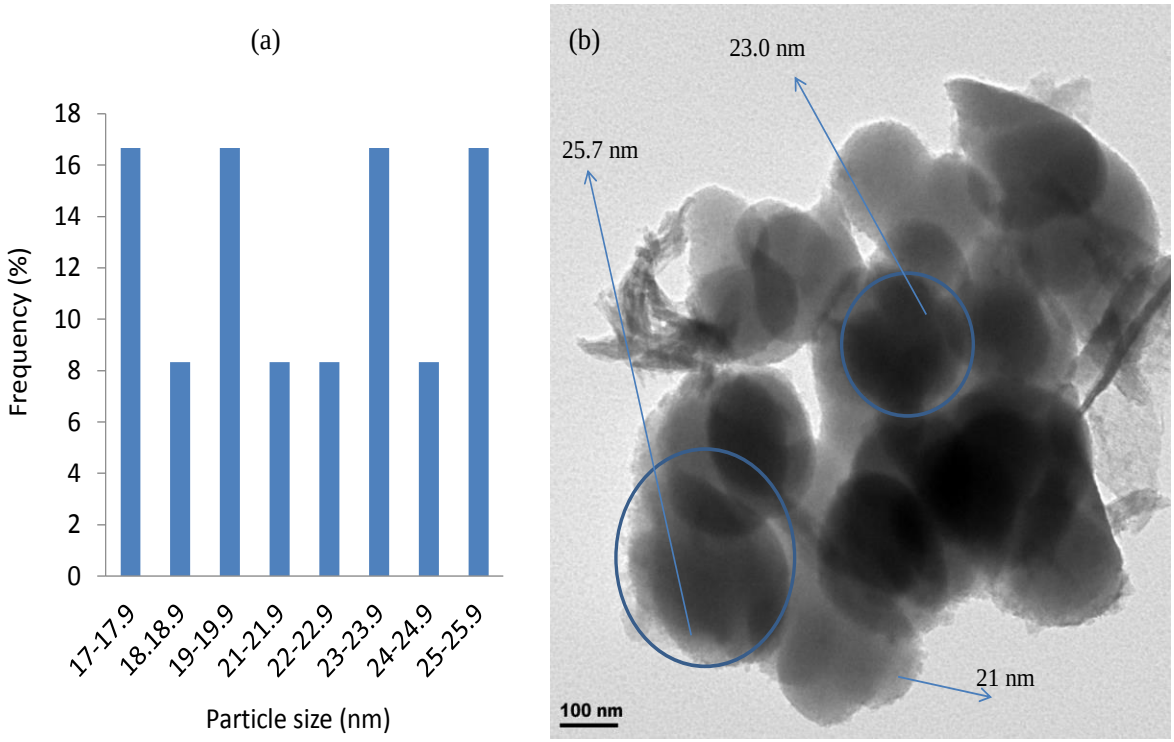

Figure 4.16:(a) Particle size distribution histogram of Ag-Co NPs determined from TEM image (b) Representative TEM image of the bimetallic Ag-Co NPs under *C. indica*-Influenced synthesis using 2.0 mM metal precursor mixture

Figure 4.16 (a, b) are the particle size distribution histogram and TEM micrograph of the bimetallic Ag-Co nanoparticles prepared from 2.0 mM precursor mixture solution, under *C. indica* influenced synthesis.The representative TEM image showed a unique full Ag-Co hybridization. Spherical monodispersed morphology of cluster-in-cluster structural arrangement was obtained. The structural elucidation also revealed less capping by the extract; instead, several overlapping as Co assumed spheroid shape at the same time with Ag. In addition, an intimate association of Co with Ag took place during the reduction process. The structure formed was more of alloy. The sizes of the particle ranged from 17.31 to 25.83 nm, with an average particle size of 21.63 ± 3.14 nm.

4.2.9 XRD Patterns of *C. indica*-Influenced Ag-Co Bimetallic Nanoparticles

Figure 4.17 portrays the XRD patterns of Ag-Co bimetallic nanoparticles formed using the extract of *C. indica* leaves at 70℃.

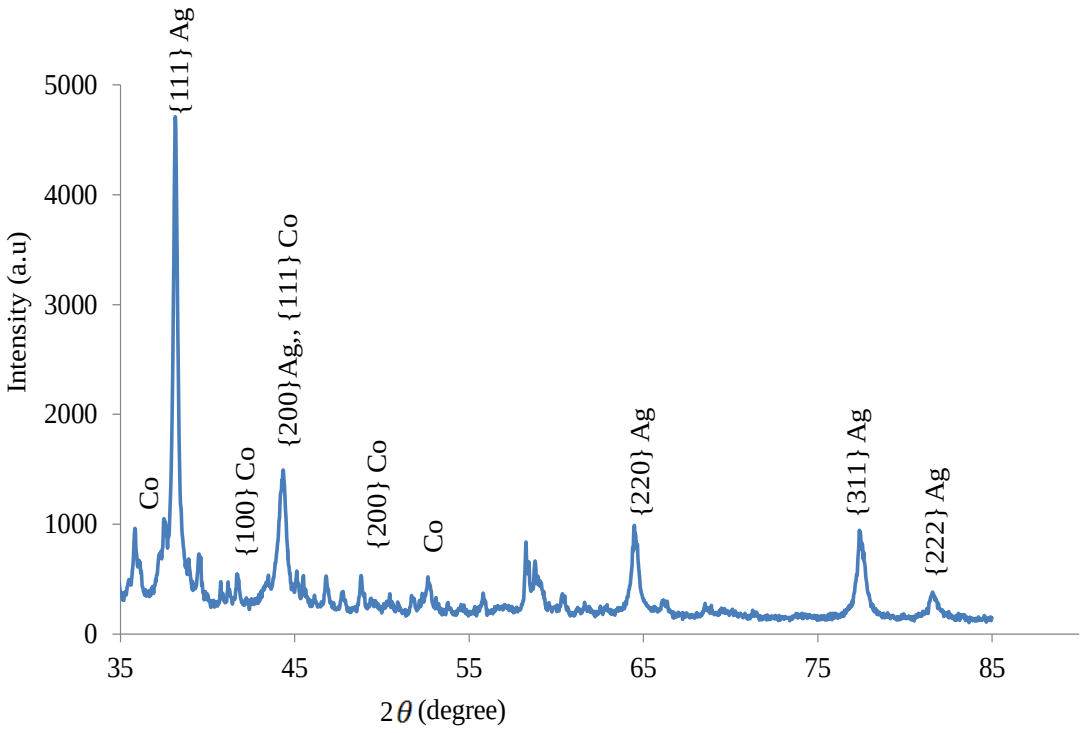

Figure 4.17: XRD patterns of Ag-Co bimetallic nanoparticles formed with the extract of *C. indica* leaves using 2.0 mM metal precursor mixture at **70** ℃

The XRD measurements of the silver allied nanoparticles over a range of 20-80° at an angular resolution 0.05° showed the reflection peaks at 2θ values of 38.15°, 44.37°, 64.57°, 77.39° and 81.08° corresponding to the reflections of {111}, {200}, {220}, {311} and {222} respectively; equivalent to the face-centred cubic crystalline Ag. However, Figure 4.17 also shows the 2θ values of Co at major diffraction peaks at 41.78°{100}, 44.37° {111}, 48.83°, {001} hcp, 52.64° and 58.29°. The diffraction patterns depicted core-shell structural morphology of the Ag-Co nanohybrid, corroborated with the TEM analysis of the nanocluster prepared using 1.0 mM precursor mixture (Figure 4.14).

4.2.10 FTIR Analysis of the Bimetallic Ag-Co Nanoparticles

The FTIR spectrum for the synthesis of Ag-Co NPs is shown in Figure 4.18.

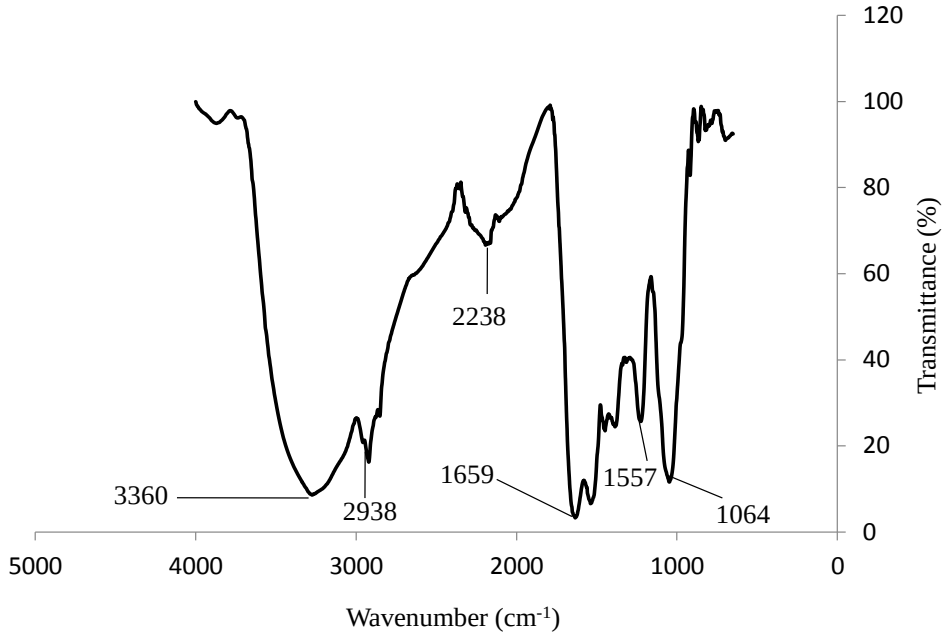

Figure 4.18: FTIR spectrum of synthesized Ag-Co nanohybrid particles using the extract of *C. indica* leaves

The broad strong peak observed at 3360 cm^{-1} was assigned to O-H stretchimg in phytochemicals. The broad peak overshadowed the N-H stretching in terpenoid which fell within this region. The medium and sharp peak at 2938 cm^{-1} was assigned to C-H stretching. The C=C stretching was observed at 1659 cm^{-1} while C=N stretching and the C-O deformation were observed at 1557 cm^{-1} and 1065 cm^{-1} respectively. Based on these observations, glycosides and terpenoids might be responsible for the stability as a result of capping and adsorption on the surface of the Ag-Co nanoparticles.

4.2.11 Optical (UV-Vis) Properties of Ag-Co Bimetallic Nanoparticles under *C. indica*-Influenced Synthesis at Room Temperature

The optical properties of silver hybrid nanoparticles using the extract of *C. indica* leaves as a reducing agent/capping agent are depicted in Figure 4.19.

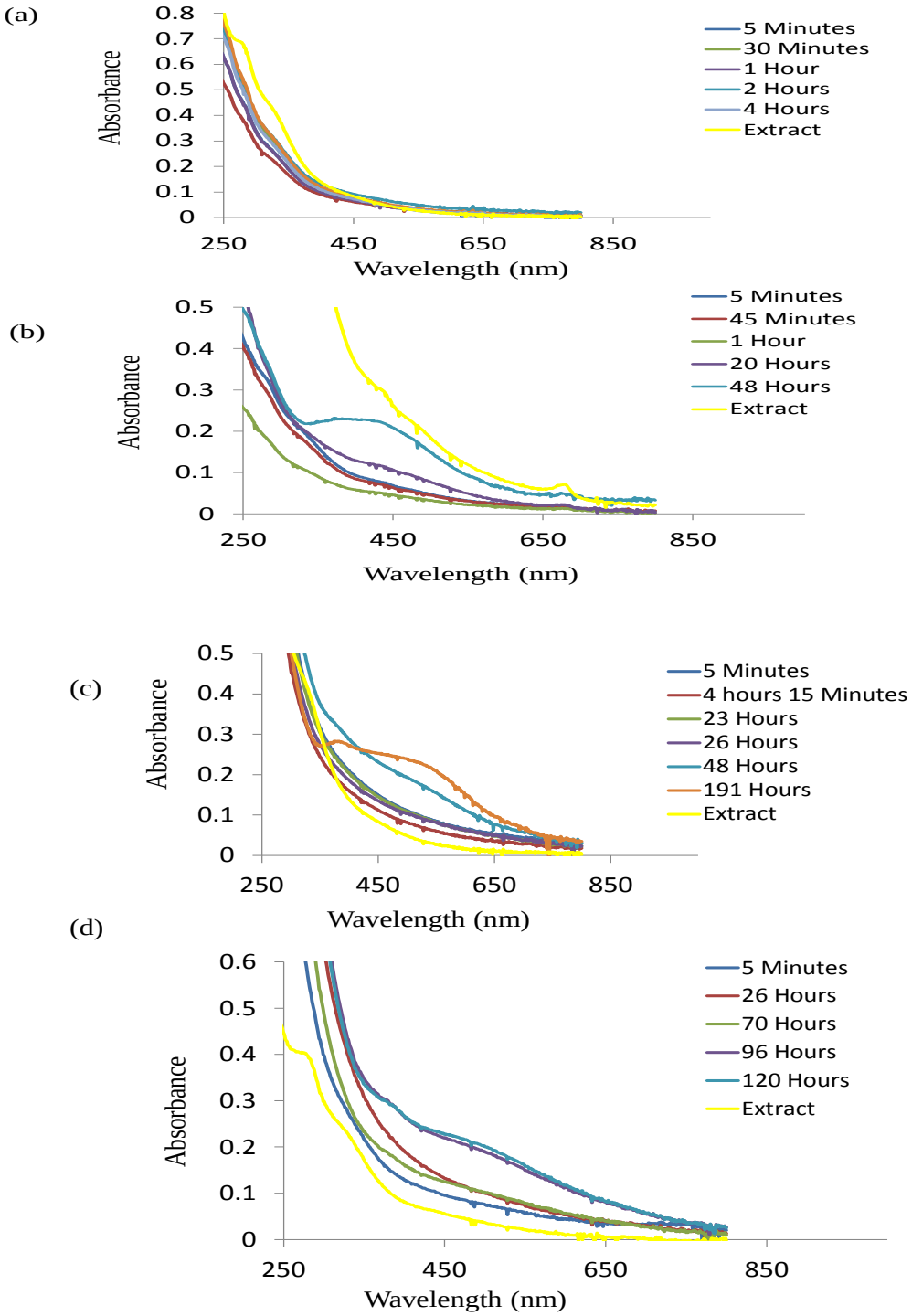

Figure 4.19: Room temperature time-resolved UV-Vis spectra of Ag-Co nanoparticles prepared by reducing (a) 0.5 mM (b) 1.0 mM (c) 2.0 mM (d) 3.0 mM precursor solutions using the extract of *C. indica* leaves

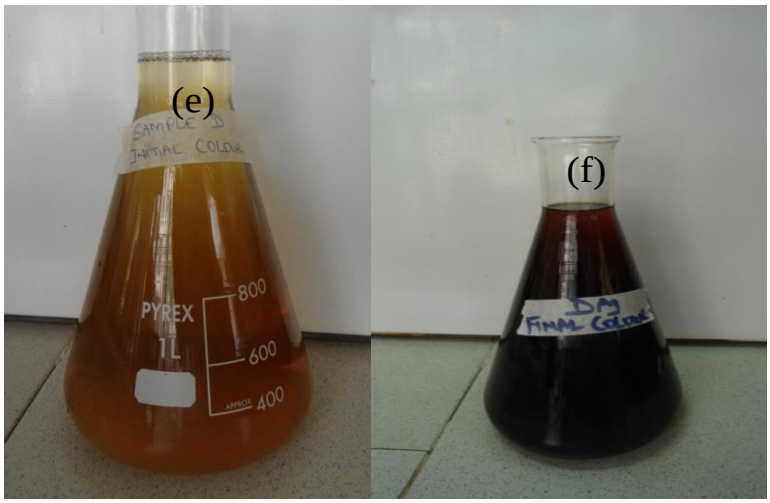

Figure 4.19: (e) is the $AgNO_3$ solution with extract before reduction
(f) is the final silver dispersion formed after reduction

Table 4.6: Bioreduction parameters for the syntheses of silver and its hybrid nanoparticles using *Canna indica* leaf extract at room temperature

NPs	Maximum intensity at specified time 0.5 mM		Maximum intensity at a specified time 1.0 mM		Maximum intensity at specified time 2.0 mM		Maximum intensity at specified time 3.0 mM	
	Abs	λ_{max} (nm)	Abs	λ_{max} (nm)	Abs	λ_{max} (nm)	Abs	λ_{max} (nm)
Ag	Broad		0.11	420-480	0.247	420-480	0.373	443
	24 hrs		24 hrs		24 hrs		24 hrs	
		No SPR	0.299	450-550	0.235	450-550	0.25	450-550
Ag-Co			48 hrs			191 hrs	120 hrs	

The leaf extract did not fully support Ag-Co bimetallic NPs formation at room temperature reaction condition. The nucleation and onset growth occurred at a very slow rate, as the reacting solutions were considered not supersaturated to generate extremely small size particles (Pokropivny *et al*., 2007). Similarly, the strong interaction between bimolecules in the leaf extract and the growing NPs was a contributing factor. A change in colour from light brown to deep brown was an indication of nanoparticles formation due to the reduction of Ag^{+} to Ag^{0} in the synthesis (Figure 4.19 e, f).

The appearance of surface plasmon resonance (SPR), an evidence of nanoparticles formation was noticed at the 48th, 120th and 191st hour of the reaction time from the cluster prepared from 1.0, 2.0 and 3.0 mM precursor solutions respectively (Figure 4.19 a,b,c,d). No growth was observed in 0.5 mM precursor. Peak broadening indicating polydispersed particles was seen (Link *et al.*, 1999). The particles were expected to be large in size due to the longer reaction time, as plant-mediated green syntheses are time dependent. Ageing of particles was also expected. Table 4.6 shows the onset growth comparison between Ag and Ag-Co bimetallic NPs prepared at room temperature.

The red shift in the SPR band (450-550 nm) is thought to be the effect of Co in the hybrid nanoparticles. The maximum absorption wavelength in the Ag-Co bimetallic NPs was more

shifted than that of single metal Ag NPs (420-480 nm) as presented in Table 4.6. No characteristic plasmon band resonance (PBR) peak was observed in the particles synthesized in 0.5 mM precursor solution. This indicated that the reducing agent at this concentration was not significant for hybrid NPs synthesis (Dare *et al*., 2014). This could plausibly be that the working concentration was too low for the reduction of metal ion. In addition, PBR was not pronounced in the particles at 3.0 mM precursor solution, possibly because high concentration of metal salt proved to inhibit the synthesis of nanoparticles.

4.3 Optical (UV-Vis) Properties of Ag Nanoparticles under *Senna occidentalis*-Influenced Synthesis at 70℃

Figure 4.20 depicts the absorption spectra of Ag NPs prepared at 70℃ using the extract of *S. occidentalis* leaves as a reducing agent.

Table 4.7: Bioreduction parameters for the syntheses of silver and its hybrid nanoparticles using *S. occidentalis* leaf extract at 70 ℃, 30 minutes

NPs	**Maximum intensity (0.5 mM)**		**Maximum intensity (1.0 mM)**		**Maximum intensity (2.0 mM)**		**Maximum intensity (3.0 mM)**	
	Abs	$\boldsymbol{\lambda_{max}}$ **(nm)**	**Abs**	$\boldsymbol{\lambda_{max}}$ **(nm)**	**Abs**	$\boldsymbol{\lambda_{max}}$ **(nm)**	**Abs**	$\boldsymbol{\lambda_{max}}$ **(nm)**
Ag	1.182	341	1.056	341	0.583	341	0.6	400-500 (Broad)
Ag-Ni					0.573	327	0.48	330

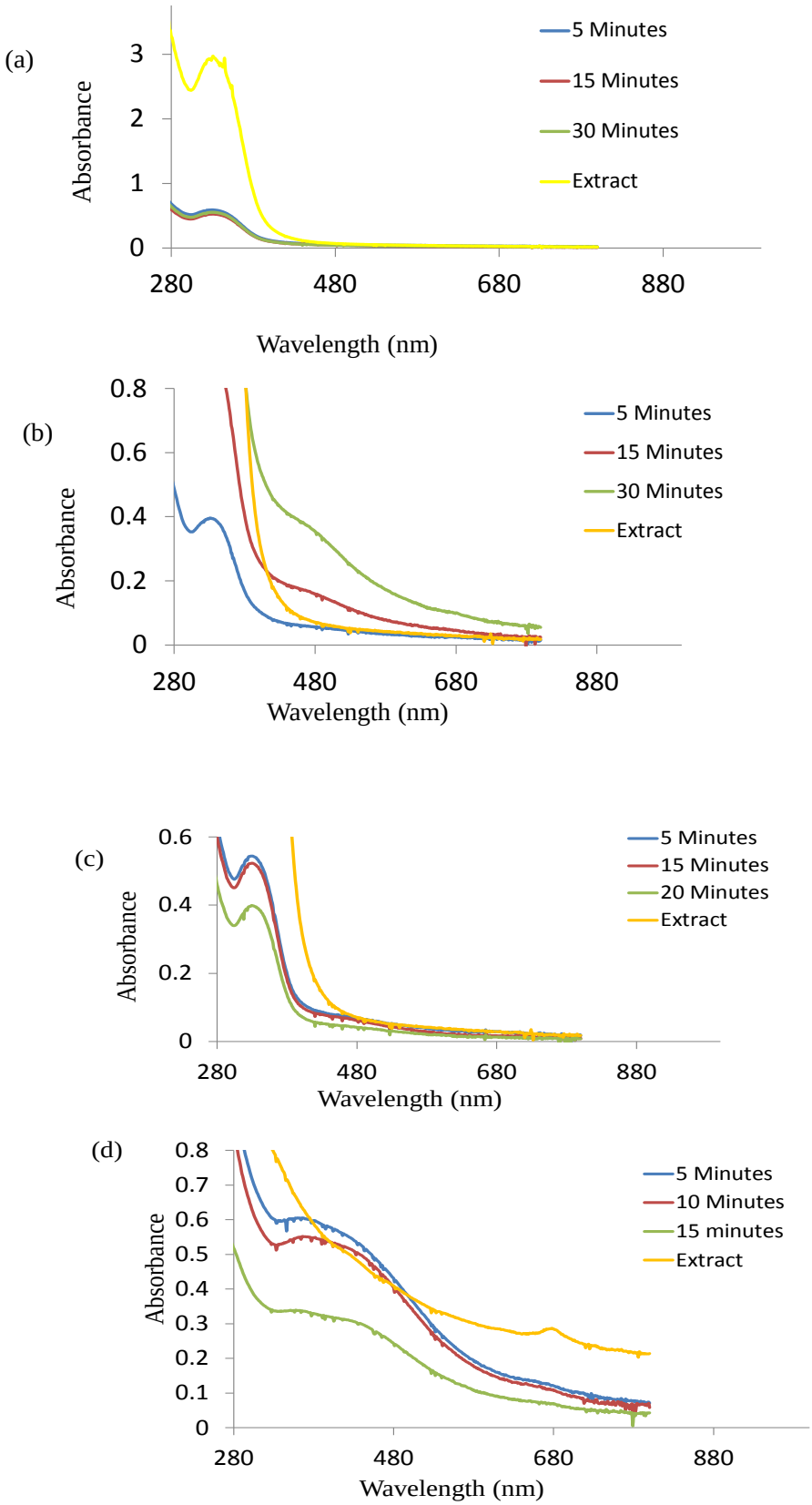

Figure 4.20: UV-Vis spectra of Ag NPs prepared from (a) 0.5 mM (b) 1.0 mM (c) 2.0 mM (d) 3.0 mM $AgNO_3$ at 70℃ using the extract of *S. occidentalis*

The surface plasmon resonance for silver (400-440 nm) was not present; instead, a blue shifted absorption peaks at 334 nm, 341 nm, 341nm and broad peak for the reduced 0.5, 1.0, 2.0 and 3.0 mM metal solutions respectively (Figures 4.20 and Table 4.7). Overlap in spectra at the 15th and 20th minutes implied reaction completion; no further change in the size and intensity of absorption was observed.

The nanocluster capped with *S. occidentalis* leaf extract displayed an unprecedented nucleation and growth among all bionanoparticles achieved in this work. The particles absorbed best in the visible region. Colour changed from green to brown within 2 minutes of the reaction. This also showed that the phytochemicals (carbohydrates and glycosides) in the extract were significant with the presence of adequate reductive biomolecules for Ag^{+} to Ag^{0} reduction.

4.3.1 TEM and Size Distribution of Ag NPs under *S. occidentalis*-Influenced Synthesis

The SAED pattern, particle size distribution histogram and TEM micrograph of the Ag NPs synthesized using the extract of *S. occidentalis* leaves and 1.0 mM $AgNO_3$ solution at 70℃ are presented in Figure 4.21.

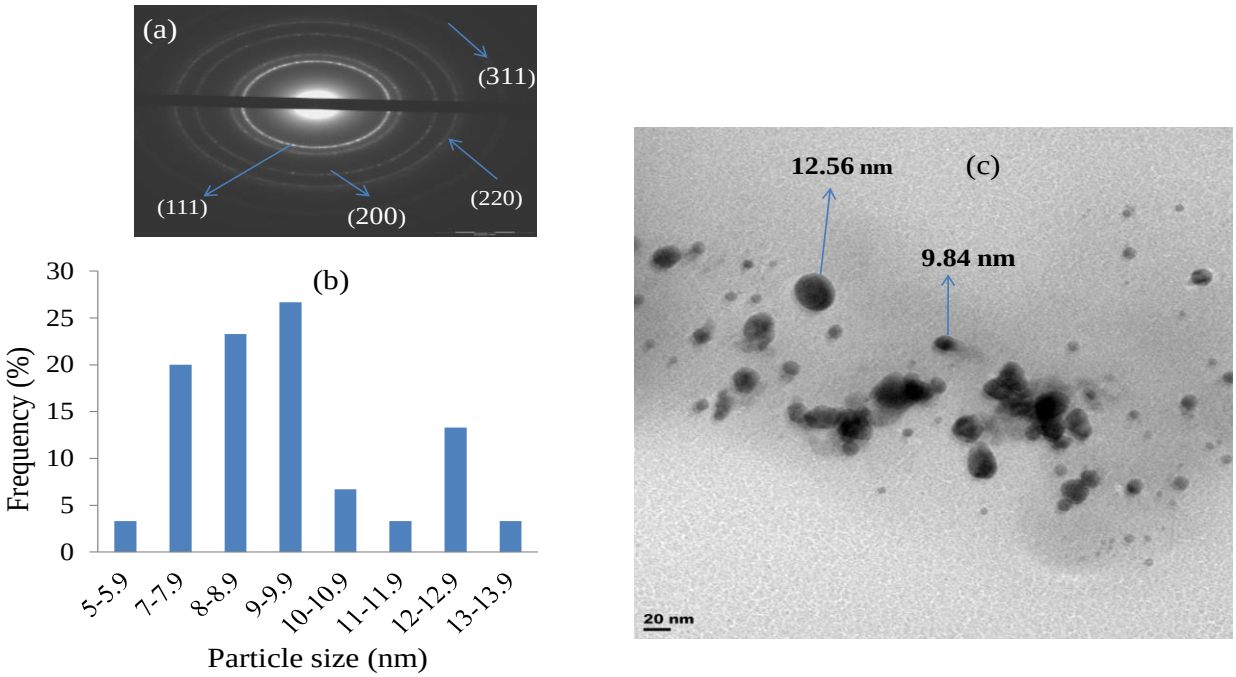

Figure 4.21: (a) Selected area electron diffraction (SAED) pattern of the Ag NPs (b) Particle size distribution histogram of Ag NPs formed using *S. occidentalis* leaf extract, determined from TEM image (c) TEM image of Ag NPs prepared with *S. occidentalis* leaf extract

Table 4.8: EDX result of Ag Ns capped with *S. occidentalis* leaf extract

Element	series	[wt.%]	[norm. wt.%]	[norm. at.%]	Error in %
Silver	L-series	47.41	74.30	81.47	1.19
Oxygen	K-series	6.67	10.30	11.78	4.62
Carbon	K-series	8.04	12.53	5.40	0.43
Nickel	K-series	0.84	1.31	0.66	0.06
Cobalt	K-series	0.88	1.38	0.69	0.06
	Sum:	63.84	100.00	100.00	

The quantitative estimate of dispersity is revealed in the histogram showing close range of particle sizes. The nanoparticles were in the range 5.5 to 12.59 nm, with mean size of 9.4 $\pm$ 1.95 nm. The nanoclusters were predominantly spherical in morphology, well separated to some extent and supported by UV-Vis spectra in Figure 4.21. The SAED pattern (Figure 4.21a) established crystal formation of the Ag NPs. Diffraction rings of the following peaks were observed: {111}, {200}, {211} and {311}, which confirmed face centre cubic metallic silver phase (Dare *et al*., 2014). The EDX measurement of the reduced silver (Table 4.8) portrayed predominant amount of silver (81.47%). Other trace elements present were obviously present in green plants.

4.3.2 Optical (UV-Vis) Properties of Ag-Ni Bimetallic Nanoparticles under *S. occidentalis*-Influenced Synthesis at 70℃

The UV-Vis spectra of the hybrid Ag-Ni NPs prepared by using the extract of *S. occidentalis* leaves as a reducing/capping agent are depicted in Figure 4.22. Figure 4.23 is the growth comparison between the hybrid Ag-Ni nanoparticles prepared from 2.0 and 3.0 mM precursor solutions at 70℃.

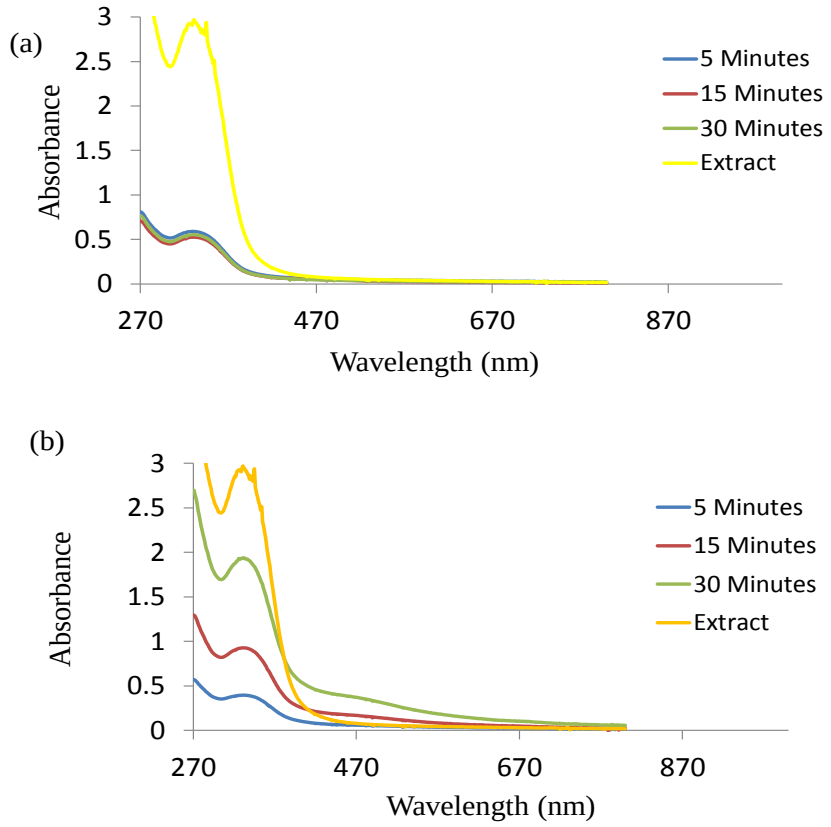

Figure 4.22: UV-Vis spectra of Ag-Ni bimetallic NPs prepared by reducing (a) 1.0 mM (b) 2.0 mM precursor solutions using the extract of *S. occidentalis* leaves at 70℃

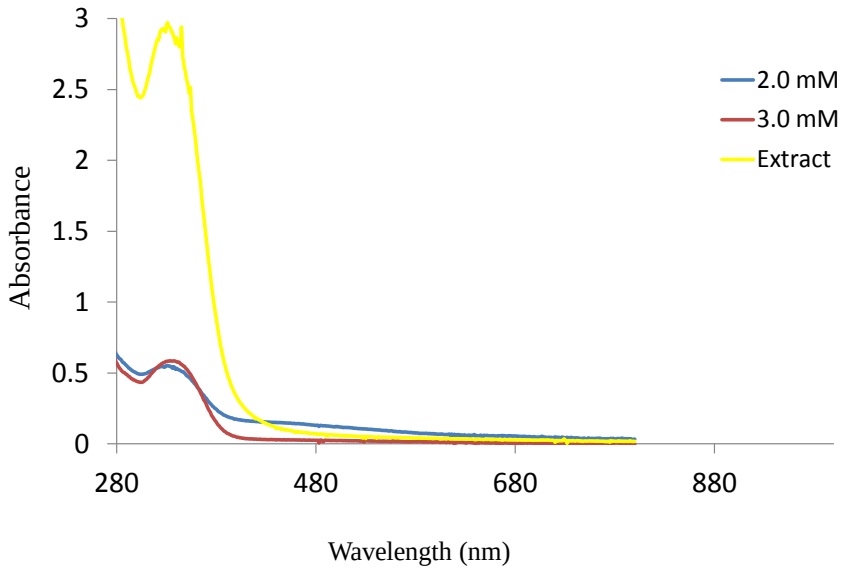

Figure 4.23: Growth comparison in Ag-Ni bimetallic nanoparticles prepared by reducing 2.0 mM and 3.0 mM precursor solutions, using the leaf extract of *S. occidentalis* at 70 ˚C, 30 minutes

The leaf extract of *S. occidentalis* displayed optical property, as it strongly absorbed in the UV/Visible region with intensity of 2.8 a.u. (Figure 4.22). The presence of n⟶π* transition (C=O) functional group of carbohydrates present in the bio-reducing agents could be accountable for this observation (Wani *et al*., 2010). The intensity of absorption of the reduced silver ions was not as intense when compared with the extract (0.4-0.8 a.u) as shown in Figure 4.22. The onset of nucleation and growth started so rapidly, as fast as 2 minutes of the reaction. The reaction colour changed from green to dark brown due to the excitation of electron and change in the electronic energy levels of metal NPs. The surface plasmon band (SPB) occurred at 327 and 330 nm in 2.0 and 3.0 mM precursor solutions respectively (Table 4.7). Higher absorption intensity was attained in the reduced 3.0 mM precursor.

The presence of Ni in the hybrid nanoparticles formation resulted in blue shifted absorbance wavelengths when compared with the corresponding monometallic Ag NPs (341 to 327 nm in 2.0 mM precursor solution). Broad band around 330 nm was observed at 3.0 mM precursor solution. The observed single peak suggested formation of alloy nanoparticles. The blue shifted wavelength in the synthesis also proposed an application for medical purpose.

4.3.3 TEM and Size Distribution of the Ag-Ni Nanoparticles

Figure 4.24 a and b show the particle size distribution histogram and TEM micrograph of Ag-Ni bimetallic nanoparticles synthesized with *S. occidentalis* leaf extract; 2.0 mM metal precursor mixture.

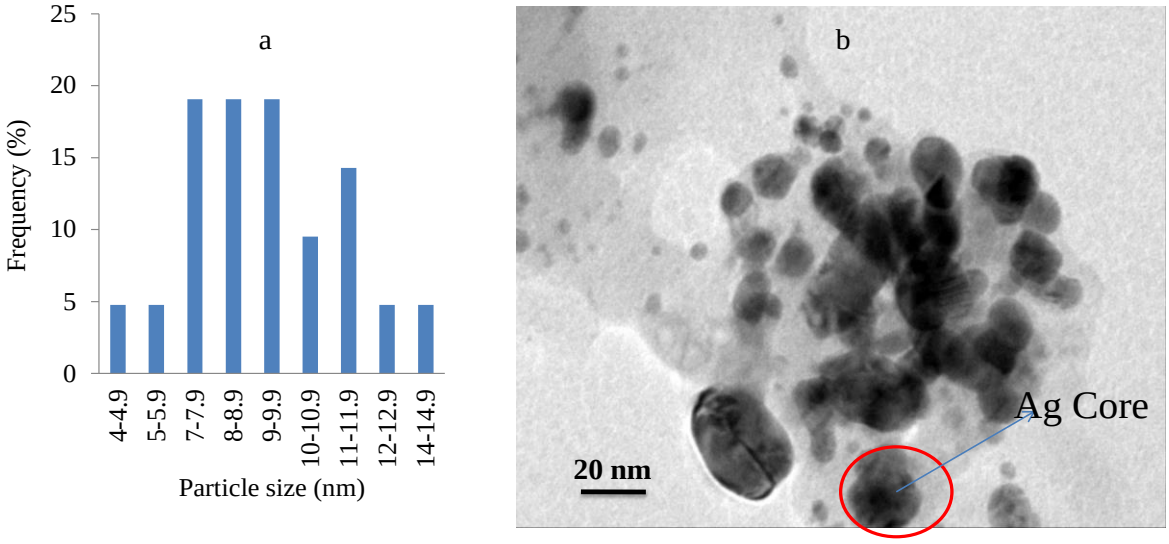

Figure 4.24: (a) Particle size distribution histogram of Ag-Ni hybrid nanoparticles determined from TEM image (b) TEM image of Ag-Ni bimetallic nanoparticles under *S. occidentalis*-influenced synthesis using 1.0 mM metal precursor mixture

Table 4.9: The EDX result of Ag-Ni bimetallic nanoparticles prepared using S. *occidentalis* leaf extract and 1.0 mM metal precursor mixture

Element	series	[wt.%]	[norm. wt.%]	[norm. at.%]	Error in %
Silver	L-series	29.54	49.59	63.30	1.59
Oxygen	K-series	7.51	5.77	5.44	0.06
Carbon	K-series	8.13	10.50	10.47	0.14
Nickel	K-series	20.87	34.10	20.71	5.13
Cobalt	K-series	0.09	0.14	0.08	0.04
Phosphorus	K-series	0.00	0.00	0.00	0.00
Sulphur	K-series	0.00	0.00	0.00	0.00
	Sum:	66.34	100.00	100.00	

Sizes of the particles ranged from 4.51 to 14.28 nm. The TEM micrograph further revealed the morphology of the nanoparticles which were mostly face-centred cubic shape with truncated edges as a result of incomplete reduction by the plant extract. The average particle size was 9.22 ± 2.21 nm. Core-shell nature of Ag-Ni is elucidated in the TEM micrograph. Silver with darker colour was inside a nickel shell, which was in agreement with a previous work done to synthesize Au-Ag core-shell bimetallic nanoparticles (Shankar *et al*., 2004).

The EDX attested the synthesis of the bimetallic nanoparticles. Silver and nickel were present approximately in the ratio 3:1. Oxygen and carbon were present with the atomic composition of 5.44% and 10.47, respectively, which signified the presence of organic capping agent that provided stability (Table 4.9).

Table 4.10: The EDX result of Ag-Ni bimetallic nanoparticles prepared from 2.0 mM metal precursor mixture using the extract of *S. occidentalis* leaves

Element	series	[wt.%]	[norm. wt.%]	[norm. at.%]	Error in %
Silver	L-series	32.33	50.64	56.11	1.11
Oxygen	K-series	7.10	10.90	17.23	3.20
Carbon	K-series	13.20	16.22	12.20	0.26
Nickel	K-series	18.88	22.12	24.11	0.02
Cobalt	K-series	1.00	0.12	0.08	0.04
Phosphorus	K-series	0.00	0.00	0.03	0.03
Sulphur	K-series	0.00	0.00	0.00	0.00
	Sum:	75.51	100.00	100.00	

Figures 4.25 (a, b) showed particle size distribution histogram and TEM image of bimetallic Ag-Ni nanoparticles prepared from 2.0 mM metal precursor mixture using *S. occidentalis* plant at 70℃. Average size of 8.67 $\pm$ 2.28 nm was found for the as-prepared nanoparticles. The hybrid formed cluster arrangement as indicated on the TEM micrograph. The EDX analysis confirmed the formation of Ag-Ni hybridization (Table 4.10). The silver and nickel were present approximately in the ratio of 2:1, unlike the hybrid prepared from 1.0 mM precursor mixture. Moreover, the atomic composition of silver (56.11%) and nickel (24.11%) were lower compared with the corresponding synthesis using 1.0 mM metal precursor mixture.

4.3.4 Optical (UV-Vis) Properties of Ag NPs under *S. occidentalis*-Influenced Synthesis at Room Temperature

The optical properties of monometallic Ag NPs via reduction of the aqueous silver ions during exposure to the extract of *S. occidentalis* leaves at room temperature are presented in Figure 4.26. Comparison of onset growth at varied precursor solution concentrations is shown in Figure 4.27.

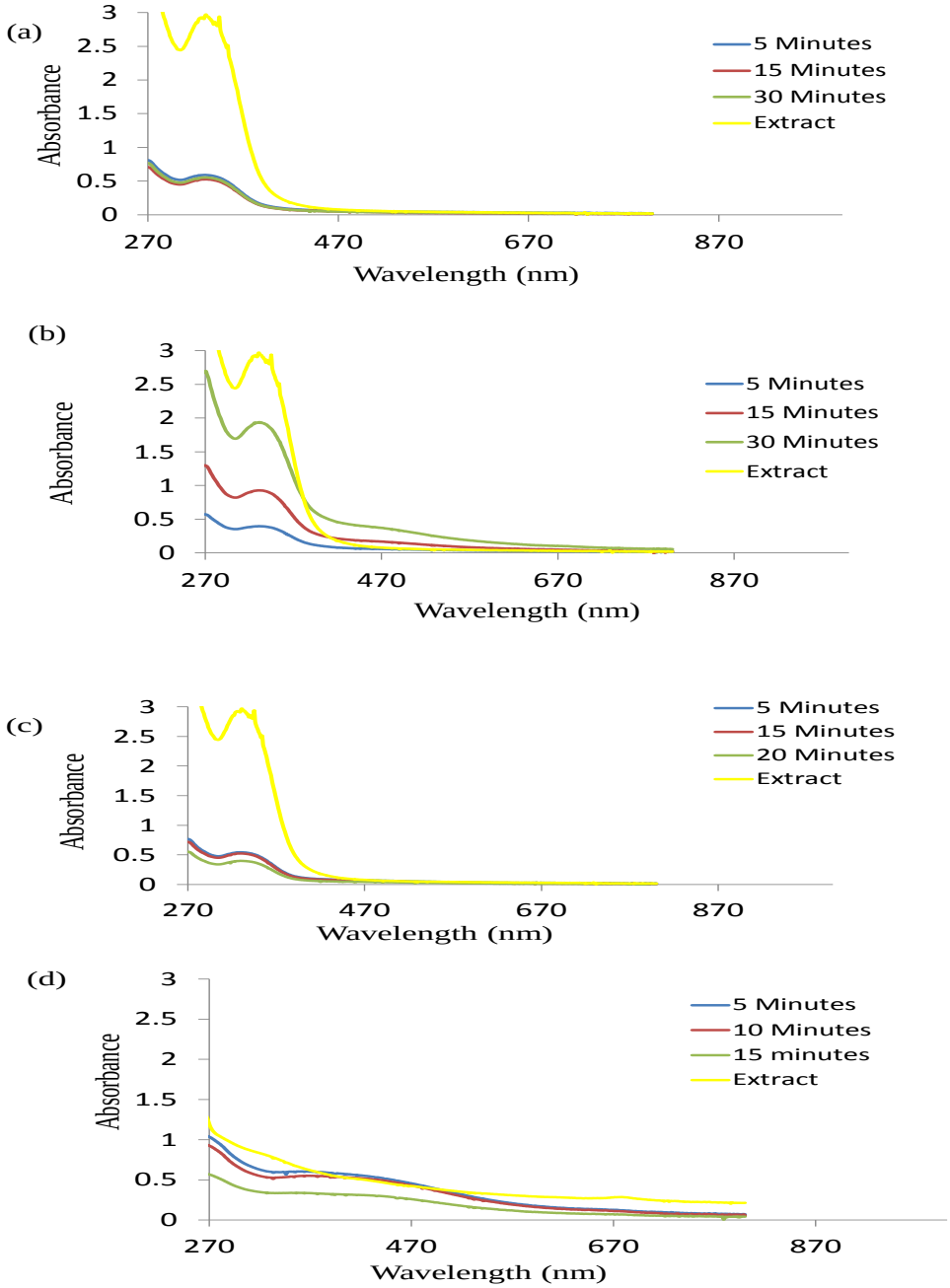

Figure 4.26: Room temperature time-resolved spectra of Ag nanoparticles prepared by reducing (a) 0.5 mM (b) 1.0 mM (c) 2.0 mM (d) 3.0 mM precursor solutions using the extract of *S. occidentalis*

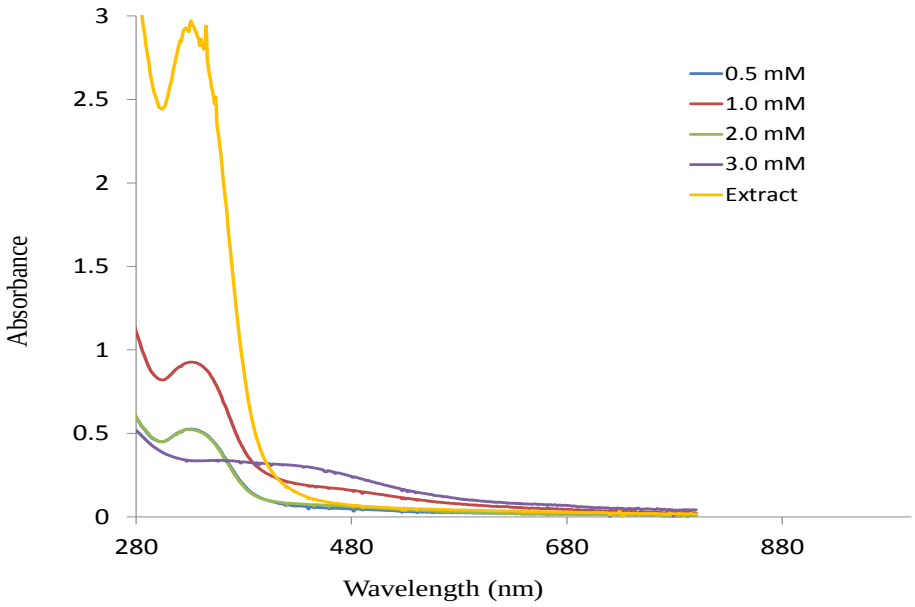

Figure 4.27: Comparison of growth in Ag NPs prepared from varied $AgNO_3$ solutions synthesized with the extract of *S. occidentalis* leaves at room temperature

Table 4.11: Bioreduction parameters for the synthesis of silver nanoparticles formed with the extract of *S. occidentalis* leaves at 70℃, 30 minutes

	Maximum intensity 0.5 mM		Maximum intensity 1.0 mM		Maximum intensity 2.0 mM		Maximum intensity 3.0 mM	
	Abs	λ_{max} (nm)	Abs	λ_{max} (nm)	Abs	λ_{max} (nm)	Abs	λ_{max} (nm)
Ag NPs	0.518	316	0.4	300-340 (Broad peak)	0.41	305	0.311	360-430 (Broad peak)

The leaf extract of *S. occidentalis* displayed visual property as it strongly absorbed in the UV/Visible region with intensity of 2.8 a.u. (Figure 4.26). The presence of n⟶ π* transition (C=O) functional group of carbohydrates present in the bio-reducing agents could be responsible for this observation (Wani *et al.*, 2010). The intensity of absorption by the corresponding nanohybrid formed (0.4 - 0.8 a.u) was not as intense when compared with the extract.

The nucleation and formation of nanoclusters were very rapid, as early as 2 minute, similar to the same reaction at 70℃ reaction conditions. Ag NPs exhibited brownish colour in water, as a result of excitation of surface plasmon vibrations in the metal nanoparticles (Mulvaney, 1996). However, this supported the presence of adequate boimolecules (carbohydrates and glycosides) in the extract for the nanoparticles formation. The SPR band occurred at 316 nm with absorption intensity of 0.518 (a.u.), 300-340 nm (0.4 a.u.), 305 and 350-430 nm in 0.5, 1.0, 2.0 and 3.0 mM precursor solutions respectively (Table 4.11).The blue shift wavelength of absorption also suggests medical application of *S. occidentalis* Ag NPs.

4.4 Optical (UV-Vis) Properties of Ag NPs under *Nicotiana tobacuum*-Influenced Synthesis at 70℃

Figure 4.28 reveals the combined absorption peak of Ag NPs prepared using *N. tobacuum* laef extract. Figure 4.29 illustrates the optimum growth in Ag NPs (2.0 mM $AgNO_3$ solution) and the comparison of growth kinetics. Table 4.12 presents the onset growth time and absorbance intensity values.

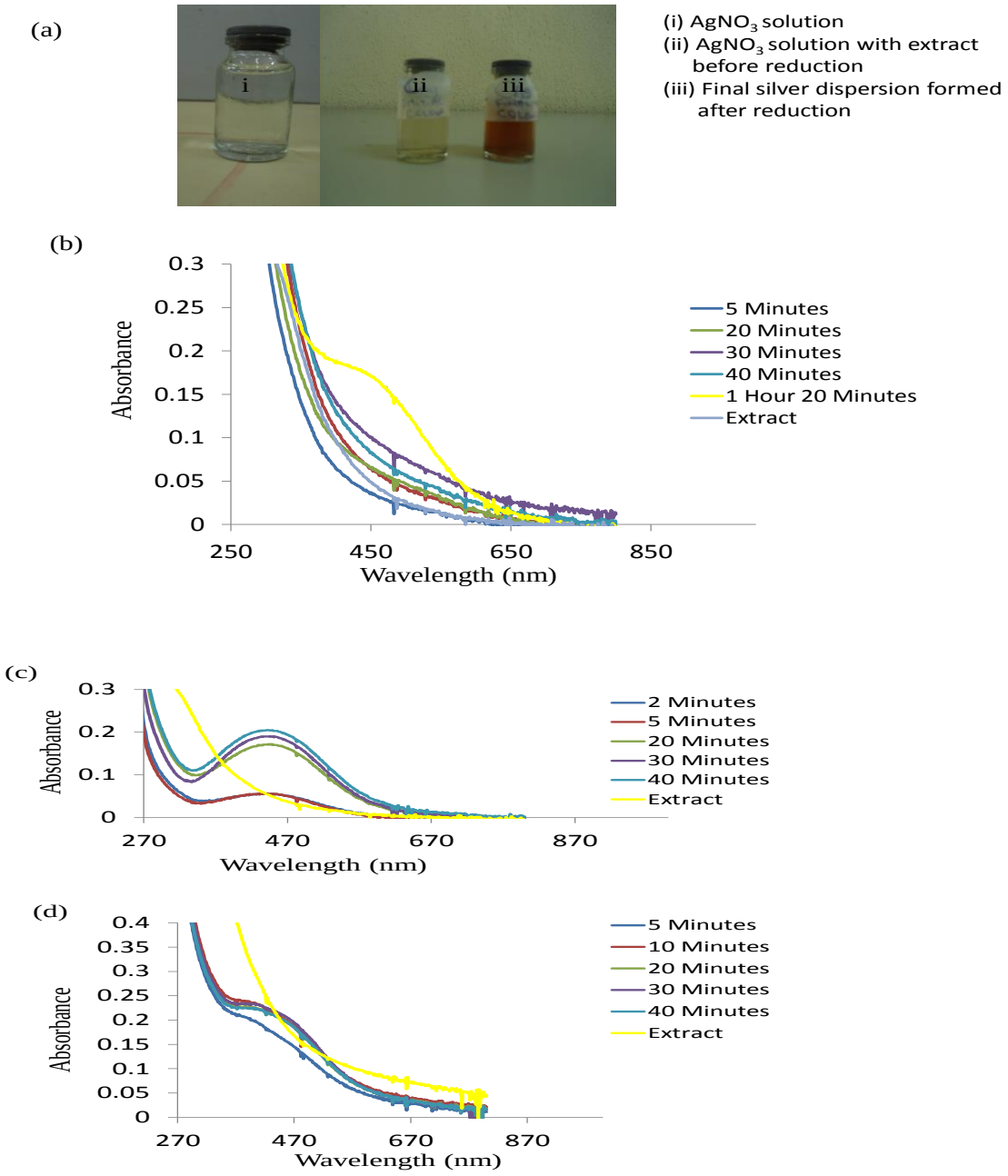

Figure 4.28: (a) Silver dispersion before and after nanoparticles formation. UV-Vis spectra of Ag NPs prepared from (b) 1.0 mM (c) 2.0 mM (d) 3.0 mM $AgNO_3$ solution concentrations using the extract of *Nicotiana tobacuum* leaves as a reducing/capping agent at 70℃

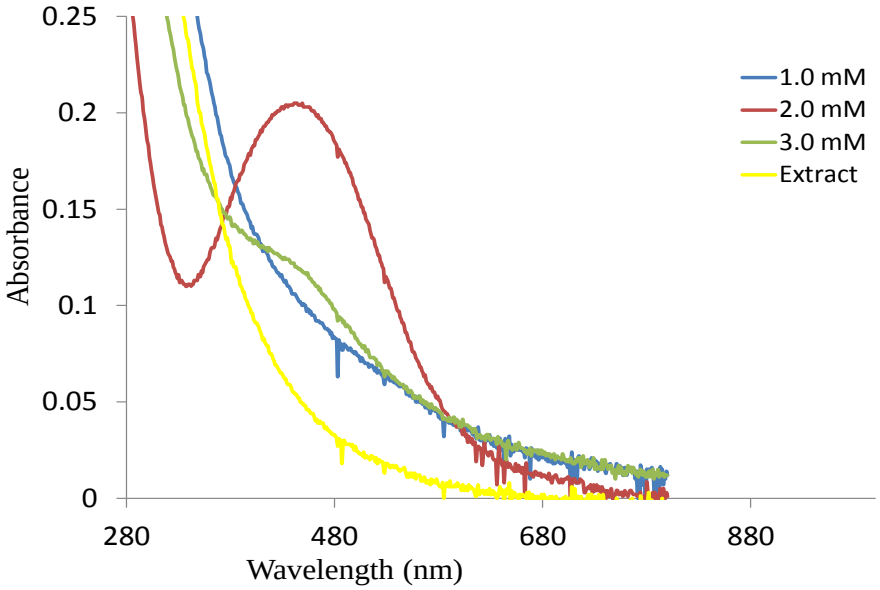

Figure 4.29: Growth comparison in Ag NPs prepared from different precursor solution concentrations at 70 ˚C and 40 minutes, using the extract of *Nicotiana tobacuum* leaves as a reducing/capping agent

Table 4.12: Bioreduction parameters for the yntheses of silver and its hybrid nanoparticles prepared with the extract *N. tobacuum* leaves at 70℃, 40 minutes

NPs	Maximum intensity 0.5 mM		Maximum intensity 1.0 mM		Maximum intensity 2.0 mM		Maximum intensity 3.0 mM	
	Abs	λ_{max} (nm)	Abs	λ_{max} (nm)	Abs	λ_{max} (nm)	Abs	λ_{max} (nm)
Ag			0.162	400-430	0.312	438	0.232	400-450 (Broad)
Ag-Ni			0.046	420-450			0077	430
Ag-Co		No SPR		No SPR		No SPR		No SPR

The reaction between extract of *N. tobacuum* leaves and $AgNO_3$ solution (precursor) led to a change in colour from light green to dark brown, as an evidence of nanoparticles formation (Figure 4.28a). The nucleation and onset growth started as early as 2 to 5 minutes in the Ag NPs from 2.0 and 3.0 mM metal solutions. In contrast, there was no noticeable excitation of plasmon in the nanocluster obtained from 1.0 mM solution until 1 hour of the reaction. Consequently, the slow growth rate of Ag NPs at this concentration could be attributed to strong interactions between the biomolecules and the growing silver particles which was time dependent (Huang *et al*., 2007). An enhanced optical property was exhibited in the UV-Vis spectra of Ag NPs synthesized from 2.0 mM precursor solution - optimum concentration (Deng & Li, 2003; Moon *et al*., 2006; Lu, Wei, Peng, Yu & Qian, 2003; Zhang, Dalpian and Fluegel, 2006). Highest absorption intensity (0.312 a.u.) was noticed in the reduced 2.0 mM $AgNO_3$. Red shifted absorbance peaks at the varied concentrations indicated complete reduction and increase in particle size according to Lifshitz and Slyozov (1961). Hence, this verified the metallic nature of the nanoparticles. The broad peaks in the nanoparticles prepared from 1.0 and 3.0 mM metal precursors suggested polydispersed particles. Nevertheless, complete reduction took place within 40 minutes as indicated in the spectra overlap.

4.4.1 TEM and Size Distribution of Ag NPs Using *N. tobacuum* at 70℃

There was no evidence of reduction of Ag^{+} ions to Ag^{0} when the extract of *N. tabacuum* leaves reacted with 1.0 mM precursor solution; no visible morphology. Hence, the reaction did not proceed in the presence of *N. tobacuum* leaf extract at this precursor concentration (Figure 4.30).

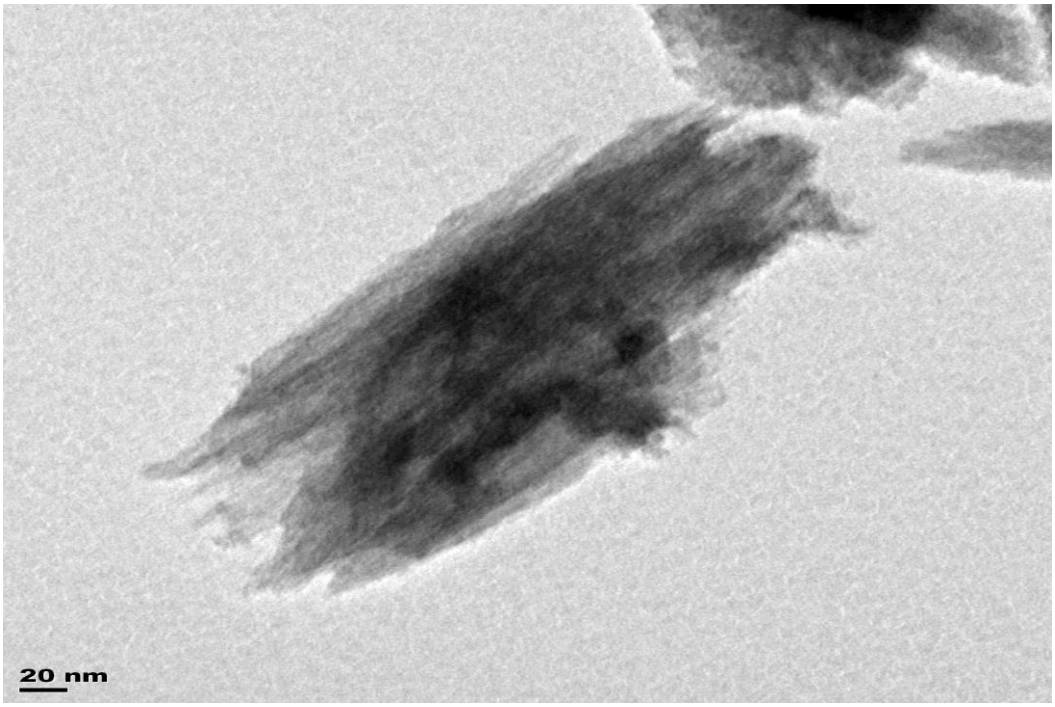

Figure 4.30: TEM image of Ag NPs prepared under *N. tobacuum*-influenced synthesis using 1.0 mM metal precursor solution

Table 4.13 The EDX results of Ag NPs prepared from the extract of *N. tobacuum* leaves and 1.0 mM metal precursor

Element	series	[wt.%]	[norm. wt.%]	[norm. at.%]	Error in %
Silver	L-series	2.11	4.21	4.42	1.31
Oxygen	K-series	32.34	51.10	55.45	0.06
Carbon	K-series	54.22	43.44	39.11	0.47
Nickel	K-series	0.12	0.96	0.87	0.99
Cobalt	K-series	0.20	0.29	0.15	0.04
	Sum:	75.12	100.00	100.00	

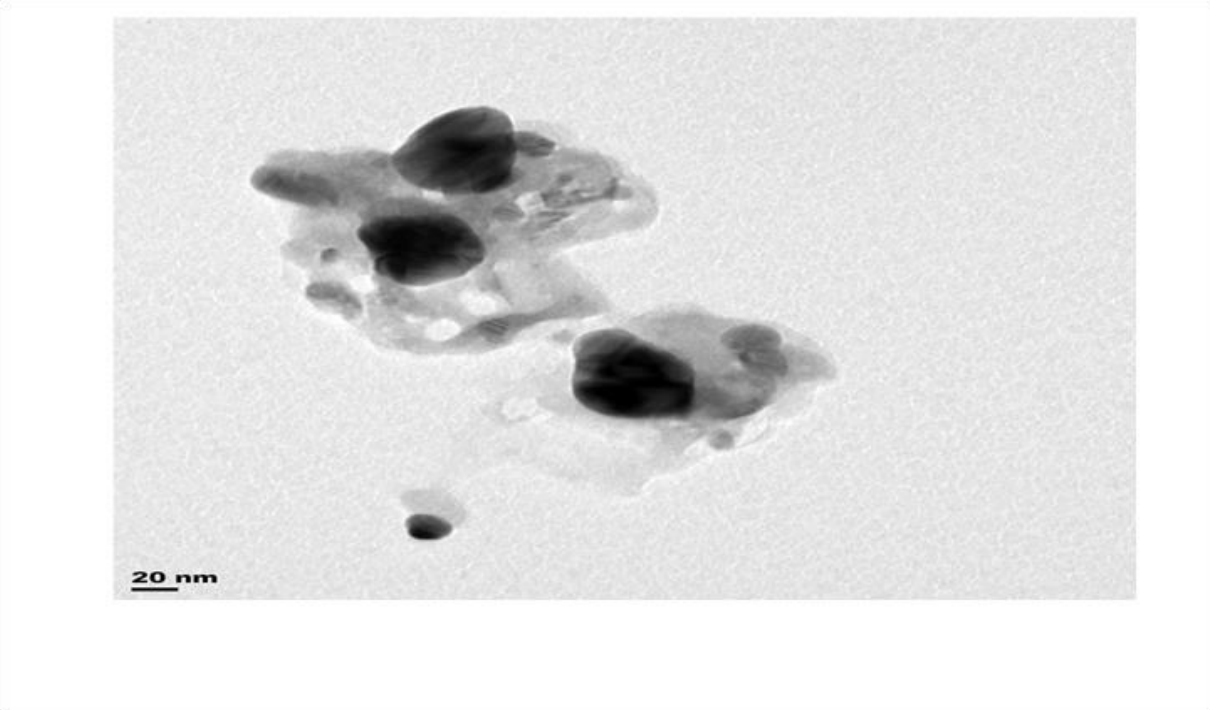

Figure 4.31: TEM image of Ag NPs under *N.tobacuum*-influenced synthesis using 2.0 mM metal precursor solution

Table 4.14: The EDX result of Ag nanoparticles prepared from the extract of *N. tobacuum* leaves and 2.0 mM metal precursor

Element	series	[wt.%]	[norm. wt.%]	[norm. at.%]	Error in %
Silver	L-seris	71.22	89.11	85.52	0.77
Oxygen	K-series	5.28	3.99	9.87	1.11
Carbon	K-series	6.66	4.78	3.38	0.36
Nickel	K-series	0.83	0.99	0.62	0.09
Cobalt	K-series	0.03	1.11	0.60	0.09
Phosphorus	K-series	0.01	0.02	0.01	0.00
Sulphur	K-series	0.00	0.00	0.00	0.00
	Sum:	84.03	100.00	100.00	

The EDX analysis also corroborated the result as the atomic composition of silver (4.42%) was small in the synthesis. However, oxidation of Ag^+ to Ag_2O took place which resulted in high percentage yield of oxygen (55.45) and carbon (39.11) from the plant extract (Table 4.14). This indicated that none of the phytochemicals (carbohydrates, glycosides and the alkaloids) present could reduce the Ag^+ at this concentration. However, the synthesis at higher metal precursor concentration: 2.0 mM produced quasi cube and spherical shaped nanoparticles. The morphology of Ag NPs (Figure 4.31) gave a mean size of cube and sphere of 13.28 nm. The composition of elements present in the biosynthesized Ag NPs at 2.0 mM is shown in Table 4.14. The EDX analysis confirmed the formation of Ag NPs. Silver was present in 85.52 atomic %. Oxygen (9.84 atomic %) and carbon (3.38 atomic %) originated from the plant extract.

4.4.2 XRD Patterns of *N. tobacuum*-influenced Ag NPs

Figure 4.32 is the XRD patterns of Ag NPs synthesized using the extract of *N. tobacuum* leaves at 70℃.

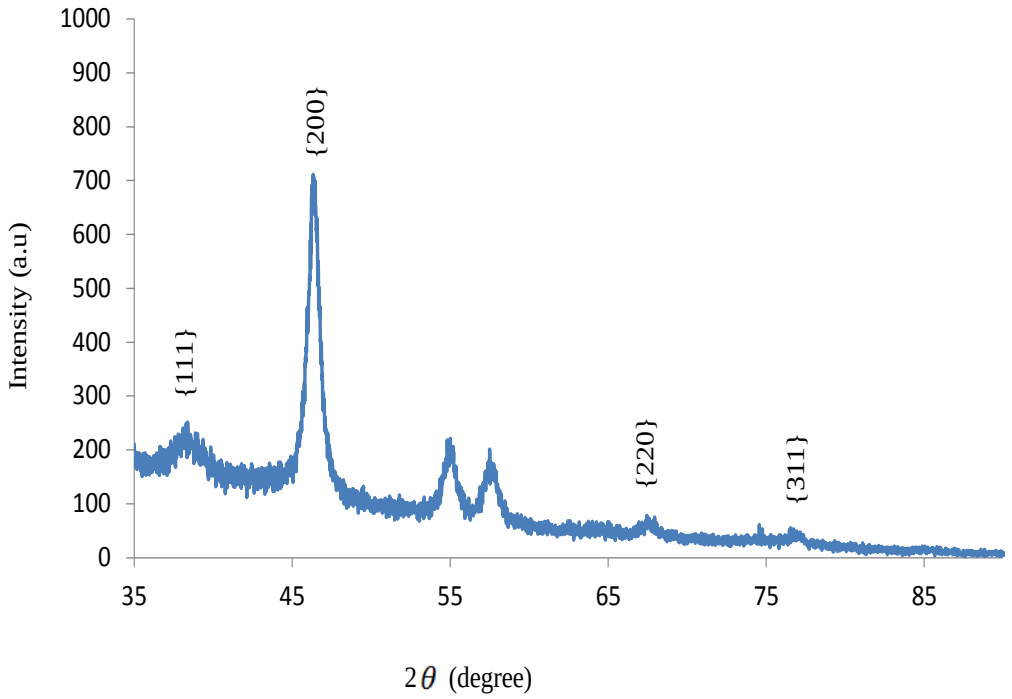

Figure 4.32: XRD patterns of Ag NPs prepared using the extract of *N. tobacuum* leaves with 2.0 mM metal precursor solution at 70 ^{o}C

In the X-ray diffractogram of Ag nanoparticles prepared with *N. tobacuum* laef extract (Figure 4.32), the band characteristics of Ag appeared in four peaks, attributed to Ag were present at 2θ = 38.38°{111}, 46.36° {200}, 67.59°{220} and 76.54°{311}. Nonetheless, the intensities were not strong as other biosynthesized nanoparticles. The observed crystallographic planes of the fcc structure still supported crystallinity of the as-produced Ag nanoparticles. Other peaks noticed suggested the presence of impurities.

4.4.3 FTIR Analysis of the Ag NPs

Representative FTIR absorption spectrum of Ag nanoparticles prepared with the leaf extract of *N. tobacuum*, at 70℃ is presented in Figure 4.33.

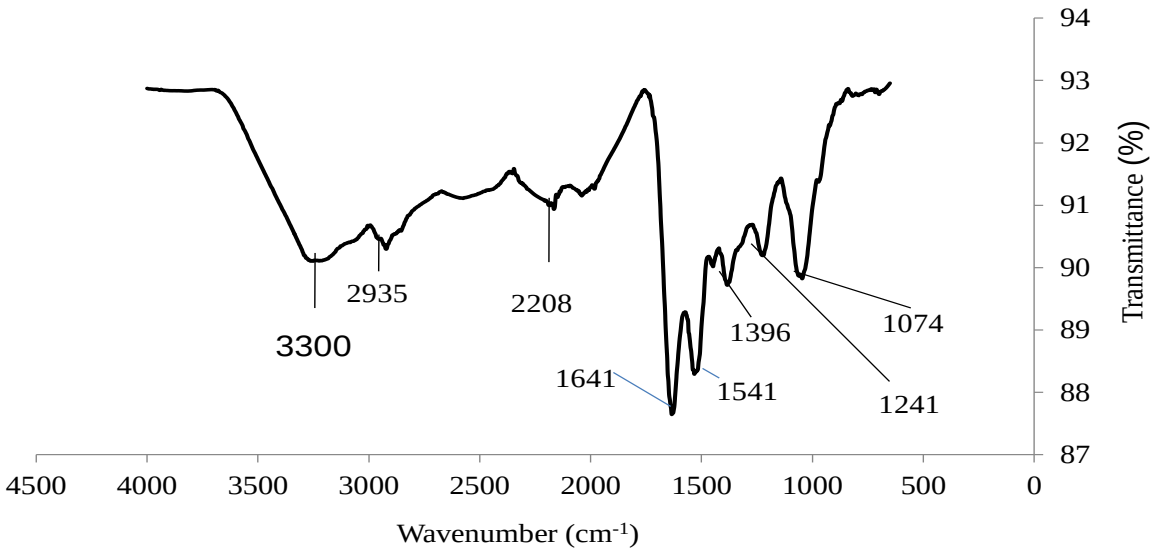

Figure 4.33: FTIR spectrum of Ag NPs using the extract of *Nicotiana tobacuum* leaves

The spectrum was characterized by some peaks at 3300 cm^{-1} (O-H stretching due to broad band) hydroxyl group from pytochemicals, 2935 cm^{-1} (C-H stretching from SP^3 hybridization), 1641 cm^{-1} (C=C stretching), 1241 cm^{-1} (C-N stretching). The biosynthesis reaction took place through the active site created by nitrogen present in the alkaloids of *N. tobacuum***,** resulting in the attachment of methylene group to nitrogen formed on the surface of Ag nanoparticles (Scheme 3). There appeared to be no peak in the carbonyl (C=O) region characteristic of carbohydrate and glycosides. The observed peaks were more of features of abundant alkaloids in the tobacco plant. This suggested that the reduction of Ag^+ ions to Ag^0 could be responsible by alkaloids in the plant extract.

4.4.4 Optical (UV-Vis) Properties of Ag-Ni Bimetallic Nanoparticles under *Nicotiana tobacuum*-Influenced Synthesis at 70°C

The optical properties of Ag-Ni nanoparticles are presented in Figure 4.34.

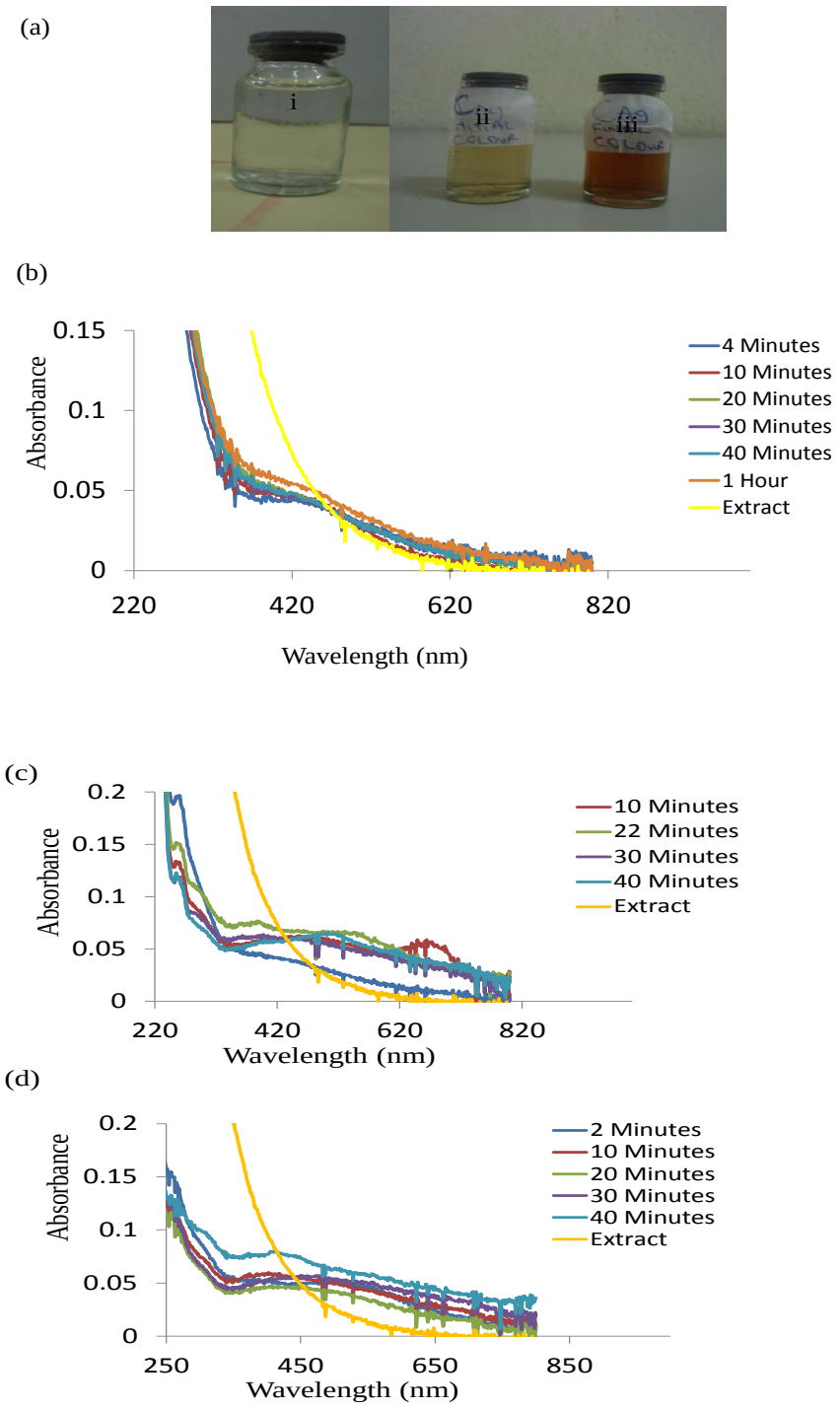

Figure 4.34: (a) Colour change before and after nanoparticles formation. UV-Vis spectra of Ag-Ni bimetallic nanoparticles prepared by reducing (b) 1.0 mM (c) 2.0 mM (d) 3.0 mM precursor solutions using the extract of *N. tobacuum* at 70℃

Table 4.15: Bioreduction parameters for the syntheses of silver and its hybrid nanoparticles using the extract of *N. tobacuum* leaves at 70 ℃, 40 Minutes

	Maximum intensity 1.0 mM		Maximum intensity 2.0 mM		Maximum intensity 3.0 mM	
NPs	Abs	λ_{max} (nm)	Abs	λ_{max} (nm)	Abs	λ_{max} (nm)
Ag	0.162	400-430	0.312	438	0.232	400-450 (Broad)
Ag-Ni	0.046	420-450	0.06	516	0.077	419
Ag-Co		No SPR		No SPR		No SPR

The gradual change in colour (light green to dark brown) signalled the formation of nanoparticles (Figure 4.34a). Furthermore, the bioreduction indicated reducing agent/capping agents in the extract. The exhibition of surface plasmon resonance (SPR) peak confirmed the presence of nanoparticles. The peak assigned to silver in the Ag-Ni bimetallic nanoparticles was broader than the SPR peak in the pure Ag NPs solution (Table 4.15) as a result of the effect of nickel. Figure 4.35 connotes the comparison of growth in Ag-Ni bimetallic nanoparticles at varied concentrations, 70℃ temperature and 40th minute of the reaction.

In this study, the SPR peaks of the hybrid Ag-Ni particles at varied precursor mixture solution concentrations were 420-450 nm (1.0 mM) and 516 nm (3.0 mM). The effect of Ni in the hybrid was a red shift of 78 nm to the parent Ag NPs. This could be as a result of the overlap of the electronic states of the constituents of the bimetallic particles; resulting in the modification of the surface plasmon resonance (Steiner, Mokari, Banin & Millo, 2005; Yu *et al*., 2005). Moreover, the red shift may also be as a result of Ag portion of the hybrid nanoparticles partially covered with Ni, the surface was enriched with Ag. Thus, this suggested an existence of a core-shell, which was confirmed by TEM micrograph (Xia *et al.*, 2010; Kishore *et al.*, 2013).

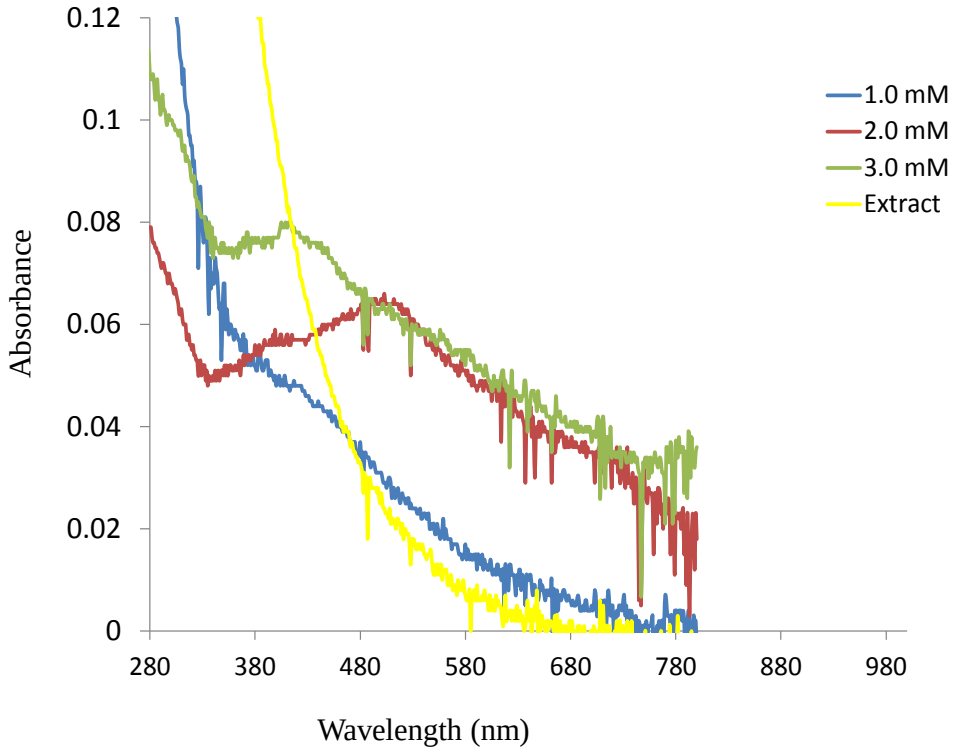

Figure 4.35: Growth comparison in Ag-Ni bimetallic NPs prepared from varied precursor solution concentrations at 70 ˚C , 40 minutes using the extract of *Nicotiana tobacuum*

4.4.5 TEM and Size Distribution of Ag-Ni Bimetallic Nanoparticles under *N. tobacuum*-Influenced Synthesis

The particle size distribution histograms and TEM images of the biosynthesized bimetallic Ag-Ni nanocluster using the extract of *N. tobacuum* for the bioreduction of 1.0 mM and 3.0 mM precursor mixture at 70℃ are shown in Figure 4.36 and 4.37 respectively.

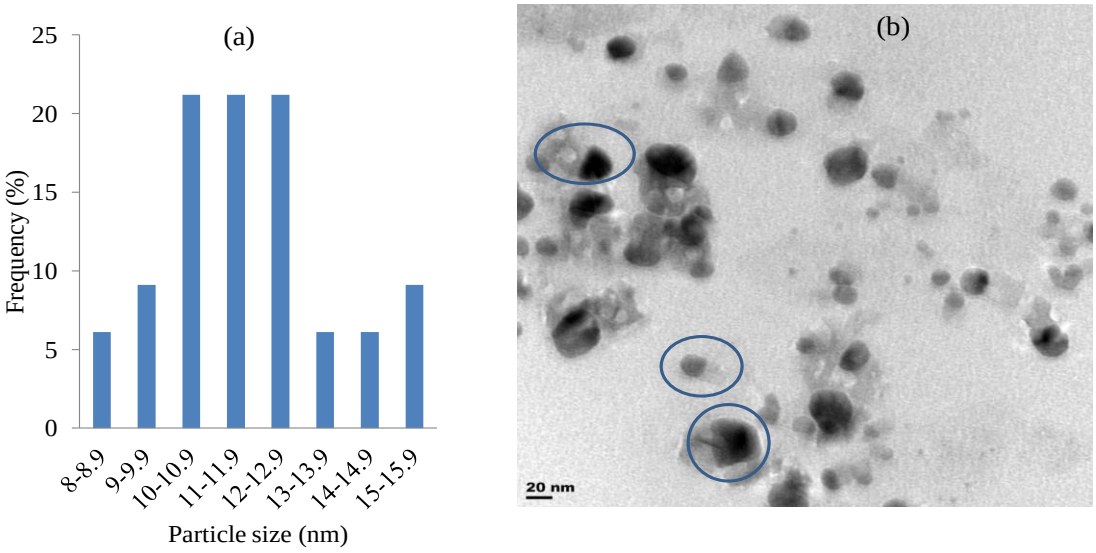

Figure 4.36: (a) Particle size distribution histogram of Ag-Ni NPs determined from TEM image (b) Representative TEM image of the bimetallic Ag-Ni NPs using *N. tobacuum*i and 1.0 mM metal precursor mixture, 70^0C

Table 4.16: EDX result of Ag-Ni bimetallic nanoparticles prepared with the extract of *N. tobacuum* leaves using 1.0 mM metal precursor

Element	series	[wt.%]	[norm. wt.%]	[norm. at.%]	Error in %
Silver	L-series	34.92	54.63	60.26	1.50
Oxygen	K-series	6.52	11.48	15.88	5.47
Carbon	K-series	11.37	12.15	1.90	0.21
Nickel	K-series	20.04	21.63	19.87	0.08
Cobalt	K-series	0.07	0.11	0.06	0.04
Phosphorus	K-series	0.00	0.00	0.03	0.00
Sulphur	K-series	0.00	0.00	0.00	0.00
	Sum:	63.92	100.00	100.00	

The size of the particles ranged from 8.14 to 14.66 nm with an average size of 11.46 ± 1.63 nm (Figure 4.36). The observed quasi spheres and cubes with various degrees of edges and corner were due to the reducing power of the plant extract. The EDX investigation proved the formation of Ag-Ni hybrid nanoparticles, with the atomic quantities of predominating silver to be 60.26%. Nickel (19.89%) was also present. However, the nanohybrid was Ag enriched (Table 4.16).

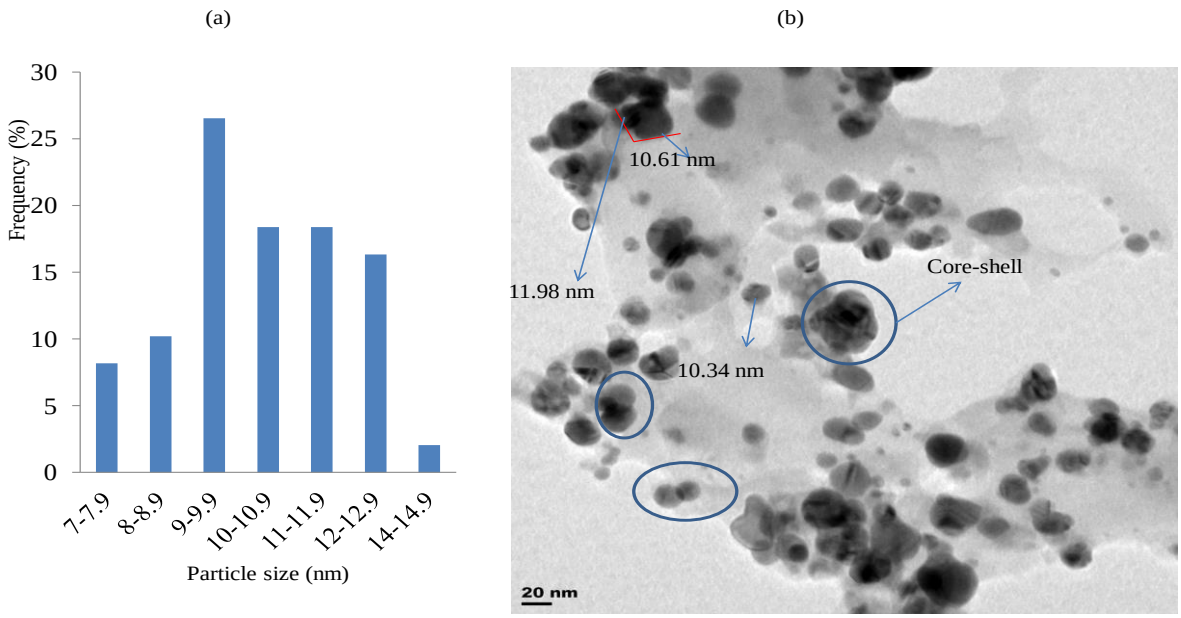

Figure 4.37: (a) Particle size distribution histogram of Ag-Ni NPs determined from TEM image (b) Representative TEM image of the bimetallic Ag-Ni NPs using *N. tobacuum* and 3.0 mM precursor mixture, 70^0C

Table 4.17: EDX result of Ag-Ni bimetallic nanoparticles prepared with the extract of *N. tobacuum* leaves using 3.0 mM metal precursor

Element	series	[wt.%]	[norm. wt.%]	[norm. at.%]	Error in %
Silver	L-series	39.75	63.76	69.70	0.77
Oxygen	K-series	7.77	18.51	5.95	5.77
Carbon	K-series	13.03	14.85	13.70	0.21
Nicke	K-series	10.70	11.13	10.43	0.06
Cobalt	K-series	0.79	1.26	0.48	0.06
Phosphorus	K-series	0.27	0.44	0.32	0.04
Sulphur	K-series	0.03	0.06	0.04	0.00
	Sum:	62.35	100.00	100.00	

Different shapes peculiar to Ag and nickel metals i.e. spheres, core-shell, cubes with truncated edges, multiply-twinned with various edges and corner truncation were observed in morphology of the formed bimetallic Ag-Ni clusters as shown in Figure 4.37. The sizes of particles ranged from 7.24 to 12.77 nm. The morphology of the hybrid nanoparticles as shown in Figure 4.37 had a mean size of 10.41 ± 1.82 nm. Polydispersed particles were observed. The structural elucidation based on TEM Figure 4.35(b) revealed the formation of core-shell; multipl-twin, alloy sphere and cubes.

The EDX analysis supported the formation of Ag-Ni hybrid nanoparticles (Table 4.17). Ag and Ni were in the approximate ratio of 4:1 weight composition. The atomic composition of silver was 69.70% and Ni was 10.43%. Carbon (13.70 atomic %) and oxygen (5.95 atomic %) were from the plant used.

4.4.6 Optical (UV-Vis) Properties of Ag NPs under *N. tobacuum*-Influenced Synthesis at Room Temperature

Optical properties of the biosynthesized Ag NPs using the extract of *N. tobacuum* leaves as a reducing agent/capping agent at room temperature are shown in Figure 4.38.

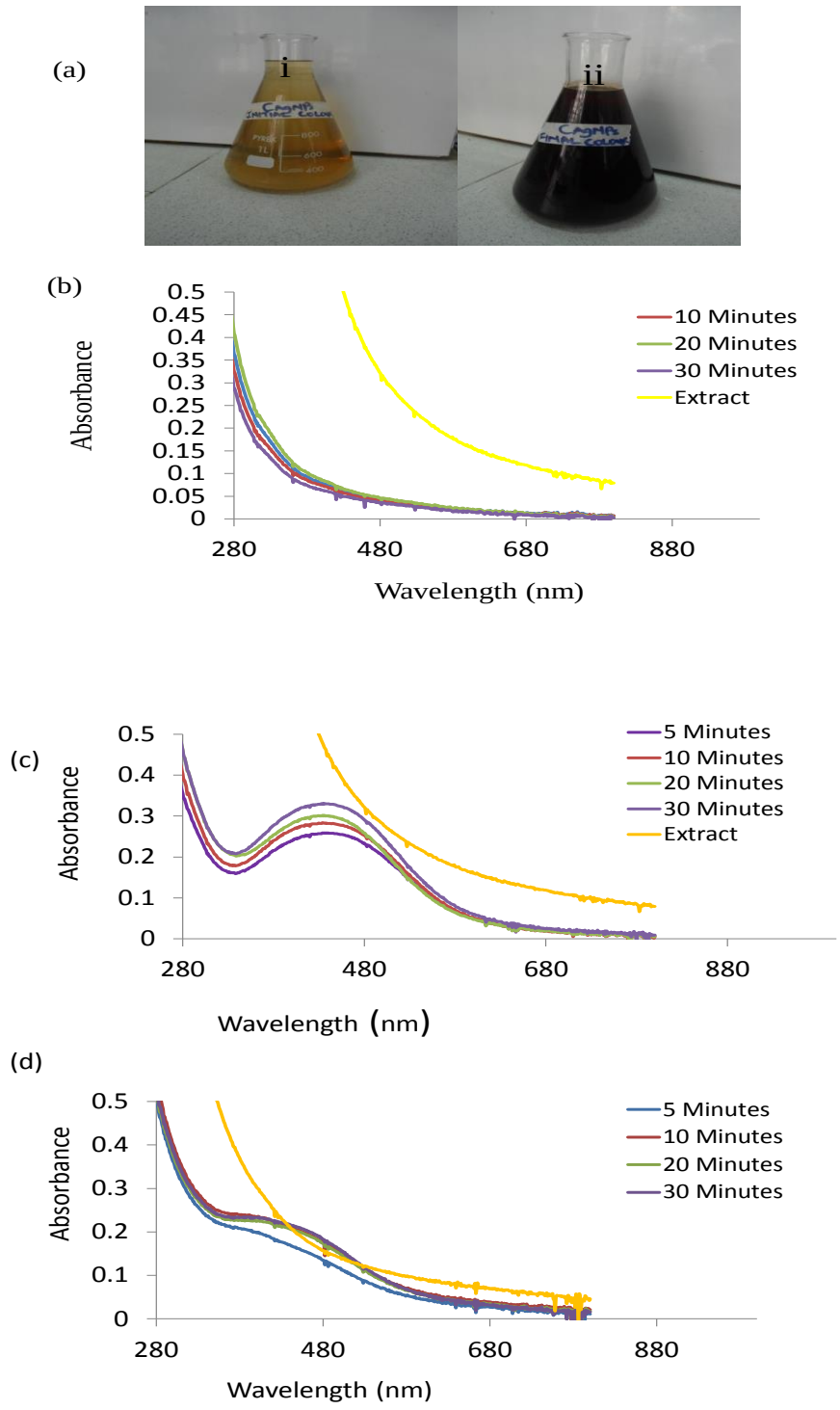

Figure 4.38: Room temperature time-resolved UV-Vis spectra of Ag NPs prepared from varied precursor solution using the extract of *N. tobacuum*, 30 minutes

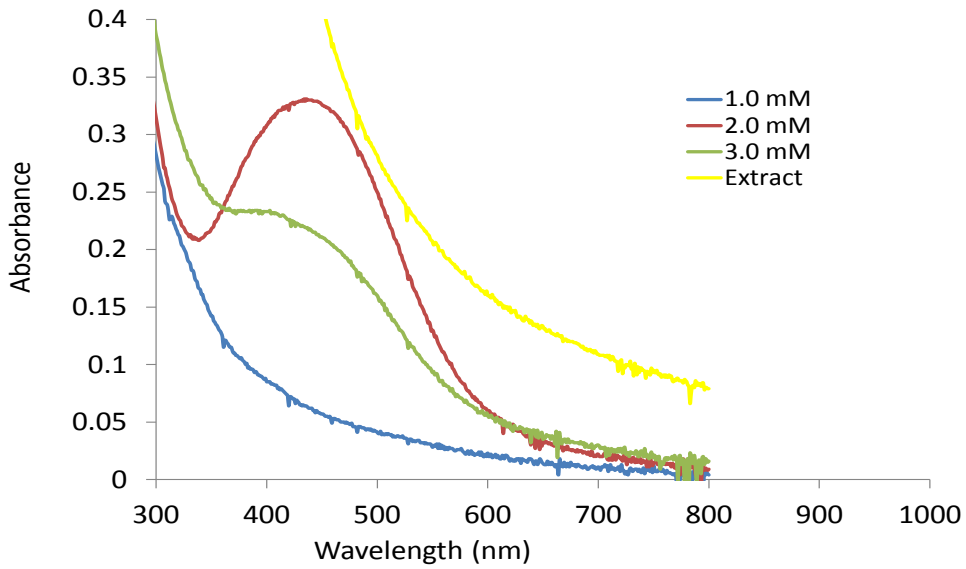

Figure 4.39: Growth comparison of Ag NPs prepared from varied precursor solution concentrations at room temperature and 30 minutes, using the extract of *N. tobacuum* leaves as a reducing agent

The bioreduction process was fast. Nucleation and growth commenced within 5 minutes of the reaction with an observed steady change in colour from slight yellowish brown to dark brown. Figure 4.38(a) indicates the formation of nanoparticles. The appearance of SPR band between 400-430 nm at varied precursor solution concentrations, corresponding to monometallic Ag NPs band confirmed the formation of Ag NPs before further characterizations (Daisy, 2009). Figure 4.39 represents growth comparison in Ag NPs from the reduced 0.5 - 3.0 mM precursor solutions.

The Ag NPs exhibited surface plasmon resonance (SPR) band due to the collective oscillation of free conduction electrons by the interacting field (Mulvaney, 1996). Rapid formation of Ag NPs was attained in 2.0 and 3.0 mM precursor solutions, despite the fact that the reaction took place at room temperature. Higher intensity of absorbance (0.312) with SPR was observed in the nanocluster formed in 2.0 mM solution. Optimum growth condition was achieved in this reduced solution concentration. Figure 4.38 displays red shift wavelength at 436 nm (2.0 mM precursor solution) and a broad peak 400-430 nm (3.0 mM precursor solution). The broad peak suggested polydispersed particles. High absorption wavelength also proposed increase in particle size. The peak increased gradually as a function of reaction time from 5 to 30 minutes, completed by exhibiting overlap in the spectra between 20th and 30th minutes, with no further changes in the size and peak intensity.

4.5 Optical (UV-Vis) Properties of Ag NPs under *M. charantia*-Influenced Synthesis at 70°C

Optical properties of the biosynthesized Ag NPs using the extract of *M. charantia* leaves as a reducing agent/capping agent at 70°C are shown in Figure 4.40.

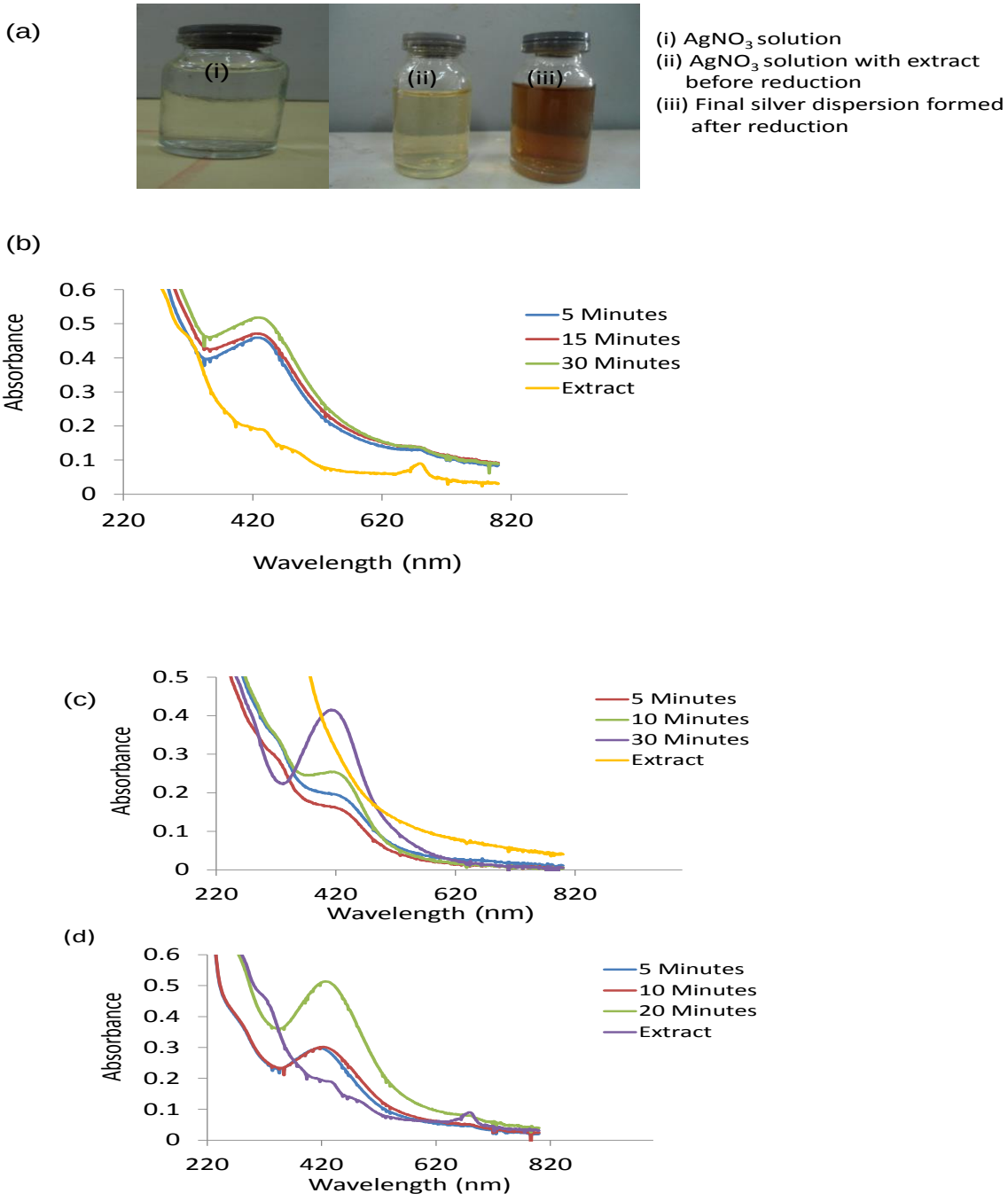

Figure 4.40: (a) Colour change before and after nanoparticles formation. UV-Vis spectra of Ag NPs prepared by reducing (b) 1.0 mM (c) 2.0 mM (d) 3.0 mM precursor solutions using the extract of *M. charantia* at 70℃

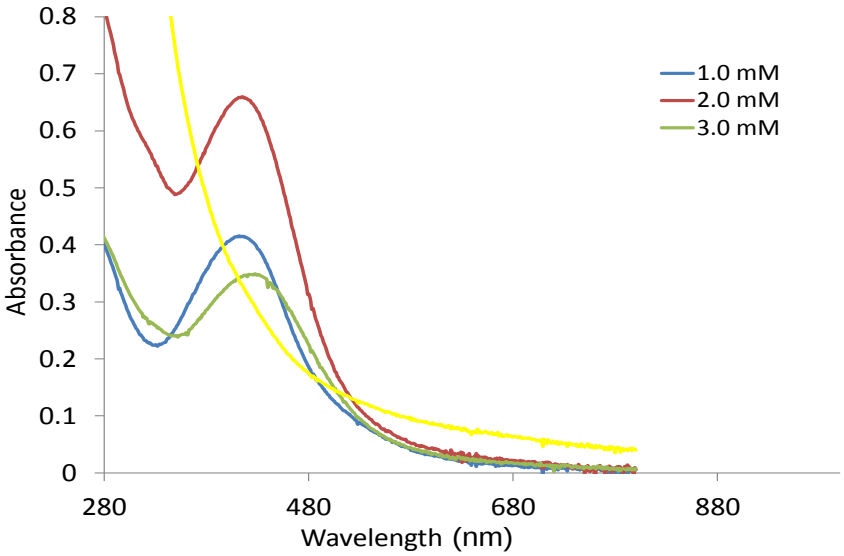

Figure 4.41: Growth comparison in Ag NPs prepared from varied precursor solution concentrations at 70 ˚C and30 minutes using the extract of *M. charantia* leaves as a reducing agent

Table 4.18: Bioreduction parameters for the syntheses of silver and its hybrid nanoparticles formed using the extract *M. charantia* leaves at 70 ℃, 30 minutes

	Maximum intensity 1.0 mM		Maximum intensity 2.0 mM		Maximum intensity 3.0 mM	
NPs	Abs	λ_{max} (nm)	Abs	λ_{max} (nm)	Abs	λ_{max} (nm)
Ag	0.508	432	0.518	403	0.415	436
Ag-Ni	0.172	420-450	0.242	420-450 (Broad)	0.212	427
Ag-Co	0.38 (1 hour)	400-600				

The surface plasmon absorption for silver usually observed at 400-440 nm was present. A narrow red shift absorption peak appeared at 432, 403 and 436 nm in the nanocluster synthesized from 1.0, 2.0 and 3.0 mM metal precursor solutions respectively (Table 4.18). A low wavelength of 403 nm as a result of strong quantum confinement effect was revealed in the green particle synthesized from 2.0 mM precursor solution (Deng & Li, 2003). Highest absorption intensity of 0.508 a.u. was exhibited in the nanoparticles formed from the reduced 2.0 mM precursor solution. Hence, this proposed catalytic ability of the bionanopaticles (Roduner, 2006). There was also a noticeable increase in the intensity of absorption as a function of time of reaction with no further shift in the peak wavelength and sizes. Onset growth and nucleation began within 5 minutes of the reaction. The appearance of SPR band confirmed Ag NPs formation. A gradual colour change was observed from light brown to deep brown (Figure 4.40 a). Reaction completion took place between the 10th and 15th minutes of the reaction as a result of overlap observed in the spectra.

Furthermore, the rapid synthesis of Ag NPs indicated the presence of adequate phytochemicals: saponins and glycosides present in the extract of *M. charantia* which acted as the reducing/ capping agents for the newly synthesized nanoparticles (Shankar *et al*., 2004). The narrow peak also suggested monodispersed spherical nanoparticles. Figure 4.41 shows the growth comparison of the bionanoparticles in different metal precursor concentrations.

4.5.1 Optical (UV-Vis) Properties of Ag-Ni Bimetallic Nanoparticles under *M. charantia*–Influenced Synthesis at 70℃

The UV-Vis spectra of Ag-Ni hybrid nanoparticles are presented in Figure 4.42.

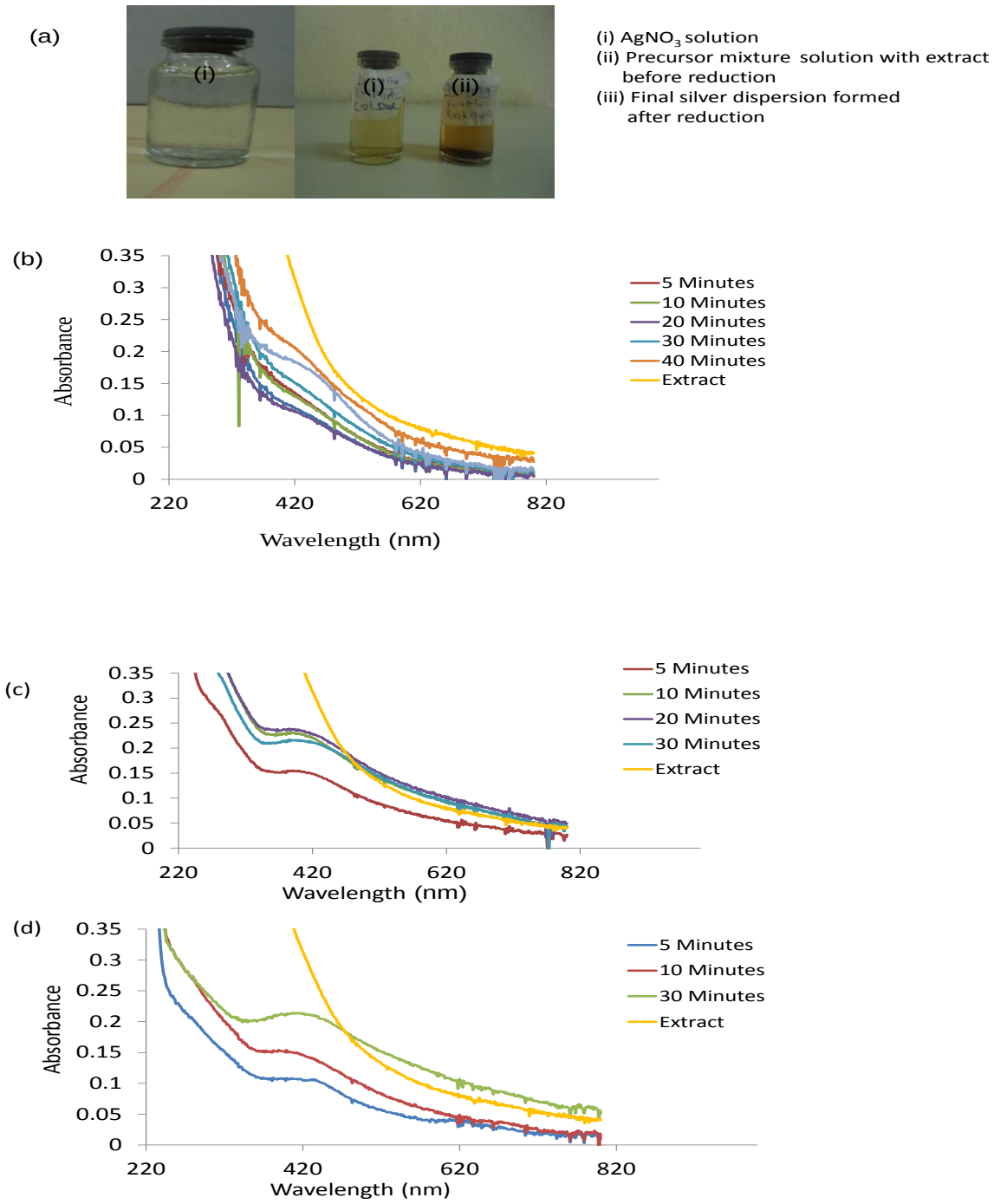

Figure 4.42: (a) $AgNO_3$ solution (i), Precursor mixture solution with extract before reduction (ii), and the final silver dispersion formed after reduction. UV-Vis spectra of Ag-Ni bimetallic nanoparticles prepared from (b) 1.0 mM (c) 2.0 mM (d) 3.0 mM using the extract of *M. charantia* leaves

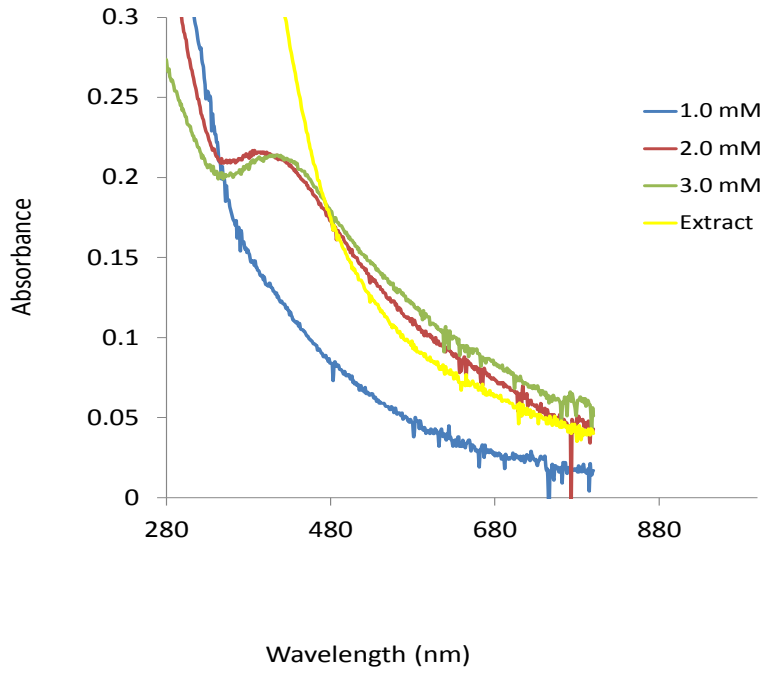

Figure 4.43: Growth comparison in Ag-Ni bimetallic nanoparticles prepared from different precursor solution concentrations at 70°C and 30 minutes using the extract of *M. charantia* leaves as a reducing agent

The observed colour changed from yellowish brown to dark brown (Figure 4.42a). This shows a reduction of Ag^{+} to $Ag^{0.}$ This could be explained as the result of excitation of conductive electrons due to characteristic vibrations in the electronic energy levels. The nucleation and onset growth occurred at the 5th minute of the reaction in all the reduced concentration solutions. Nanohybrid formation was confirmed by the appearance of surface plasmon resonance (SPR) with broader peaks (400-450 nm), and weak absorbance intensity when compared with the corresponding monometallic Ag NPs (Table 4.18). This is noted to be the effect of Ni in the Ag-Ni bimetallic nanoparticles. Completion of reaction was revealed in the spectra overlap which took place between 10th and 20th minute of the reaction. Figure 4.43 presents the growth comparison at 30 minutes and varied metal precursor concentrations (1.0-3.0 mM).

4.5.2 TEM and Size Distribution of Ag Nanoparticles under *M. charantia*-Influenced Synthesis at 70℃

The particle size distribution histograms and transmission electron micrographs of the Ag nanocluster prepared from the reaction of 1.0 mM $AgNO_3$ and the extract of *M. charantia* leaves are presented in Figure 4.44 and 4.45 respectively.

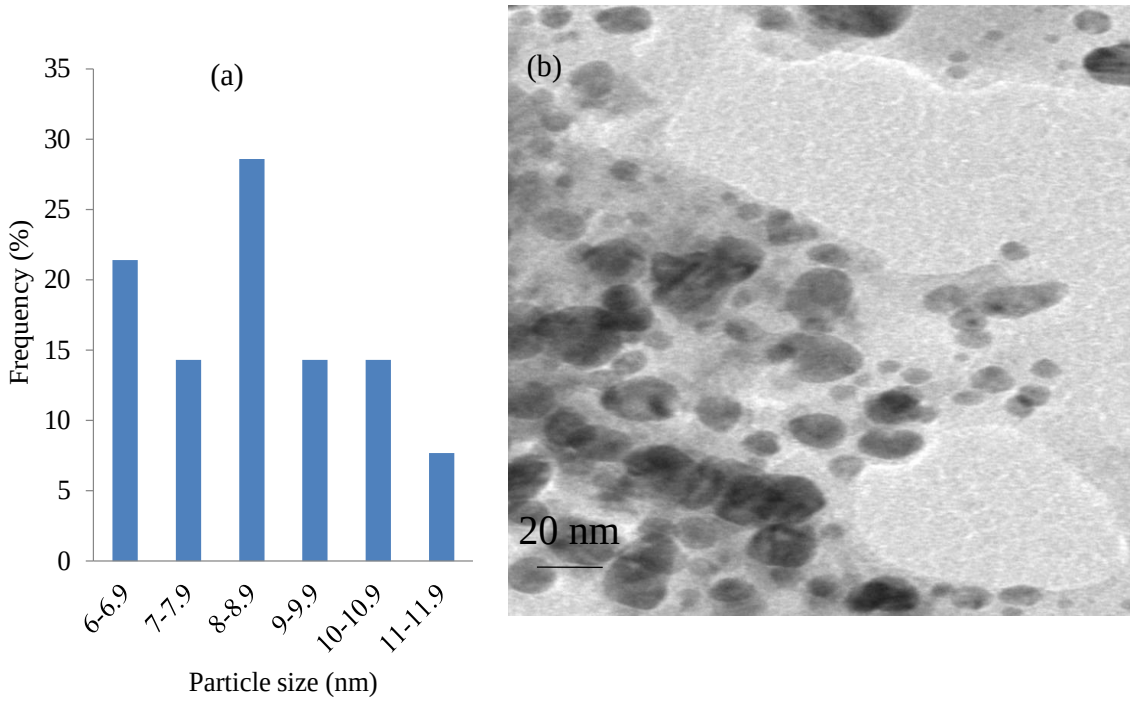

Figure 4.44: (a) Particle size distribution histogram of Ag nanoparticles determined from TEM image (b) Representative TEM image of the Ag nanoparticles under *M. charantia* -influenced synthesis using 1.0 mM metal precursor

Table 4.19: EDX result of Ag NPs capped with the extract of M. *charantia* leaves using 1.0 mM metal precursor

Element	series	[wt.%]	[norm. wt.%]	[norm. at.%]	Error in %
Silver	L-series	80.46	80.46	90.66	0.45
Oxygen	K-series	10.14	10.14	1.68	2.70
Carbon	K-series	7.92	7.90	6.97	0.15
Nickel	K-series	0.42	0.42	0.13	0.04
Cobalt	K-series	0.18	0.18	0.06	0.04
Phosphorus	K-series	0.88	0.88	0.51	0.06
	Sum:	100.00	100.00	100.00	

Spherical morphological structures of Ag NPs were revealed. The sizes of particles were of close range. The particles were mostly populated between 8 and 8.9 nm size range as shown with mean diameter of 8.56 $\pm$ 1.42 nm. The EDX examination confirmed the formation of silver nanoparticles (Table 4.19), with predominant composition of silver (90.66 atomic %).

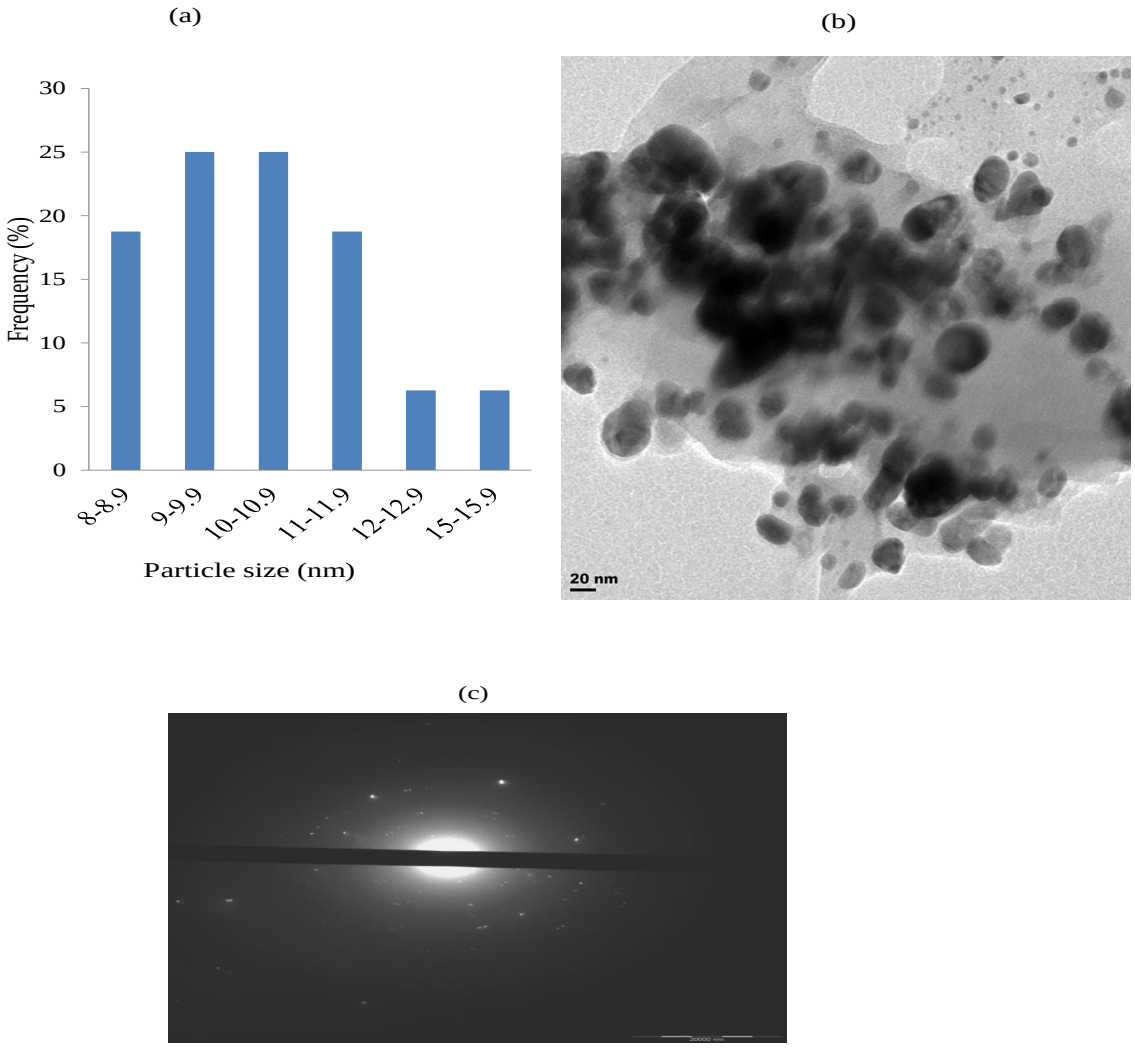

Figure 4.45: (a) Particle size distribution histogram of Ag nanoparticles determined from TEM image (b) Representative TEM image of the Ag nanoparticles under *M. charantia*-influenced synthesis using 2.0 mM metal precursor (c) SAED pattern of the Ag nanoparticles

Table 4.20: The EDX result of Ag nps capped with the extract of *M. charantia* leaves using 2.0 mM metal precursor

Element	series	[wt.%]	[norm. wt.%]	[norm. at.%]	Error in %
Silver	L-series	39.39	57.93	87.28	5.67
Oxygen	K-series	13.11	24.00	7.60	1.00
Carbon	K-series	13.37	14.96	3.37	0.24
Nickel	K-series	1.14	1.68	0.69	0.07
Cobalt	K-series	0.10	0.15	0.06	0.04
Phosphorus	K-series	0.87	1.28	1.00	0.06
	Sum:	67.99	100.00	100.00	

Figures 4.45 (a, b and c) represent the particle size distribution histogram, TEM micrograph of Ag nanoparticles and SAED pattern respectively, as synthesized from the reaction of 2.0 mM $AgNO_3$ solution and the extract of *M. charantia* leaves at 70℃**.** The particles were close in size range (advantage of plant-mediated synthesis). The particles portrayed quasi-spherical shapes. The mean sizes of both large and smaller conjugate particles of the Ag NPs formed were found to be 10.50 ± 1.74 nm. Particle agglomeration as a result of Ostwald ripening was also observed in the TEM micrograph.

The EDX analysis showed the weight and atomic composition of silver as 39.39% and 87.28% respectively (Table 4.20). The synthesis at 1.0 mM precursor concentration resulted in higher percentage yield of nanosilver than the preparation from 2.0 mM precursor.

4.5.3 Optical (UV-Vis) Properties of Ag-Co Bimetallic Nanoparticles under *M. charantia*-Influenced Synthesis at 70°C

The optical property of Ag-Co hybrid nanoparticles prepared from 1.0 mM precursor solution is depicted in Figure 4.46.

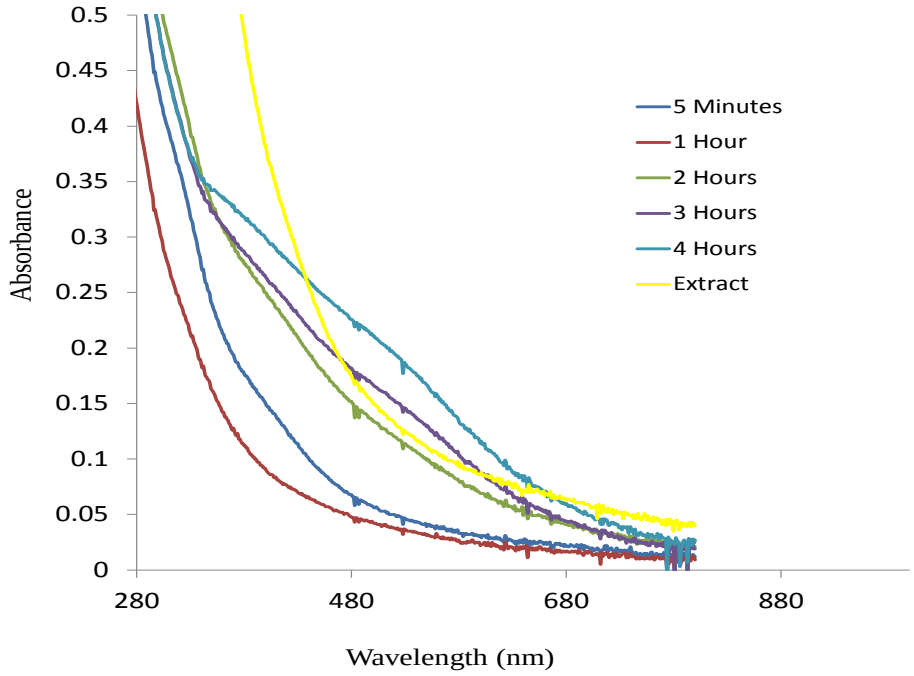

Figure 4.46: UV-Vis spectra of Ag-Co bimetallic nanoparticles prepared from 1.0 precursor solution at 70°C, using the extract of *M. charantia* leaves as a reducing/capping agent

The nucleation and onset growth were delayed till 1 hour of the reaction, unlike the syntheses of Ag NPs and Ag-Ni which commenced as early as 5 minutes. The delay suggested different mechanistic character to particle formation (Dare *et al.*, 2014), and strong interactions between the biomolecules and the growing nanoparticles. The sluggish growth rate as observed in the SPR ended up in change in colour of the reaction medium. This indicated the presence of requisite bioreducing agents: saponins and glycosides in the plant extract. The surface plasmon absorption for silver (400-450 nm) was absent; instead, a very broad peak (400-600 nm) was observed. The presence of Co in the hybrid nanoparticles restrained narrow peak/surface plasmon absorption (Huang *et al.*, 2010; Xu, Zhu, Zhao & Ma, 2007), thereby causing red shift which implied particle size increase as an outcome of bimolecular-capped nanoparticles (Velicov *et al.*, 2003; Smith *et al.*, 2006).

4.5.4 TEM and Size Distribution of Ag-Co Bimetallic Nanoparticles under *M. charantia*-Influenced Synthesis at 70 ℃

The particle size distribution histogram and TEM image of bimetallic Ag-Co nanoparticles are depicted in Figure 4.47 (a and b).

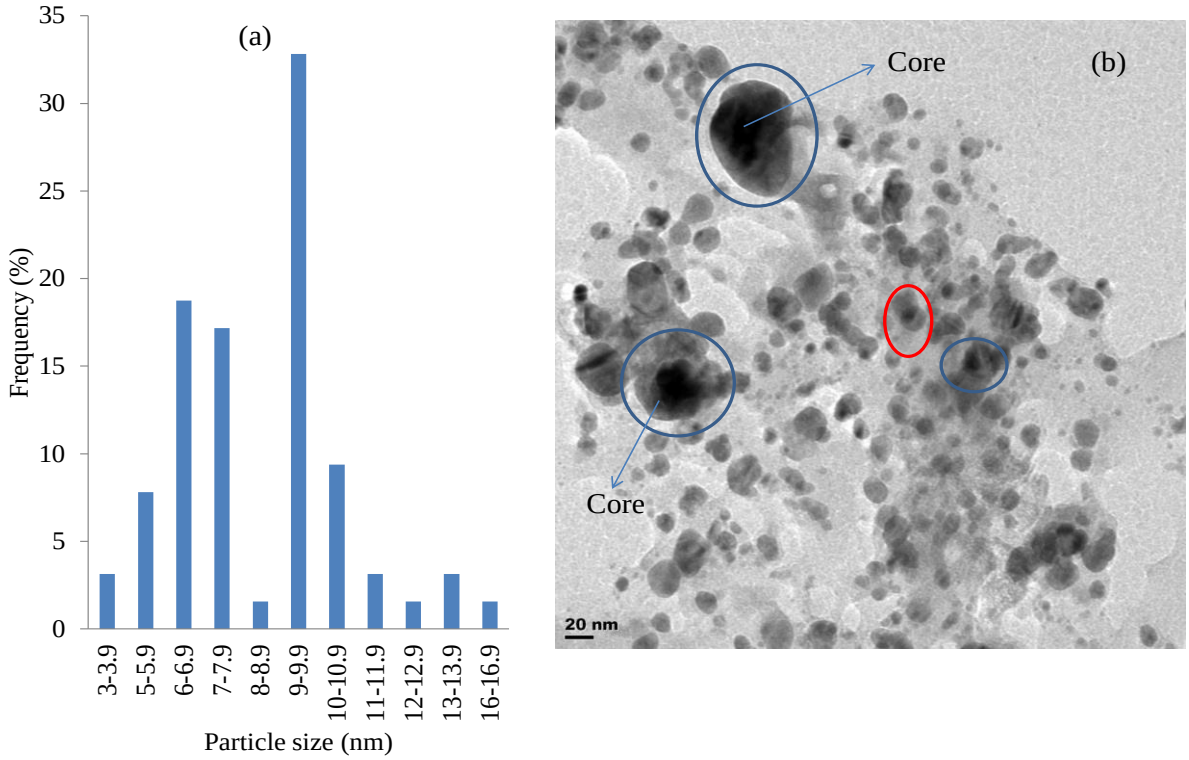

Figure 4.47: (a) Particle size distribution histogram of Ag-Co bimetallic nanoparticles determined from TEM image (b) Representative TEM image of the Ag-Ni hybrid nanoparticles under *M. charantia* -influenced synthesis using 1.0 mM metal precursor mixture

Table 4.21: EDX result of Ag-Co bimetallic nanoparticles prepared from the extract of *M. charantia* leaves and 1.0 mM metal precursor mixture

Element	Series	[wt.%]	[norm. wt.%]	[norm. at. %]	Error in %
Silver	L-series	39.88	41.30	44.32	1.11
Oxygen	K-series	5.36	1.71	8.59	0.07
Carbon	K-series	6.98	7.84	9.00	0.34
Nickel	K-series	2.51	1.04	2.18	0.08
Cobalt	K-seres	30.00	44.59	34.65	1.39
Phosphorus	K-series	2.97	2.66	1.19	0.16
Sulphur	K-series	0.53	0.86	0.07	0.06
	Sum:	88.23	100.00	100.00	

The nanoparticles were in the range 9.6 to 16.71 nm, with an average particle size of 12.99$\pm$ 2.53 nm. The TEM images revealed the morphology of the nanoparticles as alloy, containing cubic shapes with truncated edges and multiply twinned nanoparticles. The morphology also showed that the particles were not well separated from each other. Thus, large particles were capped with smaller ones, as a result of Ostwald's ripening. Preliminary energy dispersive analysis by X- rays (EDX) indicated that the silver and cobalt were present in ratio 1:1 (Table 4.21), representating the reduced silver and cobalt ions in the nanostructure.

4.5.5 XRD Pattern of Ag-Co Nanohybrid Particles Formed using the Extract of *M. charantia* Leaves

The investigation of crystallinity in the silver allied nano hybrid Ag-Co prepared using the extract of *M. charantia* leaves is shown in Figure 4.48.

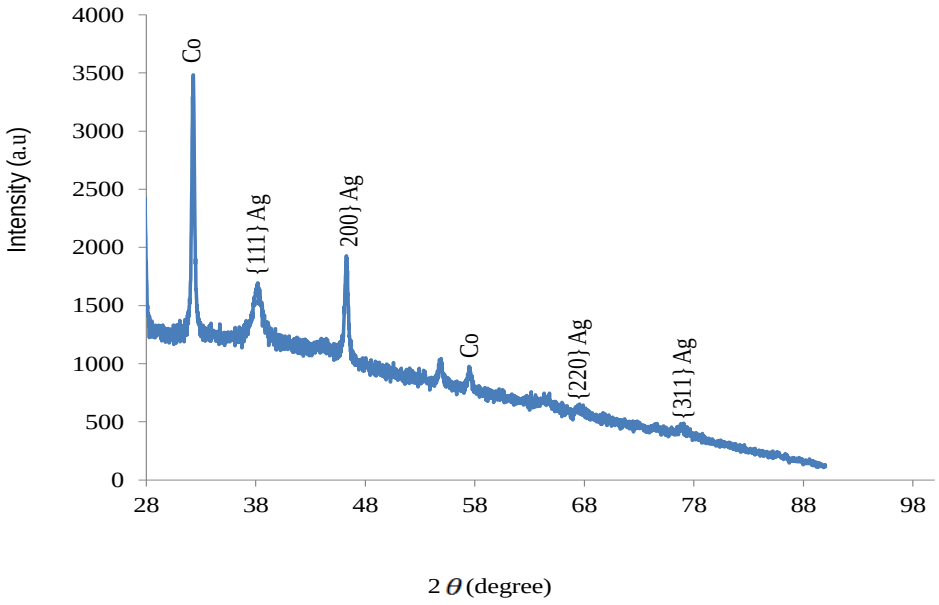

Figure 4.48: XRD patterns of Ag-Co bimetallic nanoparticles formed using the extract of *M. Charantia* leaves and 1.0 mM metal precursor solution at 70℃

The diffraction was carried out over a range of 10-90°. Reflection peaks were observed with 2θ values of 32.32°(Co), 38.21°(Ag), 46.32° (Ag), 57.57° (Co), 64.58 (Ag) and 82.10° of crystal planes corresponding to the reflections of {111}, {200}, {220} and {311) Ag fcc structure. The diffratogram showed the presence of Co peaks, thus the hybrid was more of Ag-Co core-shell morphological structure.

4.5.6 FTIR Analysis of the Ag-Co Hybrid Nanoparticles

The FTIR measurement was used to identify the possible functional groups in Ag-Co hybrid nanoparticles synthesized using the leaf extract of *M. charantia* at 70℃. The result is presented in Figure 4.49.

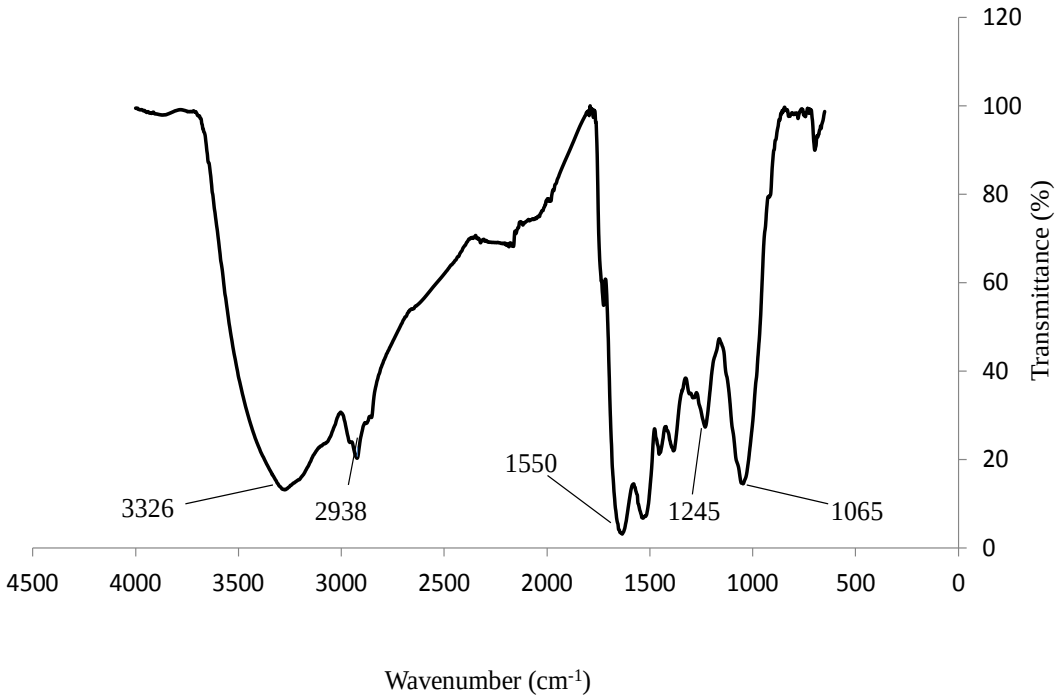

Figure 4.49: FTIR spectrum of synthesized Ag-Co bimetallic nanoparticles using the extract of *M. charantia* leaves

The absorption peaks observed in Ag-Co bimetallic nanoparticles at 3326 cm^{-1} (O-H stretching), 2936 cm^{-1} (C-H stretching), 1664 cm^{-1} (C=C), 1550 cm^{-1} (1405 cm^{-1} , and 1065 cm^{-1} (C-O single bond), suggests the presence of phytochemicals on the surface of nanohybrid plausibly through O-H which lost hydrogen ion in order to interact with the metal precursor mixture.

4.5.7 TEM and Size Distribution of Ag-Ni Bimetallic Nanoparticles under *M. Charantia*-Influenced Synthesis

The particle size distribution histogram and TEM image of bimetallic Ag-Ni nanoparticles are depicted in Figure 4.50.

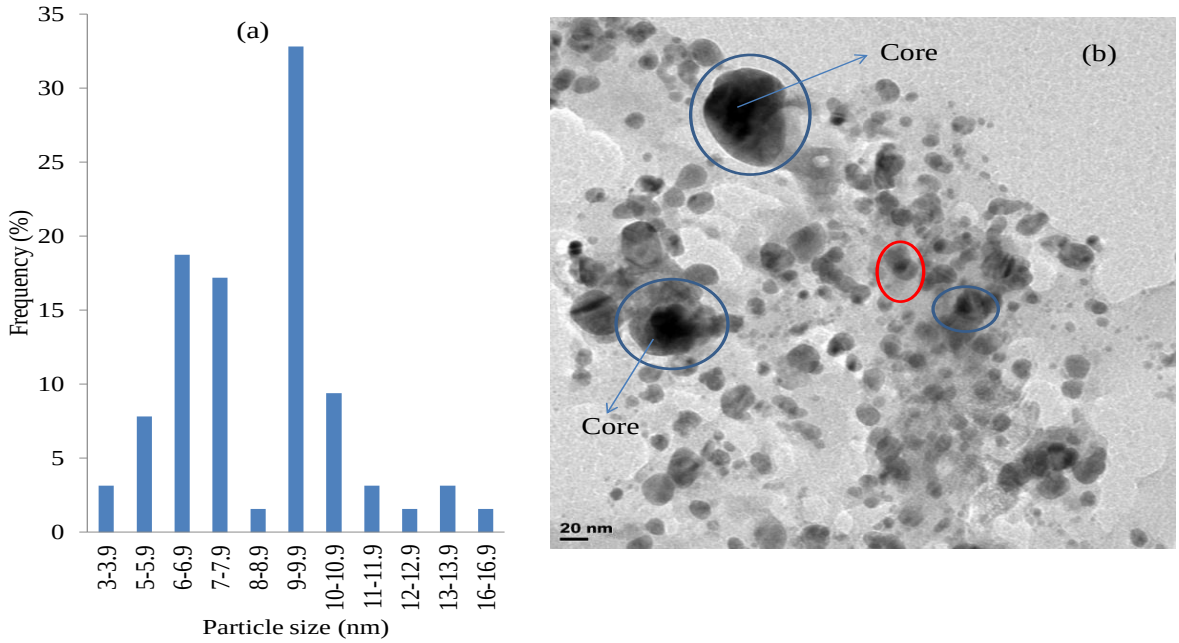

Figure 4.50: (a) Particle size distribution histogram of Ag-Ni bimetallic nanoparticles determined from TEM image (b) Representative TEM image of the Ag-Ni hybrid nanoparticles using *M. charantia* and 1.0 mM metal precursor mixture, 70^0C

Table 4.22: EDX result of Ag-Ni bimetallic nanoparticles formed using the extract of *M. charantia* leaves and 1.0 mM metal precursor mixture

Element	Series	[wt.%]	[norm. wt.%]	[norm. at.%]	Error in %
Silver	L-series	20.31	31.30	50.11	1.11
Oxygen	K-series	10.51	10.04	10.31	1.39
Carbon	K-series	6.98	7.84	7.00	0.34
Nickel	K-series	28.06	44.59	30.06	1.39
Cobalt	K-series	0.36	0.58	0.22	0.07
Phosphorus	K-series	2.97	4.26	1.22	0.16
Sulphur	K-series	0.53	0.88	0.10	0.06
	Sum:	69.72	100.00	100.00	

The size distribution showed that the particles were of non-uniform diameters, which ranged from 5.53 to 10.84 nm, with a mean size of 9.23 $\pm$ 1.18 nm. The highest number of particles was formed in the range of 9 to 9.9 nm (Figure 4.50a). The TEM image of Ag-Ni nanoparticles revealed Ag core (the darkened part) and Ni shell. The nickel nanoparticles formed after the equilibration of silver nanoparticles density, afterwards assembled onto the surface of silver nanoparticles to form a core-shell arrangement observed (Figure 4.50b). Capping by the biomolecules was observed; hence, providing stability for the synthesized nanoparticles. The observed shapes were quasi-spherical due to the reducing power of the plant extract. EDX analysis indicated the formation of more Ag with the atomic compositions of 50.11%., while the atomic composition of silver in the nanocluster was 30.06% (Table 4.22).

4.5.8 Optical (UV-Vis) Properties of Ag NPs under *M. Charantia-Influenced* Synthesis at Room Temperature

The combined UV-Vis spectra of green synthesized Ag NPs using the extract of *M. charantia* leaves at room temperature are shown in Figures 4.51.

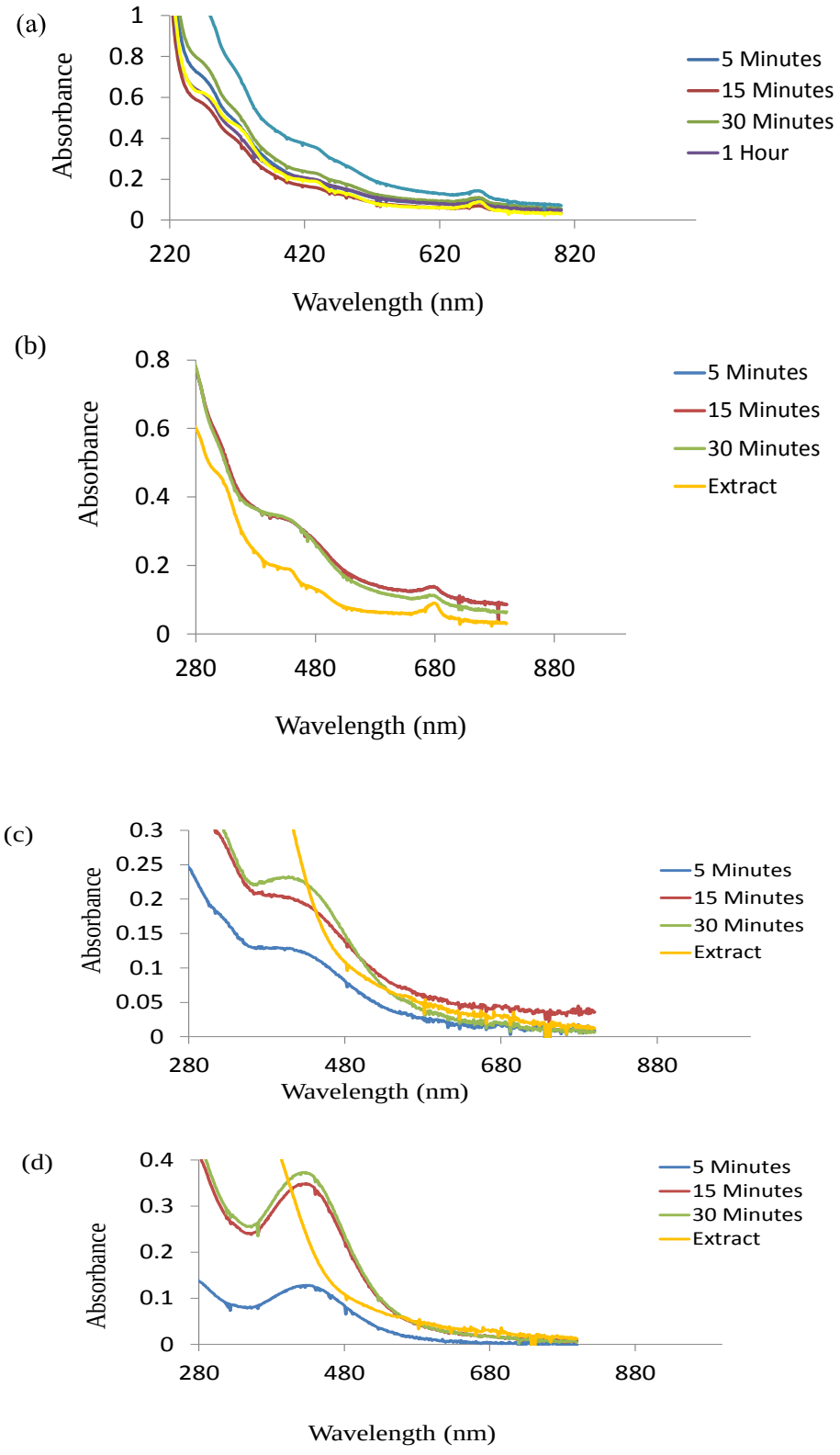

Figure 4.51: Room temperature time-resolved UV-Vis spectra of Ag NPs prepared from (a) 0.5 mM (b) 1.0 mM (c) 2.0 mM (d) 3.0 mM solutions capped with the extract of *M. charantia*

Figure 4.51e (i) = $AgNO_3$ solution with extract before reduction
(ii) = Final silver dispersion formed after reduction

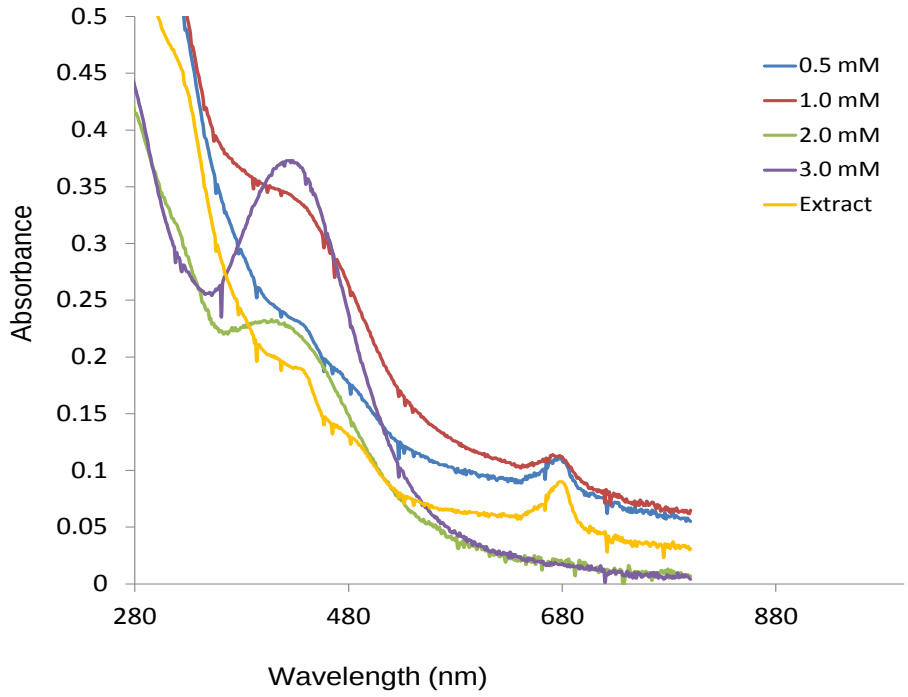

Figure 4.52: Comparison of onset growth in Ag NPs prepared from varied precursor solution concentrations at room temperature and 30 minutes, using the extract of *M. charantia* leaves as a reducing agent

Table 4.23: Bioreduction parameters for the syntheses of silver and its hybrid nanoparticles formed using the extract M. *charantia* leaves at 70℃, 30 minutes

	Maximum intensity at specified time 1.0 mM		Maximum intensity at specified time 2.0 mM		Maximum intensity at specified time 3.0 mM	
NPs	λ_{max} (nm)	Abs	λ_{max} (nm)	Abs	λ_{max} (nm)	Abs
Ag	Broad peak	0.357 (2 hours)	435	0.343 (30 minutes)	430	0.367
Ag-Co		0.158 (120 hours)	450-550	0.896 (192 hours)	392, 500 (2 Peaks)	0.376 (120 hours)

The nanoparticles exhibited surface plasmon resonance (SPR) due to the collective oscillation of free conduction electrons induced by interacting electromagnetic field (Mulvaney, 1996). Nucleation and onset growth took longer time (1 hour) in 0.5 mM precursor solution. This could plausibly be the result of strong interaction between phytochemicals: saponins and glycosides in the extract and the growing particles.

At higher metal precursor concentrations: 1.0 -3.0 mM, rapid formation of Ag NPs took place within 5 minutes of the reaction. This was noticed with a change in colour from light brown to dark brown (Figure 4.51e). Overlap in the spectra signified reaction completion between 15th and 30th minute of the reaction time (Table 4.23). Narrow and highest intensity of absorption (0.367 a.u.) which increased in intensity as a function of reaction time between 15 and 30 minutes occurred at 435 nm in the reduced 3.0 mM precursor solution, while broad peaks (400-450 nm), indicating polydispersed nanoparticles were observed at lower precursor solutions concentrations (Figure 4.51). Comparison in the growth of Ag NPs at varied precursor solution concentrations is depicted in Figure 4.52.

4.5.9 Optical (UV-Vis) Properties of Ag-Co Nanoparticles under *M. charantia*-Influenced Synthesis at Room Temperature

The optical properties of the biosynthesized Ag-Co bimetallic nanoparticles synthesized using the extract of *M. charantia* leaves nanoparticles at room temperature are shown in Figure 4.53.

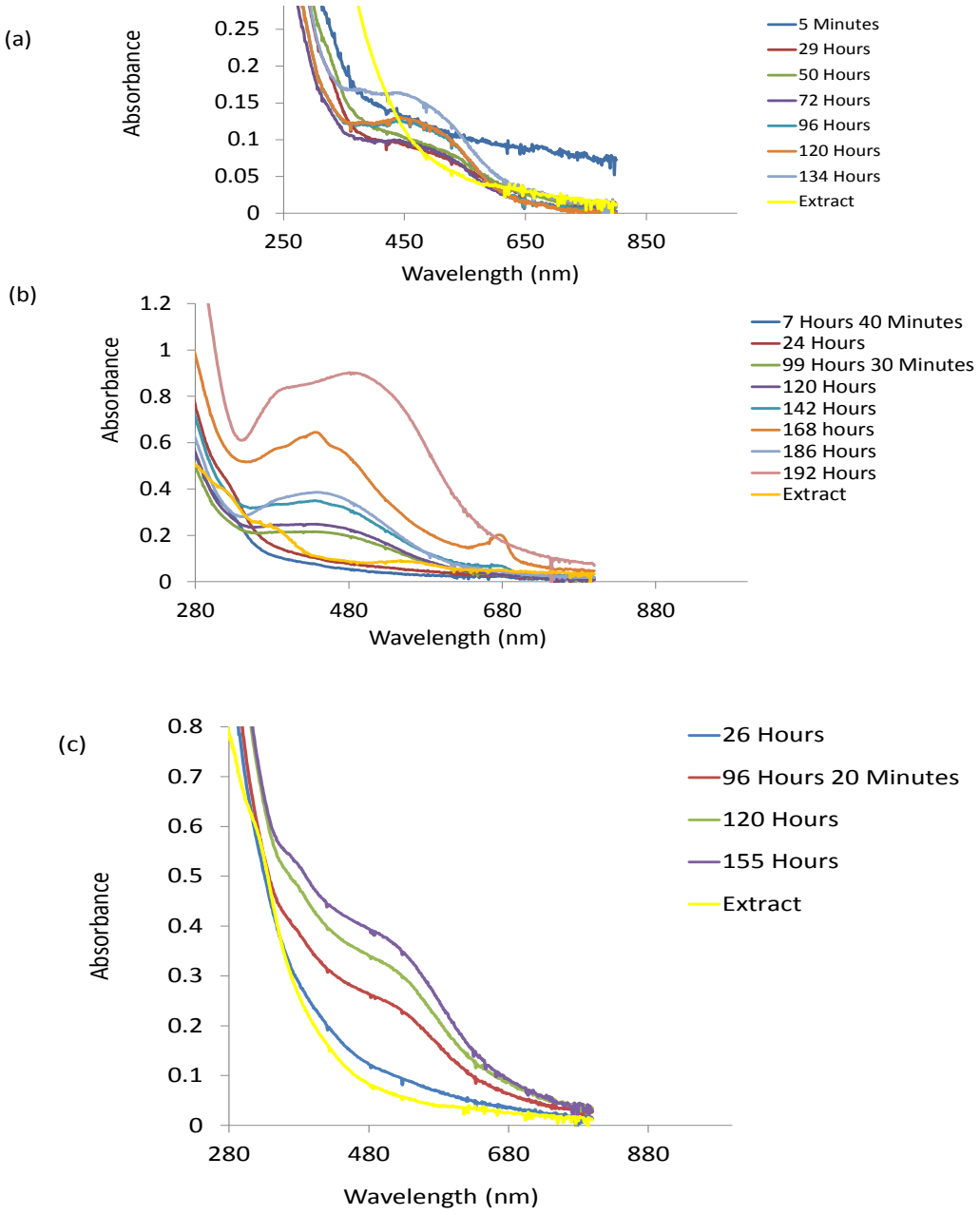

Figure 4.53: Room temperature time-resolved UV-Vis spectra of Co-Ag bimetallic nanoparticles prepared from (a) 1.0 mM (b) 2.0 mM (c) 3.0 mM precursor, capped with the extract of *M. charantia* leaves

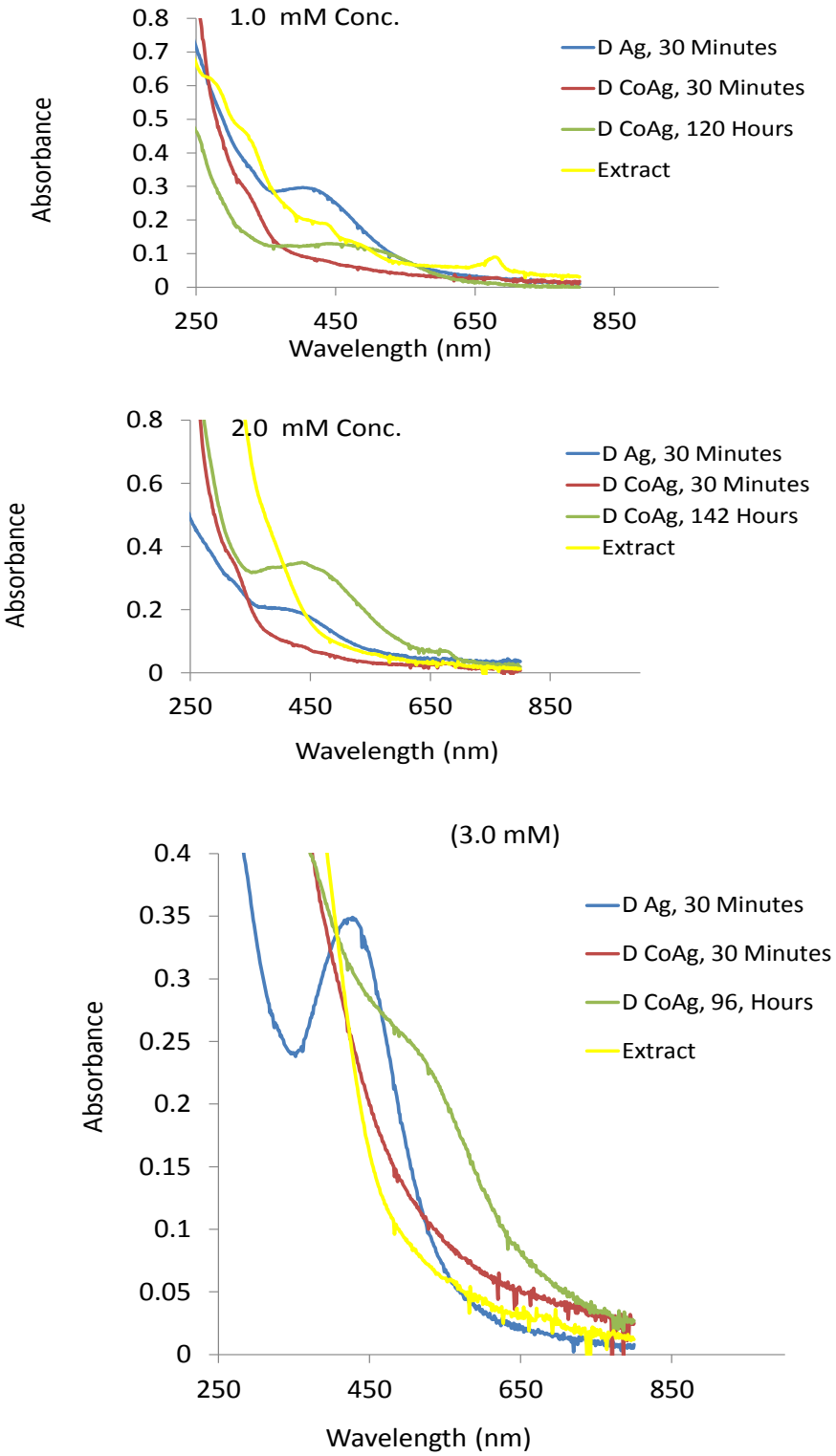

Figure 4.54: Comparison of onset growth between Ag NPs and Co-Ag bimetallic nanoparticles prepared with the extract of *M. charantia* leaves at room temperature

Room temperature reaction condition was not suitable for the extract of *M. charantia* leaves to act as a reducing agent/capping agent in the formation of Ag-Co hybrid nanoparticles, due to the long delay observed in the exhibited SPR. This may be as a result of strong interaction between the biomolecules and the growing nanoparticles. However, the observed colour change in the reaction suggested the reduction of Ag^{+} to Ag^{0}. Nucleation and onset growth took a longer time (above 24 hours), unlike the corresponding hybrid carried out at 70℃, where nucleation and onset growth commenced about 1 hour (Figure 4.53). The temperature increased the kinetic energy of the reaction by increasing the rate of collision between Ag^{+} and the reducing agents (phytochemicals) present in the plant extract. The appearance of surface plasmon resonance signalled formation of nanoparticles in all the concentrations of metal precursors (Figures 4.53 a, b, c), similar to maximum absorption wavelength of monometallic Ag NPs. This also implied that the surface of the hybrid nanoparticles was enriched with silver.

Figure 4.54 represents the comparison in the onset growth between Ag-Co NPs and the corresponding monometallic Ag NPs at specified time. In this reaction condition, the presence of Co in the hybrid led to a broader wavelength (400-650 nm) of absorption as observed in the spectra of Ag-Co NPs, whereas the absorption wavelength of the corresponding monometallic Ag NPs was between 400- 450 nm. The disparity could be due to the overlap of the electronic states of components of the bimetallic particles which led to the modification in the SPR (Yu *et al.*, 2005; Steiner *et al.*, 2005). The hybrid nanoparticles strongly absorbed light in the UV/Vis region. The two peaks observed in 2.0mM precursor solution suggested existence of a core-shell structure as reported in previous works (Xia *et al*., 2010; Kishore *et al*., 2013).

4.6 Optical (UV-Vis) Properties of Ag NPs under *Momordica charantia*-Influenced Synthesis at 70℃

Figure 4.55 depicts the optical properties of plant-mediated synthesis of Ag NPs using the xtract of *M. charantia* stem as a reducing agent at 70℃.

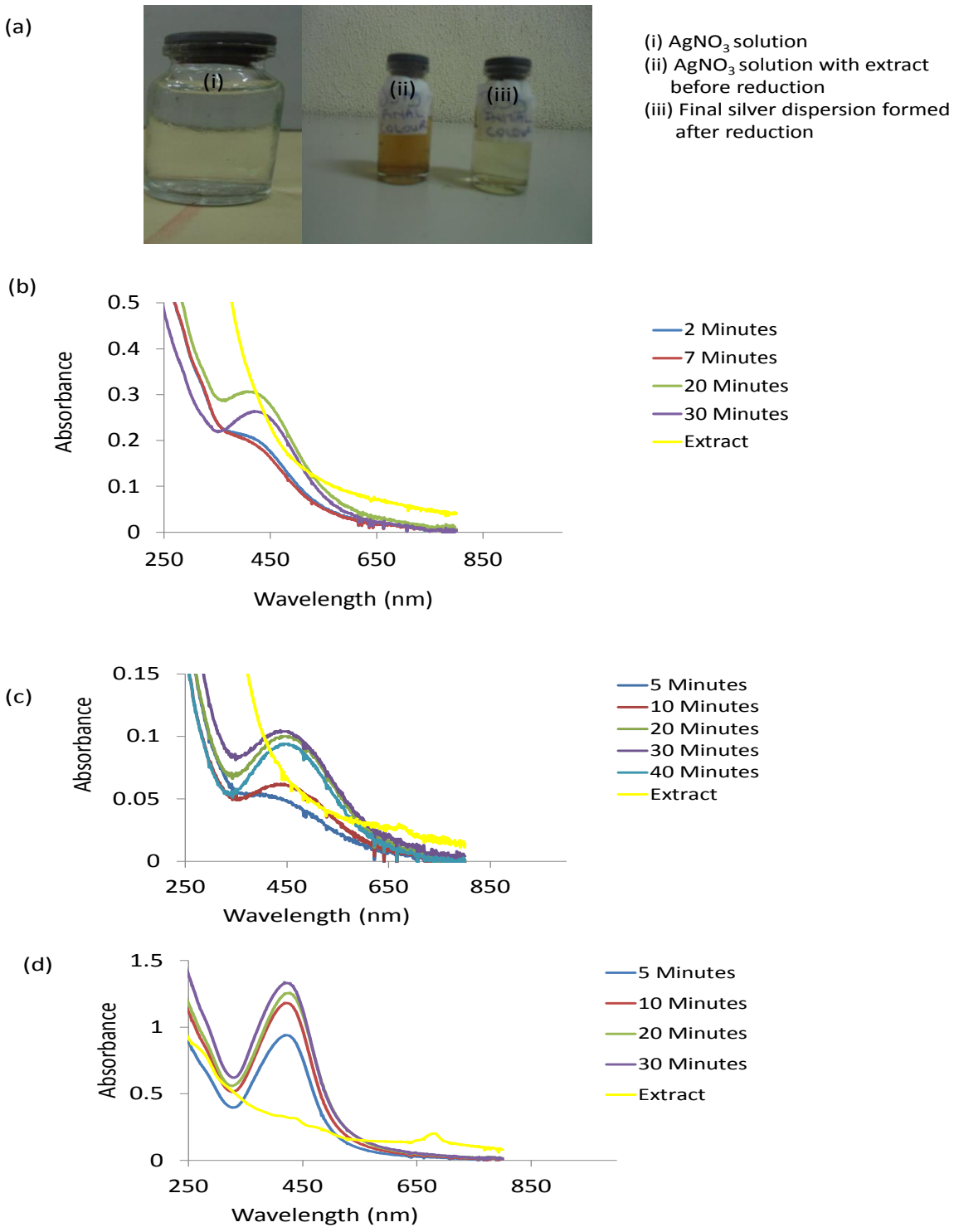

Figure 4.55: (a) $AgNO_3$ solution (i), $AgNO_3$ solution with extract before reduction (ii) and the final silver dispersion formed after reduction (iii). UV-Vis spectra of Ag NPs prepared from (b) 1.0 mM (c) 2.0 mM (d) 3.0 mM solution, using stem extract of *M. charantia* at 70℃

Table 4.24: Bioreduction parameters for the syntheses of silver and its hybrid nanoparticles using the extract *M. charantia* stem at 70℃, 30 minutes

	Maximum intensity 1.0 mM		Maximum intensity 2.0 mM		Maximum intensity 3.0 mM	
	Abs	Wavelength (nm)	Abs	Wavelength (nm)	Abs	Wavelength (nm)
Ag	0.056	420-460 (Broad peak)	1.248	420	0.1	437
Ag-Ni			0.047	400-600 (Broad peak)	0.108	400-650 (Broad peak)

In this study, the SPR peak was located between 400- 460 nm, 420 nm and 437 nm in the reduced 1.0, 2.0 and 3.0 mM metal precursor solutions respectively, which confirmed the formation of Ag NPs (Daisy, 2009). The highest intensity of absorption (1.248 a.u.) was obtained in the reduced 2.0 mM precursor solution. The peak intensity increased gradually as a function of reaction time from 5 to 30 minutes. SPR was shown by the Ag nanoparticles prepared in all precursor solution concentrations. Rapid bioreduction was observed, as nucleation and onset growth commenced within 5 minutes of the reaction. Moreover, a gradual change in colour from colourless Ag^+ to a brown colour indicated the formation of Ag NPs (Figure 4.55)

The red shift observed in the surface plasmon band was an indication of size increment due to capping of the newly formed nanoparticles by the biomolecules, as this is noted for application in optical materials. The observed narrow SPR peak around 400 nm suggested the presence of monodispersed spherical nanoparticles. This is similar to the wavelength band of silver nanoparticles. The red shifted absorbance peak and overlap in the spectra between 20th and 30th minutes indicated reaction completion (Lifshitz & Slyozov, 1961). Bioreduction took place using the extract of *M. charantia* stem due to the presence of suitable phytochemicals (saponins and alkaloids) in the stem part of the biomass used. Similar shapes and peaks (400-450 nm) were observed in the spectra Ag NPs formed using *M. charantia* leaf and stem. This could be explained as the presence of common bioreducing agents present in them.

4.6.1 TEM and Size Distribution of Ag NPs using the Stem of *M. charantia*

The particle size distribution histogram, TEM micrograph and SAED pattern of the Ag NPs formed with the stem extract of *M. charantia* at 70^0C are presented in Figure 4.56.

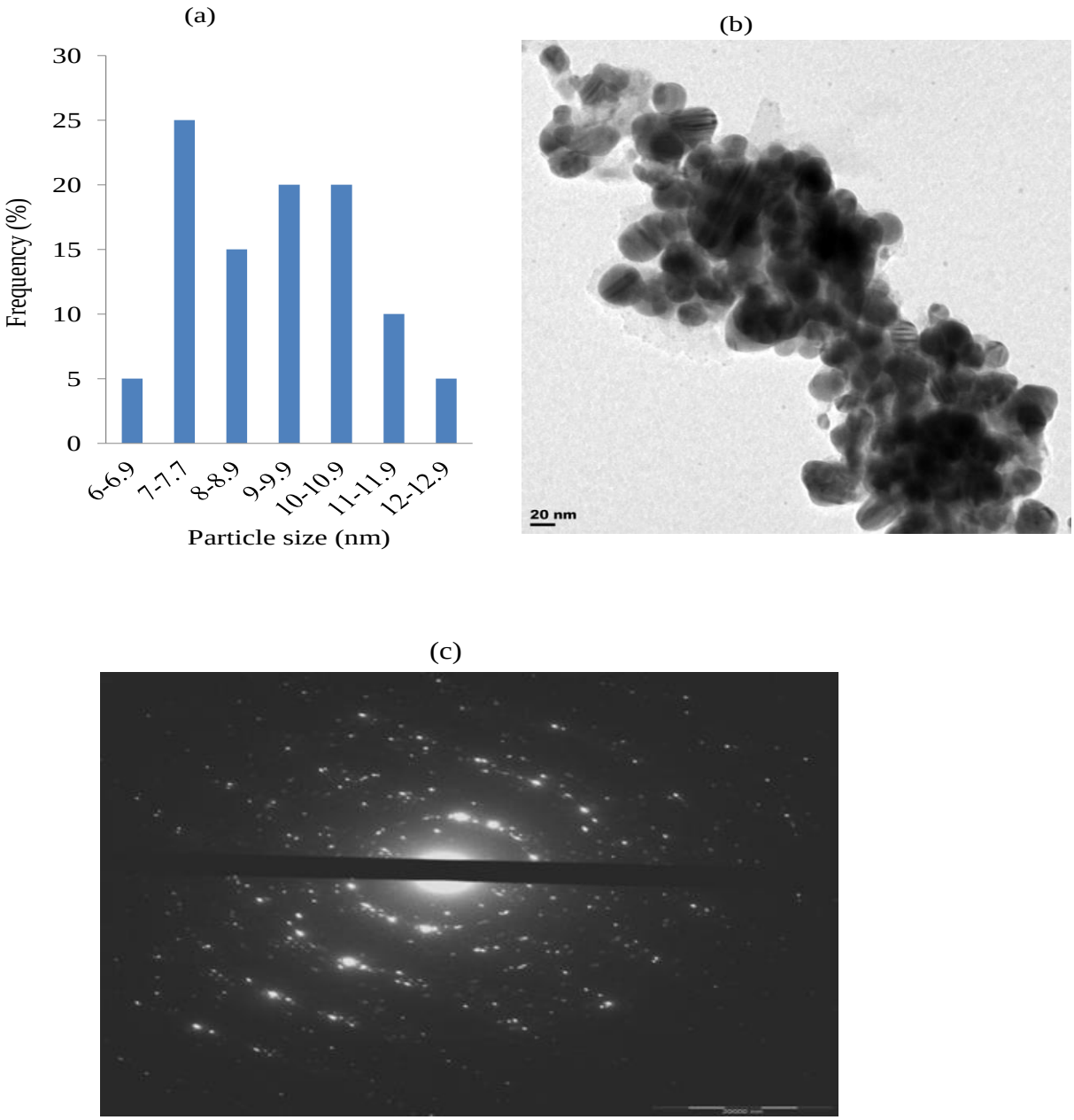

Figure 4.56: (a) Particle size distribution histogram of Ag nanoparticles determined from TEM image (b) Representative TEM image of the Ag nanoparticles synthesized from the stem of *M. charantia* and 2.0 mM metal precursor (c) SAED pattern of the Ag nanoparticles

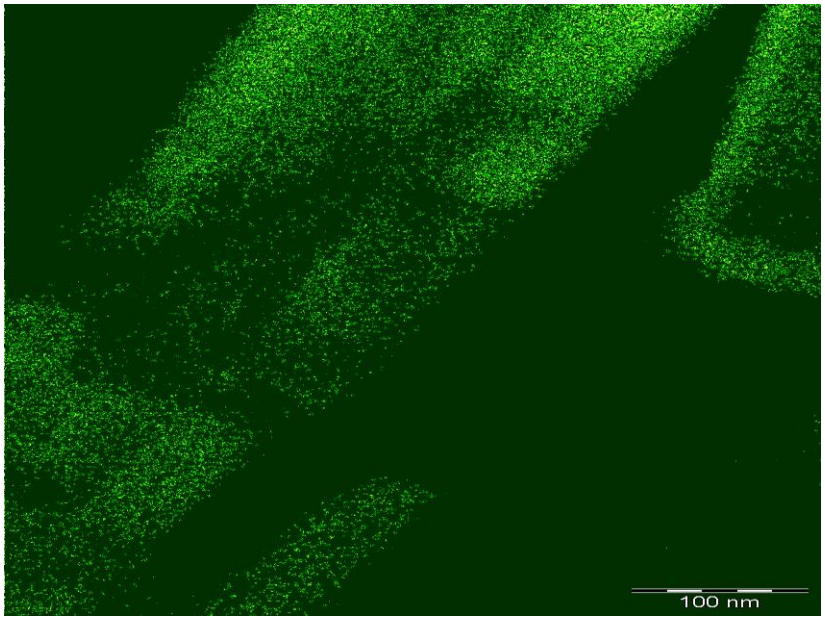

Figure 4.57: Elemental mapping of the Ag nanoparticles prepared from the stem of *M. charantia* and 2.0 mM metal precursor

Table 4.25: EDX result of Ag NPs prepared from 2.0 mM precursor using *M. charantia* stem extract at 70℃

Element	Series	[wt.%]	[norm. wt.%]	[norm. at.%]	Error in %
Silver	L-series	31.50	46.12	71.37	1.31
Oxygen	K-series	20.58	34.12	11.72	5.03
Carbon	K-series	14.99	17.31	15.82	0.32
Nickel	K-series	0.66	0.96	0.46	0.06
Cobalt	K-series	0.18	0.26	0.12	0.04
Phosphorus	K-series	0.04	0.05	0.05	0.00
Sulphur	K-series	0.35	0.52	0.45	0.04
	Sum:	68.29	100.00	100.00	

The particles range in size from 8.24 to 14.28 nm, with a mean diameter of 9.11 $\pm$ 1.64 nm. The size distribution as shown in Figure 4.56(b) shows relatively uniform particle sizes, which is an advantage of plant-mediated green synthesis. TEM image of the nanoparticles portrayed aggregates of quasi-spherical and nanocube with irregular contour due to self-assembly of the particles, which confirmed the caging nature of the extract, thereby providing high stability of the as-prepared Ag NPs. The SAED ring pattern were indexed to (111), (200), (220) and (311) of Ag metals with fcc structure. Hence, this verified the crystalline phases of the Ag NPs. The result of the EDX analysis signified the presence of significant amount of Ag with the atomic composition of 71.37 % in the synthesis (Table 4.25). Figure 4.57 is the mapping showing orientation of the Ag NPs obtained in TEM micrograph. It is an evidence of capping of the newly formed nanoparticles by the biomolecules, demonstrated by the diagonal orientation of the nanoparticles.

4.6.2 XRD Pattern of the Ag NPs

XRD pattern indicating the crystalline nature of the as- synthesized Ag nanoparticles using the extract of *M. charantia* stem is presented in Figure 4.58.

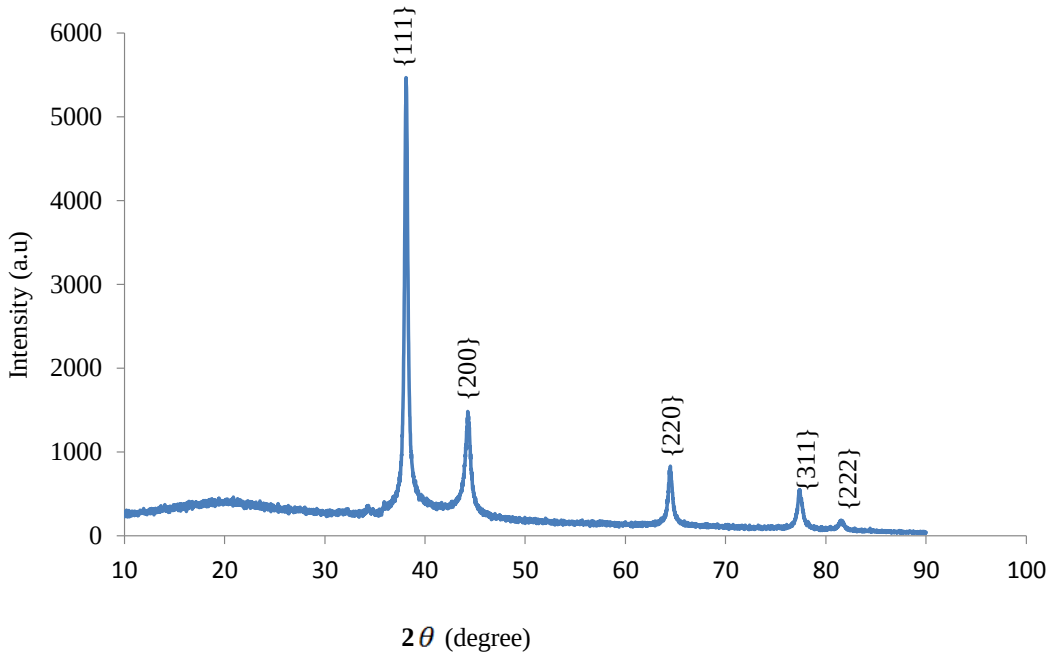

Figure 4.58: XRD patterns of the Ag NPs reduced with the extract of *M. charantia* stem using 2.0 mM metal precursor solution at **70** °C

Outstanding peak reflections were portrayed in the plant-mediated green route synthesis. The intensity of reflection was similar to that of chemical synthesis. The Ag NPs were highly crystalline as depicted in the X-ray diffractogram (Figure 4.58). Characteristics reflections which appeared at 2θ values of 38.17°, 44.39°, 64.57° and 77.49° were indexed to {111}, {200}, {220} and {311} Ag planes of the face-centred cubic structure. The nanocluster reflection displayed very sharp peaks and strong intensity. This is an indication that the Ag NPs capped with the extract from stem part of *M. charantia* were void of impurities. Thus, the nanoparticles were highly crystalline as corroborated by the SAED ring pattern (Figure 4.54a).

4.6.3 FTIR Analysis of the Ag NPs

Figure 4.59 shows the FTIR spectrum capped Ag nanoparticles, formed with the stem extract of *M. charantia*.

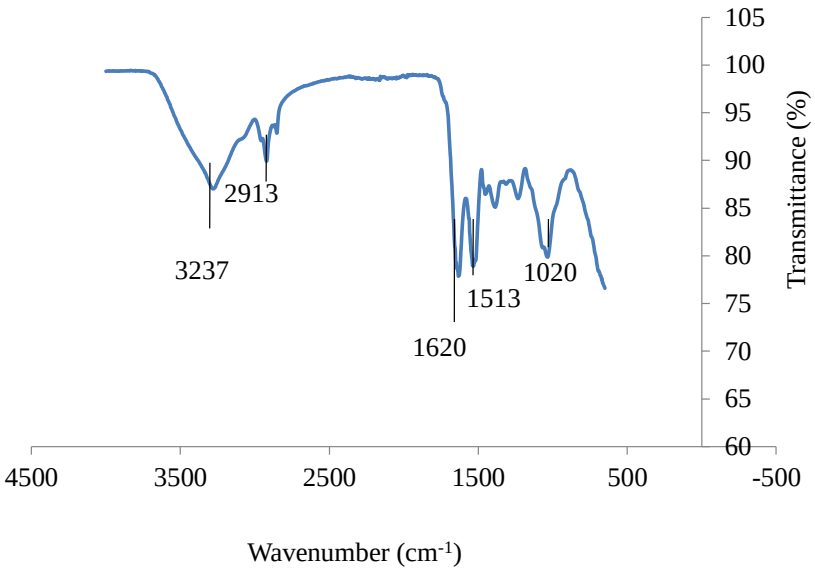

Figure 4.59: FTIR spectrum of the synthesized Ag NPs using the extract of *M. charantia* stem

The FTIR spectrum showed the presence of hydroxyl groups (−OH) stretching, (−CH) stretching, N-H bending, C=C stretching and C−N group in the bioactive chemicals that capped the nanoparticles at 3237, 2913, 1620, 1513 and 1021 cm^{-1} respectively. The phytochemical screening indicated the existence of saponins and the alkaloids in the stem extract of *M. charantia*. The presence of C−N proposed coordination through the lone pair electron present in the nitrogen attached to the methyl group, hereby leading to the formation of double bond as Ag^{+} is reduced to Ag^{0}. The nanocluster was then capped by the alkaloid present in the phytochemical to provide stability. This is illustrated in Scheme 3 (Mechanism of the reaction page).

4.6.4 Optical (UV-Vis) Properties of Ag-Ni Bimetallic Nanoparticles under *M. charantia*-Influenced Synthesis at 70℃

The stem extract of *M. charantia* also supported formation of Ag-Ni bimetallic NPs at 70℃. This is depicted in Figure 4.60.

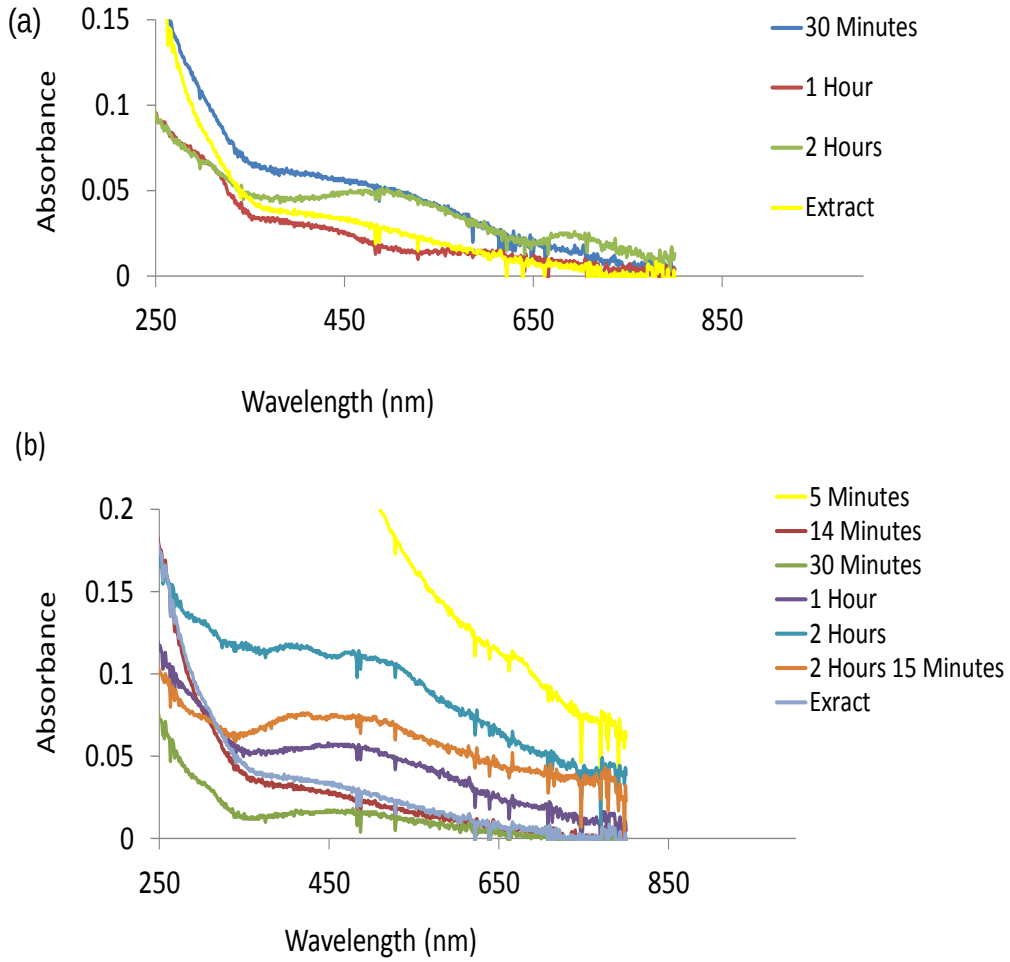

Figure 4.60: UV-Vis spectra of Ag-Ni bimetallic nanoparticles prepared from (a) 2.0 mM (b) 3.0 mM precursor mixture using the extract of *M. charantia* stem as reducing/capping at 70℃

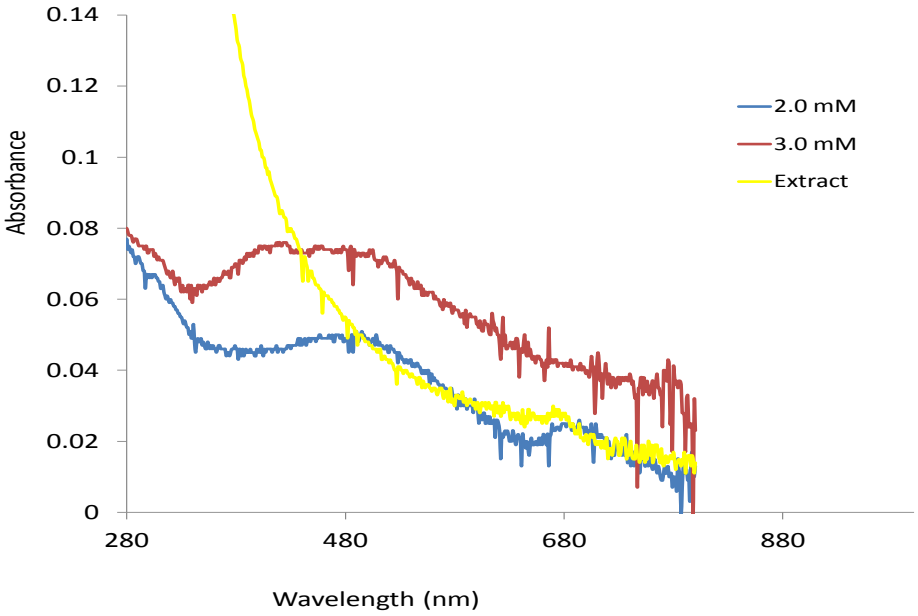

Figure 4.61: Growth comparison between Ag-Ni NPs prepared from 2.0 mM and 3.0 mM precursor mixture using the extract of *M. charantia* stem at 70°C, 3 hours

Though, the rate of reaction was slow compared to its corresponding Ag NPs formation. The nucleation and onset growth started over 1 hour of the reaction. This may be due to the effect of the strong interaction between the bimolecules in the extract and the growing nanoparticles. However, the phytochemicals (saponins and alkaloids) were considered to be more concentrated in the leaf than the stem part of the plant utilized. The appearance of SPR authenticated the formation of nanoparticles. The broad peak also suggested the presence of spheres in the nanoparticles. Large particle sizes were as well expected due to the longer reaction time; because plant- mediated green synthesis is time dependent.

The absorption wavelength in Ag-Ni bimetallic NPs was more shifted; but, with low absorption intensity than the corresponding Ag NPs (420-450 nm). The effect of Ni in the Ag-Ni bimetallic was observed in the broadening and red shift of the wavelength band (450-650 nm) in 2.0 and 3.0 mM precursor solutions (Table 4.19 & Figure 4.60). The detected longer wavelength of absorption predicted higher degree of delocalization in the nanoparticles ($\pi \longrightarrow \pi*, n \longrightarrow \pi*$) according to Nemade and Waghuley (2013). Figure 4.61 shows comparison between the growths of hybrid Ag-Ni NPs prepared from 2.0 and 3.0 mM precursor solutions.

4.6.5 TEM and Size Distribution of Ag-Ni NPs Prepared using the Stem of *M. Charantia*

Figure 4.62 shows TEM micrograph of the bimetallic Ag-Ni nanoparticles prepared by reducing 3.0 mM precursor mixture, using the extract of *M. charantia* stem of at 70℃.

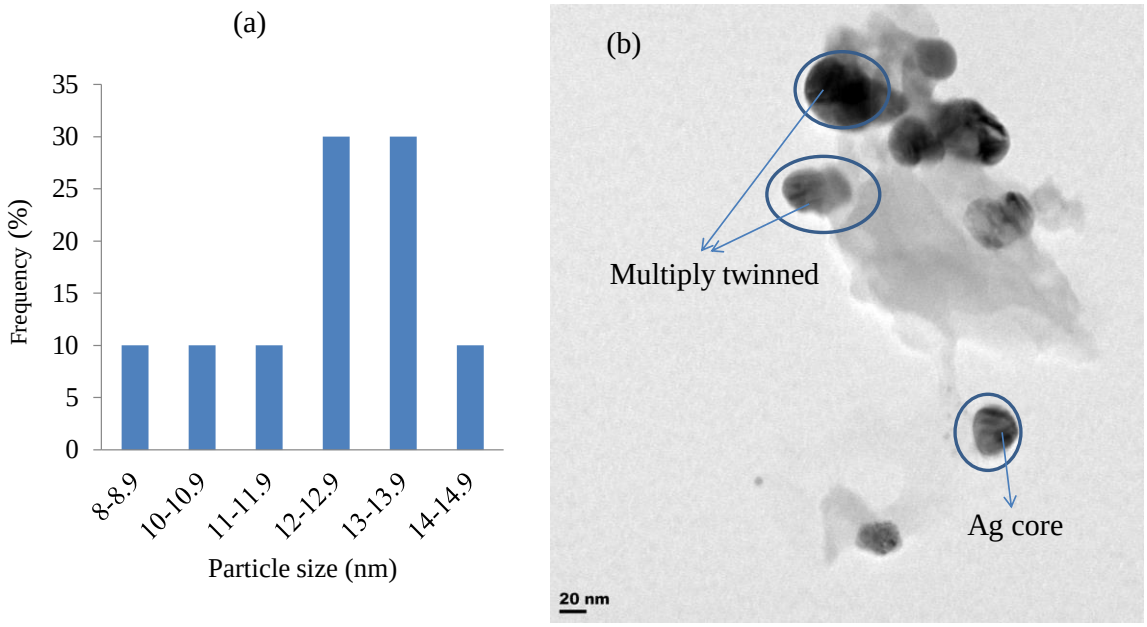

Figure 4.62:(a) Particle size distribution histogram of Ag-Ni bimetallic nanoparticles determined from TEM image (b) Representative TEM image of the Ag-Ni nanoparticles synthesized by the reduction of 3.0 mM metal precursor mixture using the stem extract of *M. Charantia*

Table 4.26: EDX result of Ag-Ni bimetallic nanoparticles prepared from 3.0 mM precursor using *M. charantia* stem extract at 70℃

Element	Series	wt.%]	[norm. wt.%]	[norm. at.%]	Error in %
Silver	L-series	0.17	60.27	78.16	0.93
Oxygen	K-series	0.48	0.71	0.28	5.77
Carbon	K-series	3.38	15.07	13.35	0.24
Nickel	K-series	1.39	12.10	6.96	0.05
Cobalt	K-series	0.25	0.37	0.15	0.04
Phosphorus	K-series	0.46	0.68	0.52	0.05
Sulphur	K-series	0.54	0.80	0.59	0.05
	Sum:	6.66	100.00	100.00	

The non-uniform nanoparticles were in the size range 8.44 to 14.09 nm, with a mean size of 12.38 $\pm$ 1.74 nm. The morphology showed multiply-twinned particles and a core (Ag) - shell (Ni) heterostructure. EDX analysis illustrated higher percentage composition of silver in the hybrid as 78.18 atomic%, Ni 6.96 atomic %, carbon as 13.35 atomic % and oxygen 0.28 atomic % (Table 4.26).

4.6.6 Optical (UV-Vis) Properties of Ag NPs under *M. charantia*-influenced Synthesis at Room Temperature

UV-Vis absorption spectra of the biosynthesized Ag NPs stabilized with the leaf extract of *M. charantia* (stem) is presented in Figure 4.63. Figure 4.64 shows the comparison in the growth of Ag NPs in all the precursor solution concentrations.

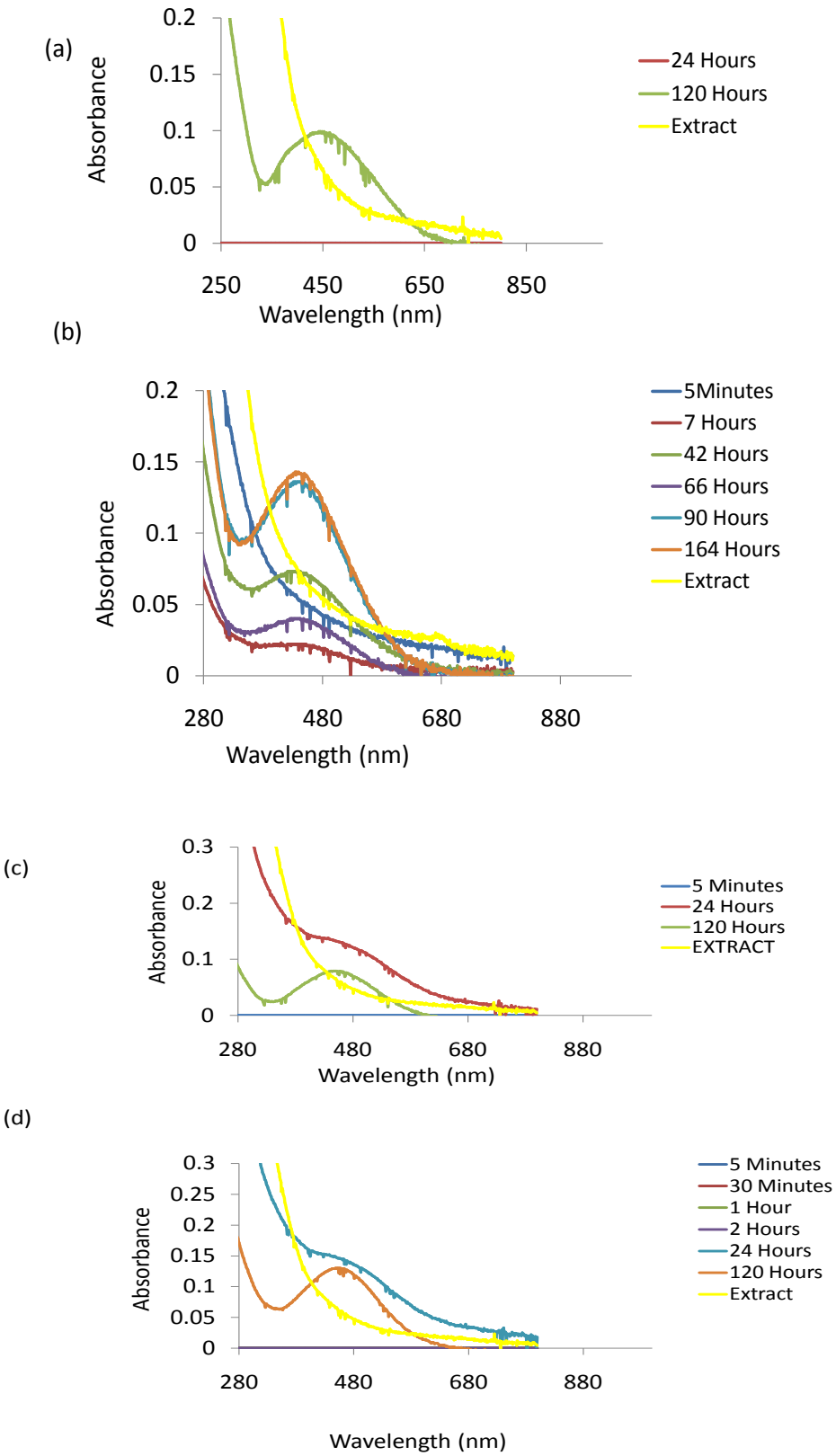

Figure 4.63: Room temperature time-resolved UV-Vis spectra of Ag NPs prepared from the reduced (a) 0.5 mM (b) 1.0 mM (c) 2.0 mM (d) 3.0 mM precursor solutions using the stem extract of *M. charantia*

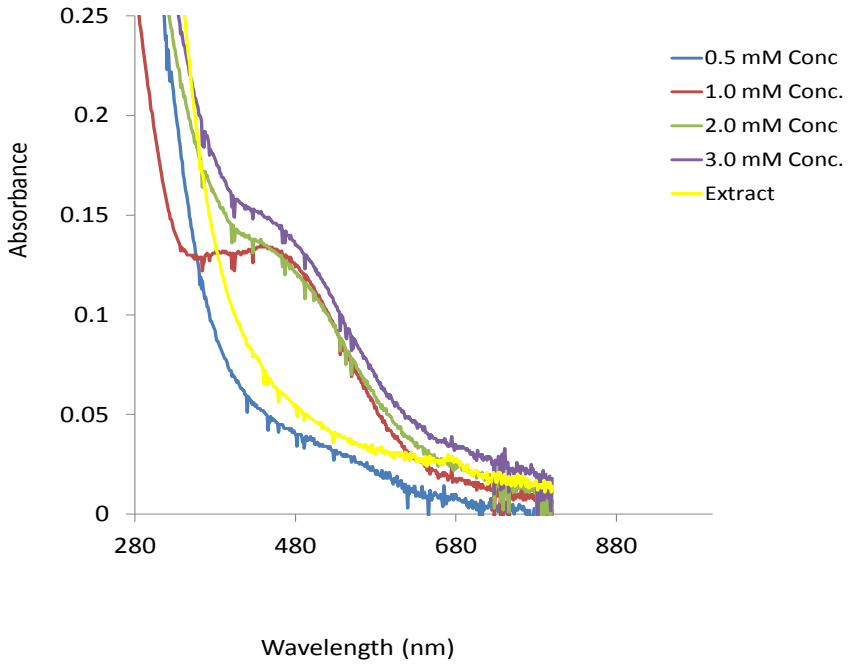

Figure 4.64: Comparison of onset growth in Ag NPs prepared from varied precursor concentrations using M. charantia stem extract at room temperature, 24 hours

Table 4.27: Bioreduction parameters for the synthesis of Ag NPs prepared using the extract *M. charantia* stem at room temperature, 24 hours

NPs	Maximum intensity 0.5 mM		Maximum intensity 1.0 mM		Maximum intensity 2.0 mM		Maximum intensity 3.0 mM	
	Abs	λ_{max}	Abs	λ_{max}	Abs	λ_{max}	Abs	λ_{max}
Ag	0.1 (120 hours)	350-450	0.1	400-450	0.127	400-500	0.14	400-450

The extract of *M. charantia* stem supported the formation of nanoparticles at room temperature; however, the rate of reaction was very slow when compared with the same biosynthesis carried out at 70℃ (Figure 4.56). The nucleation and onset growth commenced at 120th hour (0.5 mM precursor solution), 90th hour (1.0 mM precursor solution) and 24 th hour in 2.0 and 3.0 mM precursor solutions. The sluggish reaction was an indication that the reacting solutions were not supersaturated to generate extremely small particle size. Likewise, the biomolecules which acted as the reducing and capping agents in the stem were considered of less concentration compared with the quality in the leaves. The presence of SPR band (400-450 nm), but with low intensity of absorption (0.1 a.u.) specified the formation of nanoparticles (Table 4.27). This occurred in all the precursor solution concentrations of the synthesis. The broad peaks observed proposed the presence of polydispersed nanoparticles and spheres in the nanoparticles structure. Large particle sizes were inevitable due to the longer reaction time.

4.7 Optical (UV-Vis) Properties of Ag NPs under *Cassytha filiformis*-influenced Synthesis at 70^{o}C

Figure 4.65 is the absorption spectra of the biosynthesized Ag NPs at 70℃ using the extract of *Cassytha filiformis* (whole part) as a reducing agent/capping agent for the newly formed nanoparticles.

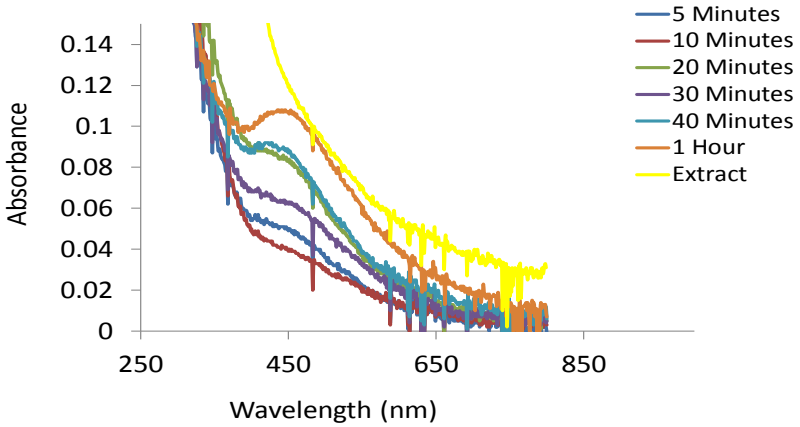

Figure 4.65: UV-Vis spectra of Ag NPs prepared by reducing 0.3 mM $AgNO_3$ solution using the extract of *C. filiformis* (whole part) at 70℃

Table 4.28: Bioreduction parameters for the syntheses of silver and its hybrid nanoparticles using the extract C*assytha filiformis* (whole part)

Nps	Maximum intensity 1.0 mM		Maximum intensity 2.0 mM		Maximum intensity 3.0 mM	
	Abs	λ_{max} (nm)	Abs	λ_{max} (nm)	Abs	λ_{max} (nm)
Ag					0.116	400-450
Ag-Ni	0.262 (1 hour)	424	0.107 (1 hour)	431	0.082 (1 hour)	420-493
Ag-Co			0.081	400-600		

The observed rapid change in colour from faint yellow to dark brown signalled the formation of nanoparticles (Figure 4.65a). The nucleation and onset growth commenced from 20th minute of the reaction. Appearance of surface plasmon resonance (SPR) occurred in the nanoparticles synthesized in 3.0 mM precursor solution; indicating the presence of nanoparticles (Daisy, 2009). Low peak intensity was observed (0.116 a.u.) in the optical spectra. Moreover, red shifted broad peak took place between 400-450 nm (Figure 4.65 & Table 4.11), which corresponded to the surface absorption for silver. The peak broadening suggested polydispersed particles, similar to the work done by Link *et al.* (1999).

4.7.1 Optical (UV-Vis) Properties of Ag-Ni Bimetallic Nanoparticles under *Cassytha filiformis*-Influenced Synthesis at 70°C

The optical properties depicted by the intensity of absorption of Ag-Ni nanohybrid are presented in Figure 4.66.

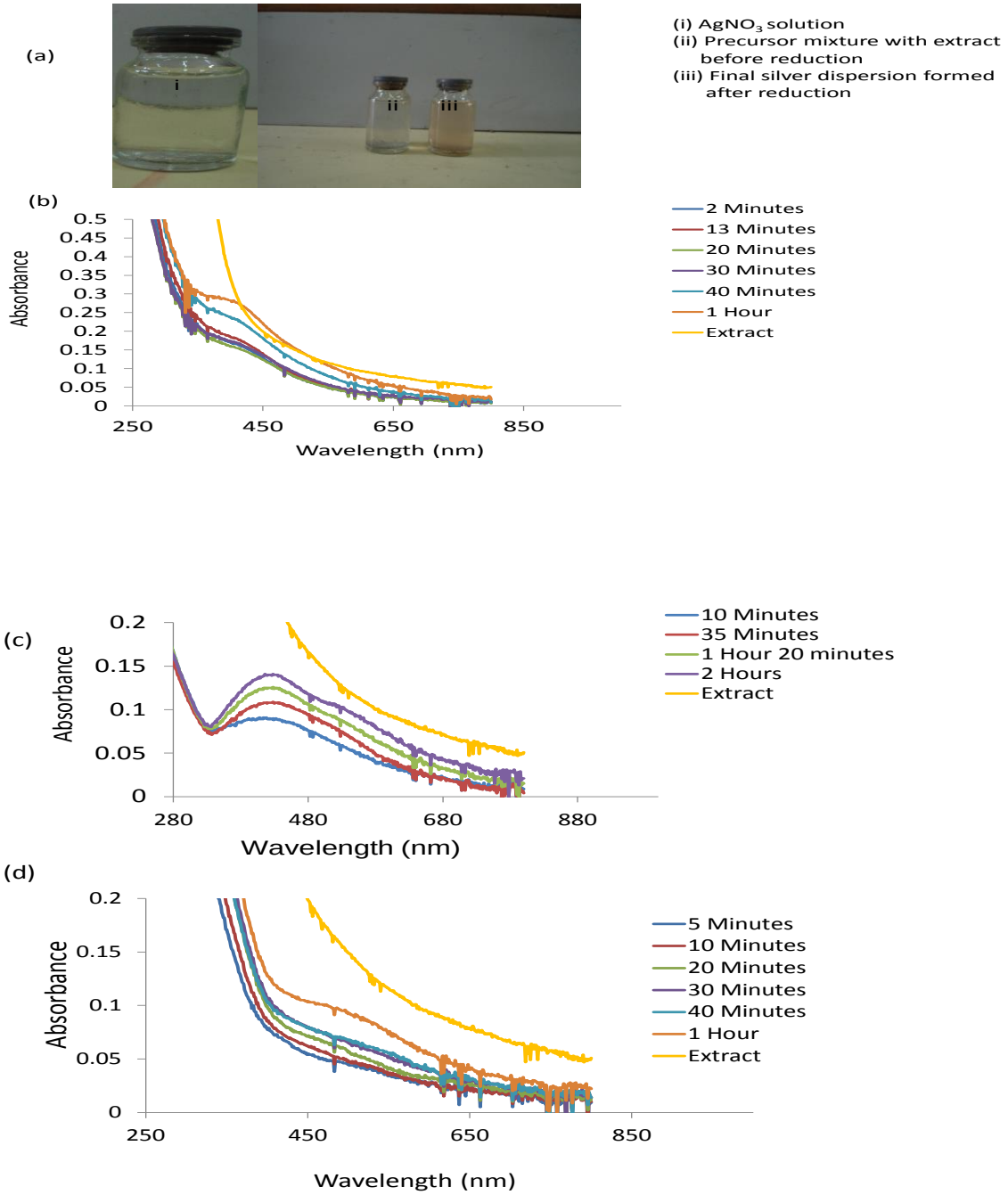

Figure 4.66: (a) $AgNO_3$ solution (i), precursor mixture solution with extract before reduction (ii) and the final silver dispersion formed after reduction (iii). UV-Vis spectra of Ag NPs prepared from (b) 1.0 mM (c) 2.0 mM (d) 3.0 mM solution, using the extract of *C. filiformis* (whole part) at 70℃

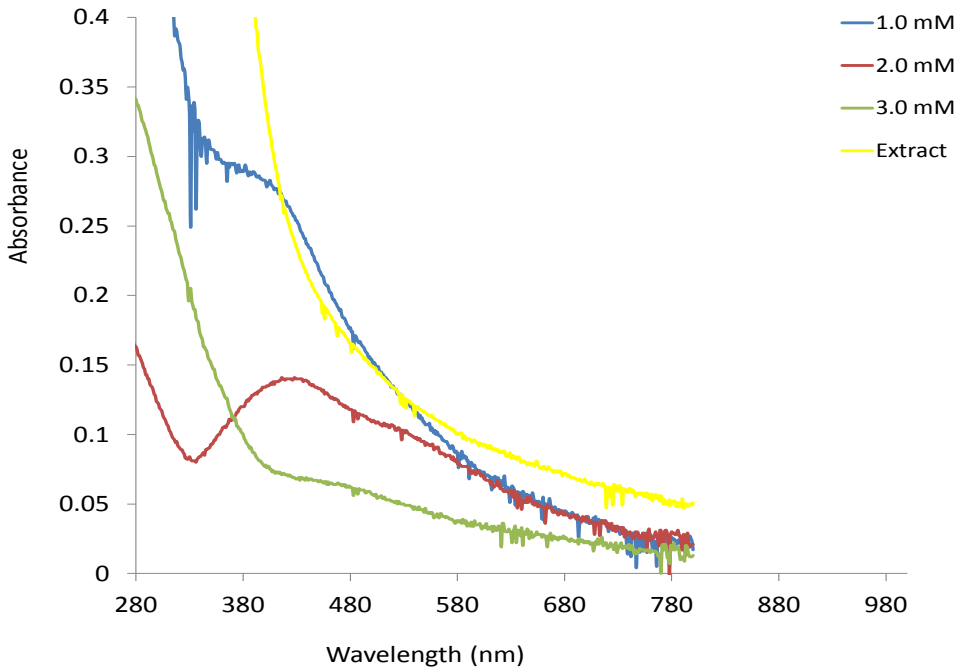

Figure 4.67: Growth comparison among varied precursor concentrations of Ag-Ni NPs formed using the extract of *C. filiformis* (whole part) at 70°C, 1 hour

4.7.2 TEM and Size Distribution of the Ag-Ni Bimetallic Nanoparticles

Figure 4.68 (a) is the particle size distribution histogram of bimetallic Ag-Ni NPs synthesized from 2.0 mM metal precursor mixture using *Cassytha filiformis* at 70℃.

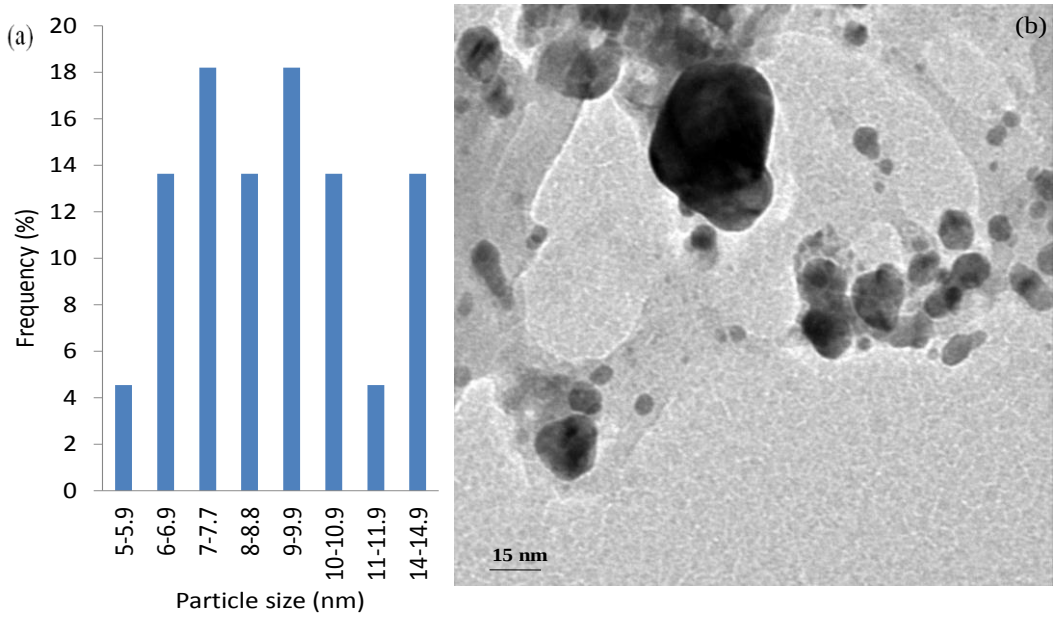

Figure 4.68: (a) Particle size distribution histogram of Ag-Ni bimetallic nanoparticles determined from TEM image (b) Representative TEM image of the Ag-Ni nanoparticles synthesized from *Cassytha filiformis* and 2.0 mM metal precursor mixture

Table 4.29: EDX result of Ag-Ni bimetallic nanoparticles prepared from 2.0 mM metal precursor mixture using the extract of *Cassytha filiformis*

Element	Series	[wt.%]	[norm. wt.%]	[norm. at.%]	Error in %
Silver	L-series	33.07	47.11	33.32	1.42
Oxygen	K-series	10.61	10.87	10.45	4.61
Carbon	K-series	8.45	12.03	10.35	0.45
Nickel	K-series	17.89	29.74	45.75	0.06
Cobalt	K-series	0.18	0.25	0.13	0.04
	Sum:	70.19	100.00	100.00	

Particle sizes were relatively uniform, and this suggests the application as conductive filler in gaps between Ag flakes for electronically conductive adhesives (ECA), according to Chen *et al*. (2009). The TEM micrograph of the Ag-Ni nanocluster (Figure 4.68b) reveals cubic nanoparticles with contour and edges, multiply twinned hybrid and core-shell nanostructures. An average size of 9.37 $\pm$ 2.62 nm was also discovered. The observed core-shell nanostructure conformed to the shape of SPR in the UV-Vis spectra of Ag-Ni nanocluster prepared from 2.0 mM precursor mixture (Figure 4.66 b). Table 4.29 is the EDX result confirming the formation of hybrid nanoparticles. Ni dominated the nanoparticles with atomic composition of 45.75 %, and Ag was present in 33.32 atomic %; Oxygen (10.45 atomic %) and Carbon (10.35 atomic %) originated from the plant used.

4.7.3 TEM and Size Distribution of Ag-Ni Bimetallic Nanoparticles Synthesized from 3.0 mM Precursor Mixture using *Cassytha filiformis* at 70℃

Particle size distribution histogram and TEM image of the bimetallic Ag-Ni nanocluster synthesized from the reaction of 3.0 mM precursor mixture and the extract of *C. filiformis* are shown in Figure 4.69.

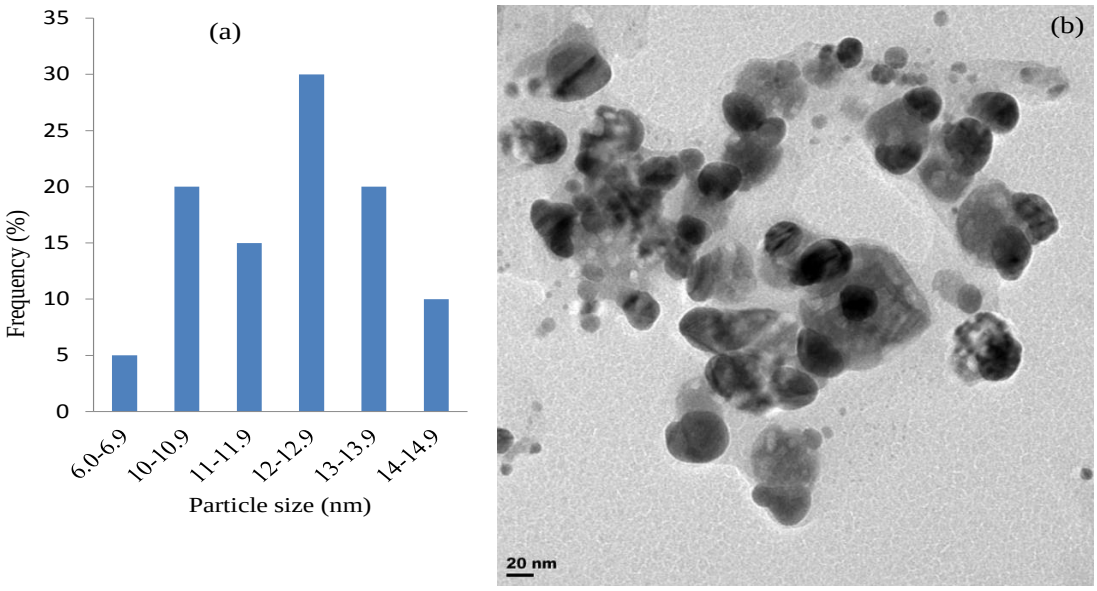

Figure 4.69: (a) Particle size distribution histogram of Ag-Ni bimetallic nanoparticles determined from TEM image (b) Representative TEM image of the Ag-Ni nanoparticles synthesized from 3.0 mM metal precursor mixture using *Cassytha filiformis* extract

Table 4.30: The EDX Result of Ag-Ni bimetallic nanoparticles prepared from 3.0 mM metal precursor mixture using the extract of *Cassytha filiformis*

Element	Series	[wt.%]	[norm. wt.%]	[norm. at.%]	Error in %
Silver	L-series	34.50	53.28	37.82	1.43
Oxygen	K-series	0.82	1.42	5.33	0.06
Carbon	K-series	9.28	13.84	11.10	0.47
Nickel	K-series	22.29	31.19	45.20	3.60
Cobalt	K-series	0.26	0.10	0.15	0.02
	Sum:	67.15	100.00	100.00	

Figure 4.69 (a) illustrates the particles range in size from 6.4 to 17.41 nm with a mean size of 21.49 $\pm$ 3.40 nm. The TEM micrograph of Ag-Ni nanoparticles revealed multiply twinned nanoparticles, core-shell in which Ag core was inside Ni shell. The image also showed the existence of Ni core between two Ag shells. The shape of the nanoparticles was modulated in this synthesis. The atomic compositions of Ag and Ni as revealed in the EDX analysis were low- 37.82 and 45.20 atomic % respectively. The result further corroborated the formation of Ag-Ni nanoparticles by EDX (Table 4.30).

4.7.4 XRD Pattern of Ag-Ni Nanohybrid Particles prepared using the Extract of *Cassytha filiformis* Leaves

Figure 4.70 is the XRD pattern for Ag-Ni bimetallic nanoparticles in which the extract of *Cassytha filiformis* leaves acted as a reducing agent.

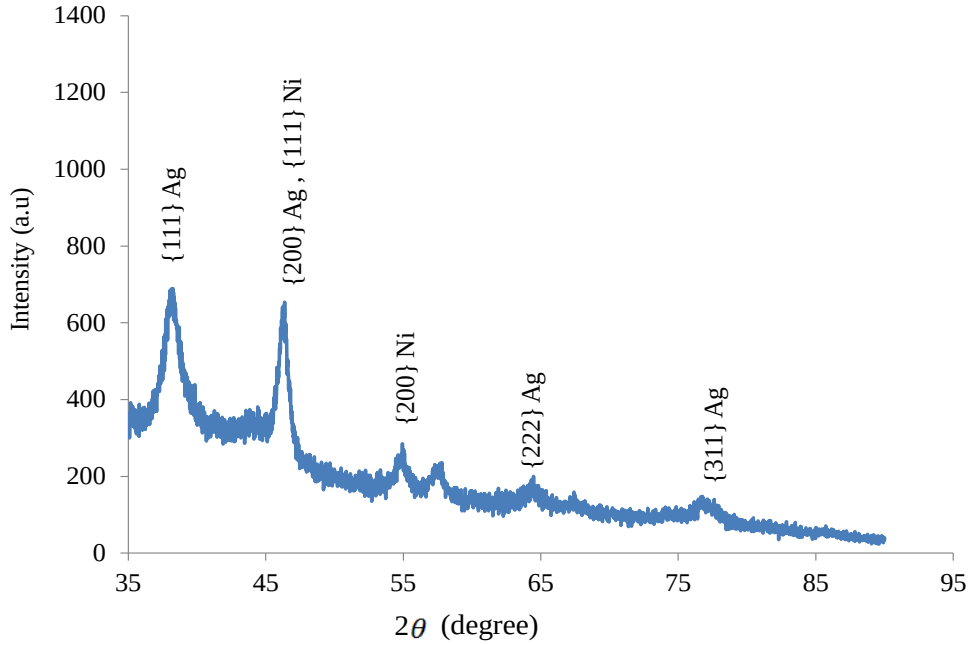

Figure 4.70: XRD patterns of Ag-Ni bimetallic nanoparticles prepared using 2.0 mM precursor mixture and the extract of *C. filiformis*

The hybrid displayed different reflections at 2θ values of 38.24°, 46.36°, 64.83° and 77.61° indexed to {111}, {220}, {311}, and {222} Ag planes of the face-centred cubic structure. The characterization also depicted two peaks- {111} diffracted at 46.36° and {200} at 53.03° for crystal plane of Ni. The characteristic peak of Ni at 2θ (46.36°{111}) was considered to have an overlap with that of the {200} plane of Ag. This is similar to previous work (Adekoya, Mlowe, Dare, Mesubi & Revaprasadu, 2015). The overlap signalled core-shell morphology of the fcc structure in both Ni and Ag.

4.7.5 FTIR Analysis of Ag-Ni Bimetallic Nanoparticles

Figure 4.71 is the FTIR result of Ag-Ni nanocluster synthesized using the extract of *C. filiformis* as a reducing agent, recorded within the wavenumber range 4500-500 cm^{-1}.

Figure 4.71: FTIR spectrum of Ag-Ni bimetallic nanoparticles

The spectrum portrayed absorption bands at 3243 cm^{-1} (O−H stretching), 2912 cm^{-1} (C−H stretching), 1627 cm^{-1} (N−H bending of 1° amine in the alkaloid), 1510 cm^{-1} (C=C stretching), 1365 cm^{-1} (C−H rock) and 1071 cm^{-1} (C−N stretching of 1° amine). The presence of alkaloid in the leaf extract of *Cassytha filiformis* may be accountable for the reduction of Ag and Ni metal ions and formation of Ag-Ni nanohybrid. There was an electron loss on hydrogen attached to the nitrogen present in alkaloids; hence, forming a double bond in N=C. There appears to be no peak at region of C=O functionality. This is an indication that the reaction took place through the nitrogen present in the alkaloids and not through the OH in the saponins.

4.7.6 Optical (UV-Vis) Properties of Ag-Co Bimetallic under *Cassytha filiformis*-Influenced Synthesis at 70°C

The UV-Vis optical characterization of the as-prepared hybrid Ag-Co nanoparticles prepared by reducing 2.0 mM metal precursor mixture with *Cassytha filiformis* (Whole part) is shown in Figure 4.72.

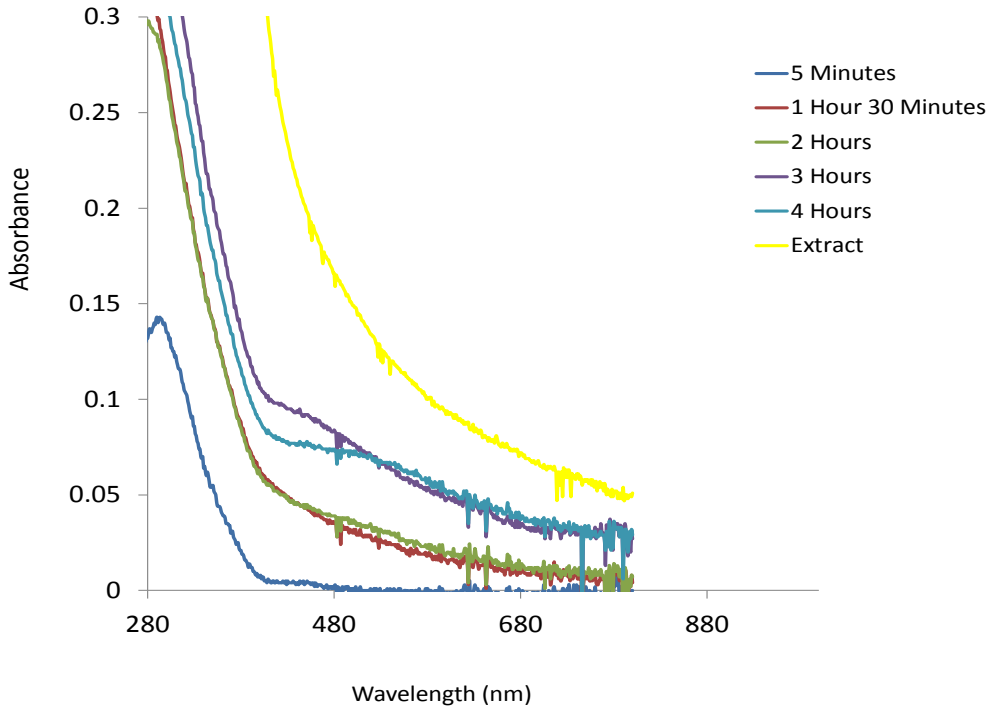

Figure 4.72: UV-Vis spectra of Ag-Co bimetallic NPs prepared using 2.0 mM precursor mixture and *C. filiformis* extract at 70°C

There was a clear evidence of nanoparticles formation, as a result of the manifestation of surface plasmon band (SPB) between 400 and 500 nm which is similar to the maximum wavelength of monometallic Ag NPs. The appearance of SPR took as long as 3 hours, suggesting interaction between the particles. The delay observed in the nucleation and onset growth was an indication of large particle size. Low absorption intensity was observed in the nanobimetallic. Moreover, the observed broad peak in the shape of the spectra proposed polydispersed nanoparticles. The presence of Co in the Ag-Co hybrid of course was responsible for the red shift.

4.7.7 TEM and Size Distribution of Ag-Co Bimetallic Nanoparticles Synthesized using *Cassytha filiformis*

Figures 4.73 (a and b) are the TEM micrographs of Ag-Co hybrid nanoparticles prepared from 1.0 and 2.0 mM metal precursor mixtures respectively using the extract of *C. filiformis* at 70℃.

(a)

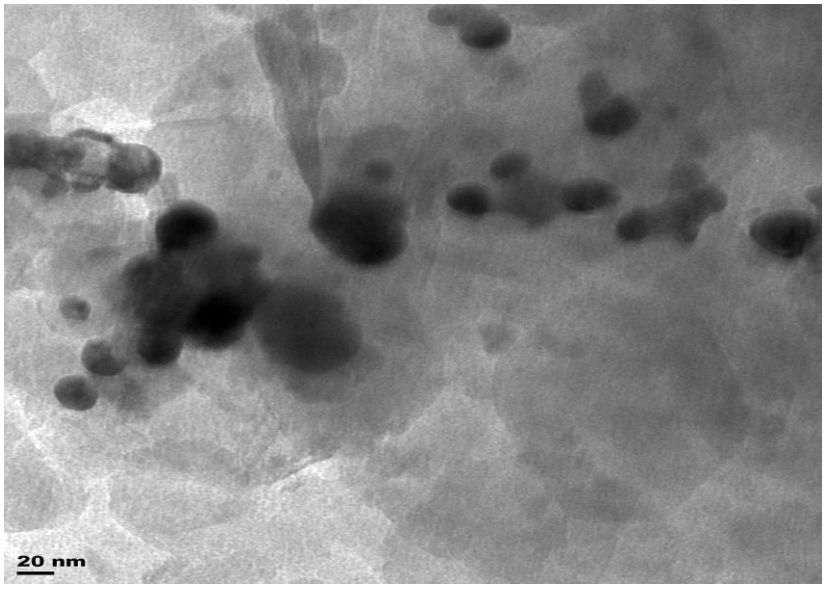

(b)

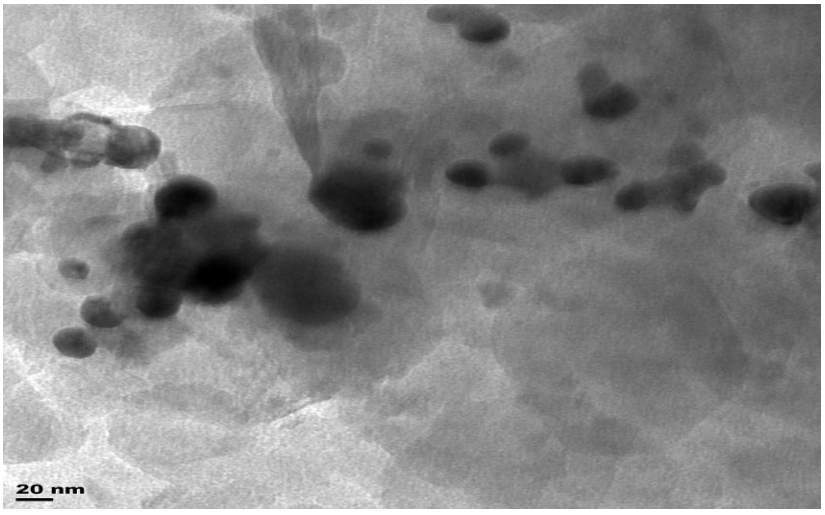

Figure 4.73: Representative TEM images of Ag-Co bimetallic nanoparticles prepared using (a) 1.0 mM (b) 2.0 mM precursor mixture and *C. filiformis* extract

Table 4.31: The EDX result of Ag-Ni bimetallic nanoparticles prepared using 1.0 mM metal precursor mixture and the extract of *Cassytha filiformis*

Element	Series	[wt.%]	[norm. wt.%]	[norm. at.%]	Error in %
Silver	L-series	29.54	49.59	23.30	1.59
Oxygen	K-series	0.09	0.14	0.08	0.04
Carbon	K-series	8.13	10.50	10.47	0.14
Nickel	K-series	7.51	5.77	5.44	0.06
Cobalt	K-series	20.87	34.10	60.71	5.13
Phosphorus	K-series	0.00	0.00	0.00	0.00
Sulphur	K-series	0.00	0.00	0.00	0.00
	Sum:	66.34	100.00	100.00	

Figure 4.73 (a) shows polydispersed nanoparticles. Under a close observation, the cobalt nanoparticles were formed between two Ag shells, thereby forming a planar structure rather than spherical nanoparticles. Figure 4.73(b) depicts capped Ag nanoparticles. It is noteworthy that the shape of metal nanoparticles greatly changed the optical and electronic properties, according to Mulvaney (1996). The analysis by EDX confirmed the synthesis of Ag-Co hybrid. The atomic composition of silver to Cobalt existed about ratio 1:2 (23.30 % Ag, 60.71 % Co), (Table 4.31).

4.7.8 FTIR Analysis of Ag-Co Hybrid Nanoparticles

Figure 4.74 is the representative FTIR spectrum of bimetallic Ag-Co nanoparticles synthesized using *Cassytha filiformis* extract.

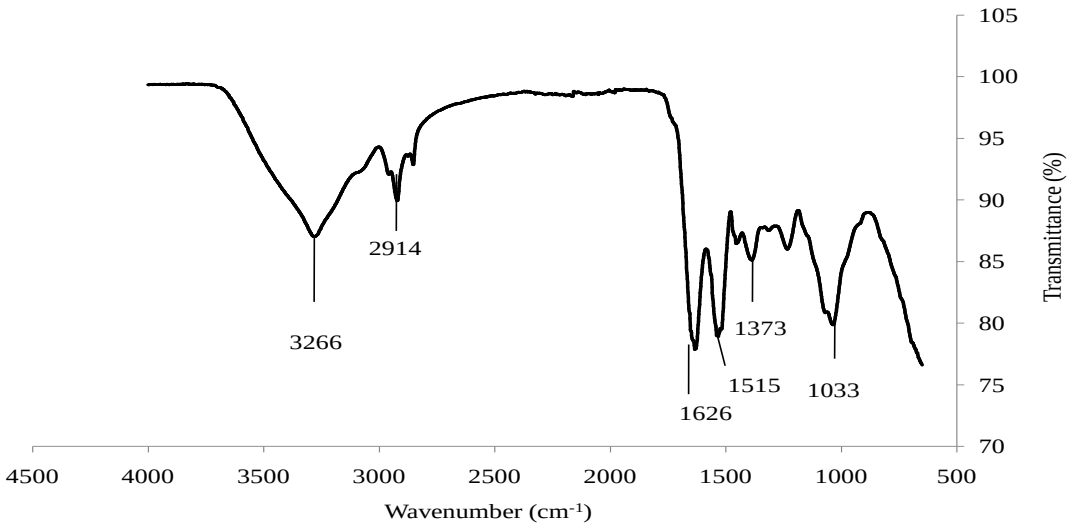

Figure 4.74: FTIR spectrum of the biosynthesized Ag-Co bimetallic nanoparticles

The following absorption peaks were observed in the spectrum: 3266 cm^{-1} (O−H stretching and N−H stretching), 2914 cm^{-1} (C−H stretching), 1626 cm^{-1} (N−H bending), 1515 cm^{-1}, 1373 cm^{-1} (C−H stretching), 1209 cm^{-1} (C−O stretching through ether linkage) and 1033 cm^{-1} (C−N stretching). However, the phytochemicals adsorbed on the surface of Ag-Co nanohybrid particles could be possible through active site created by lone pair electron present in nitrogen attached to the methyl group, thereby forming a double bond in N=C.

4.7.9 Optical (UV-Vis) Properties of Ag NPs under *Cassytha filiformis*-Influenced Synthesis at Room Temperature

Figure 4.75 is the absorption spectra of Ag NPs synthesized using C. *filiformis* at room temperature.

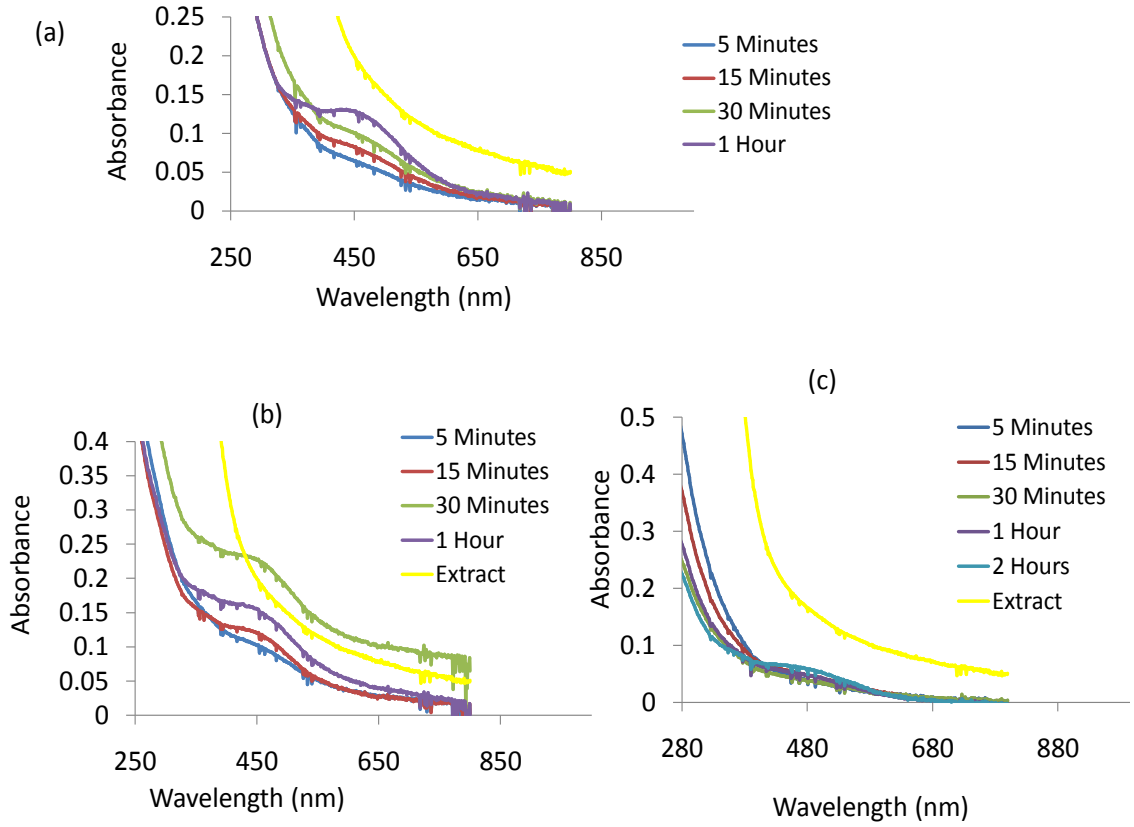

Figure 4.75: Room temperature time-resolved UV-Vis spectra of Ag NPs prepared from (a) 1.0 mM (b) 2.0 mM (c) 3.0 mM precursor solutions using *C. filiformis* extract as a reducing/capping agent

Table 4.32: Bioreduction parameters for the syntheses of silver and its hybrid nanoparticles using the extract *C. filiformis* (whole part) at room temperature for 1hour

NPs	Maximum intensity 0.5 mM		Maximum intensity 1.0 mM		Maximum intensity 2.0 mM		Maximum intensity 3.0 mM	
	Abs	λ_{max} (nm)	Abs	λ_{max} (nm)	Abs	λ_{max} (nm)	Abs	λ_{max} (nm)
Ag	0.029	455	0.129	400-450	0.23 (30 min.)	400-450	0.063	400-450
Ag-Co			0.405,0.39	373, 447				

The surface plasmon band (SPB) for silver usually observed at 400-440 nm was observed in all the metal precursor solution concentrations. Change in colour was noticed during the bioreduction process from light brown to brown. The nucleation and onset growth were slow compared with the same reaction carried out at 70℃. The appearance of SPB, an indication of nanoparticles formation took place at 1 hour, 20 minutes and 2 hours in the Ag NPs prepared by reducing 1.0, 2.0 and 3.0 mM precursor solutions respectively; unlike the synthesis at 70℃ in which onset growth commenced as early as at 20 minutes in all the concentrations. The absorbance by the nanoparticles was relatively low compared with the corresponding nanohybrid.

However, the slow nucleation and growth rate observed could be as a result of slow supersaturation of the reaction solution for nucleation to take place (Murray *et al.*, 2000; Huang *et al*., 2007). No doubt, there was a strong interaction between the biomolecules and the growing particles. The observed broad peak in the spectra signalled occurrence of polydispersed nanoparticles. Hence, the growth in 2.0 mM precursor solution was considered to be the optimum condition for the synthesis of Ag NPs at room temperature. Highest intensity of absorption (0.23 a.u.) also occurred at this concentration (Figure 4.75b).

4.7.10 Optical (UV-Vis) Properties of Ag-Co Bimetallic Nanoparticles under *Cassytha filiformis*-Influenced Synthesis at Room Temperature

Figure 4.76 depicts the optical spectra of Ag-Co bimetallic nanoparticles prepared by reducing 1.0 mM precursor solution, using the extract of *C. filiformis* (whole part) at room temperature.

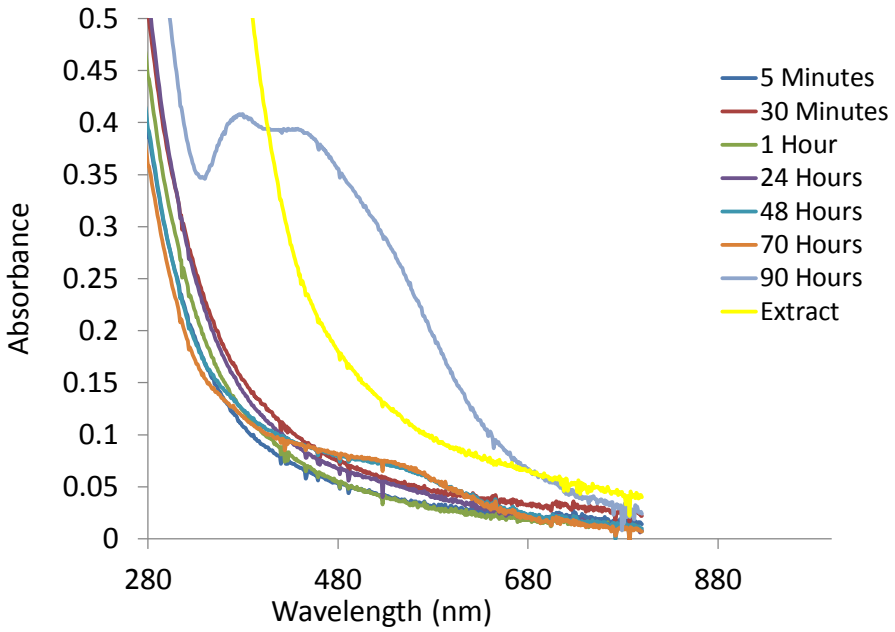

Figure 4.76: Room temperature time-resolved UV-Vis spectra of Co-Ag bimetallic nanoparticles prepared from 1.0 mM precursor solutions mixture using the extract of *M. charantia* leaves as a reducing agent

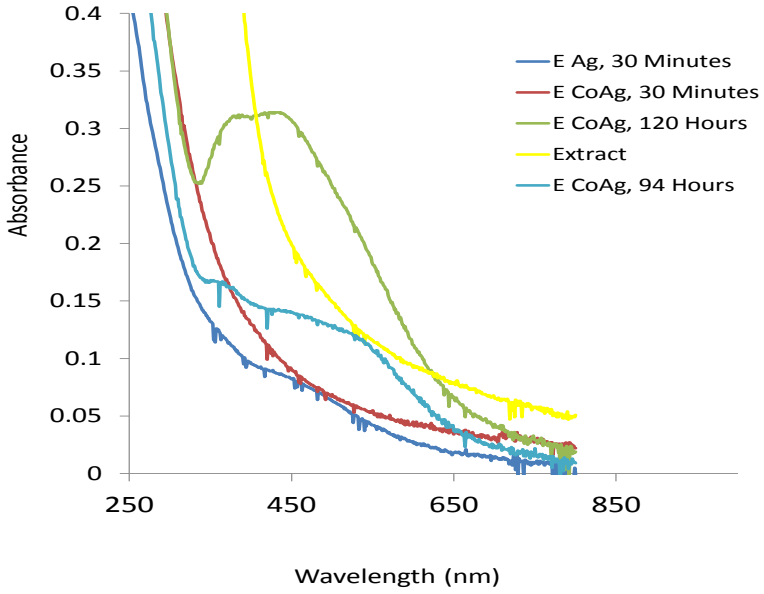

Figure 4.77: Growth comparison between Ag NPs and Ag-Co NPs prepared from 1.0 mM precursor concentration using the extract of *Cassytha filiformis* (whole plant) as a reducing agent at room temperature

The appearance of SPR confirmed the presence of nanoparticles. The reaction occurred at a very slow rate as nucleation and onset growth were delayed till 48th - 70th hours of the reaction time. Interaction between the biomolecules in the plant extract and the growing particles took place (Huang *et al*., 2007). The long-time duration in the reduction process also hinted formation of large particle size. The presence of Co in the hybrid nanoparticles led to the formation of two peaks (337 and 447 nm) as shown in Figure 4.76. Very strong absorption intensity took place at the 90th hour of the reaction (Table 4.32). The shape of the spectra indicates nickel core and silver shell arrangement.

4.8 Optical (UV-Vis) Properties of Ag NPs under *Hibiscus sabdariffa*-Influenced Synthesis at 70℃

The extract of *H. sabdariffa* (Roselle) contained chromophores which were able to absorb light in the 200-800 nm range, as shown in Figure 4.78. The comparison in the growth of Ag NPs in all the varied precursor solution concentrations is presented in Figure 4.79.

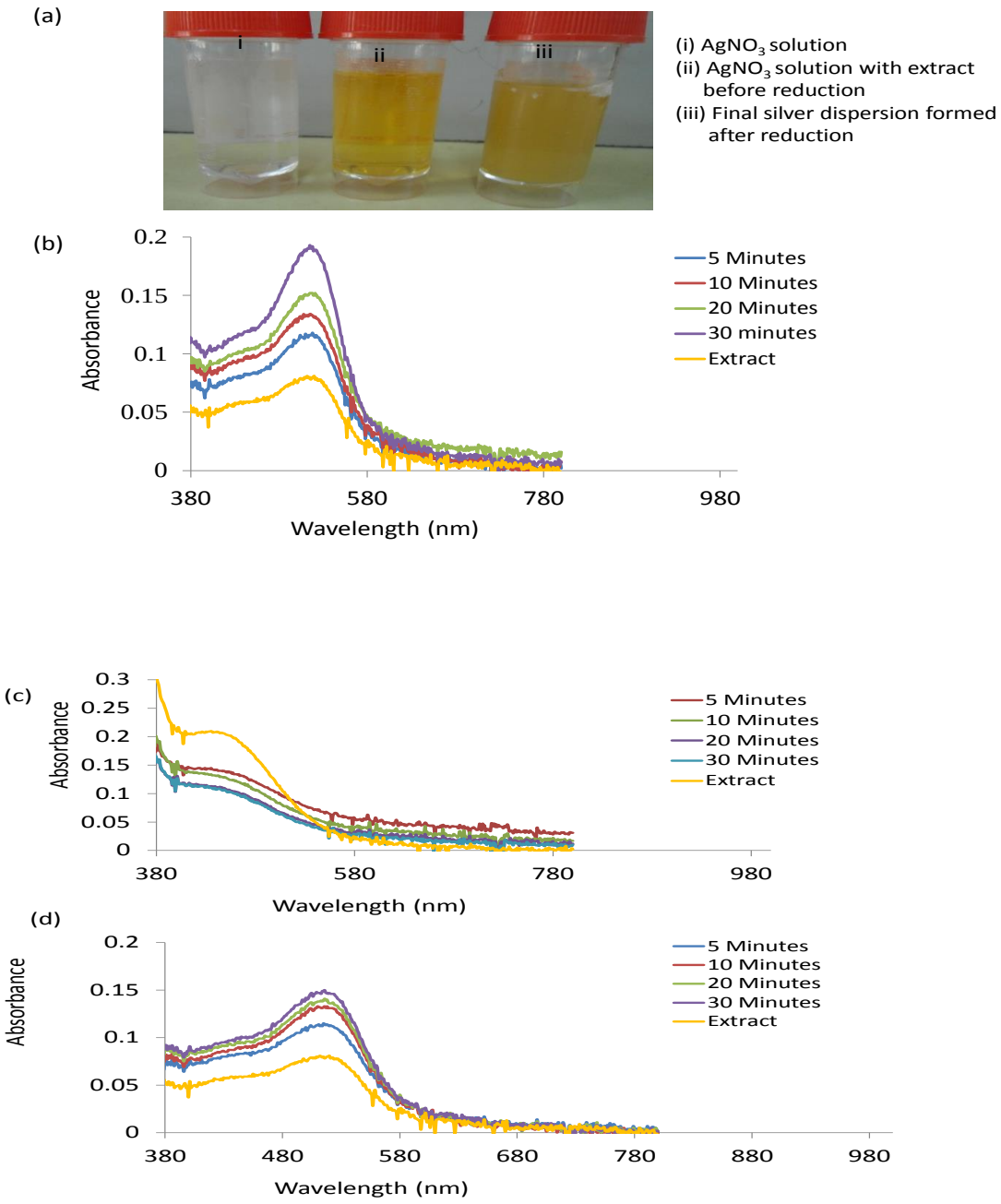

Figure 4.78: (a) $AgNO_3$ solution (i), $AgNO_3$ solution with extract before reduction (ii), and the final silver dispersion formed after reduction.UV-Vis spectra of Ag NPs prepared using (b) 1.0 mM (c) 2.0 mM (d) 3.0 Mm precursor solutions using the extract of *H. sabdariffa* (calyces) at 70℃

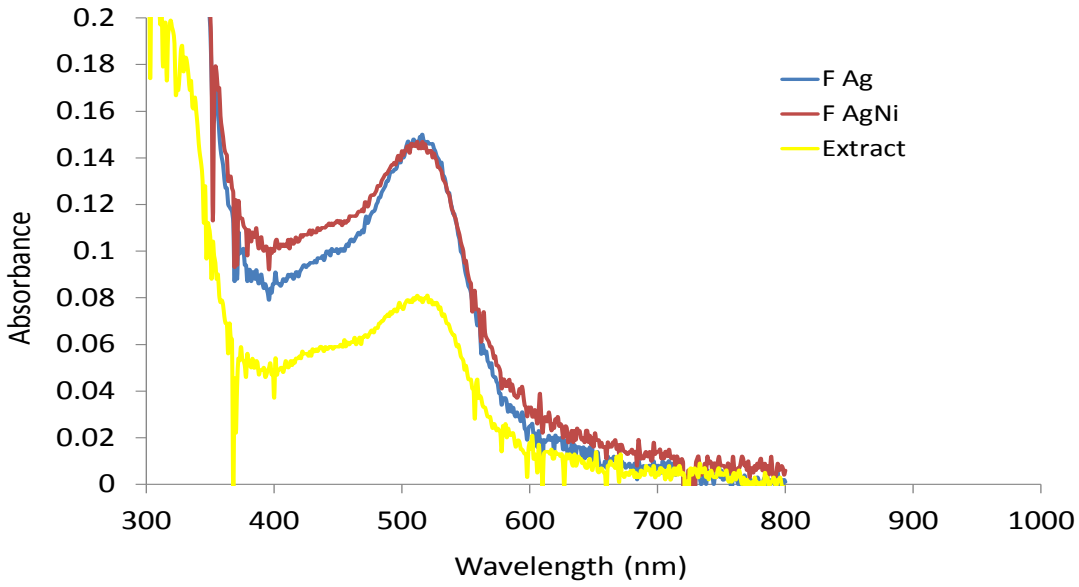

Figure 4.79: Growth comparison between Ag NPs and Ag-Ni NPs prepared from 1.0 mM precursor concentrations using the extract of *H. sabdariffa* (calyces) as a reducing agent at 70 ˚C, 30 minutes

Table 4.33: Bioreduction Parameters for the Syntheses of Silver and Its Hybrid Nanoparticles using the Extract of *Hibiscus Sabdariffa* (Calyces) at 70 ℃, 30 Minutes

	Maximum intensity 1.0 mM		Maximum intensity 2.0 mM		Maximum intensity 3.0 mM	
NPs	Abs	Wavelength (nm)	Abs	Wavelength (nm)	Abs	Wavelength (nm)
Ag	0.312	510			0.141	503
Ag-Ni	0.204	513	0.091	510	0.132	510

The Roselle extract displayed an optical property as the SPR in the molecule was localized around 500 nm due to the presence of $\pi \longrightarrow \pi^*$ (C=C in phenol) and $n \longrightarrow \pi^*$ transition of C=O moiety of the proteins, carbohydrates and steroids present in the biomass (Wani *et al.*, 2010). A slight change in colour was noticed after the reduction, from yellow to yellowish brown, which signalled the formation of nanoparticles to some extent (Figure 4.78a).

The surface plasmon absorption for silver usually noticed around 400 - 400 nm was absent; instead, a red shift to a longer wavelength was observed. Intensity of absorption occurred at 510 nm (0.312) and 503 nm (0.141) in the Ag NPs prepared from 1.0 mM and 3.0 mM $AgNO_3$ solutions (Table 4.33). Increase in intensity as a function of time was also noticed from 5 - 30 minutes. The nucleation and onset growth commenced within 5 minutes of the reaction. Though, the extract of Roselle displayed SPR band, the reduced Ag^+ showed stronger intensity of absorption than the extract (Figure 4.78). The shift denotes an excitation of electrons from $n \longrightarrow \pi^*$ and longer wavelength as a result of lower energy of absorption. The extract considered as the reducing agent contains more of chromophores which induced photoactivity.

4.8.1 Optical (UV-Vis) Properties of Ag-Ni Bimetallic Nanoparticles under *Hibiscus sabdariffa*-Influenced Synthesis at 70℃

The combined UV-Vis spectra of the green synthesized Ag-Ni bimetallic nanoparticles prepared using the extract of *Hibiscus sabdariffa* (calyces) at 70℃ are displayed in Figure 4.80. Figure 4.81 is the growth comparison in Ag-Ni bimetallic nanoparticles prepared from varied precursor solution concentrations at 70℃ and 30 minutes of the reaction time.

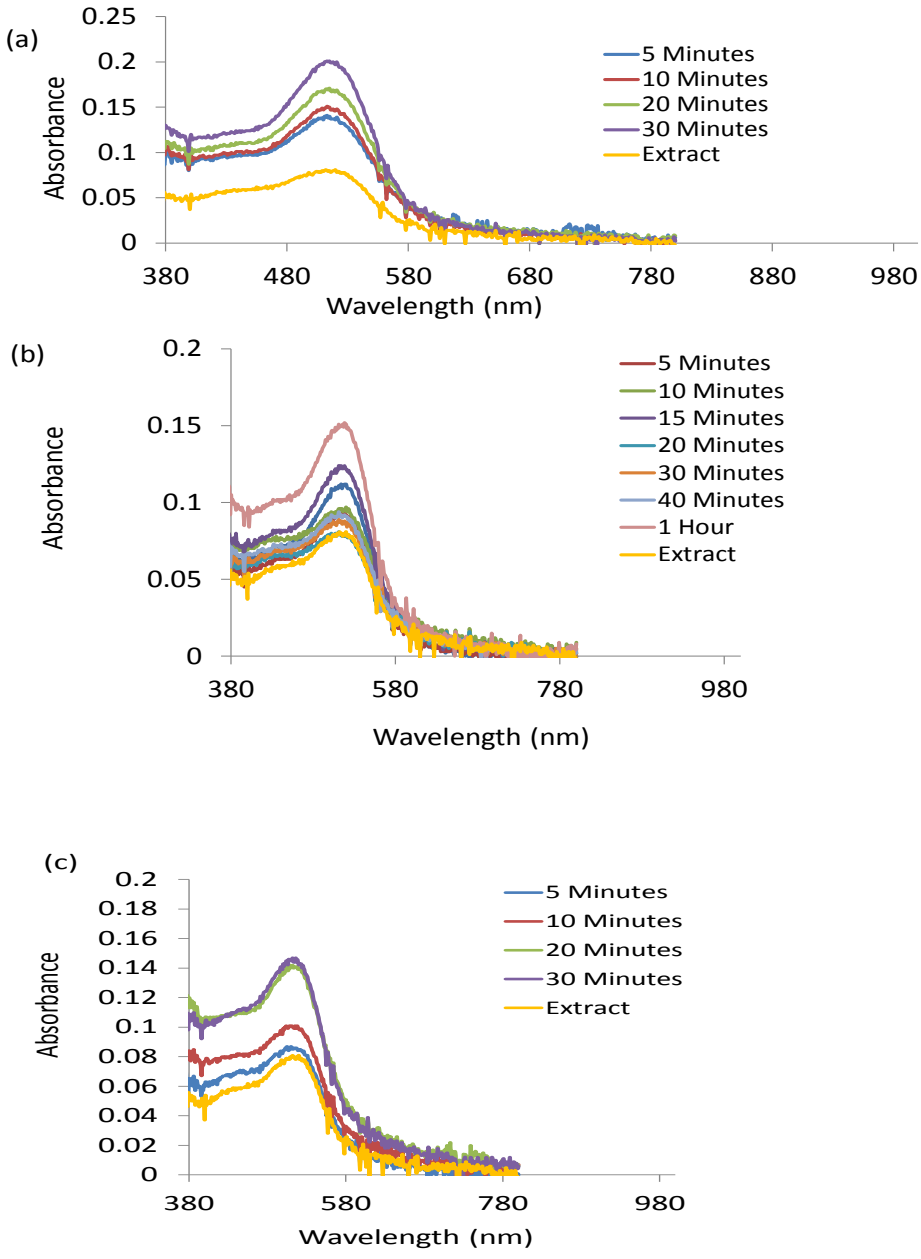

Figure 4.80: UV-Vis spectra of Ag-Ni bimetallic nanoparticles prepared by reducing (a) 1.0 mM (b) 2.0 mM (c) 3.0 mM precursor solution using the extract of *Hibiscus sabdariffa* at 70℃

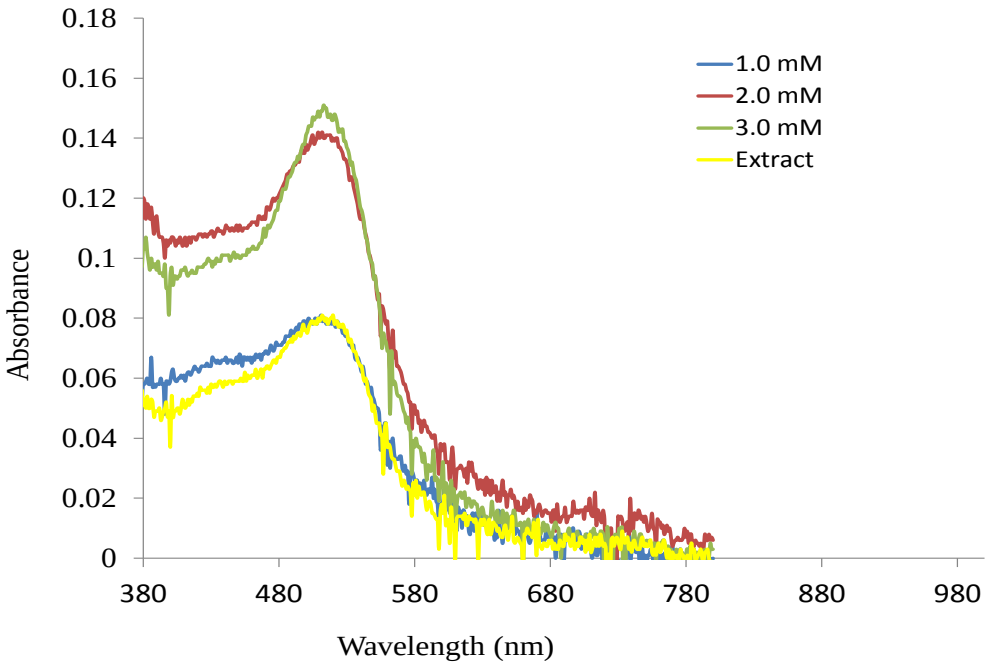

Figure 4.81: Growth comparison in Ag-Ni bimetallic nanoparticles prepared from varied precursor concentrations using the extract of *H. sabdariffa* (calyces) at 70 ˚C, 30 minutes

A gradual change in colour from light brown to black signified the formation of nanoparticles. This was confirmed by the appearance of SPR. In this work, the optical spectra showed that the SPR was localized at 513 nm in Ag-Ni nanoparticles prepared from 1.0 mM precursor solution concentration and 510 nm in 2.0 and 3.0 mM precursor solution concentrations. It was contrast to the SPR of the corresponding monometallic Ag NPs in which SPB was located at 510 nm and 503 nm in 1.0 and 3.0 mM precursor solutions respectively. The intensity of absorbance was strong around 0.2 (a.u), which increased gradually as a function of time from 5-30 minutes.

Photoactivity of the nanohybrid displayed in the optical spectra was enhanced by the presence of $\pi \longrightarrow \pi^*$ (C=C) and $n \longrightarrow \pi^*$ transition of (C=O) functional groups present in the bio-reducing agents, as the extract exhibited optical property; though, not as intense as the corresponding nanohybrid (Wani *et al*., 2010). The effect of Ni in the Ag-Ni hybrid was the observed red shift of 3 nm and 7 nm relative to the parent Ag NPs (Table 4.34). The disparity could be as a result of overlap of the electronic states of the different constituents of the hybrid particles which modified the SPR (Steiner *et al.,* 2005; Yu *et al.,* 2005). Moreover, the detected shift could also signal the coverage of the Ag portion of the hybrid with Ni, which was revealed in the TEM micrograph. In addition, there might also be a possibility of the

presence of higher index of refraction in the solvent used, as the presence of higher index of refraction in materials results in plasmon towards longer wavelengths as reported in previous work (Templeton, Pietron, Murray & Mulvaney, 2000; Thomas, Zajicek & Kamat, 2002).

4.8.2 TEM and Size Distribution of Ag-Ni Bimetallic Nanoparticles Synthesized using *Hibiscus Sabdariff* Extract

Figure 4.82a is the particle size distribution histogram of the as-prepared hybrid Ag-Ni nanoparticles from the reaction of *Hibiscus sabdariffa* and 2.0 mM metal precursor mixtures and TEM micrograph 4.82b.

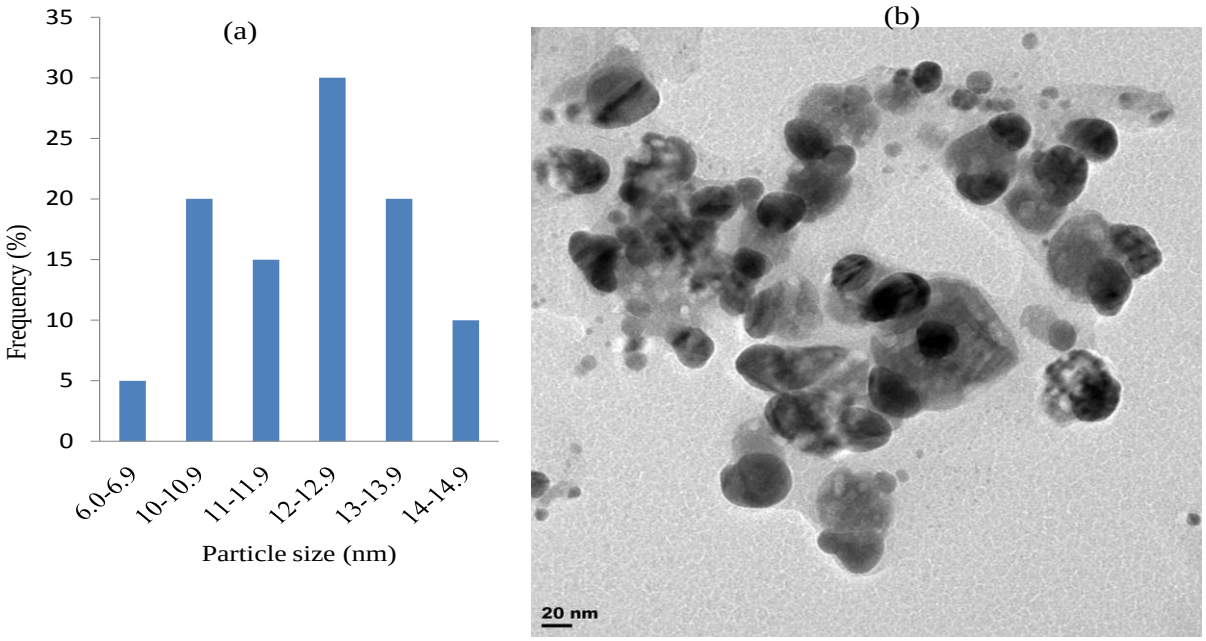

Figure 4.82: (a) Particle size distribution histogram of Ag-Ni bimetallic nanoparticles determined from TEM image (b) Representative TEM image of the Ag-Ni nanoparticles prepared from 2.0 mM metal precursor mixture using the extract of *H. sabdariffa* (calyces)

Table 4.34: The EDX result of Ag-Ni bimetallic nanoparticles prepared using 2.0 mM metal precursor mixtures and the extract of *Hibiscus sabdariffa* at 70℃

Element	Series	wt.%]	[norm. wt.%]	[norm. at.%]	Error in %
Silver	L-series	37.16	46.94	78.60	0.80
Oxygen	K-series	8.07	12.83	5.67	5.85
Carbon	K-series	13.30	14.17	3.15	0.38
Nickel	K-series	18.89	23.87	10.89	0.60
Cobalt	K-series	0.38	0.48	0.22	0.06
Phosphorus	K-series	1.17	1.48	1.28	0.09
Sulphur	K-series	0.18	0.23	0.20	0.04
	Sum:	79.15	100.00	100.00	

The particle sizes with highest frequency were in the 12-12.9 nm size range. The TEM image revealed no free particles; instead multiply-twinned nanoparticles of Ag-Ni were observed. Average particle size of 12.66 $\pm$ 2.40 nm was obtained. Moreover, structural morphology of Ag-core and Ni-shell were revealed, as depicted in the TEM image shown in Figure 4.82(b). The Roselle extract displayed an optical property as the SPR in the molecule was localized around 500 nm due to the presence of $\pi \longrightarrow \pi^*$ (C=C in phenol) and $n \longrightarrow \pi^*$ transition of C=O moiety of the proteins, carbohydrates and steroid present in the biomass (Wani *et al*., 2010). EDX proved the formation of bimetallic Ag-Ni nanoparticles prepared from green plant source. Table 4.34 shows the composition of elements present in the nanohybrid. Ag dominated the hybrid with atomic % composition of 78.60. 10.89 atomic % of Ni was also present.

4.8.3 XRD Pattern of the Ag-Ni Nanohybrid Particles

Figure 4.83 is the XRD pattern for Ag-Ni nanohybrid under *Hibiscus sabdariffa*- influenced synthesis.

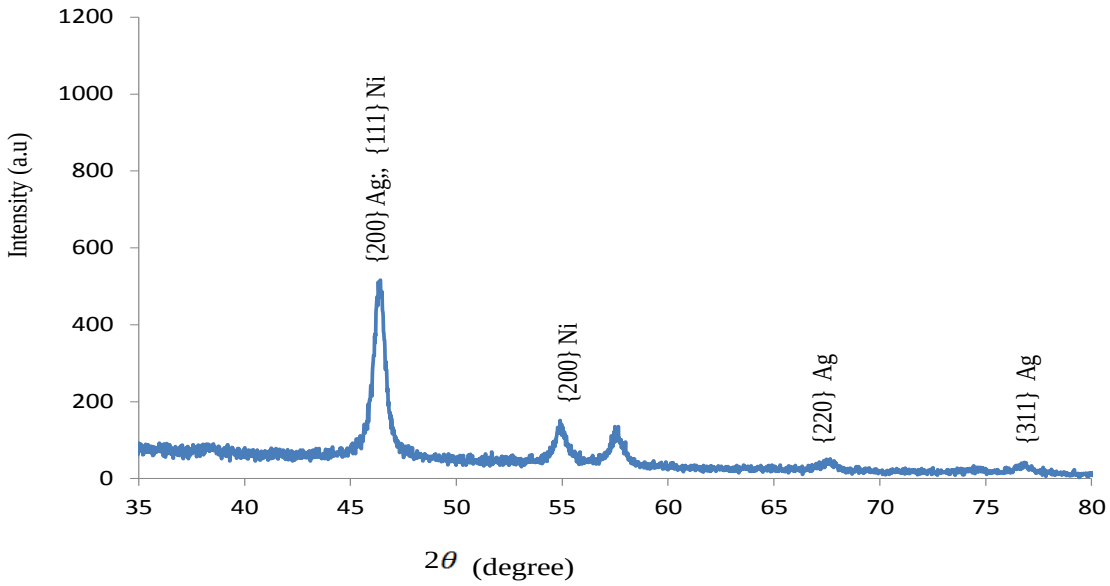

Figure 4.83: XRD pattern of Ag-Ni bimetallic nanoparticles prepared using the extract of *H. sabdariffa*

The bimetallic nanocluster displayed different reflections at 2θ values of 46.48°, 68.09° and 77.16° indexed to {220}, {311} and {222} Ag planes of the face-centred cubic structure. The characterization also depicted two peaks- {111} diffracted at 46.48° and {200} at 54.17° for crystal plane of Ni. The characteristic peak of Ni at 2θ, 46.48°{111}, was considered to have an overlap for the {200} plane of Ag, similar to the Ag-Ni hybrid synthesis using *C. filiformis* leaf extract. The overlap confirmed Ag core and Ni shell morphology of the fcc structure in both Ni and Ag.

4.8.4 FTIR Analysis of Ag-Ni Hybrid Nanoparticles

The result of FTIR analysis Ag-Ni nanohybrid obtained using the extract of *Hibiscus sabdariffa* (Calyces); which capped the newly formed nanoparticles is illustrated in Figure 4.84.

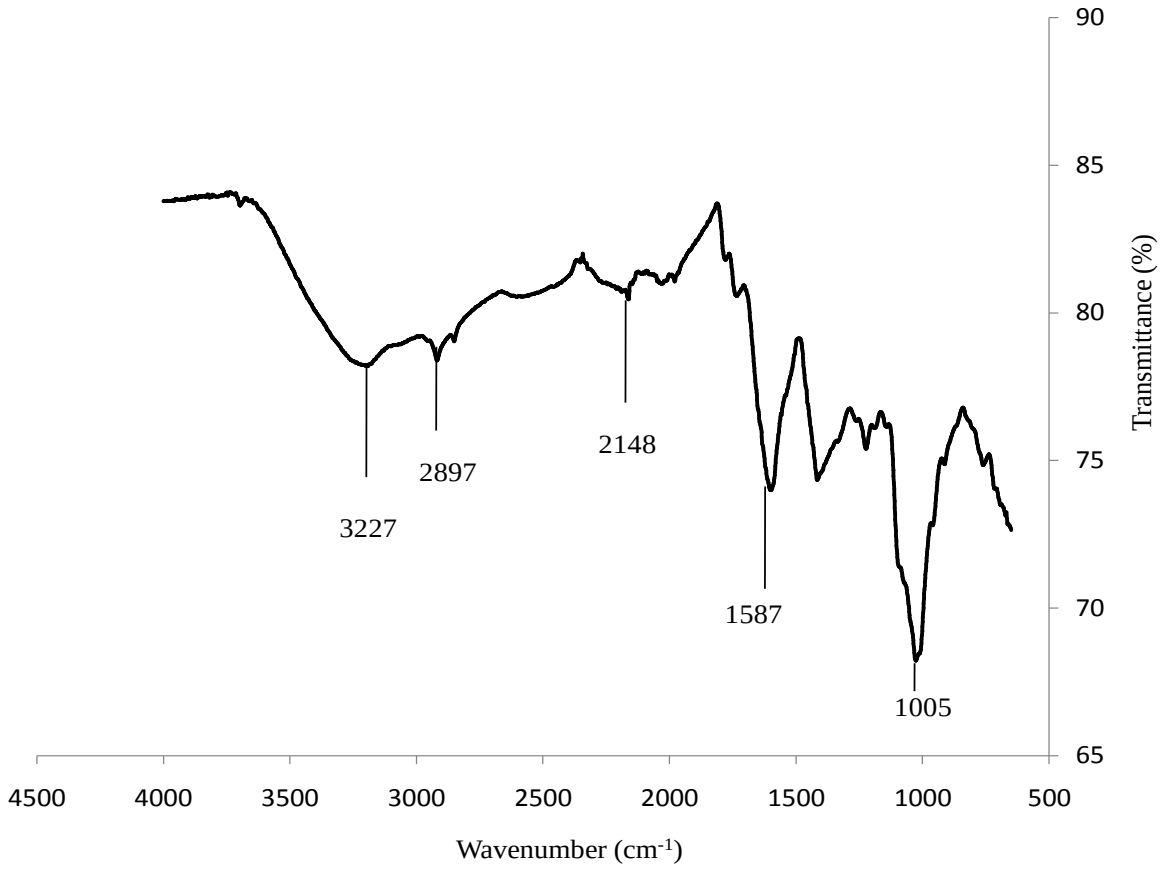

Figure 4.84: FTIR spectrum of Ag-Ni bimetallic nanoparticles

The following absorption peaks were observed in the FTIR spectrum of Ag-Ni nanoparticles: 3227 cm^{-1} (O−H stretching), 2897 cm^{-1} (C−H aliphatic stretching), 1587 cm^{-1} (C=N sretching; C−C stretching in ring) and 1005 cm^{-1} (C-O stretching).

4.8.5 Optical (UV-Vis) Properties of Ag NPs under *Lawsonia inermis*-Influenced Synthesis at 70℃

Figure 4.85 depicts the UV-Vis spectra of Ag NPs under *Lawsonia inermis*-influenced synthesis at 70℃.

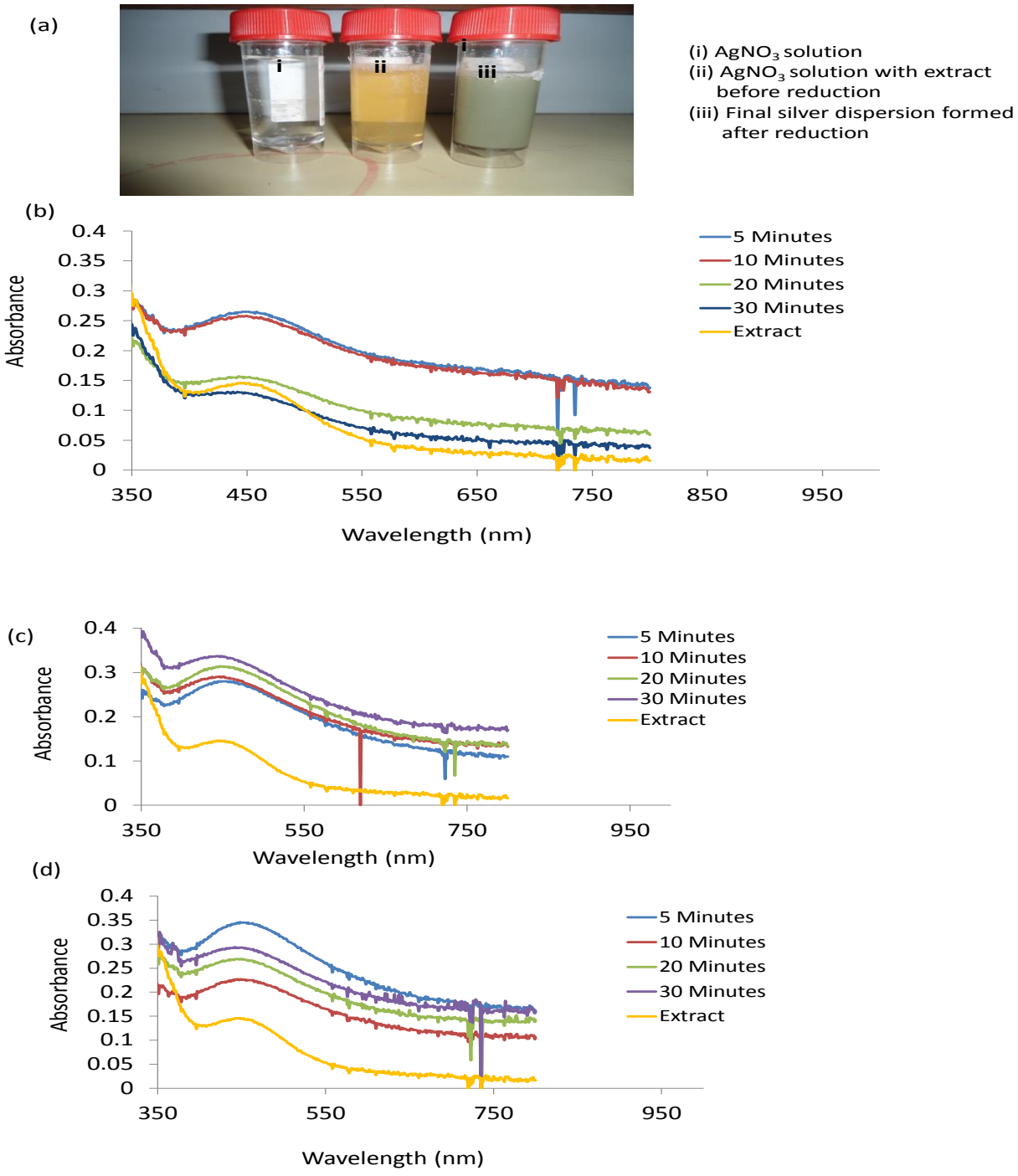

Figure 4.85: (a) $AgNO_3$ solution (i), $AgNO_3$ solution with extract before reduction (ii), and the final silver dispersion formed after reduction. UV-Vis spectra of Ag NPS prepared from (b) 1.0 mM (c) 2.0 mM (d) 3.0 mM precursor solution using the extract of *L. inermis* leaves at 70℃

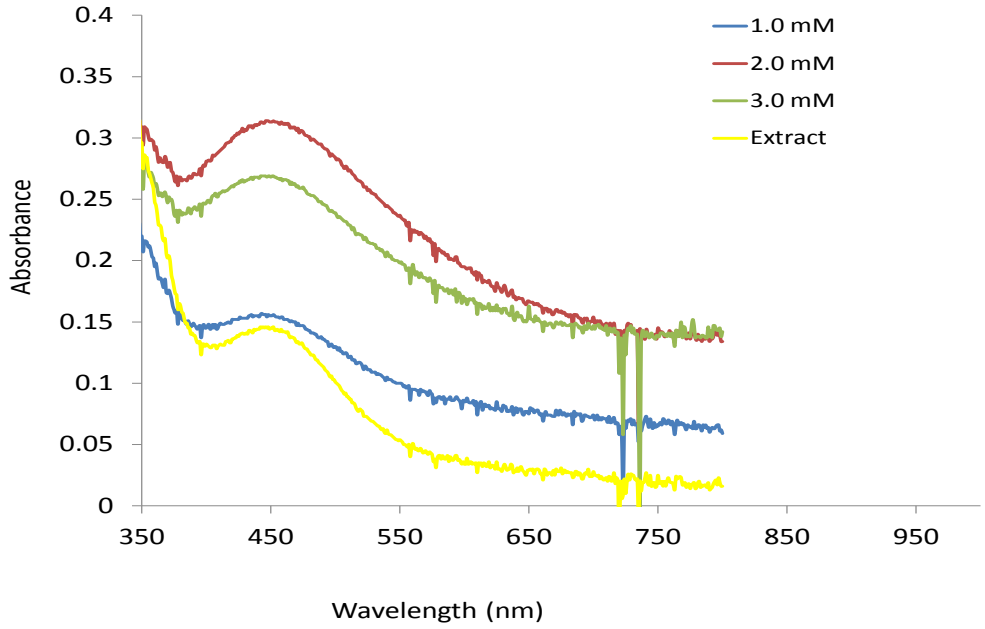

Figure 4.86: Growth comparison of Ag NPs prepared from varied precursor concentrations using the extract of *L. Inermis* as a reducing/capping agent at 70°C, 30 minutes

Table 4.35: Bioreduction parameters for the syntheses of silver and its hybrid nanoparticles using the extract of *L. inermis* (leaves) at 70℃, 30 minutes

NPs	Maximum intensity 1.0 mM		Maximum intensity 2.0 mM		Maximum intensity 3.0 mM	
	Abs	Wavelength (nm)	Abs	Wavelength (nm)	Abs	Wavelength (nm)
Ag	0.128	447	0.335	447	0.292	451
Ag-Ni	0.12	452	0.163	460	0.11	450-460 (Broad)

The *L. inermis* extract contained chromophores which absorbed light in the visible region, with SPR band around 450 nm. The presence of $\pi \longrightarrow \pi^*$ (C=C) and $n \longrightarrow \pi^*$ transition (C=O) functional groups in the carbohydrates and glucosides (phytochemicals) in the extract were accountable for this (Wani *et al.*, 2010). Nonetheless, a rapid change in colour from colourless Ag^+ solution to dark brown was noticed during the synthesis, as this hinted the formation of nanoparticles (Figure 4.85a). The intensity of absorption was stronger in the Ag NPS compared with the extract. Figure 4.86 shows the comparison of growth in Ag NPs in all the varied precursor solution concentrations.

The metal nanoparticles exhibited SPR, which was blue shifted from 450 nm as observed in the extract to 447 nm in 1.0 mM $AgNO_3$ solution, and red shifted to 451 nm at 2.0 and 3.0 mM precursor solutions (Table 4.35). This is a result of collective oscillation of free conduction electrons (Daisy, 1999). The peak intensity increased with time from 5-30 minutes. Thus, the presence of chromophores in the pigmented extract was considered to be responsible for the distinct nature of the observed bioreduction. The broad band around 447 nm with shoulder at 420 nm indicated a broad particle size distribution. Moreover, the shape indicated the presence of spheres or rod which conformed to TEM.

4.8.6 TEM and Size Distribution of Ag NPs Synthesized using the Leaf Extract of *Lawsonia inermis*

Figures 4.87 and 4.88 are the TEM micrographs of Ag nanoparticles generated from the reactions of *L. inermis* with 1.0 and 2.0 mM $AgNO_3$ respectively.

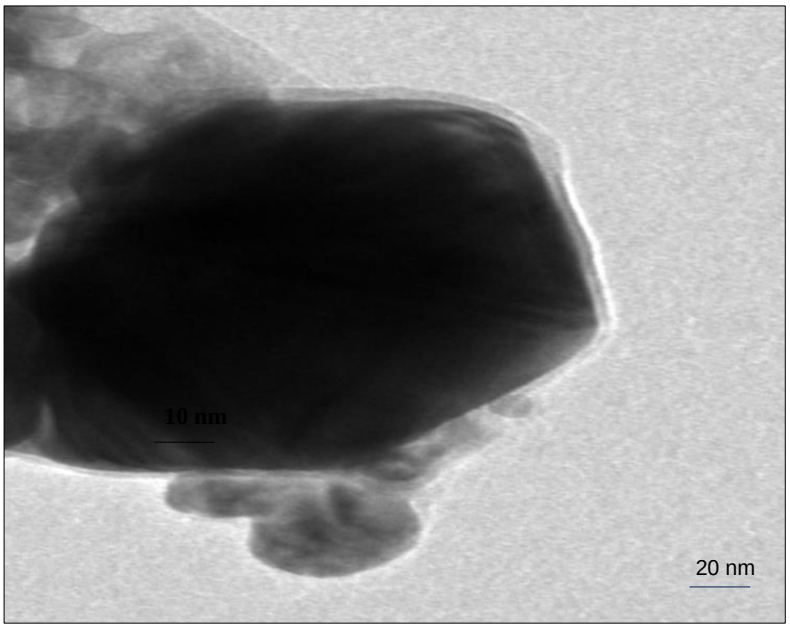

Figure 4.87: Representative TEM image of Ag NPs prepared using 1.0 mM precursor solution and the leaf extract of *L. inermis*

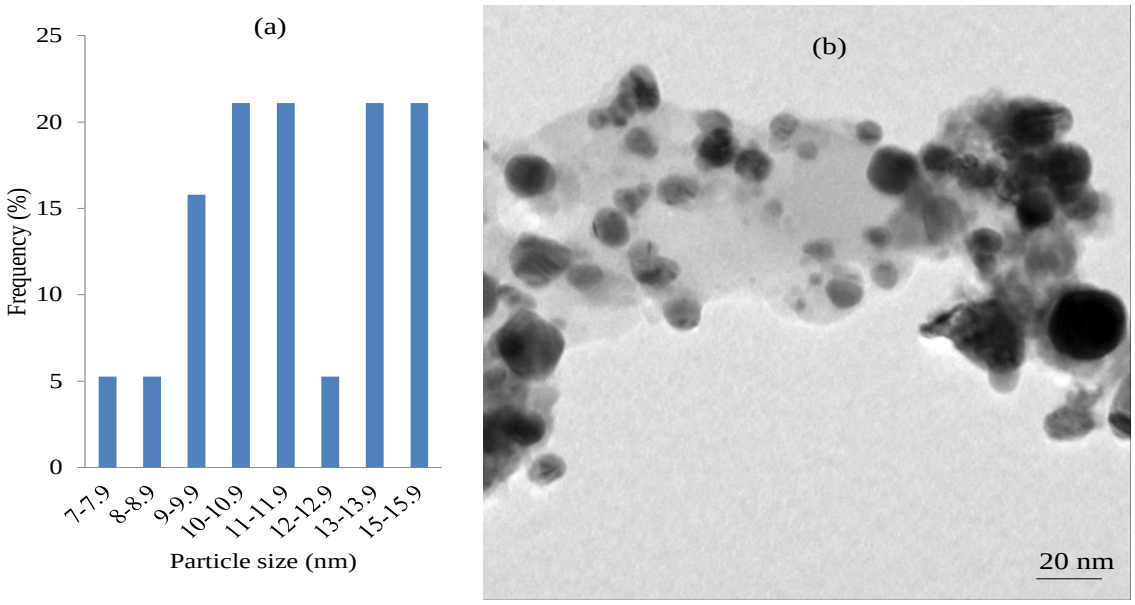

Figure 4.88: (a) Particle size distribution histogram of Ag NPs determined from TEM image (b) Representative TEM image of Ag NPs prepared from 3.0 mM precursor using the extract of *L. inermis* as a reducing agent

Hexagonal shaped nanoparticles with truncated edges were observed in the Ag NPs produced from 1.0 mM metal precursor. The average particle diameter of 18.0 $\pm$ 5.3 nm was obtained from the TEM image. Figure 4.87 reveals spherical shaped nanoparticles with less aggregation. The particles size range from 7.0 to 13.0 nm with mean size of 11.33 $\pm$ 2.02 nm was achieved. However, the particle size distribution histogram shown in Figure 4.88(a) displays a close size range of particles.

4.8.7 XRD Pattern of Ag NPs under *Lawsonia inermis*-Inflenced Synthesis

The XRD pattern of the as synthesized Ag nanoparticles prepared using the extract of *L. inermis* at 70 ^{o}C is presented in Figure 4.89.

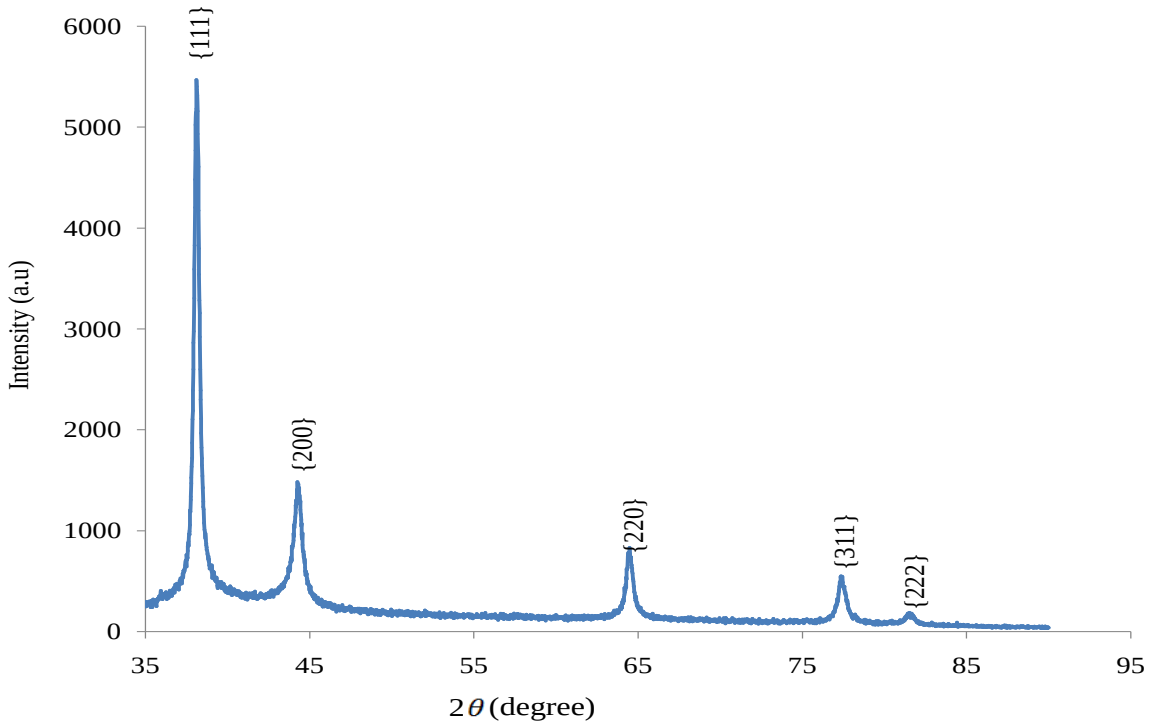

Figure 4.89: XRD patterns of Ag NPs prepared by reducing 3.0 mM precursor solution using the extract of *L. inermis*

Outstanding peak of reflections were portrayed in Figure 4.89. The intensity of reflection was similar to that of chemical synthesis. The Ag NPs were highly crystalline as depicted in the X-ray diffractogram (Figure 4.90). Characteristics reflections which appeared at 2θ values of 38.17°, 44.39°, 64.57° and 77.49° were indexed to {111}, {200}, {220} and {311} Ag planes of the face-centred cubic structure. The nanocluster reflection planes were very sharp and strong in intensity. The pattern also showed that the nanocluster was void of impurities.

4.8.8 Optical (UV-Vis) Properties of Ag-Ni Hybrid Nanoparticles under *Lawsonia inermis*-Influenced Synthesis at 70℃

The optical spectra of the synthesized Ag-Ni hybrid nanoparticles using the extract of *L. inermis* leave at 70℃ are shown in Figure 4.90.

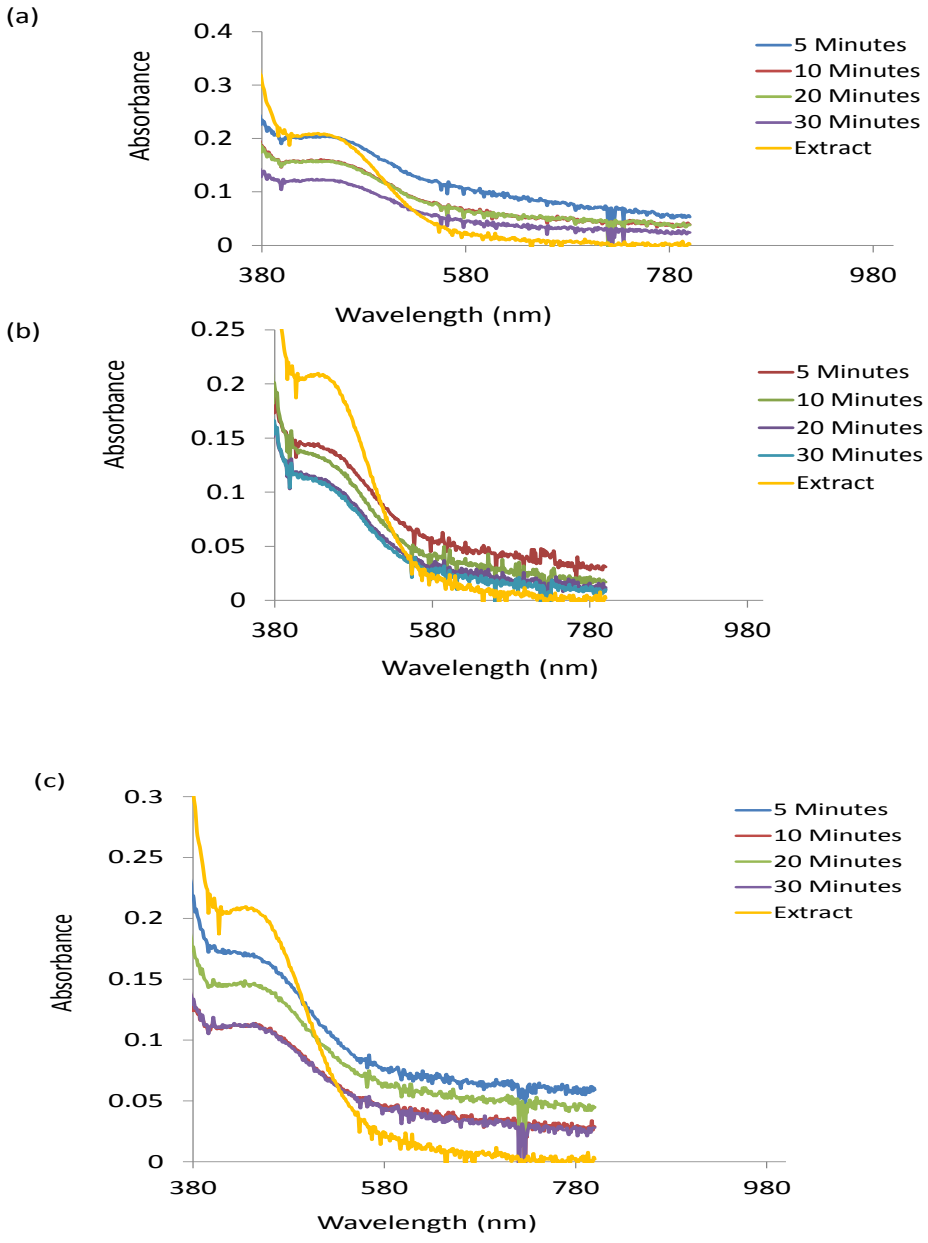

Figure 4.90: UV-Vis spectra of Ag-Ni bimetallic nanoparticles prepared from (a) 1.0 (b) 2.0 (c) 3.0 mM precursor solutions using the extract of *L. inermis* leaves at 70℃

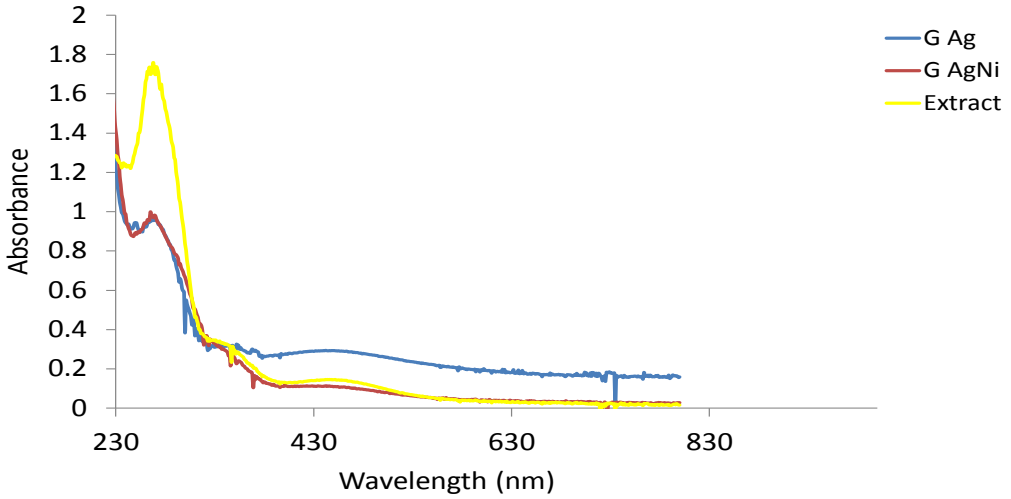

Figure 4.91: Growth comparison between Ag NPs and Ag-Ni NPs prepared from 3.0 mM precursor solution using the leaf extract of *L. inermis* as stabilizer/capping agent at 70 ˚C, 30 minutes

There was a noticeable steady change in colour from light yellow to dark brown which indicated the formation of nanoparticles. The nucleation and onset growth commenced from the 5th minute of the reaction. The observed increase in the peak intensity was a function of reaction time till the 30th minute of the reaction time. However, the nanoparticles were confirmed by the manifestation of SPR with a broad band shoulder due to n → π^* transition C=O bond from 427 nm to 452 nm and 460 nm in the hybrid nanoparticles prepared from 1.0 and 2.0 precursor solutions respectively.

Figure 4.91 is the growth comparison in Ag-Ni bimetallic nanoparticles at 70˚C and 30th minute of the reaction time. The presence Ni in the Ag-Ni hybrid nanoparticles was the red shift of the absorption wavelength from 447 nm as observed in the parent Ag NPs to 452 nm and 460 nm in 1.0 mM and 2.0 mM precursor solutions respectively. Broad band absorption was noticed in the hybrid particle prepared from 3.0 mM precursor solution. The shifting could be attributed to the excitation of electrons from n → π^* which shifted the wavelength to a longer band, as a consequence of lower energy of absorption. Moreover, it could also be due to the overlap in the electronic states of the components present in the hybrid particles, similar to the research carried by Steiner *et al* (2005). The intensity of absorption in both the Ag NPs and Ag-Ni nanohybrid were not as strong when compared with the intensity of absorption observed in *L. inermis* extract.

4.8.9 TEM and Size Distribution of Ag-Ni Bimetallic Nanoparticles Synthesized from 3.0 mM Precursor Mixture using the Extract of *Lawsonia Inermis* Leaves

The structural morphology and particle size distribution histogram of Ag-Ni nanoparticles synthesized from 3.0 mM metal precursor mixture, using the extract of *Lawsonia inermis* leaves as a reducing agent are elucidated in Figure 4.92.

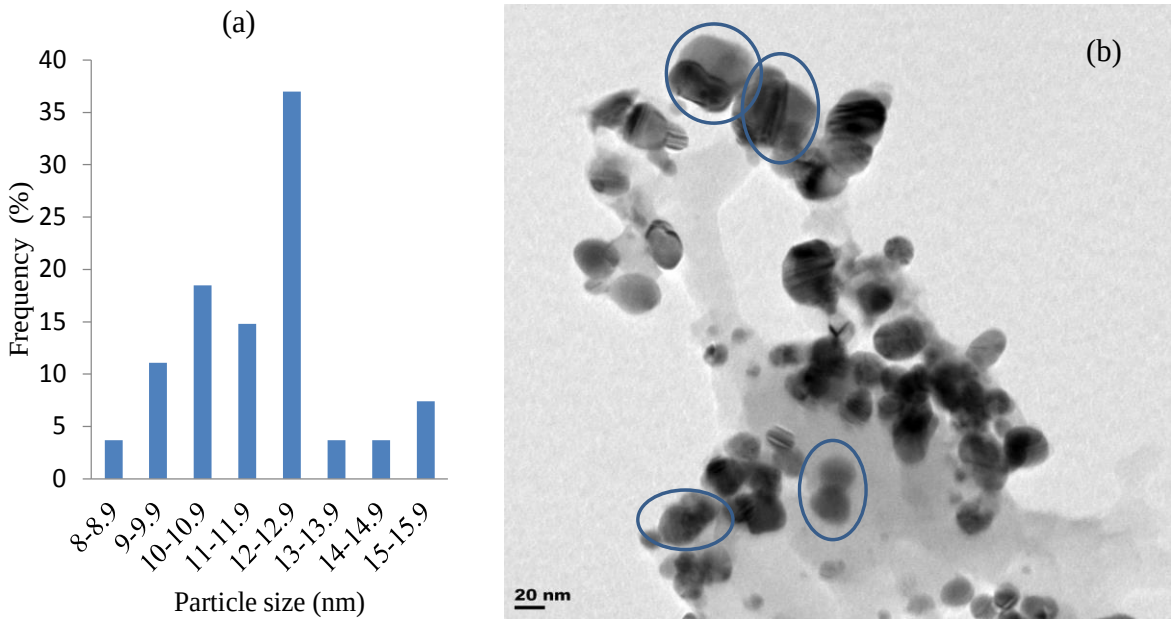

Figure 4.92:(a) Particle size distribution histogram of Ag-Ni bimetallic nanoparticles determined from TEM image (b) Representative TEM image of the Ag-Ni nanoparticles synthesized from 3.0 mM metal precursor mixture using the extract of *L. inermis* as a reducing agent at 70 ^{o}C

Table 4.36: EDX result of Ag-Ni bimetallic nanoparticles prepared using 3.0 mM metal precursor mixture and L*awsonia inermis* extract

Element	Series	[wt.%]	[norm. wt.%]	[norm. at.%]	Error in %
Silver	L-series	20.94	31.92	7.12	0.94
Oxygen	K-series	37.41	57.02	85.72	8.42
Carbon	K-series	2.38	3.63	2.46	0.42
Nickel	K-series	1.09	1.66	0.68	0.12
Cobalt	K-series	0.79	1.20	0.49	0.10
Phosphorus	K-series	2.47	3.76	2.92	0.15
Sulphur	K-series	0.54	0.82	0.61	0.06
	Sum:	65.61	100.00	100.00	

The micrograph contained multiply twinned nanoparticles of Ag-Ni and rough edge cube (due to the reducing power of the plant extract). The mean size of 11.80 $\pm$ 1.66 nm was also obtained from the image. The particle size distribution histogram showed that most of the particles were formed within 12-12.9 nm size range (Figure 4.92a).

However, the reaction between the extract of *Lawsonia inermis* leaves and 3.0 mM metal precursor mixture was void of Ag^0 as indicated in the EDS analysis; instead, oxidation of silver to silver oxide (Ag_2O) was formed in the reaction. This was affirmed in the atomic composition of oxygen in the nanocluster 85.72%. The hybrid also contained 7.12% atomic % of Ag. Carbon (2.46 atomic %) originated from plant source. Other elements present were considered to be due to the effect of carbon-coated copper from the grid used for TEM analysis (Table 4.36).

4.9 Optical (UV-Vis) Spectra Comparison of Ag NPs among Different Plant Extracts

Figures 4.93, 4.94 and 4.95 are the combined UV-Vis spectra of the biosynthesized Ag nanoparticles, comparing maximum absorption intensity at 70^{o}C among all the plant extracts utilized in this work using 1.0, 2.0 and 3.0 mM $AgNO_3$ precursor solutions respectively.

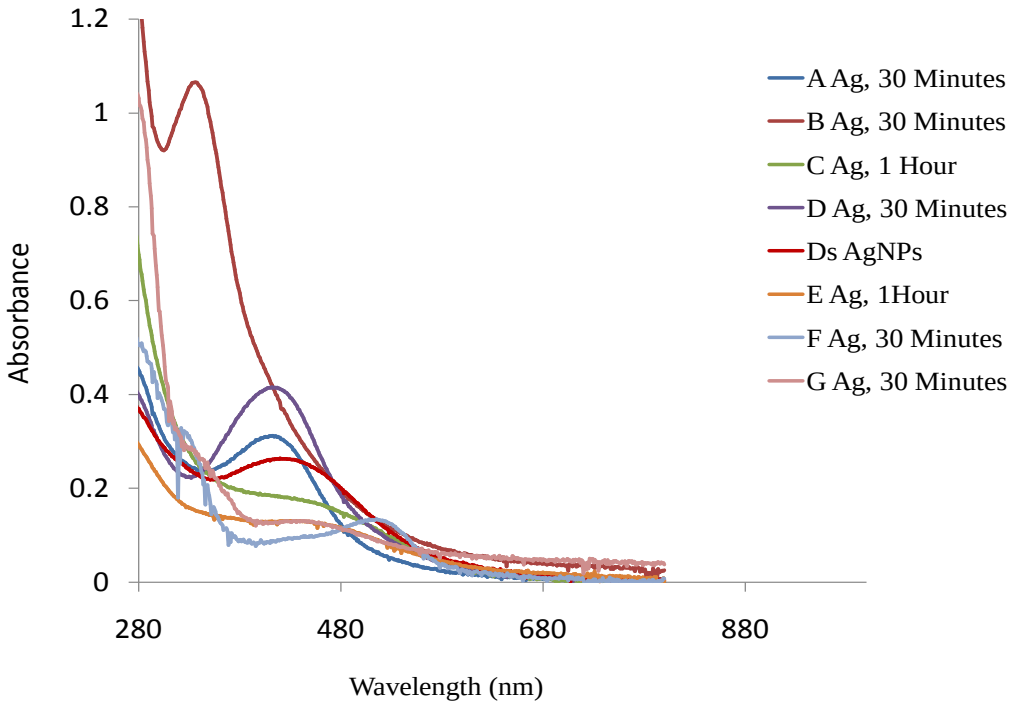

Figure 4.93: Comparison of maximum absorption intensity of Ag NPs prepared by reducing1.0 mM $AgNO_3$ using different plant extracts as reducing/capping agents at 70℃ A= *Canna indica*, B= *Senna occidentalis*, C = *Nicotiana tobacuum*, D = *Momordica charantia* leaf, D_s = *Momordica charantia* stem, E = *Cassytha filiformis*, F = *Hibiscus sabdariffa*, G = *Lawsonia inermis*

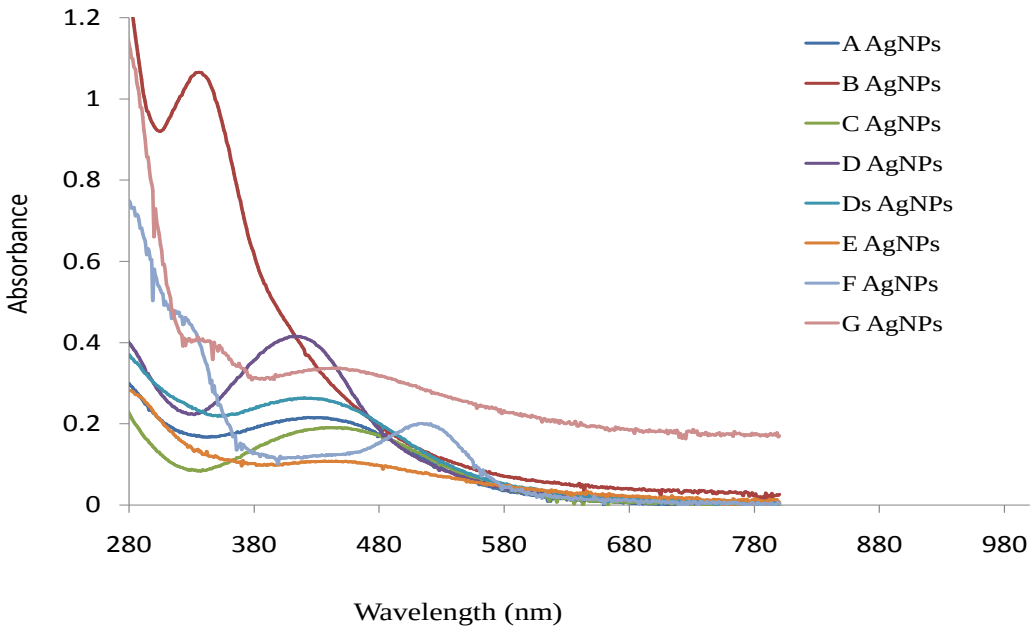

Figure 4.94: Comparison of maximum absorption intensity of Ag NPs prepared by reducing 2.0 mM $AgNO_3$ using different plant extracts as reducing/capping agents at 70℃. A= *Canna indica*, B= *Senna occidentalis*, C = *Nicotiana tobacuum*, D = *Momordica charantia* leaf, D_s = *Momordica charantia* stem, E = *Cassytha filiformis*, F = *Hibiscus sabdariffa*, G = *Lawsonia inermis*

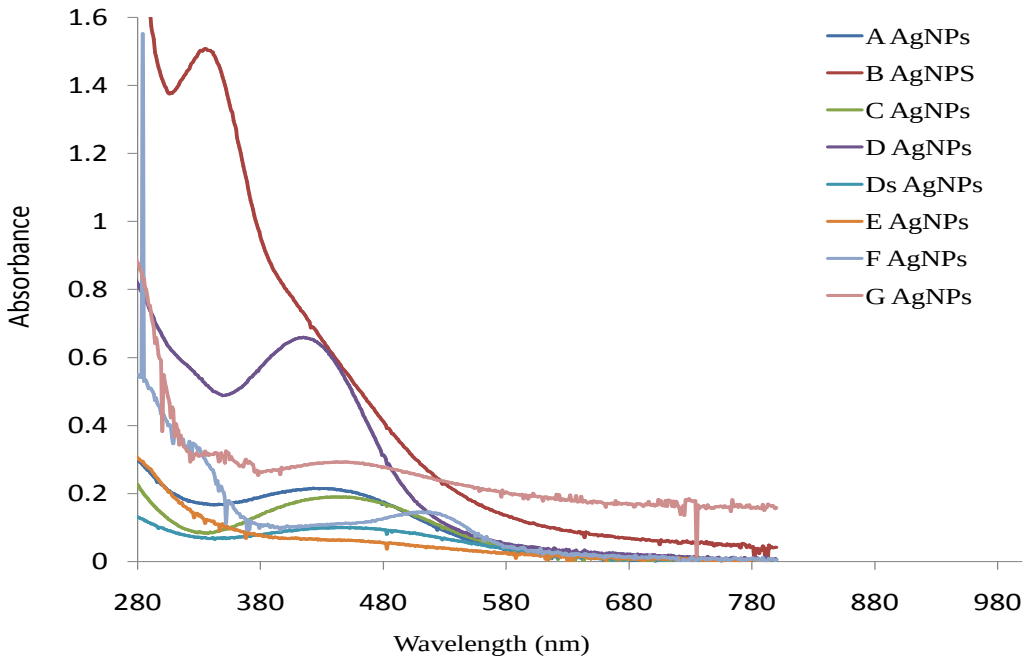

Figure 4.95: Comparison of maximum absorption intensity of Ag NPs prepared by reducing 3.0 mM $AgNO_3$ using different plant extracts as reducing/capping agents at 70℃
A= *Canna indica*, B= *Senna occidentalis*, C = *Nicotiana tobacuum*, D = *Momordica charantia* leaf, D_s = *Momordica charantia* stem, E = *Cassytha filiformis*, F = *Hibiscus sabdariffa*, G = *Lawsonia inermis*

Table 4.37: Bioreduction parameters for the syntheses of silver and its hybrid nanoparticles using different plant extract at 70℃, 30 minutes

NPs	Maximum 0.5 mM		Maximum 1.0 mM		Maximum 2.0 Mm		Maximum 3.0 mM	
	Abs	λ_{max} (nm)	Abs	λ_{max} (nm)	Abs	λ_{max} (nm)	Abs	λ_{max} (nm)
A Ag	0.118	Broad peak	0.312	416	0.222	Broad peak		
A AgNi	0.086	425	0.108	427 Broad peak	0.395	421		400-420 Broad peak
A CoAg			0.251	427	0.223	504		
B Ag	0.182	334	1.056	341	1.555	400-425	1.6	400-450 Broad peak
B AgNi					0.573	327	0.48	330
C Ag			0.162	400-430	0.312	438	0.232	400-450 Broad peak
C AgNi			0.046	420-450	0.06	516	0.077	419
C CoAg		No SPR		No SPR		No SPR		No SPR
D Ag			0.415	417				
D AgNi			0.172	420-450	0.242	420-450 Broad peak	0.212	427
D CoAg			0.38 (1hour)	400-600				

Ds Ag	0.056	420-460 Broad peak	1.248	420	0.1	437
Ds AgNi			0.047	40-600 Broad peak	0.108	400-650
E Ag					0.116	400-450 Broad peak
E AgNi	0.262 (1 hour)	424	0.107 (1hour)	431	0.082 (1hour)	420-493
E CoAg			0.081	400-600		
F Ag	0.312	510			0.141	503
F AgNi	0.204	513	0.091	510	0.132	510
G Ag	0.128	447	0.335	447	0.292	451
G AgNi	0.12	452	0.163	460	0.11	450-460 Broad peak

A Ag = Silver nanoparticles of specified precursor concentration using *C. indica* leaf extract, A Ag-Ni = Silver-nickel bimetallic nanoparticles of specified precursor concentration using *C. indica* leaf extract, B Ag = Silver nanoparticles of specified precursor concentration using *S. occidentalis* leaf extract, B Ag-Ni= Silver-nickel nanoparticles of specified precursor concentration using *S. occidentalis* leaf extract, D Ag= Silver nanoparticles of specified precursor concentration using *M. charantia* leaf extract D Ag-Ni = Silver-nickel nanoparticles of specified precursor concentration using *M. charantia* leaf extract, E Ag = Silver nanoparticles of specified precursor concentration using *C. filiformis* leaf extract, E Ag-Ni = Silver nanoparticles of specified precursor concentration using *C. filiformis* leaf extract

Table 4.38: Bioreduction parameters for the syntheses of silver and its hybrid nanoparticles using different plants at room temperature

Plant Code	Maximum intensity at specified time 0.5 mM		Maximum intensity at specified time 1.0 mM		Maximum intensity at specified time 2.0 mM		Maximum intensity at specified time 3.0 mM	
	Abs	λ_{max} (nm)	Abs	λ_{max} (nm)	Abs	λ_{max} (nm)	Abs	λ_{max} (nm)
A Ag	Broad, 24 hours		0.11 24 hours	420-480	0.247 24 hours	420-480	0.373 24 hours	443
A Ag-Co		No SPR	0.299 48hours	450-550	0.235	450-550 191 hours	0.25 120 hours	450-550
B Ag	0.518 30 Min.	316	0.4	400-450	0.41	305	0.311	360-430
C Ag		No SPR		No SPR	0.331	436	0.242	350-430
D Ag			0.357 2 hours	435	0.343 30 min.	430	0.367	435
D Ag-Co			0.158 120 hours	450-550	0.896 192 hours	392, 500 (2 Peaks)	0.376 120 hours	450-550
Ds Ag	0.1 120 hours	350-450	0.1 24 hours	400-450	0.127 24 hours	400-500	0.14	400-450
E Ag	0.029 1 hour	455	0.1291 1hour	400-450	0.23 30 min.	400-450	0.063	400-450
E Ag-Co			0.405, 0.39	373, 447				

The biosynthesized Ag nanoparticles, hybrid Ag-Co and Ag-Ni nanoparticles in this study displayed optical properties both at room temperature and 70℃. On the other hand, the intensity of absorption varied in each synthesis as a result of the nature of bioreducing agent considered (Table 4.37 & 4.38).

Highest intensity of absorbance with narrow peaks ranging from 1.503-1.061 a.u. were noticed in the spherical nanoparticles capped with the extract of *S. occidentalis* in all precursor concentrations, followed by the spherical nanoparticles formed with the leaf extract of *M. charantia* leaf which displayed maximum absorption intensities with broad peaks of 0.414, 1.061 and 0.66 a.u in 1.0, 2.0 and 3.0 mM $AgNO_3$ solutions respectively. Next in the intensity of absorbance were the spherically shaped silver nanoparticles in which the leaf extract of *Lawsonia inermis* was the bioreducing agent, with the arbitrary broad peaks with intensity values of 0.332 and 0.286 in 2.0 and 3.0 mM precursor solutions respectively. Sharp peak with intensity of absorbance was stronger when *C. indica* reducing agent was used in 1.0 mM $AgNO_3$, followed by stem extract of *Momordica charantia* which showed broad peak of absorbance (0.263 a.u.), *Nicotiana tobacuum* (0.173 a.u.), sharp absorbance peak was also observed in *Hibiscus sabdariffa*-influenced synthesis (0.128 a.u.) and least in *Lawsonia inermis* with broad absorption peak (0.11 a.u.).

The decreasing order in the absorption intensities by nanoparticles prepared from 2.0 mM $AgNO_3$ was observed when the following plant extracts (reducing agents) were utilized: *Lawsonia inermis* (0.332 a.u.) followed by stem extract of *Momordica charantia* (0.258 a.u), *C.indica* leaf (0.215a.u), *Nicotiana tobacuum* (0.19 a.u.) and least in *Hibiscus sabdariffa* (0.128 a.u.). The absoption intensities indicated optical properties of the as-prepared nanoparticles which qualify them as potential materials in optical devices.

The Ag NPs prepared from 3.0 mM $AgNO_3$ precursor solution absorbed in the visible region with the following intensity values when prepared with different plant extracts in a decreasing order of: 0.286 a.u. (Hexagonally shaped nanoparticles with truncated edges formed with *Lawsonia inermis*), 0.214 a.u. (Spherical nanoparticles prepared from *C. indica*), 0.19 a.u. (*Nicotiana tobacuum*), 0.128 a.u. (*Hibiscus sabdariffa*), 0.076 a.u. (*Momordica charantia* stem) and 0.054 a.u. (*Cassytha filiformis* and *Lawsonia inermis*).

In all the varied precursor metal concentrations, the plasmon band resonance showed a red shift around 400 -500 nm, except the nanoparticles formed using the leaf extract of *S. occidentalis* which showed blue shift (380 nm).

4.10 Mechanism of the Reaction

The biomolecules present in the plant extract were ascertained to be responsible for the reduction, capping and stabilisation of the newly formed nanoparticles as shown in the proposed mechanisms:

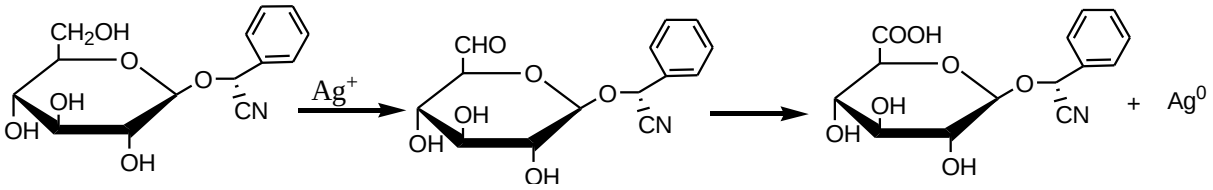

Scheme 1: Bioreduction of silver ion to silver nanoparticles by glycosides

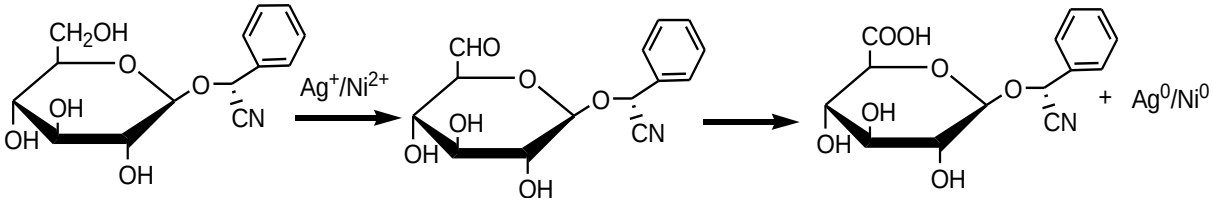

Scheme 2: Bioreduction of silver/nickel ions to silver/nickel nanoparticles by glycosides

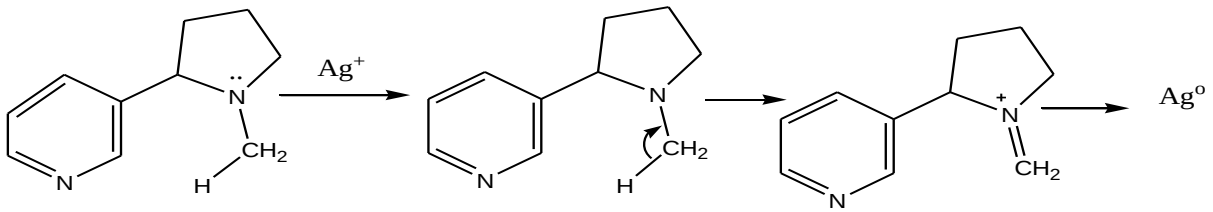

Scheme 3: Bioreduction of silver ion to silver nanoparticles by Alkaloids

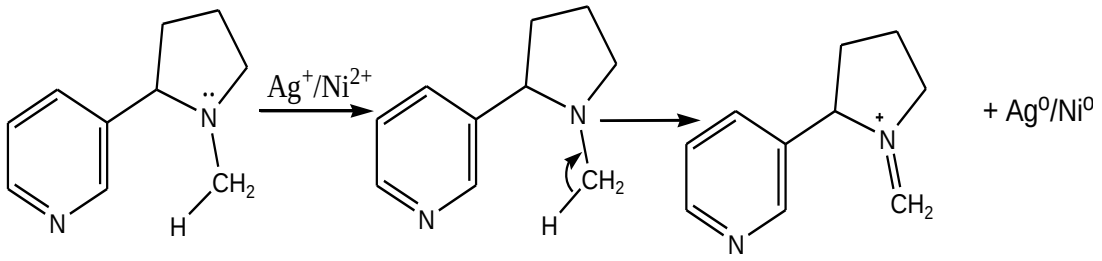

Scheme 4: Bioreduction of silver/nickel ions to silver/nickel nanoparticles by alkaloids

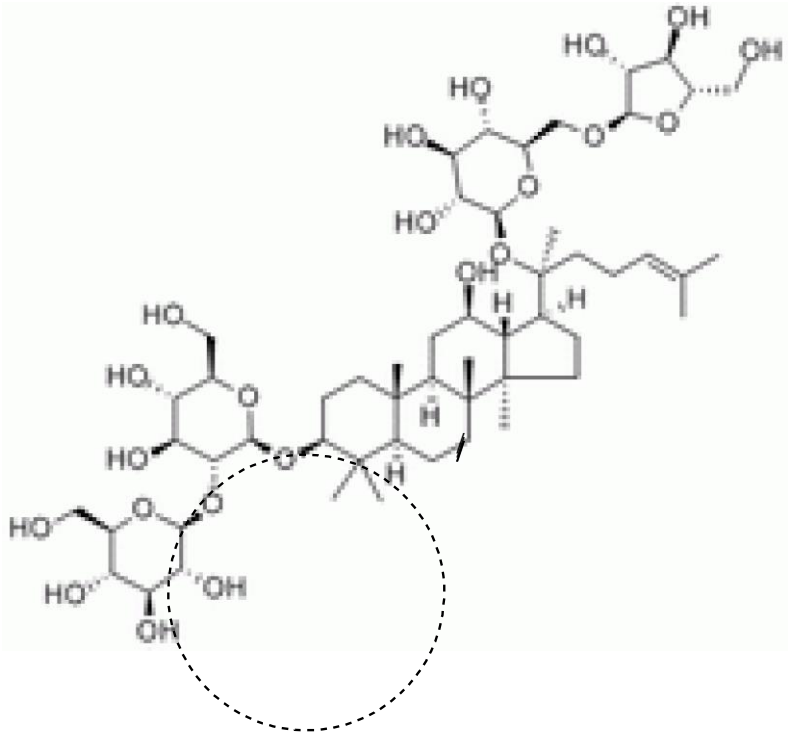

Structure of saponins
Source: Mididea, 2013

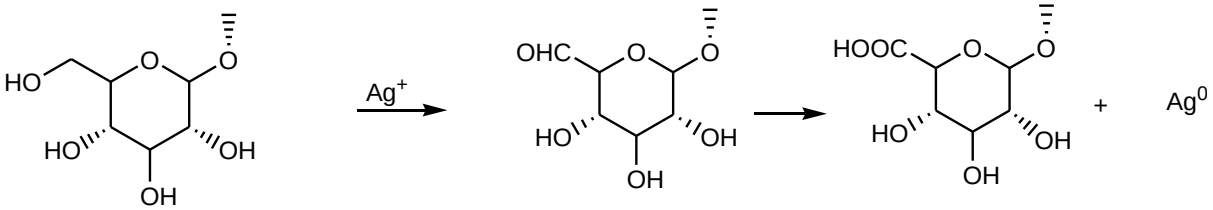

Scheme 5: Bioreduction of silver ion to silver nanoparticles by Saponins

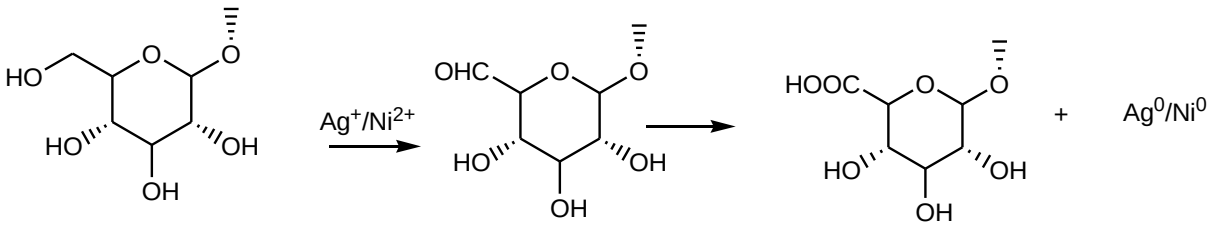

Scheme 6: Bioreduction of silver/nickel ions to silver/nickel nanoparticles by Saponins

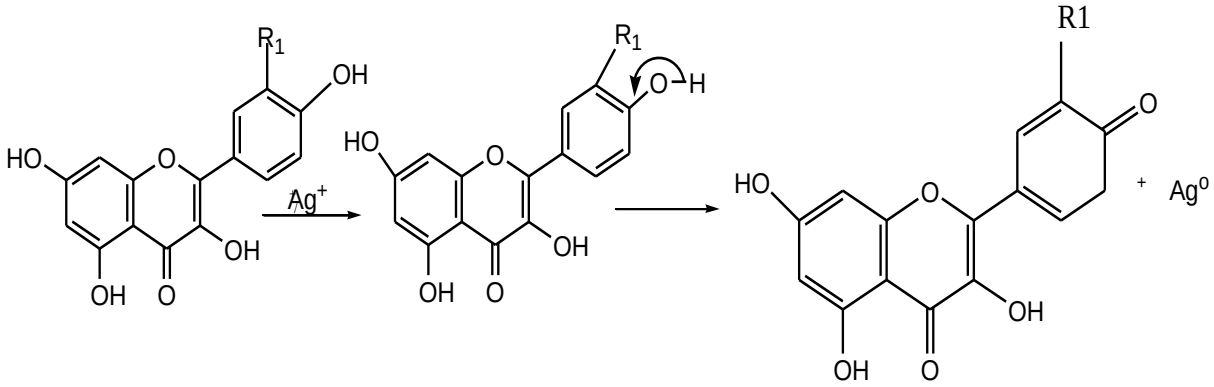

Scheme 7: Bioreduction of silver ion to silver nanoparticles by flavanoids

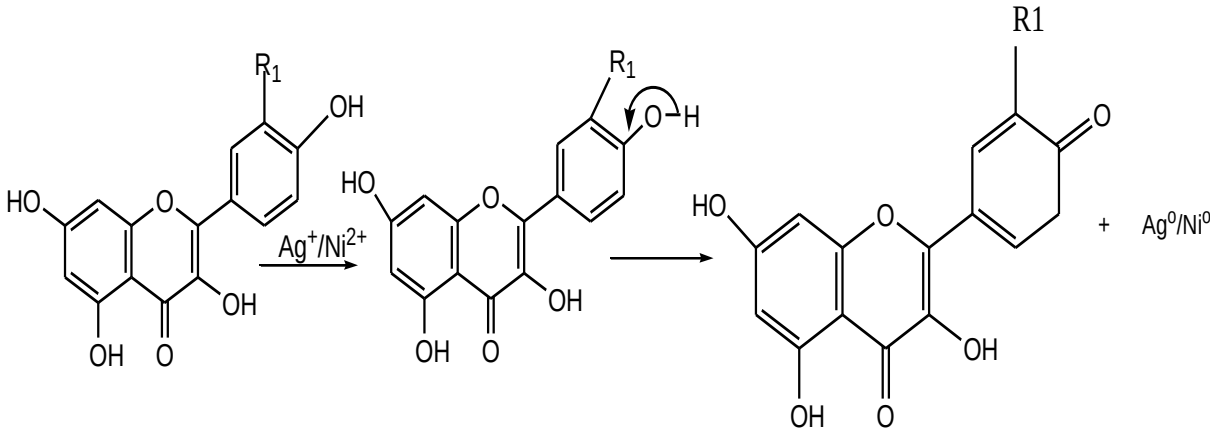

Scheme 8: Bioreduction of silvernickel ions to silver/nickel nanoparticles by flavonoids

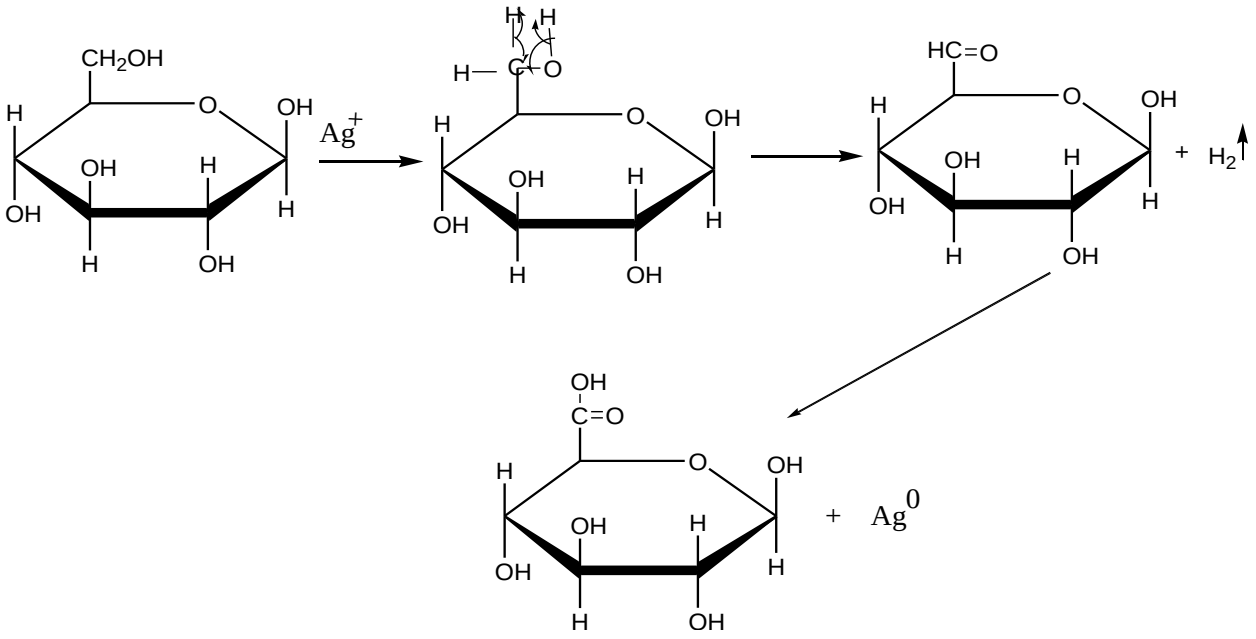

Scheme 9: Bioreduction of silver ion to silver nanoparticles by carbohydrates

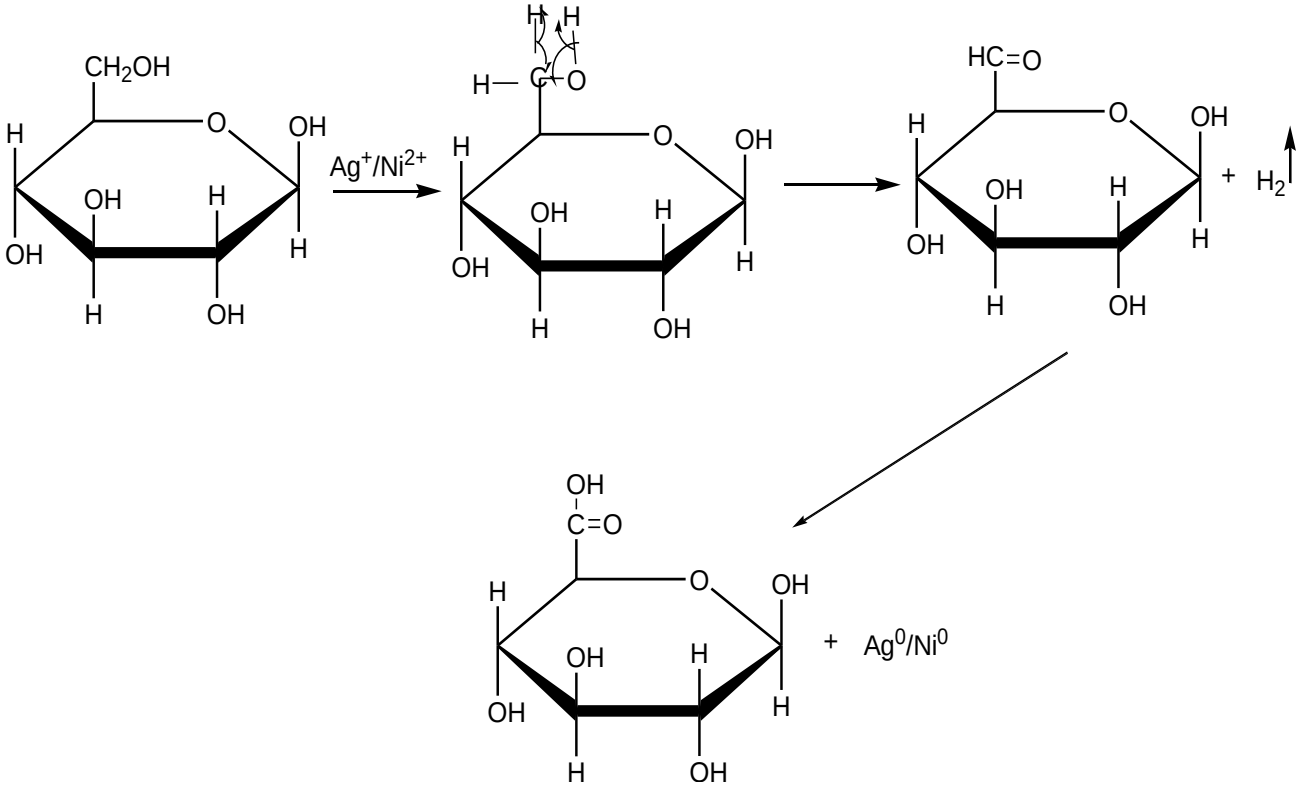

Scheme 10: Bioreduction of silver/nickel ions to silver/nickel nanoparticles bcarbohydrates

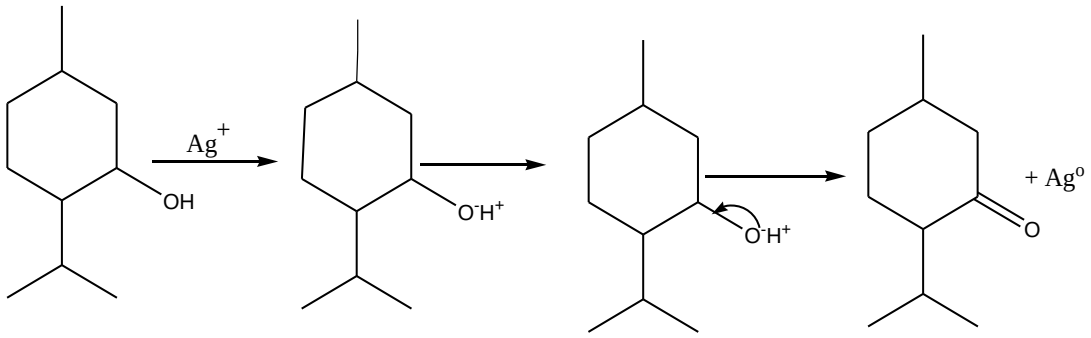

Scheme 11: Bioreduction of silver ion to silver nanoparticles by terpenoids

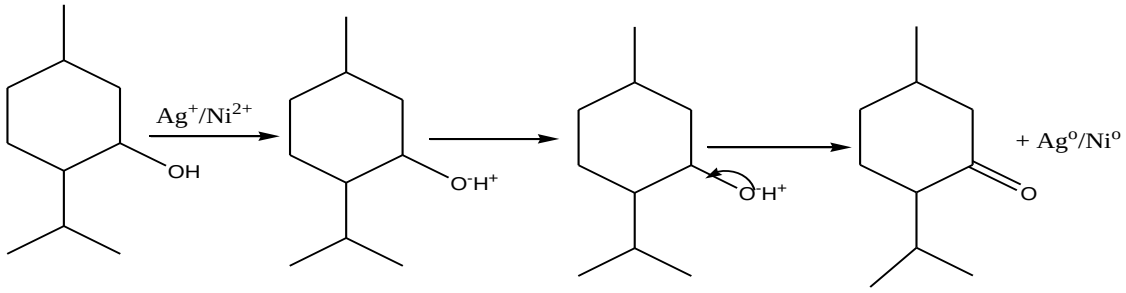

Scheme 12: Bioreduction of silver/nickel ions to silver/nickel nanoparticles by terpenoids

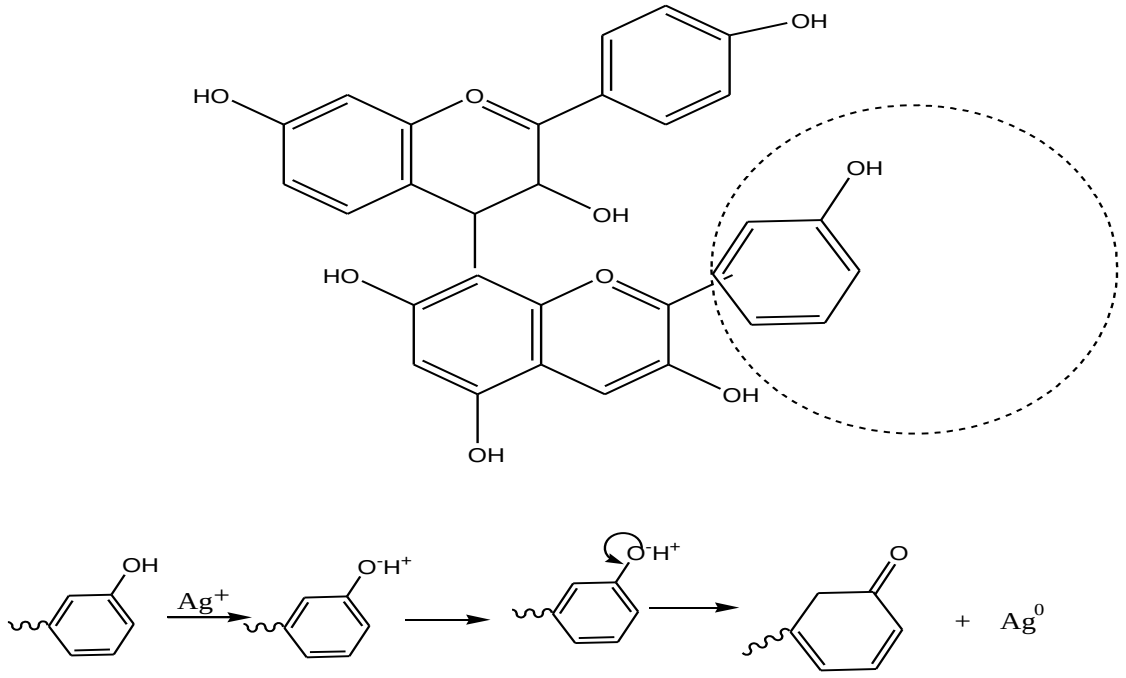

Scheme 13: Bioreduction of silver ion to silver nanoparticles by tannins

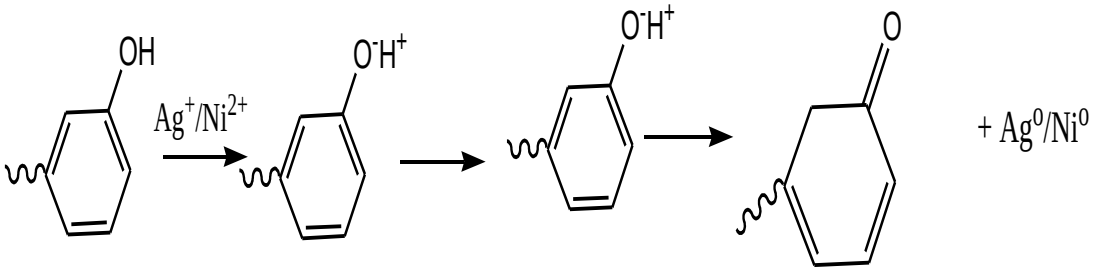

Scheme 14: Bioreduction of silver/nickel ions to silver/nickel nanoparticles by tannins

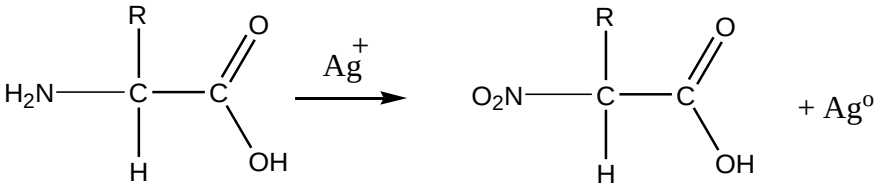

Scheme 15: Bioreduction of silver ion to silver nanoparticles by proteins

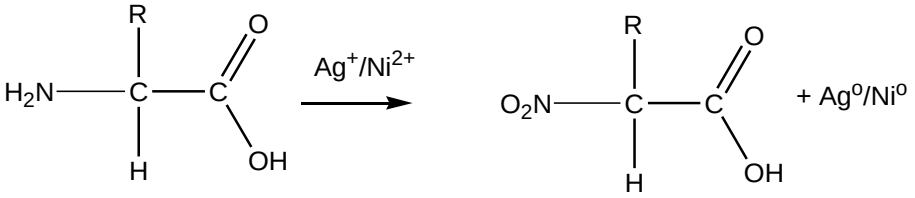

Scheme 16: Bioreduction of silver/nickel ions to silver/nickel nanoparticles by proteins

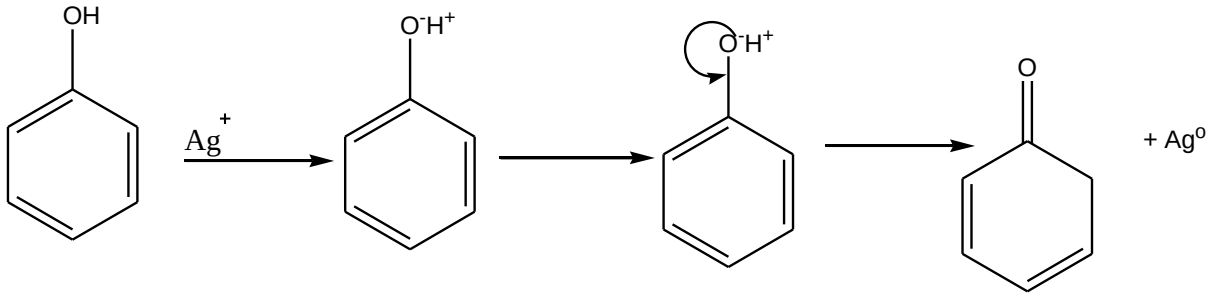

Scheme 17: Bioreduction of silver ion to silver nanoparticles by phenols

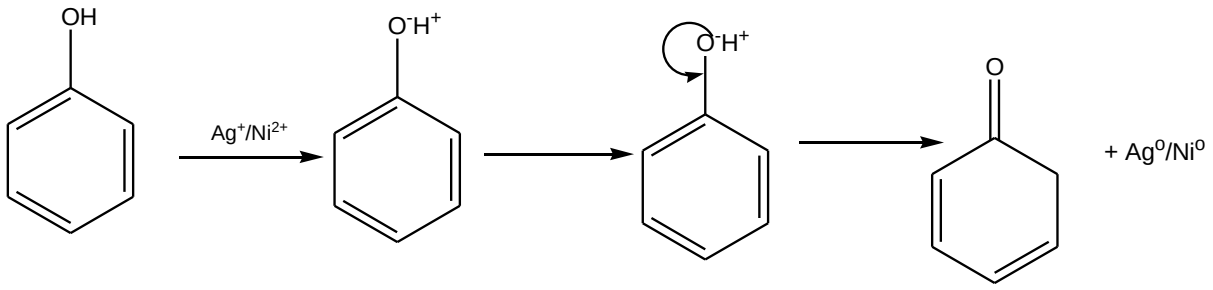

Scheme 18: Bioreduction of silver/nickel ions to silver/nickel nanoparticles by phenols

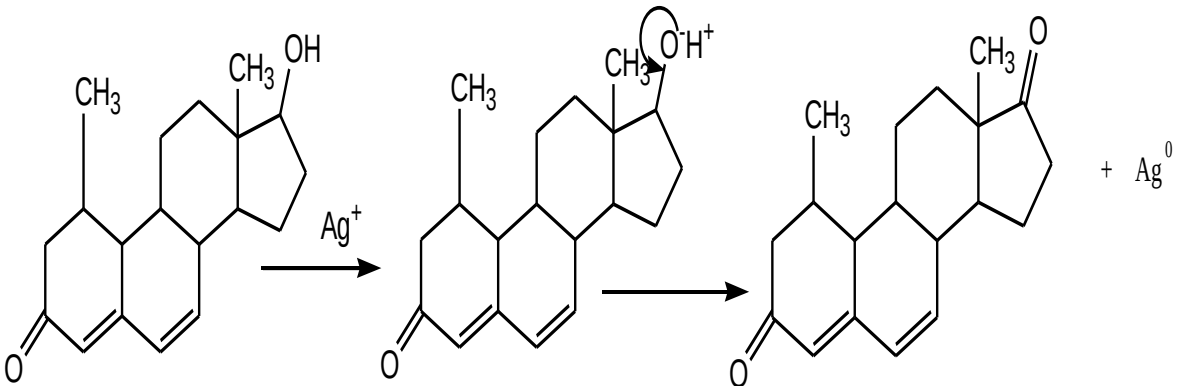

Scheme 19: Bioreduction of silver ion to silver nanoparticles by steroids

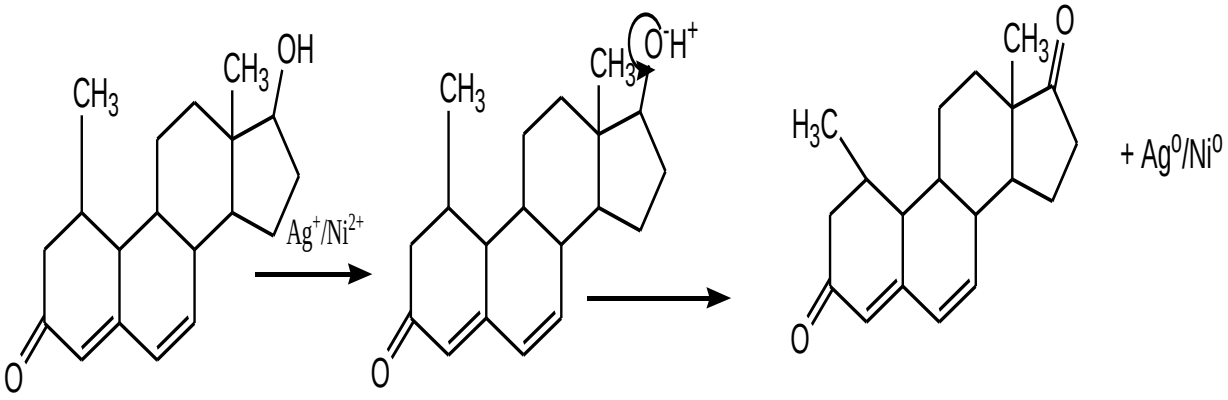

Scheme 20: Bioreduction of silver/nickel ions to silver/nickel nanoparticles by steroids

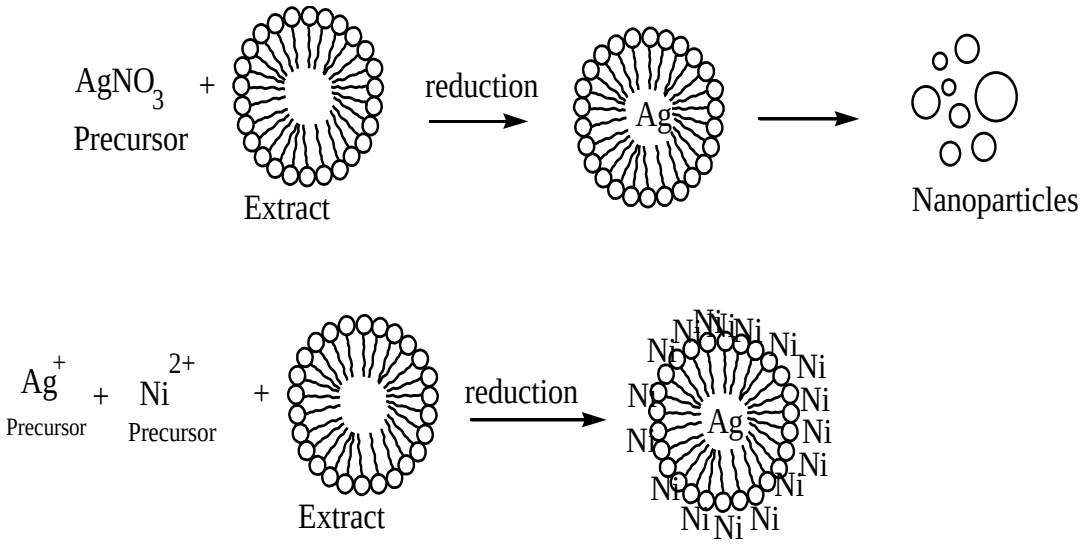

Scheme 21: Schematic illustration for the deduced process of Ag and Ag-Ni nanoparticles formation.

4.11 Results of the Optical (PL) Emission Studies

4.11.1 Optical (PL) Properties of Ag NPs Formed using *C. indica* Leaf Extract

Figure 4.96 is the photoluminescence (PL) spectrum of the as-prepared Ag nanoparticles under *C. indica*-influenced synthesis *at* 70℃ using 2.0 mM precursor solution.

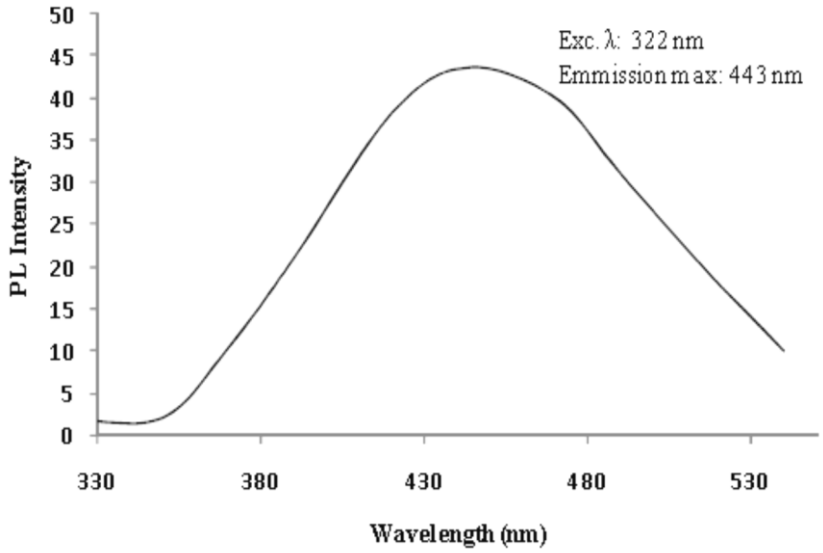

Figure 4.96: The PL emission spectrum of Ag NPs synthesized using *Canna indica* leaf extract and 2.0 mM $AgNO_3$ solution at 70℃

The PL spectrum was characterized by the presence of a single emission band at 443 nm with strong intensity, attributed to deep trap emission (Wageh, 2007). The emission was independent of excitation wavelength, which agreed with Frank Condon principle (Zielinski & Shalhoub, 1986). For an excitation at 322 nm, the Ag nanoparticles synthesized exhibited an emission at 443 nm. The uniform emission peaks (400-450 nm) also suggested that the Ag NPs was of good quality surfaces and interface properties (Pabst & Gregorová, 2007).

4.11.2 Optical (PL) Properties of Bimetallic Ag-Co Nanoparticles formed using *C. indica* Leaf Extract

The PL emission spectrum of *C.indica*-influenced silver allied nanoparticles prepared using 2.0 mM precursor mixture solution at 70℃ is presented in Figure 4.97.

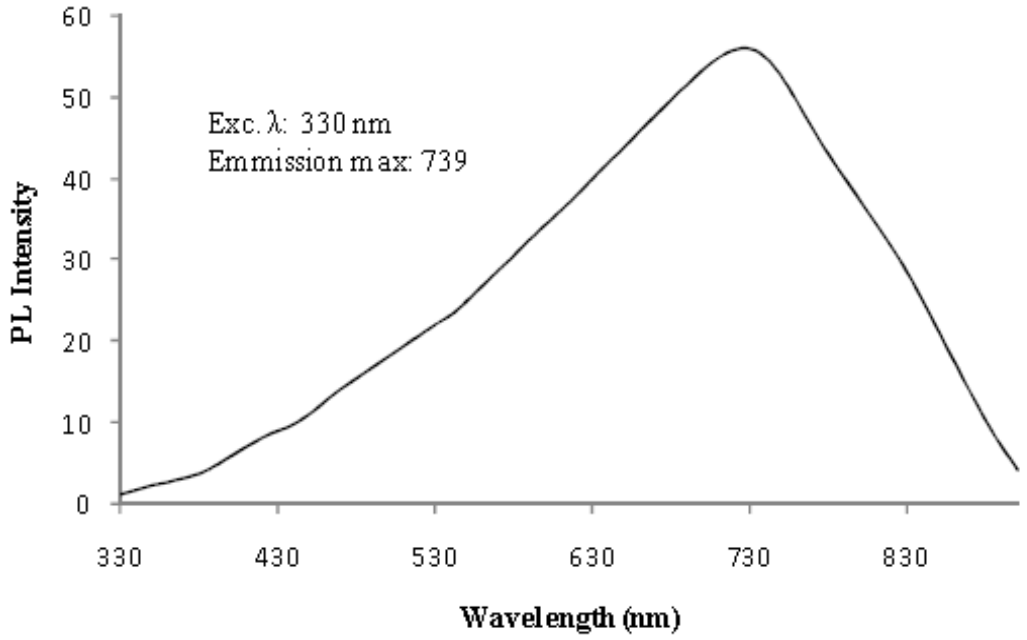

Figure 4.97: The PL emission spectrum of Ag-Co bimetallic NPs synthesized using *Canna indica* leaf extract and 2.0 mM precursor mixture at 70℃

The hybrid nanoparticles excited at 330 nm was characterized by a single emission peak. The red shift in the fluorescence spectrum was observed at 739 nm due to the surface of the hybrid nanoparticles predominantly occupied by Co atom. The existence of a single emission peak in the longer wavelength band region is probably the quantum confinement of electron (Rahim, Hashim & Ali, 2011).

Moreover, the observed higher emission wavelength suggested stokes shift. The sturdy peak intensity displayed by the silver allied nanohybrid was a consequence of the allowed vibrational transition in the nanocluster (Condon, 1928). This corroborated the morphological core-shell structure of Ag-Co in which Ag was masked by Co particle in Figure 4.14(b).

4.11.3 Optical PL Emission Properties of Ag NPs Formed using *N. tobacuum* Leaf Extract

Figure 4.98 depicts the optical (PL) emission spectrum of Ag NPs obtained by reacting the leaf extract of *N. tobacuum* and 2.0 mM $AgNO_3$ solution at 70℃.

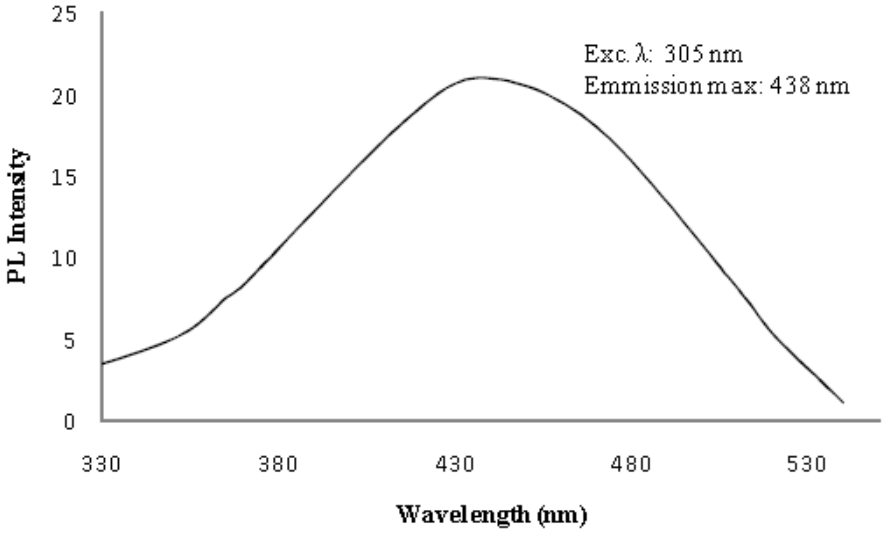

Figure 4.98: The PL emission spectrum of Ag NPs synthesized using *N. tobacuum* leaf extract and 2.0 mM $AgNO_3$ solution at 70℃

Emission of quantum yield was noticed. Monodispersity in particles was as a result of emission during vibrational relaxation to the energy ground state. A single emission peak of 438 nm was portrayed in the emission spectrum excited at 305 nm of the as-prepared nanoparticles. The intensity of emission was low compared with the emission spectra of *C. indica* aided Ag NPs synthesis.

4.11.4 Optical (PL) Properties of Ag NPs Formed using the Extract of *M. charantia* Stem

Figure 4.99 is the PL emission spectrum of Ag nanoparticles obtained by the reaction of *M. charantia* stem extract and 2.0 mM metal precursor solution at 70℃.

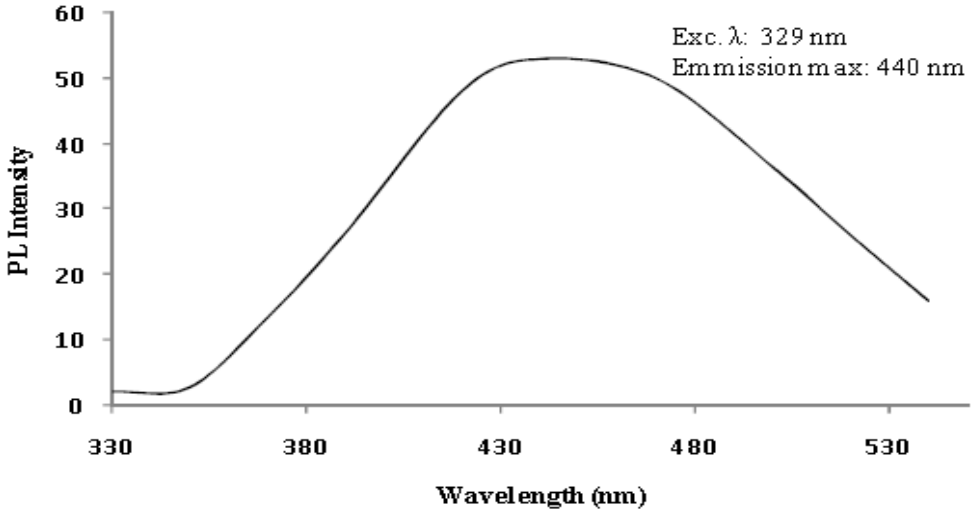

Figure 4.99: The PL emission spectrum of Ag NPs synthesized using *M. charantia* stem extract and 2.0 mM $AgNO_3$ solution of at 70℃

The spectrum indicated the excitation and emission wavelengths of nanosilver. The spectroscopy analysis was characterized with a single and strong intensity peak. The PL was excited at 322 nm wavelength with an emission wavelength was noticed at 443 nm.

4.11.5 Optical (PL) Properties of Ag-Co Bimetallic Nanoparticles formed using *M. charantia* Leaf Extract

The PL emission spectrum of silver allied nanohybrid particles formed by the reaction of *M. charantia* leaves with 2.0 mM metal precursor mixture is elucidated in Figure 4.100.

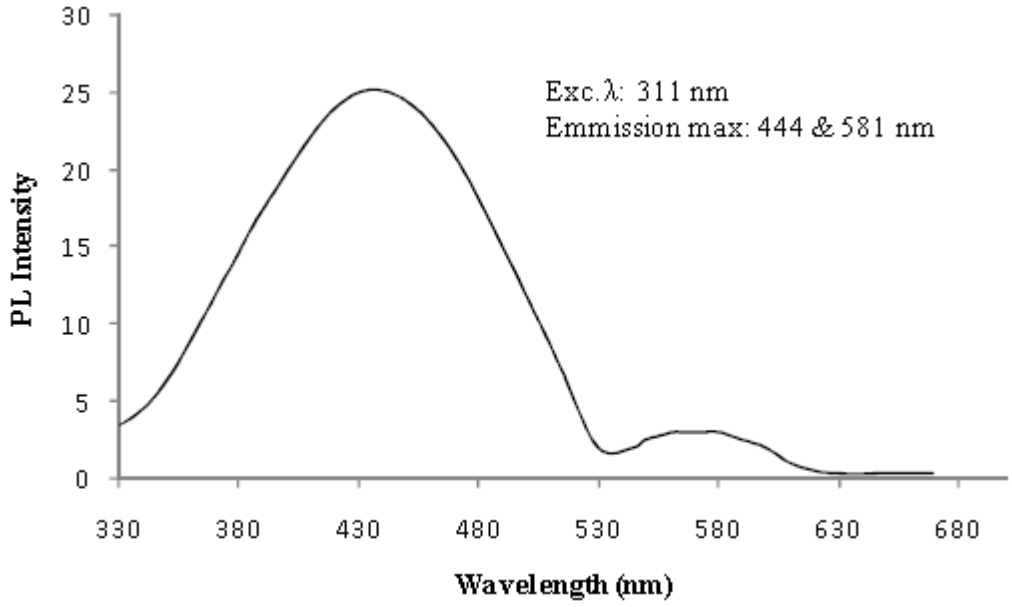

Figure 4.100: The PL spectrum of Ag-Co bimetallic nanoparticles synthesized using *M. charantia* leaf extract and 2.0 mM precursor mixture at 70℃

The bimetallic nanoparticles excited at 311 nm resulted in multiply peaks of fluorescence emission. The shorter emission wavelength was fixed at 444 nm for Ag, while the longer emission wavelength at 581 nm. The emissions of two fluorescence peaks were due to the vibrational relaxation of electrons in motion. The red shifted emission wavelength also indicated vibrational relaxation of phonons. Hence, this stimulated the electrons to lower energy levels.

4.11.6 Optical (PL) Properties of Ag-Ni Bimetallic Nanoparticles Formed using the Extract of *Cassytha filiformis* (Whole Part)

The fluorescence properties of bimetallic Ag-Ni nanoparticles biosynthesized from the reaction of *Cassytha filiformis* plant extract and 2.0 mM metal precursor are depicted in Figure 4.101.

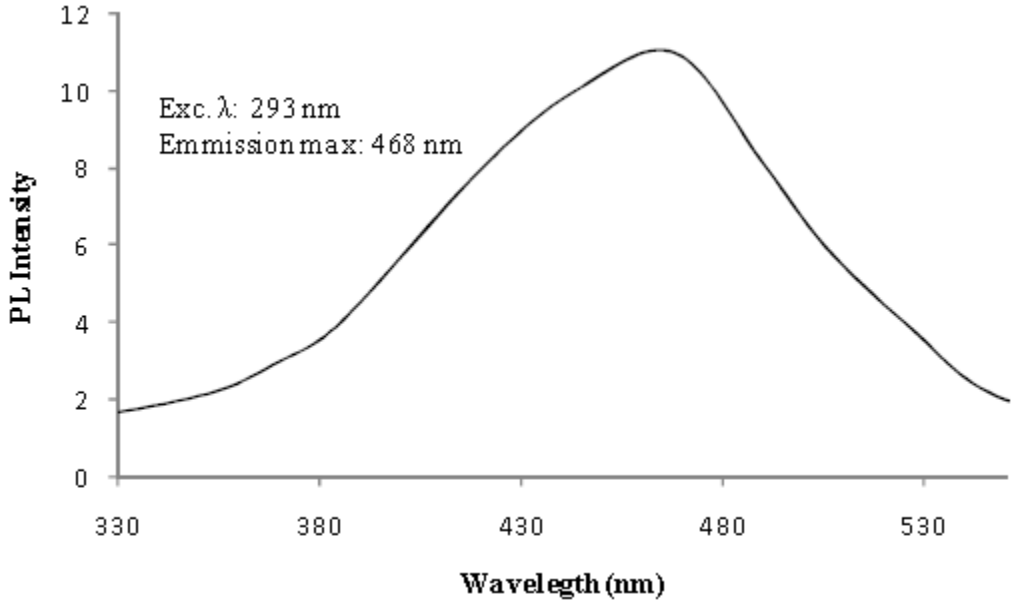

Figure 4.101: The (PL) spectrum of Ag-Co bimetallic nanoparticles synthesized using *C. filiformis* leaf extract and 2.0 mM precursor mixture

The investigation showed an excitation wavelength of the hybrid nanocluster at 293 nm. PL emission with maximum intensity was observed at 468 nm. A single strong emission peak suggests an application in optical materials.

4.11.7 Optical (PL) Properties of Ag-Co Bimetallic Nanoparticles Formed using *Cassytha filiformis* Plant Extract

The PL spectrum of Ag NPs synthesized using *C. filiformis* leaf extract and 2.0 mM $AgNO_3$ precursor mixture at 70℃

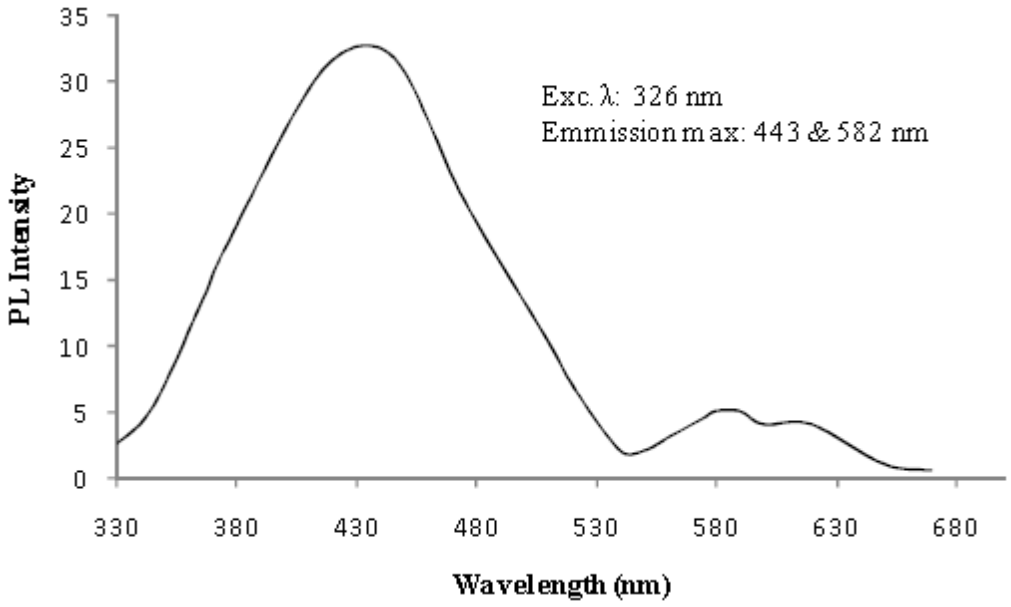

Figure 4.102**:** The PL spectrum of Ag NPs synthesized using *C. filiformis* leaf extract and 2.0 mM $AgNO_3$ precursor mixture at 70℃

An enhanced optical property was noticed in the PL emission spectrum of Ag-Co nanohybrid, obtained in the reaction between the extract of *Cassytha filiformis* and 2.0 mM precursor mixture at 70℃. Multiple peaks were observed when the nanocluster was excited at a wavelength of 328 nm. Stokes shift was also obeyed as the emitted wavelengths of 443 nm (Ag) and 582 nm (Ag-Co) were greater than the excitation wavelength. The electrons were also stimulated to the lower energy level. The red shifted maximum wavelengths were emitted in the yellow/orange region of the PL spectrum (Shinde, 2013).

4.11.8 Optical (PL) Properties of Ag-Ni Bimetallic Formed using *Hibiscus sabdariffa* Calyces

An improved optical (PL) emission is observed in the PL of hybrid of Ag-Ni nanocluster as shown in Figure 4.103.

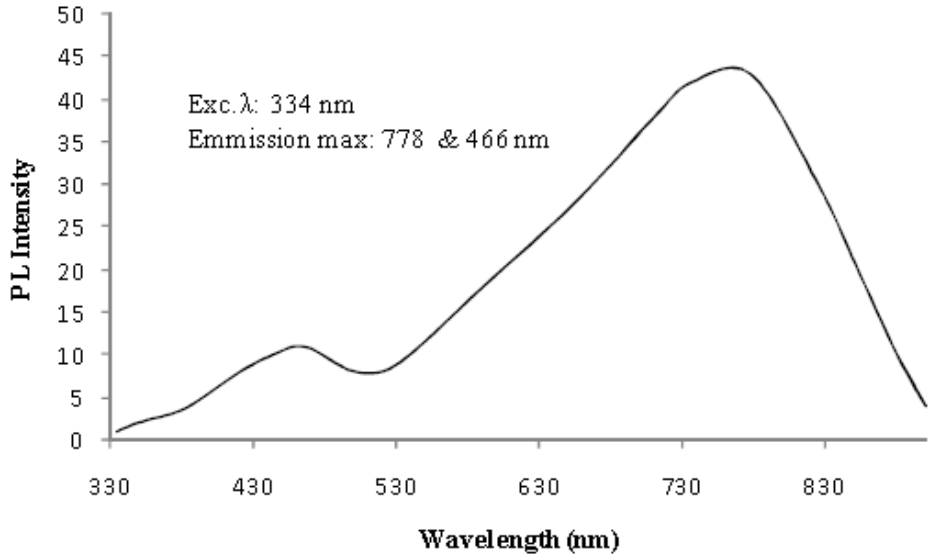

Figure 4.103: The PL spectrum of Ag NPs synthesized using *H. sabdariffa* (Calyces) extract and 2.0 mM $AgNO_3$ Solution at 70℃

The excitation of the hybrid nanoparrticles at 334 nm led to two excitation peaks 466 nm (Ag) and 778 nm (Ag-Co). The PL spectrum depicted an alloy hybrid formation. The hybrid was considered to be cobalt enriched in surface. The difference between the excitation and emission wavelength was an indication that Stoke principle was obeyed.

4.11.9 Optical (PL) Properties of Ag NPs Formed using *Lawsonia inermis* Leaf Extract

Optical property of the monometallic Ag nanoparticles prepared using *Lawsonia inermis* extract and 3.0 mM $AgNO_3$ at 70℃ is displayed in Figure 4.104.

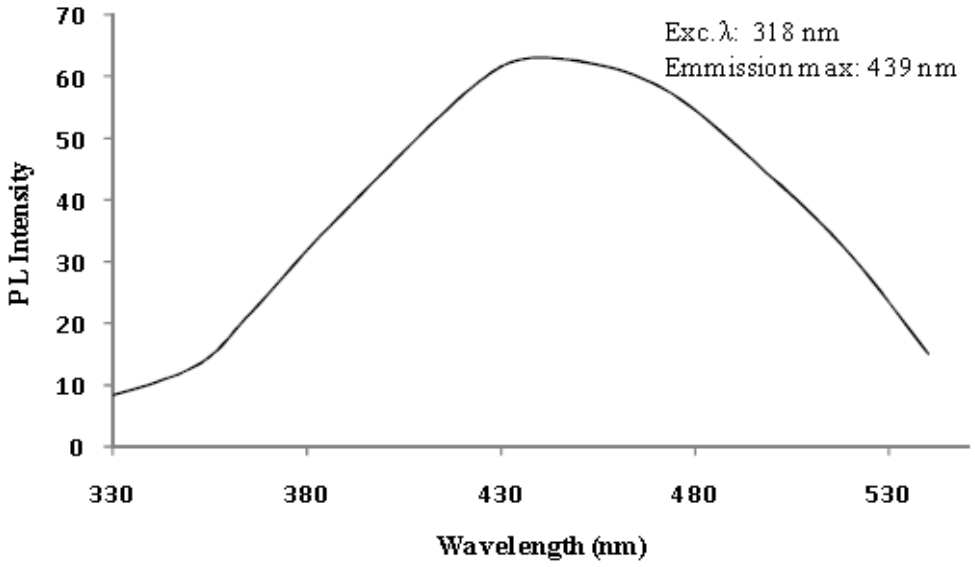

Figure 4.104: The PL spectrum of Ag NPs synthesized using *Lawsonia inermis* leaf extract and 3.0 mM $AgNO_3$ solution at 70℃

It was confirmed by the single emission peak at the wavelength of 429 nm when excited at 318 nm. Near level of uniformity observed was an indication of monodispersed nanosilver formation (Condon, 1928), as the broad peak signified different particle sizes.

4.11.10 Comparison of Optical (PL) Properties in Ag NPs formed using Different Plant Extracts

Figures 4.105, 4.106 and 4.107 are the combined PL spectra showing emission comparison among the monometallic Ag nanoparticles prepared from different biomass at 70℃.

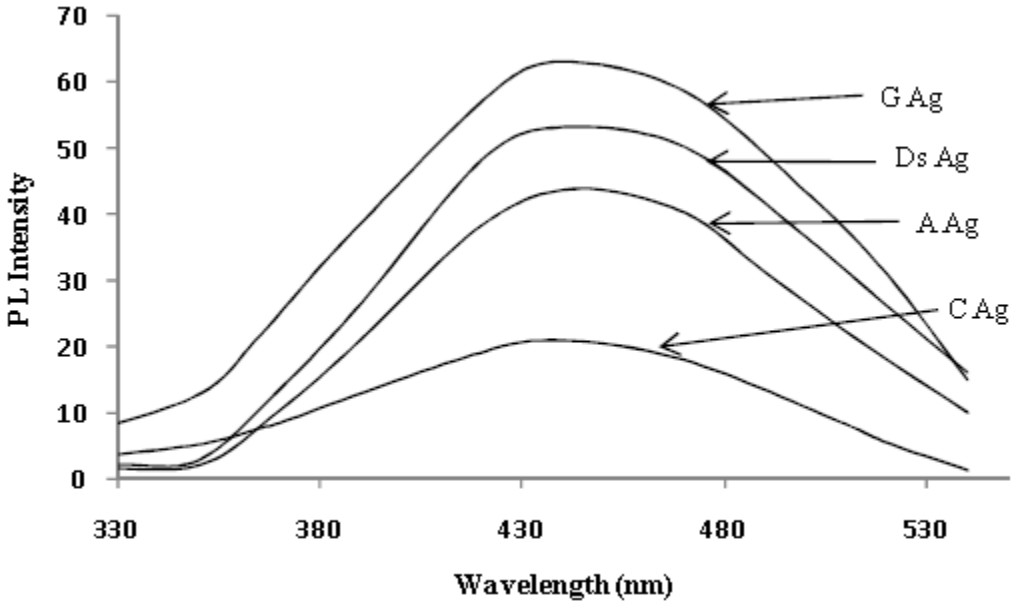

Figure 4.105: The PL emission spectra of Ag NPs formed using different plant extracts at 70^{o}C

A Ag = Silver NPs prepared using *C. indica* as a reducing/capping agent at 70℃, C Ag = Silver NPs prepared using *N. tobacuum* as a reducing/capping agent at 70℃, D_s Ag = Silver NPs prepared using *M. charantia* stem as a reducing/capping agent at 70℃, G Ag = Silver NPs prepared using *L. inermis* as a reducing/capping agent at 70℃

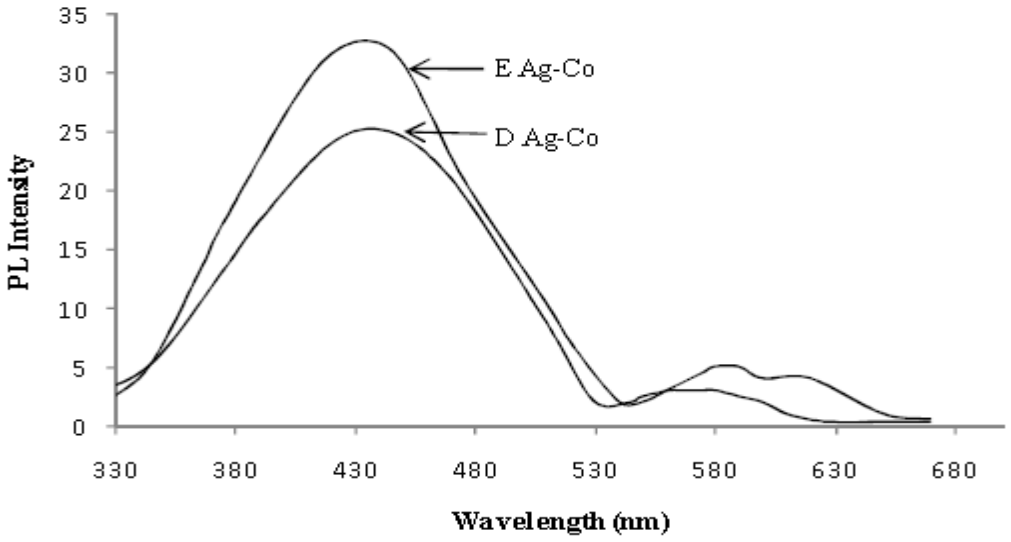

Figure 4.106: The PL emission spectra between Ag-Co hybrid nanoparticles synthesized using *M. charantia* and *C. filiformis* leaf extracts at 70^{o}C

D Ag-Co = Bimetallic silver/cobalt NPs prepared using *M. charantia* as a reducing/capping agent at 70℃, E Ag-Co = Bimetallic silver/cobalt NPs prepared using *C. filiformis* as a reducing/capping agent at 70℃

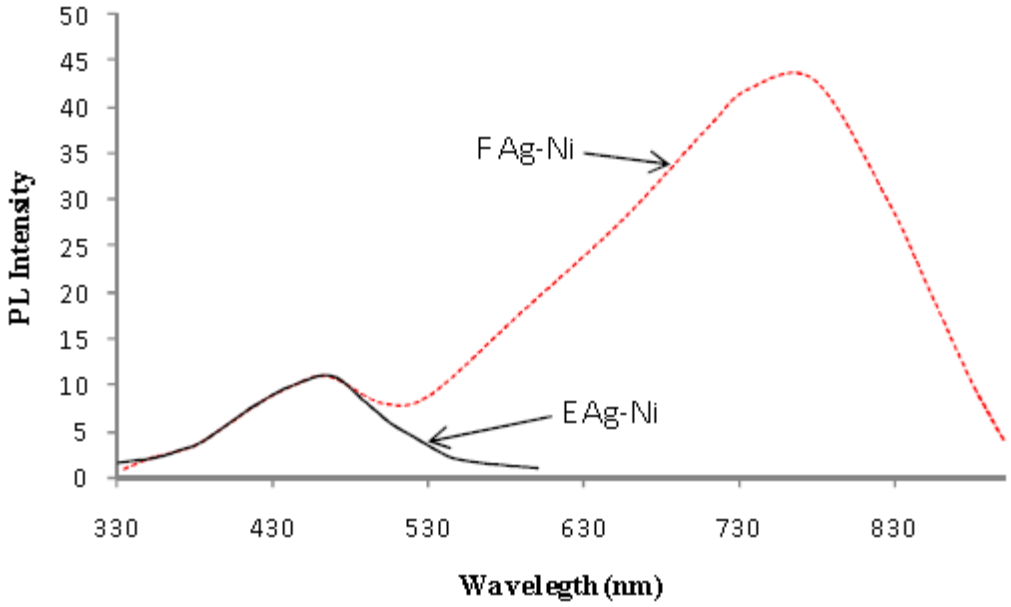

Figure 4.107: The PL emission spectra between Ag-Ni hybrid nanoparticles synthesized using *C. filiformis* and *H. sabdariffa* leaf extracts at 70^{o}C

E Ag-Ni = Bimetallic silver/nickel NPs prepared using *C. filiformis* as a reducing/capping agent at 70℃, F Ag-Ni= Bimetallic silver/nickel NPs prepared using *H. sabdariffa* as a reducing/capping agent at 70℃,

Emission took place in all the nanocluster prepared with different plant extracts considered in this study; however, the intensity of emission varied in all the nanoparticles from each plant. All the syntheses using different reducing agents (plant extracts) displayed near uniform emission (400-430 nm), irrespective of the excitation wavelengths. This suggests good quality surfaces and interface properties of the nanoparticles (Pabst & Gregorová, 2007). Moreover, it can be inferred that the biosynthesized nanoparticles were within quantum realm.

The PL emission spectra also indicated some levels of monodispersity in the bionanoparticles. Nevertheless, Franck Condon principle was obeyed during the simultaneous changes in the electronic and vibrational energy levels of the particles during emission of photon i.e. vibronic transitions. Highest emission intensity was exhibited in the Ag nanoparticles in which *L. inermis* acted as the reducing/capping agent. This is the effect of chromophores present in the plant which is responsible for ($\pi \longrightarrow \pi*, n \longrightarrow \pi*$) transition in the nanocluster. On the contrary, Ag NPs produced from *N. tobacuum* demonstrated lowest intensity in its emission indicating low optical activity and may plausibly due to low concentration of the nanoparticles formed.

PL emission properties were also observed in the hybrid syntheses. The observed emission spectrum in Figure 4.100 is an indication of vibronic transitions as a result of overlap in two wave functions displayed during electronic transition in the vibrational energy levels of the biosynthesized nanoparticles (Condon, 1928). The comparison of emission intensities in Ag-Co of *H. sabdariffa* and *M. charantia* reducing agents revealed that the former was of more localized surface as shown in its higher intensity of emission than the latter. However, *H. sabdariffa*-induced Ag-Ni nanohybrid particles displayed higher emission intensity when compared with Ag-Ni nanoparticles prepared from *C. filiformis,* as the plant extract contained fluorophores which is responsible for its additional conjugation.

Hence, the PL emission intensity (optical property) of the as-prepared nanoparticles is in the decreasing order of G Ag, Ds Ag, F Ag-Ni, A Ag-Co, A Ag, E Ag-Co, D Ag-Co, C Ag and E Ag-Ni. Interestingly, according to Kumbhakar, the optical property of nanorod present in Ag-Co nanoparticles synthesized with the extract of *C. indica* is an indicator for its application in optoelectronic device (Kumbhakar, Ray & Stepanov, 2014).

4.11 Antimicrobial Activity of the Biosynthesized Nanoparticles

Results of the preliminary screening using agar diffusion test to identify the inhibitory activity of Ag, Ag-Ni and Ag-Co nanoparticles on microorganisms at different metal precursor concentrations are presented in Figures 4.108- 4.112. General comparison of inhibition zones of Ag and Ag-Ni bimetallic nanoparticles among different plant extracts considered for this study is depicted in Figure 4.113.

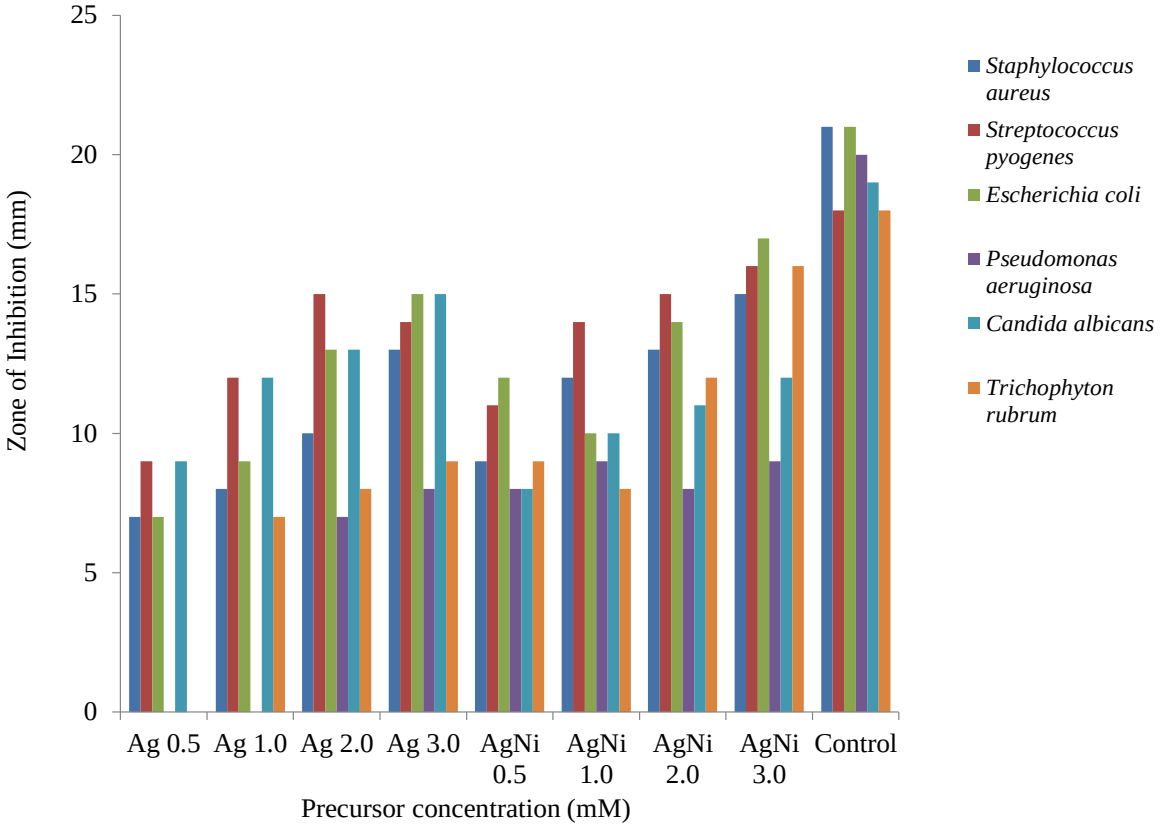

Figure 4.108: Comparison of inhibition zones between Ag Nps and Ag-Ni bimetallic nanoparticles synthesized using *C.indica* leaf extract

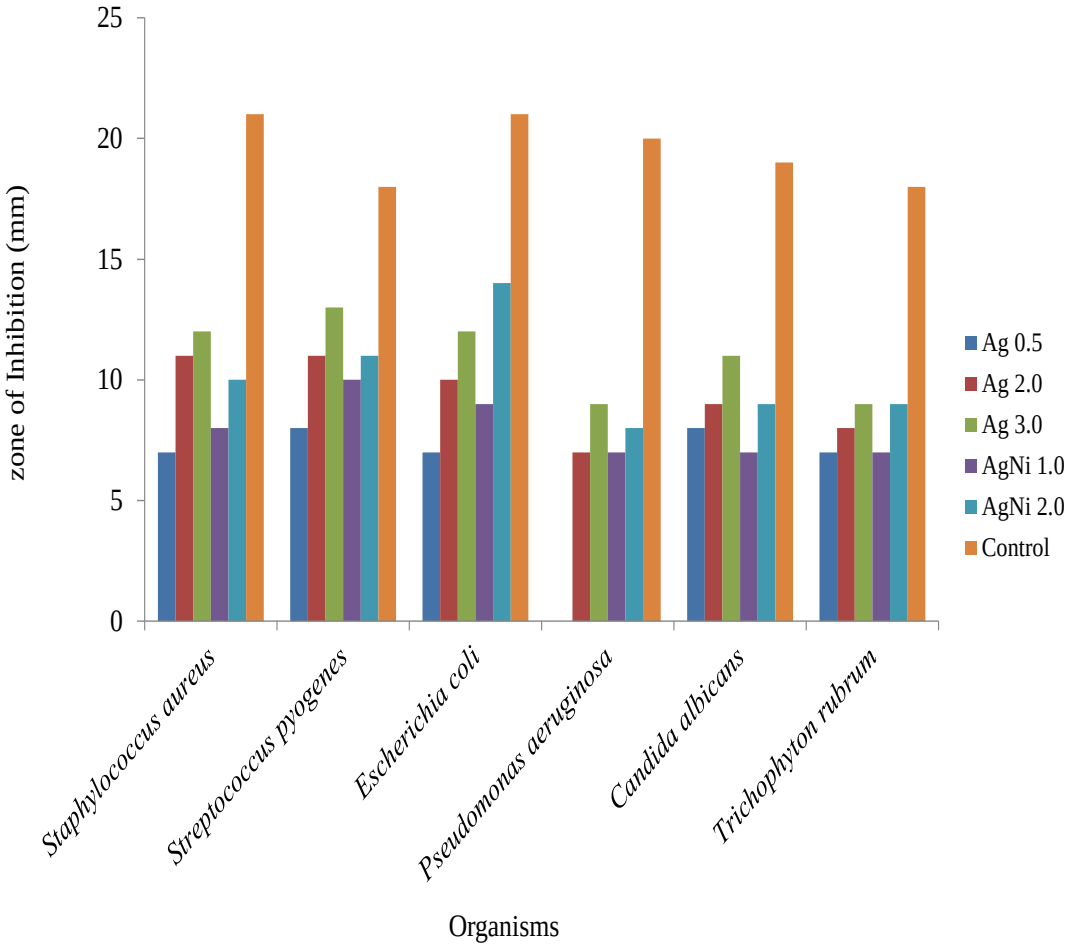

Figure 4.109: Comparison of inhibition zones between Ag NPs and Ag-Ni bimetallic nanoparticles synthesized at varied $AgNO_3$ concentrations using *S. occidentalis* leaf extract

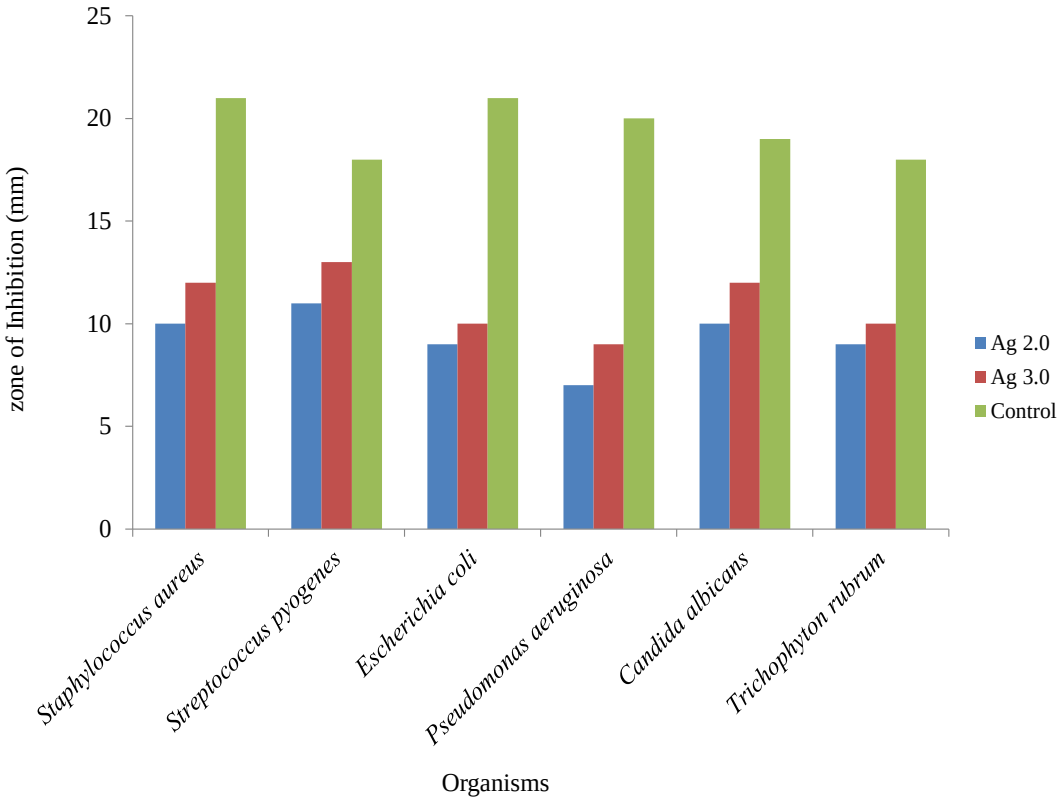

Figure 4.110: Comparison of inhibition zones between Ag NPs and Ag-Ni bimetallic nanoparticles synthesized at varied $AgNO_3$ concentrations using *N.tobacuum* leaf extract

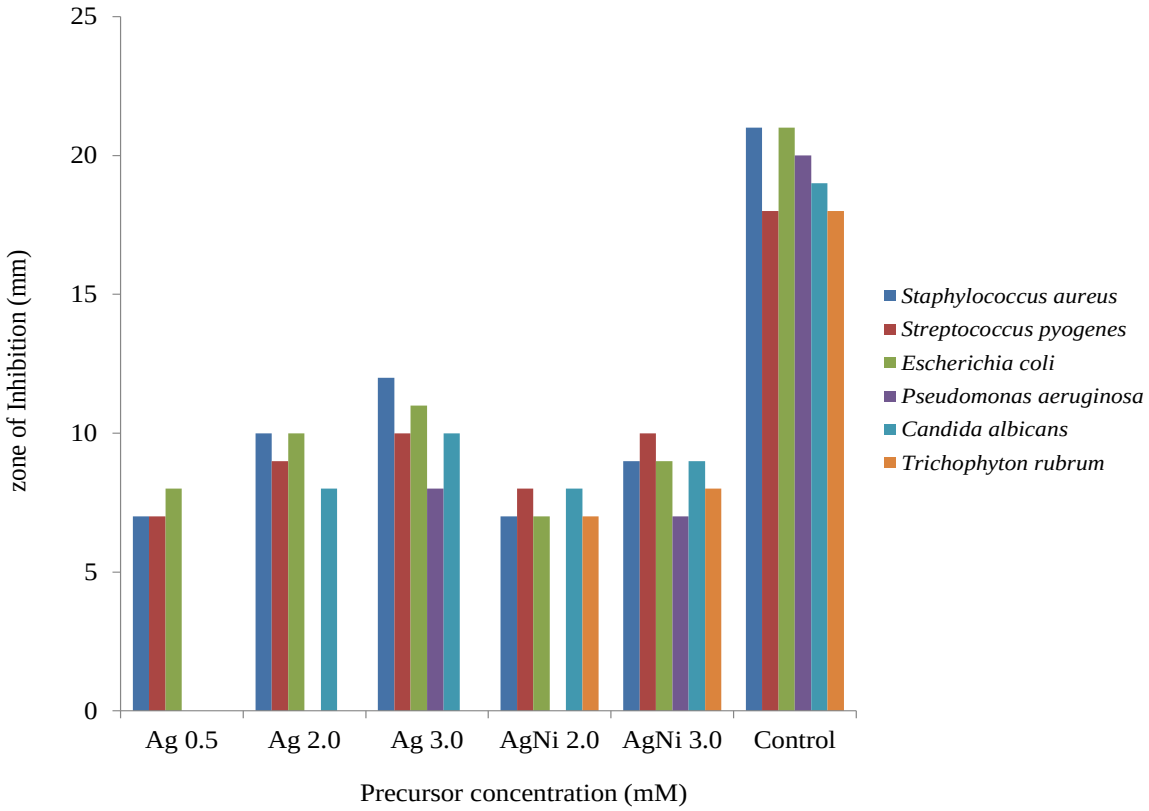

Figure 4.111: Comparison of inhibition zones between Ag NPs and Ag-Ni bimetallic nanoparticles synthesized at varied $AgNO_3$ concentrations using *C. filiformis* leaf extract

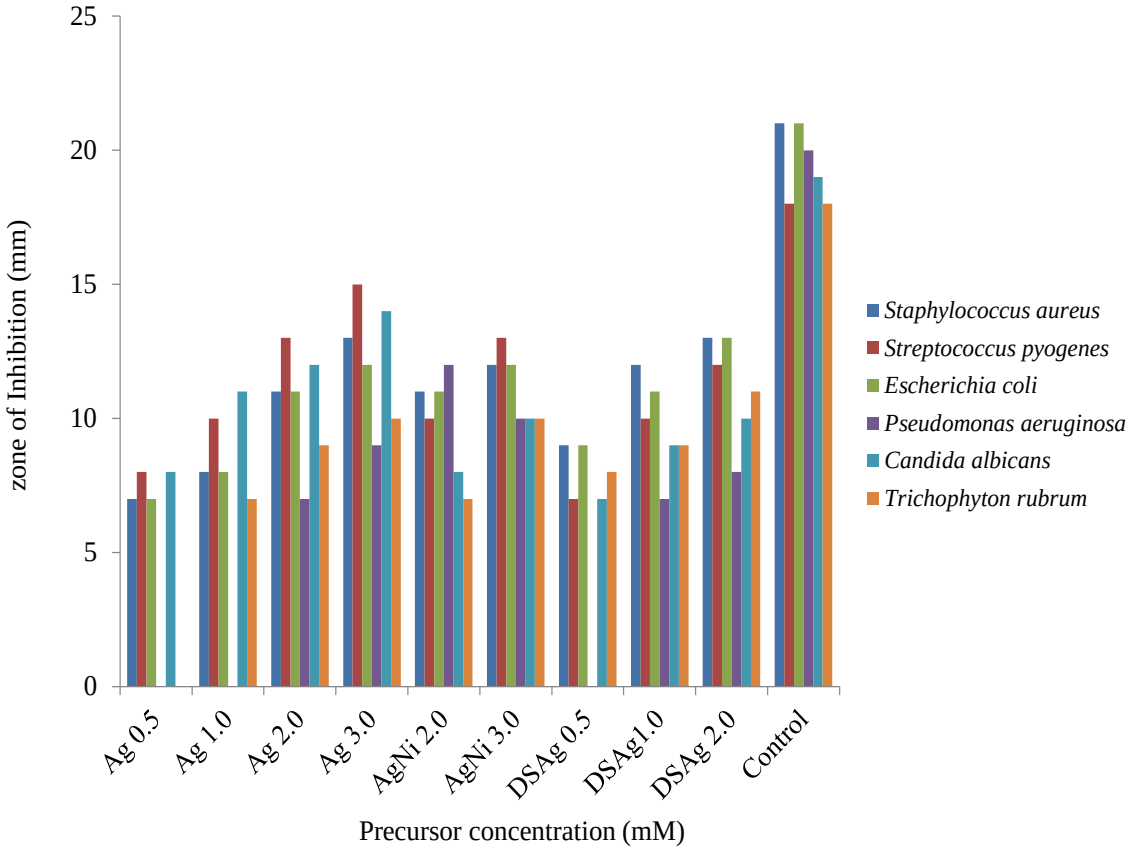

Figure 4.112: Comparison of inhibition zones between Ag Nps and Ag-Ni bimetallic nanoparticles synthesized at varied $AgNO_3$ concentrations using the extracts of *Momordica charantia* leaf and stem (DsAg)

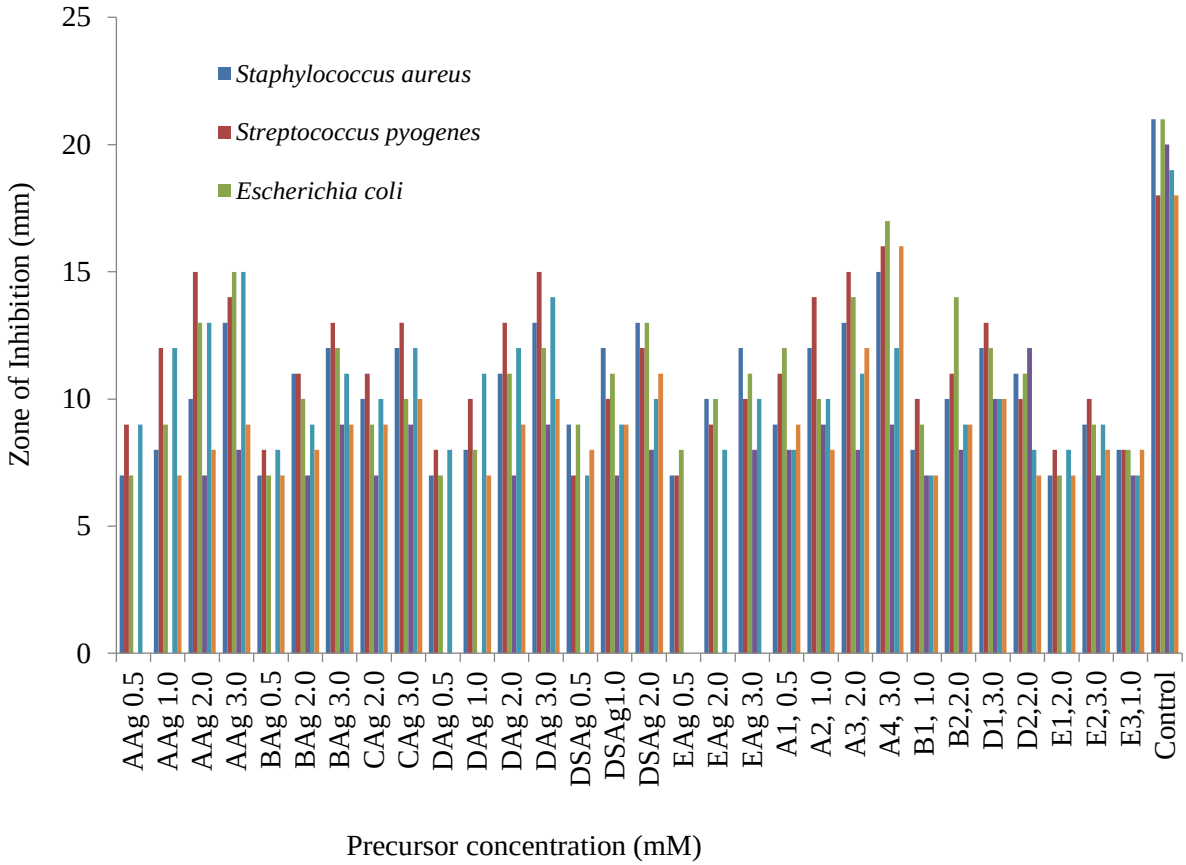

Figure 4.113: Comparison of Ag NPs and Ag-Ni nanohybrid zones of inhibition among microbes using different plant extracts, A= *Canna indica, B= Senna occidentalis,* C = *Nicotiana tobacuum,* D = *Momordica charantia leaf,* D_s = *Momordica charantia* stem, E = *Cassytha filiformis*, A2, A4, B2, D2 and E2= Ag-Ni hybrid

The test showed that the activity of the biosynthesized silver monometallic and Ag-Ni nanoparticles were based on the size of zones of inhibition in millimetre (mm) (See Appendices). Agar diffusion test revealed that the nanoparticles possessed antibacterial and antifungal properties. However, the bionanoparticles showed zones of inhibition to a reasonable level. Interestingly, screened nanoparticles exhibited activities on the organisms at higher concentration (3.0 mM) by increasing the inhibition zones. It was also observed that the silver nanocluster synthesized using the plant extracts of *C. indica* leaf, *M. charantia* leaf and stem, as well as Ag-Ni formed with *C. indica* leaf extract displayed high activity on all the organisms considered, except *P. aeruginosa* in which low activity was recorded. Ag nanoparticles prepared using the leaf extracts of *N. tobacuum, S. occidentalis, C. filiformis* extract, and hybrid Ag-Ni nanoparticles synthesized using the leaf extracts of *S. occidentalis*

and *M. charantia* had moderate activities on all the organisms except *P. aeruginosa* where low activity was likewise recorded. Low activity was displayed by Ag-Ni nanoparticles on all the test organisms. However, ANOVA and SPSS statistical tools indicated no significant difference among varied concentrations of the nanoparticles on the growth inhibition against the microbes; as $p > 0.05$ (Appendix II). This indicated similar activity at all concentrations of the nanoparticles compared with the standard - ciprofloxacin (Bacteria) and fluconazole (Fungi).

In addition, the zones of inhibition recorded in agar well diffusion test led to the conduction of Minimum Inhibitory Concentration (MIC), Minimum Bactericidal Concentration (MBC) and Minimum Fungicidal Concentration (MFC) tests. The results showed the activities of Ag and Ag-Ni nanoparticles on *S. aureus, S. pyogenes, E. coli, P. aeruginosa, C. albicans* and *T. rubrum* (Appendix III).

Interestingly, all prepared nanoparticles showed concentration-dependent inhibitory effects on the *in-vitro* antimicrobial assay (Andrighetti-Frohner *et al.*, 2009). Considering the MIC testing on Gram negative bacteria (*E. coli* and *P. aeruginosa*) and the Gram positive bacteria (*S. aureus* and *S. pyogenes*), it was observed that Ag nanoparticles produced using different plant extracts in this study inhibited the growth of *S. aureus, S. pyogenes, E. coli* at the same MIC and MBC values of 12.5 mg/mL and 25 mg/mL respectively. Highest activity was observed in Ag-Ni nanoparticles against *S. pyogenes* with MIC value of 6.25 mg/ML and 12.5 mg/ML MBC. Least activity of 50 mg/mL, 100 mg/mL MIC and MBC values respectively were observed in Ag-Ni nanoparticles synthesized using *C. filiformis* and *S. occidentalis* leaf extracts.

However, Ag NPs stabilized with *C. indica* showed activity (MIC, MFC) on the fungus -*C. albicans* (12.5 mg/mL, 12.5 mg/mL) and *T. rubrum* (50 mg/mL, 100 mg/mL). On the contrary, no activity of the nanosilver was observed on the growth inhibition of *P. aeruginosa.* On the other hand, Ag nanosilver synthesized using *S. occidentalis* leaf extract was able to inhibit the growth of *P. aeruginosa* with MIC, MBC values of 25 mg/mL, 50 mg/mL. The MIC and MFC values of growth inhibition were also recorded for *C. albicans*- (25 mg/mL, 25 mg/mL) and *T. rubrum*- (50 mg/mL, 100 mg/mL).

Furthermore, *N. tobacuum*- influenced Ag nanoparticles also displayed antimicrobial activity by inhibiting the growth of *E. coli* at the same MIC and MBC value, 25 mg/mL, 50 mg/mL

value in *P. aeruginosa*; 12.5 mg/mL (MIC) and 25mg/mL (MFC) in *C. albicans*, 25 mg/mL (MIC) and 50 mg/mL (MFC) in *T. rubrum*.

Ag nanoparticles prepared using the extract of *M. charantia* leaf demonstrated no activity on *E. coli* at 2.0 mM precursor concentration, while its corresponding Ag nanosilver at the same concentration using the stem extract displayed an inhibitory activity on the growth of the same organism with MIC, MBC values of 50 mg/mL and 100 mg/mL. However, the growth of *C. albicans* was inhibited at the values of 12.5 mg/mL (MIC) and 12.5 (MFC) using Ag nanoparticles prepared from *M. charantia* leaf. Moreover, the same MIC and MFC value of 50 mg/mL was observed on the inhibition of *C. albicans* and *T. rubrum*.

The Ag nanocluster synthesized using *C. filiformis* showed a strong activity on *S. aureus* at the same MIC and MBC values of 25 mg/mL. 25 mg/mL value of MIC and MFC on *C. albicans* was also observed. Unfortunately, the Ag nanoparticles could not inhibit growth of *P. aeruginosa* and *T. rubrum*.

In the case of hybrid Ag-Ni nanoparticles, the analysis of variance (ANOVA) in SPSS statistics indicated no significant difference in the concentrations as $P > 0.05$. *C. indica*-influenced hybrid nanoparticles displayed a better activity than its corresponding Ag nanoparticles at varied levels in the test organisms. The value of 12.5 mg/mL was observed for both MIC, MBC in *S. aureus*, 6.25 and 12.5 mg/mL values were obtained as MIC and MBC respectively in *S. pyogenes* and *E. coli*. Similar growth inhibitory pattern was detected in both *C. albicans* and *T. rubrum* with equal values of 12.5 mg/mL (MIC) and 25 mg/mL (MFC). Contrary-wise, these nanoparticles could not hinder the growth of P. *aeruginosa*.

Moreover, growth inhibition by the Ag-Ni nanoparticles prepared using the leaf extract of *S. occidentalis* showed higher activity than its Ag nanoparticles on *S. pyogenes* (25 mg/mL, 50 (mg/mL) and *E. coli* (12.5 mg/mL, 25 mg/mL) MIC, MBC values; No activity was exhibited on *P. aeruginosa*.

M charantia-influenced Ag-Ni bimetallic nanoparticles revealed antimicrobial property, but not as potent as its corresponding Ag nanoparties. The MIC, MBC values obtained was achieved in *Staphylococcus aureus* (25 mg/mL, 50 mg/mL), *Streptococcus pyogenes* (25 mg/mL, 50 mg/mL), *E. coli* (25 mg/mL, 25 mg/mL), *Pseudomonas aeruginosa* (12.5 mg/mL, 25 mg/mL). The nanocluster was unable to restrain growth in the fungi- *C. albicans* and *T. rubrum* as indicated in the MIC, MFC values (100 mg/mL, 100 mg/mL).

In addition, the bimetallic Ag-Ni nanoparticles formed using the extract of *C. filiformis* of course displayed low inhibition in the growth of all pathogens considered in this research compared with its related Ag nanoparticles. The MIC, MBC values were recorded in *S. aureus* (50 mg/mL, 100 mg/mL), *S. pyogenes* (25 mg/mL, 50 mg/mL) and E. (50 mg/mL, 100 mg/mL). No activity of these hybrid nanoparticles was shown on *P. aeruginosa*. The MIC and MFC values of 50 mg/mL and 100 mg/mL were detected against *C. albicans*. However, there was no growth inhibition against *T. rubrum*.

None of the as-synthesized nanoparticles was able to compete with ciprofloxacin and fluconazole (standards) in terms of activity. One-way analysis of variance (ANOVA) using SPSS statistical tool indicated that growth inhibition by the nanoparticles were significance at $P < 0.05$.

In this study, *S. aureus*, *S. pyogenes* and *E. coli* showed similar behaviour relative to MIC and MBC, while *P. aeruginosa* was highly resistant. The bionanoparticles were more active on C. *albicans* than *T. rubrum*. The nanoparticles were able to penetrate the thin peptidoglycan layer with the outer membrane composed by phospholipids and lipopolysaccharides (LPS) of the *E. coli* (complex gram-negative bacterium). Not only that, the bionanoparticles also passed through the thicker peptidoglycan cell wall layer which is accountable for rigidity and low activity in gram-positive bacteria, as detected in the MIC test carried out on *S. aureus* and *S. pyogenes* (Nazzaro, Fratianni, Martino, Coppola & Feo, 2013). According to Marini *et al*. (2007), the observed growth inhibition in bacteria can also be related to the reaction of thiol groups present in bacteria protein with the release of Ag^{+} which slowed down or changed the replication of DNA (Marini *et al*., 2007).

CHAPTER FIVE
CONCLUSION AND RECOMMENDATIONS

A rapid, facile and environmental-friendly synthesis of monometallic Ag nanoparticles, novel Ag-Ni and Ag-Co nanobimetallic particles by green plant-mediated method was successfully achieved via reduction of $AgNO_3$, $Ni(NO_3)_2.6H_2O$ and $CoCl_2.6H_2O$ metal precursors. It is noteworthy that a number of plant extracts considered in this study exhibited unprecedented fast and successful bioreduction. Optical properties with characteristic SPR bands above 400 nm of metals were displayed in all the nanoclusters, both at room temperature and 70 ℃, except in Ag-Co hybrid nanoparticles prepared using the extract of *N. tobacum*. Nucleation and onset growth commenced as early as 5 minutes in successful bioreduction carried out at 70 ℃ and the reactions were completed within 30 minutes. In contrast, growth was delayed till 1 hour in Ag and its hybrid nanoparticles formed with the extract of *C. filiformis* as shown on time-resolved UV-Visible spectra.

The rate of nanoparticles formation was faster at 70℃ compared with the synthesis at room temperature, except in the nanocluster formed using the leaf extract of *M. charantia.* Complete reaction occurred within 30 minutes. The improved rate of nanoparticles formation at 70℃ is due to the effect of temperature which increased kinetic energy of the reaction, leading to higher rate.

The highest intensity of absorption (1.6 a.u.) was displayed in the Ag NPs capped with the extract of *S. occidentalis* which exhibited lowest maximum of absorption (380 nm), while the least intensity of absorption was observed in the Ag NPs stabilized with *C. filiformis* and *L. inermis* extracts (0.054 a.u. in 3.0 mM). However, maximum absorption wavelength was highest in the Ag-Ni nanohybrid formed with *H. sabdariffa* (513 nm) due to the presence of $\pi \longrightarrow \pi^*$ (C=C in phenol) and $n \longrightarrow \pi^*$ transition of C=O moiety of the proteins, carbohydrates and steroids present in the calyces extract.

Moreover, optical properties of the bionanoparticles were further studied with PL spectrometer. Two emission peaks were obtained in the nanohybrid nanoparticles. Near uniform emission of fluorophores, which connoted formation of nanoparticles in the quantum realm was observed between 438-466 nm in Ag nanoclusters prepared with the different plant extracts irrespective of the excitation wavelengths. Emission in the nanohybrid ranged from 581-778 nm, as shown by PL. This suggests good quality surfaces and interface properties of

the nanoparticles. The TEM analyses of nanoparticles formed using *C. indica* leaf extract revealed a novel morphological structure of cubic cobalt core capping another alloy when 1.0 mM of Ag-Co precursor mixture was reduced. Spherical monodispersed morphology of cluster-in-cluster structural arrangement was obtained as 2.0 mM precursor mixture was reduced. Other observed morphology in this work included Ag-core and Ni- shell structure, cubes with truncated/irregular edges were also obtained in the nanoparticles prepared by reducing 3.0 mM precursor mixture.

S. occidentalis-influenced Ag nanocluster was predominantly spherical in morphology, while the corresponding Ag-Ni contained core-shell arrangement. The structural elucidation of Ag NPs under *N. tobaccum*-influenced synthesis produced by reducing 2.0 mM $AgNO_3$ precursor resulted in quasi cube and spherically shaped nanoparticles. Its allied Ag-Ni produced different shapes: spheres, core-shell, nanocubes with truncated edges, multiply-twinned with various edges and corner truncation.

Morphology of the Ag NPs capped with the leaf extract of *M. charantia* was quasi-spherical structures. Its corresponding Ag-Ni nanobimetallic formed Ag core and Ni shell arrangement. However, the Ag-Co nanohybrids using this same bioreducing agent resulted in cubic shapes with truncated edges and multiply twinned nanoparticles. Aggregates of quasi-spherical and cube with irregular contour due to self-assembly of the particles were obtained in the structure obtained for Ag-Ni formed using the stem extract. Evidence of capping of the newly formed nanoparticles by the biomolecules was demonstrated in the diagonal orientation of Ag nanoparticles through mapping.

Ag-Ni nanoparticles prepared with the extract of *C. filiformis* contained cubic nanoparticles with contour and edges, multiply-twinned hybrid and core-shell nanostructures. Polydispersed nanoparticles were also formed in which nickel nanoparticles were formed between two Ag shells. The TEM image of Ag-Ni formed with the extract of *H. sabdariffa* contained multiply twinned nanoparticles, Ag-core and Ni-shell. Hexagonal shaped nanoparticles with truncated edges were observed in the Ag NPs stabilized with *L. inermis* leaf extract. The XRD patterns further supported the formation of Ag and its hybrid nanoparticles showing characteristic peaks present in them.

The FTIR analyses revealed functional groups present in Ag NPs and the nanohybrids, which proved the evidence of cappings provided by the bioreducing agents (plant extracts) that further stabilized the newly formed nanoparticles.

The antimicrobial properties of the biosynthesized nanoparticles were also studied in which the most active nanoparticles were hybrid Ag-Ni formed by all the plants engaged in this study, as it showed activity on *S. pyogenes* and *E. coli* with MIC and MBC values of 6.25 mg/mL and 12.5 mg/mL respectively. The least active nanoparticles were the hybrid Ag-Ni particles which were synthesized using *C. filiformis.*

The highest activity of *C. indica*-influenced Ag nanoparticles was on E. *coli* and *C. albicans*, followed by *S. aureus*, *S. pyogenes* (12.5 mg/mL value of MIC and MBC), and least active on *T. rubrum* (50 mg/mL MIC, 100 mg/mL MFC). No detectable activity was found against *P. aeruginosa*. *S. occidentalis*-influenced Ag nanoparticles were most active on *S. aureus*, *S. pyogenes* and *E. coli* with MIC and MBC values of 12.5 and 25 mg/mL respectively. Ag nanoparticles stabilized with *N. tobacuum* was most active on *S. pyogenes* (12.5 mg/mL MIC, 12.5 mg/mL MBC), followed by activity on *S. aureus* (12.5 mg/mL MIC, 25 mg/mL MBC) and least active on *P. aeruginosa* (50 mg/mL MIC, 50 mg/mL MBC).

M. charantia-influenced Ag nanoparticles synthesized using the leaf and the stem extract displayed highest activity on *S. aureus, S. pyogenes* and *E. coli* with MIC and MBC value of 12.5 mg/mL. Least activity was detected against *P. aeruginosa* (50 mg/mL MIC and 100 mg/mL MBC).

Ag nanoparticles formed with the extract of *C. filiformis* showed highest activity against *S. aureus* (MIC= 12.5 mg/mL, MBC = 25 mg/mL) and least inhibition in the growth of *E. coli (*MIC=12.5 mg/mL, MBC= 50 mg/mL). No observable growth inhibition on *P. aeruginosa* and *T. rubrum.* The ANOVA in SPSS statistical tool indicated significant difference with the highest activity being $P < 0.05$ among different concentrations. Interestingly, increase in the zone of inhibition is directly proportional to the increase in concentration of the bionanoparticles; yet, their activities on the pathogens were slightly weaker compared with the antibiotics ciprofloxacin and fluconazole (standards).

5.1 Contributions to Knowledge

The following are the major contributions to knowledge in this research study:

1. Identification of indigenous eco-friendly plants that can serve as reducing/capping agents for the synthesis of nanoparticles instead of toxic and expensive chemicals.
2. Novel Ag-Ni and Ag-Co bimetallic nanoparticles were successfully produced using plant-mediated green method.
3. Antibacterial drugs against *S. pyogenes* and *E. coli* can be designed using Ag-Ni nanohybrid, based on their strong inhibition activities observed, Ag NPs formed using *Canna indica* are potential antibacterial against *E. coli* and antifungus against *C. albicans* and the Ag NPS produced with *M. charantia* leaf and stem extract could also be developed into antibacterial against *S. aureus, S. pyogenes* and *E. coli*, Ag NPs prepared with the extract of *C. filiformis* are good antibacteria against *S. aureus*.
4. The intense optical properties displayed by the Ag nanoparticles aided by the stem extract of *M. charantia*, leaf extract of *C. indica* and *L. inermis,* bimetallic Ag-Co nanoparticles prepared using the leaf extract of *C. indica* and Ag-Ni formed using extract of *H. sabdariffa* can be employed to enhance optical materials.
5. Nanoparticles with narrow size distribution can be engaged as conductive fillers in gaps between Ag flakes for electronically conductive adhesives (ECA) in order to improve conductivity: electronic device application.
6. The PL emission (optical property) of nanorod present in Ag-Co nanoparticles synthesized with the extract of *C. indica* is an indicator for its application in optoelectronic device.

5.2 Recommendations

The following are recommended for the extension of this work:

1. The PL study should be carried out at fixed excitation wavelength values of 315 nm, 320 nm and 379 nm for Ag NPs, Ag-Ni NPs and Ag-Co NPs respectively.
2. The excitation wavelength should also be varied in each nanoparticles influenced by each capping/reducing agent, in order to consider uniform emission which will further confirm the biosynthesized nanoparticles in quantum realm: 232 and 315 nm for Ag NPs, 320, 340 and 345 nm for Ag-Ni bimetallic nanoparticles, 379, 400 and 430 nm for Ag-Co NPs.
3. Surface Raman scattering and surface plasmon effect should be studied in nanohybrid nanoparticles for further applications in optoelectronic and sensors.
4. Antiviral activities of the biosynthesized nanoparticles should be carried out for HIV screening based on the sizes on nanoparticles obtained in this study.
5. Advance study should be carried out on proper isolation of compounds acting as the reducing agents in each plant extract considered in this study.
6. Toxicity of the synthesized nanoparticles should also be carried out.

REFERENCES

Abdullah, E., Raus, R. A. & Jamal, P. (2012). Extraction and evaluation of antibacterial activity from selected flowering plants. *American Medical Journal*, **3** (1), 27-32.

Aboua, L. R., Seri-Kouassi, B. P. & Oua, H. K. (2010). Insecticidal activity of essential oils from three aromatic plants on *Callosobruchus maculatus* in Cote D'ivoire.

J. A., Mlowe, S., Dare, E. O., Mesubi, M. A. & Revaprasadu, N. (2015). *European Journal of Scientific Research*, **39**, 243–250.

Adekoya, Synthesis and characterization of polyol stabilized Ag/Co allied nanocomposites. *Superlattices and Microstructures*, **78**, 97–105.

Adetunji, C. O., Olaniyi, O. O. & Ogunkunle, A. T. (2013). Bacterial activity of crude extracts of *Vernonia amygdalina* on clinical isolates. *Journal of Microbiology and Antimicrobials*, **5** (6), 60-64.

Ahmad, A., Mukherjee, P. & Senapati, S. (2003). Extracellular biosynthesis of silver nanoparticles using the fungus *Fusarium oxysporum*. *Colloids and Surfaces B: Biointerfaces*, **28** (4), 313–318.

Ahmad, N., Sharma, S., Singh, V.N., Shamsi, S. F., Fatma, A. & Mehta, B. R. (2011). Biosynthesis of silver nanoparticles from *Desmodium triflorum*: A novel approach towards weed utilization. *Biotechnology Research International*, **1**, 1-8.

Ahmad, N. & Sharma, S. (2012). Green synthesis of silver nanoparticles using extracts of *Ananas comosus*. *Green and Sustainable Chemistry*, **2** (4), 141-147.

Aida, P., Rosa, V., Blamea, F., Thomas, A. & Salvador, C. (2001). Paraguyan plants used in traditional medicine. *Journal of Ethnopharmacology*, **16**, 93-98.

Akinsiku, A. A., Ajanaku, K.O., Adekoya, J A. & Dare, E. O. (2015). Green synthesis, characterization of silver nanoparticles using Canna *indica* and Senna *occidentalis* leaf extracts. *Proceedings of* 2nd Covenant University International Conference on African Development Issues. 154-157.

Al-Fattani, M. A. & Douglas, L. J. (2004). Penetration of *Candida* biofilms by antifungal agents. *Antimicrobial Agents and Chemotherapy*, **48** (9), 3291–3297.

Anastas, P. T. & Warner, J. C. (1998). *Green Chemistry: Theory and practice*. Oxford University Press: New York, U.S.A., 30.

Andrighetti-Frohner, C. R., Oliveira, K. N., Gaspar-Silva, D., Pacheco, L. K., Joussef, A. C., Steindel, M. … & Castro, H. C. (2009). Synthesis, biological evaluation and SAR of sulfonamide 4-methoxychalcone derivatives with potential antileishmanial activity. *European Journal of Medicinal Chemistry*, **44**, 755-763.

Apte, M., Sambre, D. & Gaikawad, S. (2013). Psychrotrophic yeast *Yarrowia lipolytica* NCYC 789 mediates the synthesis of antimicrobial silver nanoparticles via cell-associated melanin. *Journal of AMB Express,* **3** (1), 32.

Arancibia, F., Bauer, T. T., Ewig, S., Mensa, J., Gonzalez, J., Niederman, M.S., …Torres, A. (2002). Community-acquired pneumonia due to gram-negative bacteria and Pseudomonas aeruginosa: incidence, risk, and prognosis. *Archnite International Medicine*, **162,** 1849–1858.

Arunasish, L., Gargi, M., Archana, S., Marina, S., Subhabrata, D., Arindam, C… Rajdip, B. (2012). A generalized three stage mechanism of ZnO nanoparticle formation in homogenous liquid medium. *Journal of Physical Chemistry C,* **116,** 24757–24769.

Averback, R. S. & Zhu, H. L. (1996). Sinitering of nanoparticle powders: Simulations and experiments. *Philosophical Magazine Letters*, **73**, 27-31.

Baillie, G. S. & Douglas, L. J. (1998a). Effect of growth rate on resistance of *Candida albicans* biofilms to antifungal agents. *Antimicrobial Agents and Chemotherapy*, **42** (8), 1900–1905.

Baillie, G. S. & Douglas, L. J. (1998b). Iron-limited biofilms of *Candida albicans* and their susceptibility to amphotericin B. *Antimicrobial Agents and Chemotherapy*, **42**, (8), 2146- 2149.

Bako, I. G., Mabrouk, M. A. & Abubakar, A. (2009). Antioxidant effect of ethanolic seed extract of *Hibiscus sabdariffa* Linn (Malvaceae) alleviate the toxicity induced by chronic administration of sodium nitrate on some haematological parameters in Wistars rats. *Advance Journal of Food Science and Technology*, **1** (1), 39–42.

Balaji, D. S., Basavaraja, S., Deshpande, R., Mahesh, D. B., Prabhakar, B. K. & Venkataraman, A. (2009). Extracellular biosynthesis of functionalized silver nanoparticles by strains of *Cladosporium cladosporioides* fungus. *Colloids and Surfaces B: Biointerfaces*, **68** (1), 88–92.

Banfield, F., Welch, S. A., Zhang, H., Ebert, T. T. & Penn, R. L. (2000). Aggregation-based crystal growth and microstructure development in natural iron oxyhydroxide biomineralization products. *Science,* **289**, 751-754.

Bessen, D. E. (2009). Population biology of the human restricted pathogen, Streptococcus *pyogenes*. *Infection, Genetics and Evolution: Journal of Molecular Epidemiology and Evolutionary Genetics in Infectious Diseases*, **9** (4), 581-593.

Bhainsa, K. C. & D'Souza, S. F. (2006). Extracellular biosynthesis of silver nanoparticles using the fungus *Aspergillus fumigatus*. *Colloids and Surfaces B: Biointerfaces*, **47**, (2), 160–164.

Bhardwaj, D. K., Seshadri, T. R. & Singh, R. (1977). Xanthones from *Lawsonia inermis.* *Phytochemistry*. **16,** 1616-1617.

Bhardwaj, D. K., Bisht, M. S. & Jain, R. K. (1980). Constituents of laxanthones II: synthetic studies. *Proceedings of the National Academy of Sciences, India*, **46** (4), 381-386.

Boca, C. & Astilean, S. (2010). Detoxification of gold nanorods by conjugation with thiolated poly(ethylene glycol) and their assessment as SERS-active carriers of raman tags. *Nanotechnology*, **21,** 23-28.

Bolade, M. K, Oluwalana, I. B. & Ojo, O. (2009). Commercial practice of roselle (*Hibiscus sabdariffa* L.) beverage production: Optimization of hot water extraction and sweetness level. *World Journal of Agricultural Sciences*, **5** (1), 126–131.

Boulos, L. (1999). Flora of Egypt. Al Hadara Publishing. Cairo, Egypt, 1, 419.

Brinker, C. J. & Scherer, G.W. (1990). Sol-Gel Science: The physics and chemistry of sol-gel processing. Academic Press.

Brynjolfsson, E. & McAfee, A. (2012). Winning the race with ever-smarter machines. MIT 60. *Sloan Management Review*. **53** (2), 53-5.

British Society for Antimicrobial Chemotherapy (BSAC, 1990).

Burkill, H. M. (1995). The useful plants of west tropical Africa. (2nd edition), **2**. *Royal Botanic Garden Kew.* (2^{nd} Edition), 160-163.

Buzea, C., Blandino, I. & Robbie, K. (2007). Nanomaterials and nanoparticles: Sources and toxicity. *Biointerphases,* **2** (4), MR17 - MR172.

Calderone, R. A. (2002). *Candida* and *Candidiasis*. American Society for Microbiology Press, Washington, DC, USA., 67.

Canningham, M. W. (2000). Pathogenesis of group A streptococcal infections. *Clinical Microbiology Reviews*, **13,** 470–511.

Cao, G. (2004). Nanostructures and nanomaterials: Synthesis, properties, and applications. Imperial College Press, London, 90.

Cao, G. & Wang, Y. (2004). Nanostructures and nanomaterials: Synthesis, properties, and applications (2nd Edition). Imperial College press.World Scientific Publishing Co. Pte. Ltd. http://www.worldscibooks.com/nanosci/7885.html

Carapetis, J. R., Steer, A. C., Mulholland, E. K. & Weber, M. (2005). The global burden of group A streptococcal diseases. *Lancet Infectious Diseases*, **5,** 685–694.

Casadevall, A. & Pirofski, L. A. *(*1999*).* Host–pathogen interactions*:* Redefining the basic concepts of virulence and pathogenicity. *Infection* and *Immunity*, **67**, 3703–3713.

Cavalieri, S.J., Bohach, G. A. & Snyder, I.S. (1984). Escherichia coli a-hemolysin: characteristics and probable role in pathogenicity. *Microbiological Reviews*, **48** (4), 326-343.

Chakrabortty, T., Podder, G. & Deshmukh, S.K. (1977). Triterpenoids and other constituents of Lawsonia inermis. *Indian Journal of Chemistry Section B Organic Chemistry Including Medicinal Chemistry*, **15,** 96-97.

Chandran, P. S., Chaudhary, M., Pasricha, R., Ahmad, A. & Sastry, M. (2006). Synthesis of gold nanotriangles and silver nanoparticles using *Aloe vera* plant extract. *Biotechnology Progress*, **22,** 577-583.

Chauhan, M. G. & Pillai, A. P. (2007). Microscopic profile of powdered drug used in Indian system of medicine. *Jamnagar*, *Gujarat*. 84-85.

Chen, X. Y., Qiao, M. H., Xie, S. H., Fan, K. N., Zhou, W. Z. & He, H. Y. (2007). Metal oxide catalysis. *Journal of American Chemical Society*, **129,** 133-135.

Chen, D., Qiao, X., Qiu, X. & Chen, J. (2009). Synthesis and electrical properties of uniform silver nanoparticles for electronic applications. *Journal of Material Science*, **44**, 1076–1081 Doi: 10.1007/s10853-008-3204-y

Chetty, K. M. (2008). Flowering plants of Chittoor. Edition 1, Andhra Pradesh. (Pp. 132).

Chopra, R. N., Nayer, S. L. &Chopra, I.C. (1956). Glossary of India medicinal Plants. CSIR Publications, New Delhi, (151).

CLSI (2006). Clinical and Laboratory Standards Institute.

Cobley, C., Chen, J., Cho, E., Wang, L. & Xia, Y. (2011). Gold nanostructures: A class of multifunctional materials for biomedical applications. *Chemical Society Review*, **40,** 44-56.

Cohen, T. & Murray, M. (2004), Modelling epidemics of multi-drug resistant *Mycobacterium tuberculosis* of heterogeneous fitness. *Nature Medicine,* **10**, 1117-1121.

Colfen, H. & Mann, S. (2003). Higher-order organization by mesoscale self-assembly and transformation of hybrid nanostructures. *Angewandte Chemie*, **42,** 2350-2365.

Colfen, H. & Antonietti, M. (2005). Mesocrystals: Inorganic superstructures made by highly parallel crystallization and controlled alignment. *Angewandte Chemie,* **44,** 5576.

Collins, C. H. & Kennedy, D. A. (Eds.). (1983). *Laboratory-acquired Infections* (4th edition). Oxford: Butterworth-Heinermann, 277-279.

Community portal of Nigeria, (2003). Retrieved from www.onlinenigeria.com

Condon, E. (1928). A theory of intensity distribution in band systems (Meeting abstract). *Physical Review,* **27,** *640*-660.

Corriu, R. & Trong, A. N. (2009). Introduction to material chemistry, in molecular chemistry of sol-gel derived nanomaterials. John Wiley & Sons, Ltd, Chichester, UK. 27-69.

Creighton, J. A., Blatchford, C. G. & Albrecht, M. G. (1979). Plasma resonance enhancement of Raman scattering by pyridine adsorbed on silver or gold sol particles of size comparable to the excitation wavelength. J*ournal of the Chemical Society, Faraday Transactions*, **75**, 790–798.

Crossley, K. B. & Archer, G. L. (1997). *The Staphylococci in human disease.* Churchill Livingstone, 682.

Croxen, M. A., Scholz, L. R., Keeney, K. M., Wlodarska, M. & Finlay, B. B. (2013). Recent advances in understanding enteric pathogenic *Escherichia coli*. *Clinical Microbiology Review Journal*, **26** (4), 822-880.

Cunningham, M. W. (2008). Pathogenesis of group A streptococcal infections and their sequelae. *Advances in Experimental Medicine and Biology, 609*, 29-42.

Cutler, J. E. (1991). Putative virulence factors of *Candida albicans*. *Annual Review of Microbiology*, **45**, 187–218.

Daisy, P. (2009). Plant mediated green syhthesis of gold nanoparticles using *Mangifera indica* leaf. *Spectrochimica Acta* A, **77,** 807-810.

Dare, E. O, Oseghale, C. O., Labulo, H. O., Adesuji, E. T., Elemike, E. E., Onwuka, J. C., … Bamgbose, J. T. (2014). Green synthesis and growth kinetics of nanosilver under bio-diversified plant extracts influence. J*ournal* of *Nanostructure* in *Chemistry.*

Deming, R. L. & Tinoi, J. (2006). Determination of major caratenoid constituents in petal extract of eight selected flowering in the North of Thailand. *Journal of Sciences,* **33** (2), 327-334.

Deng, Z. X. & Li, Y. (2003). Novel inorganic-organic-layered structures: crystallographic understanding of both phase and morphology formations of one-dimensional CdE (E=S, Se, Te) nanorods in ethylenediamine. *Inorganic Chemistry,* **42** (7), 2331–2341.

Deshpande, A. S., Khomane, R. B., Vaidya, B.K., Joshi, R. M., Harle, A. S. & Kulkarni, B. D. (2008). Sulfur nanoparticle synthesis and characterization from H_2S gas, using novel biodegradable iron chelate in W/O microemulsion. *Journal of Nanoscale Research Letter,* **3,** 221-229.

Diekema, D. J., Pfaller, M. A., Schmitz, F. J, Smayevsky, J., Bell, J., Jones, R. N., …Beach, M. (2001). Survey of infections due to *Staphylococcus* species: frequency of occurrence and antimicrobial susceptibility of isolates collected in the United States, Canada, Latin America, Europe, the Western Pacific region for the SENTRY Antimicrobial Surveillance Program 1997–1999. *Clinical Infectious Diseases,* **32** (2), 114–132.

Dierking, I., Koshbar, L. L., Afzali-Ardakani, A., Lowe, A. C. & Held, G. A. (1997). Two stage switching behaviour of polymer stabilized cholesteric textures. *Journal of Applied Physics,* **81**, 3007-3014.

Ding, J., Miao, W. F., McCormick, P. G. & Street, R. (1995). Mechanochemical synthesis of ultrafine Fe powder. *Journal of Applied Physics Letter*, **67**, 3804.

Dirksen, J. A. & Ring, T. A. (1991). Fundamentals of crystallization: Kinetic effect on size distributions and morphology. *Chemical Engineering Science,* **46**, 2389-2427.

Donega, C. D. (2011). Synthesis and properties of colloidal heteronanocrystals. *Chemical Society Reviews*, **40**, 1512–1546.

Dong, L. (2012). Optical properties of nanoparticles in composite materials. (Unpublished doctoral thesis), Royal Institute of Technology, Sweden. 70.

Donlan, R. M. & Costerton, J. W. (2002). Biofilms: survival mechanisms of clinically relevant microorganisms. *Clinical Microbiology Reviews*, **15** (2), 167–193.

Doughari, J. H., Pukuma, M. S. & De, N. (2007). Antibacterial effects of *Balanites aegyptiaca* L. Drel and *Moringa oleifera* Lam. on *Salmonella typhi. African Journal of Botechnology*, **6** (19), 2212- 2215.

Douglas, L. J. (2003). *Candida* biofilms and their role in infection. *Trends in Microbiology*, **11** (1), 30–36.

Dubeya, S. P., Lahtinenb, M., Sarkkaa, H. & Sillanpaa, M. (2010). Bioprospective of *Sorbus aucuparia* leaf extract in development of silver and gold nanocolloids. *Colloids* and *Surfaces B,* **80**, 26–33.

Dudoitis, V., Uleviėius, Raèiukaitis, V. G., Ðpirkauskaitë, N., Plauðkaitë, V. & Lithuanian, K. (2011). Generation of metal nanoparticles by laser ablation. *Journal of Physics*, **51**, 248–259.

Duran, N., Marcato, P. D., Alves, O. L., de Souza, G. I. & Esposito, E. (2005). Mechanistic aspects of biosynthesis of silver nanoparticles by several *Fusarium oxysporum* strains. *Journal of Nanobiotechnology*, **3**, (1), Article.

Eggimann, P., Garbino, J. & Pittet, D. (2004). Epidemiology of *Candida* species infections in critically ill nonimmunosuppressed patients. *Lancet Infectious Diseases*, **3** (11), 685–702.

Egharevba, H. O., Odigwe, A. C., Abdullahi, M.S., Okwute, S. K. & Okogun, J. I. (2013). Phytochemical analysis and broad spectrum antimicrobial activity of *Cassia occidentalis* L. (whole plant). *New York Science Journal*, **3** (10), 192-202.

Egziabher, T. B., Hedberg, G. O., Tadesse, M., Frils, I., Hedberg, I. & Edwards, S. (1989).*Flora of Ethiopia*. (3). Institute of Botany, Uppsala University. Addis Ababa and Asmara, Ethiopia, & Uppsala, Sweden, (3). 49-63.

Esbaugh, W. H., McClure, S. A. & Bolyard, J. L. (1985). Bush medicine studies. Proceedings of the first symposium on the botany of the Bahamas 11–14 June 1985. Edition.

Esselen, W. B. & Sammy, G. M. (1975). Applications for roselle and a red food colorant. *Food Product Development*, 37–40.

Eustis, S. & El-Sayed, M. A. (2006). Why gold nanoparticles are more precious than pretty gold: noble metal surface Plasmon resonance and its enhancement of the radiative and nonradiative properties of nanocrystals of different shapes. *Chemical Society Review*, **35**, 209–217.

Evanoff, D. D. & Chumanov-Jr., G. (2003). Size-controlled synthesis of nanoparticles measurement of extinction, scattering and absorption cross sections. *Journal of Physical Chemistry B*, **108**, 13957-13962.

Fairbrother, J. M., Nadeau, E. & Gyles, C. L. (2005). Escherichia coli in postweaning diarrhea in pigs: an update on bacterial types, pathogenesis, and prevention strategies. *Animal Health Research Reviews*, **6**, 17-39.

Feynman, R. (1959). Classic talk: "There's plenty of room at the bottom". *The free Encyclopedia Britannica.* Encyclopedia Britannica. 60-65.

Filipponi, L. & Sutherland, D. (2010). Fabrication methods. Interdisciplinary Nanoscience Centre (iNANO) Aarhus University, Denmark

Finney, E. E. & Finke, R. G. (2008). Nanocluster nucleation and growth kinetic and mechanistic studies: A review emphasizing transition-metal nanoclusters, *Journal of Colloid Interface Science*, **317**, 351-374.

Flora of China (Series). (2015, September 21). In *Wikipedia. The Free Encyclopedia*. Retrieved 11:37, April 7, 2016, from https://en.wikipedia.org/w/index.php?title=Flora_of_China_(series)&oldid=682113120

Ganguly, S. & Mitchell, A. P. (2011). Mucosal biofilms of *Candida albicans*. *Current Opinion in Microbiology*. **4**, 380-385.

Gardea-Torresdey, J. L., Parsons, J. G., Gomez, E., Peralta-Videa, J., Troiani, H.E. & Santiago, P. (2002). Formation and growth of Au nanoparticles inside live alfalfa plants. *Journal of American Chemical Society,* **2,** 397–401.

Gaya, I. B., Mohammad, O. M., Suleiman, A. M., Maje, M. I. & Adekunle, A. B. (2009). Toxicological and lactogenic studies on the seeds of *Hibiscus Sabdariffa* Linn (Malvaceae) extract on serum prolactin levels of albino wistar rats. *The Internet Journal of Endocrinology,* **5**, (2).

Ge, J. P., Hu, Y. X., Biazini, M., Beyemann, W. P. & Yin, Y. D. (2007). Superparamagnetic magnetite colloidal nanocrystal clusters. *Angewandte Chemie, International Edition.,* **46**, 4342.

Gebauer, D., Volkel, A. & Cˆlfen, H. (2008). Stable prenucleation calcium carbonate clusters. *Science*, **322**, 1819-1822.

Ghannoum, M. A. (2000). Potential role of phospholipases in virulence and fungal pathogenesis. *Clinical Microbiology Reviews,* **13** (1), 122–143.

González, A. L. & Noguezm, C. (2007). Influence of morphology on the optical propertieof metal nanoparticles. *Journal of Computational and Theoretical Nanoscience*, **4** (2), 231-238.

Gozalbo, D., Roig, P., Villam, E. & Gil, M. L. (2004). *Candida* and *candidiasis*: the cell wall as a potential molecular target for antifungal therapy. *Current Drug Targets*, **4** (2), 117–135.

Gross, M., Winnacker, M. A. & Wellmann, P. J. (2007). Electrical, optical and morphological properties of nanoparticle indium-tin-oxide layers. *Thin Solid Films*, **515** (24), 8567-8572.

Gudlaugsson, O., Gillespie, S. & Lee, K. (2003). Attributable mortality of *Nosocomial candidemia,* revisited. *Clinical Infectious Diseases*, **37** (9), 1172–1177.

Guglielmo, D., Lopez, C., Lapuente, J., Mallafre, J. M. & Suarez, M. B. (2010). Embryotoxicity of cobalt ferrite and gold nanoparticles: a first *in vitro* approach. *Reproduction Toxicolology*, **30**, 271-276.

Guo, S. & Wang**,** E. (2011). Noble metal nanomaterials: controllable synthesis and application in fuel cells and analytical sensors. *Nano Today*, **6,** 240-247.

Guoqiang, Z. & Wenying, W. (2012). Synthesis of silver nanoparticles and their antiproliferation against human lung cancer cells *in vitro*. *Oriental Journal of Chemistry*, **28** (2), 651-655.

Hahn, H. P. *(*1997*).* The type-4 pilus is the major virulence-associated adhesin of *Pseudomonas aeruginosa*– a review. *Gene*, **192,** 99–108.

Harekrishna, B., Dipak, K. B., Gobinda, P. S., Priyanka, S., Santanu, P. & Ajay, M. (2009). Green synthesis of silver nanoparticles using seed extract of *Jatropha curcas. Colloids* and *Surfaces A*: *Physicochemical* and *Engineering Aspects,* **348,** 212–216.

Hassanjani-Roshana, A., Vaezib, M. R., Shokuhfarc, A. & Rajabalic, Z. (2011). Synthesis of iron oxide nanoparticles via sonochemical method and their characterization. *Particuology*, **9**, 95–99.

Hauser, A. R. (2009). The type 3 secretion system of *Pseudomonas aeruginosa*: infection by injection. *Nature Reviews Microbiology*, **7**, 654–665.

Haverkamp, R. G., Marshall, A. T. & Agterveld, D. (2007). Pick your carats: nanoparticles of gold–silver–copper alloy produced *in-vivo*. *Journal of Nanoparticle Research*, **9,** 697–700.

Herrera, A. P., Resto, O., Briano, J. G. & Rinaldi, C. (2005). Synthesis and agglomeration of gold nanoparticles in reverse micelles. *Nanotechnology*, **16** (7), 618–625.

Heyman, D. (2004). *Control of Communicable Diseases Manual.* (18th Edition) American Public Health Association, Washington DC.

Hidron, A. I., Edwards, J. R., Patel, J., Horan, T. C., Sievert, D. M., Pollock, D. A., … Fridkin, S. K. (2008). Antimicrobial-resistant pathogens associated with healthcare-associated infections: annual summary of data reported to the National Healthcare Safety Network at the Centers for Disease Control and Prevention. *Infectction Control Hospital Epidemiol.* **29** (11), 996-1011.

Hillert, M. (1997). What are alloys? ICME (International Council on Metals and the Environment). *Newsletter,* **5** (4). Ottawa, Canada.

Hogardt, M. & Heesemann, J. (2010). Adaptation of Pseudomonas *aeruginosa* during persistence in the cystic fibrosis lung. *International Journal of Medical Microbiology*, **300,** 557–562.

Hooper, L.V. & Gordon, J. I. (2001). Commensal host-bacterial relationship in the gut. *Science*, **292**, 1115-1118.

Huang, J., Li, Q., Sun, D., Lu, Y., Su, Y., Yang, X., Wang, H., … Chen, C. (2007). Biosynthesis of silver and gold nanoparticles by novel sundried *Cinnamomum camphora* leaf. *Nanotechnology*, **105**, (104), 18.

Huang, Y. F., Wu, D. Y, Wang, A., Ren, B., Rondinini, S., Tian, Z. Q., … Amatore, C. J. (2010). *American Chemical Society*, **132** (48), 17199-17210.

Indrayan, A K., Bhojakb, N. K., Kumara, N. S. & Gaur, A. (2011). Chemical composition and antimicrobial activity of the essential oil from the rhizome of *Canna indica* Linn**.** *Indian Journal of Chemistry*, **50** (8), 1136 – 1139.

ICMSF, International Commission on Microbiological Specifications for Foods. (1996). *Microbiological specifications of food pathogens.* Springer.

Isberg, R. R., Voorhis, D. L. & Falkow, S. *(*1987*).* Identification of invasion: a protein that allows enteric bacteria to penetrate cultured mammalian cells. *Cell,* **50,** 769–778.

Ismail, A., Ikram, E. & Nazri, H. (2008). Roselle (*Hibiscus sabdariffa* L.) seeds nutritional composition protein quality and health benefits. *Food*, **2** (1), 1–16.

Jain, P. K., Eustis, S. & El-Sayed (2006). Plasmon coupling in nanorod assemblies: optical absorption, discrete dipole approximation simulation, and exciton-coupling model. *Journal of Physical Chemistry* B, **10** (37), 18243-18253.

Jain, P.K, Huang, X., El-Sayed, I.H. & El-Sayed, M.A. (2008). Noble metals on the nanoscale: optical and photothermal properties and some applications in imaging, sensing, biology, and medicine. *Accounts of Chemical Research,* **41,** 1578-1586.

John, R., Balaguru, B. & Jeyaprakash, B. G. (2012). Quantum size effect, electrical conductivity and Quantum transport NPTEL -*Electrical and Electronics Engineering – Semiconductor Nanodevices*, **12**, (16), 1714-1717.

Joshi, Y.M, Kadam, V. J. & Kaldhone, P.R. (2008). In-vitro antioxidant activity of methanolic extract of aerial parts of *Canna indica* L. *Journal of Pharmacy Research* **2** (11), 1712-1715. http://jpronline.info/article/view/921/719.

Jun, Y. W., Casula, M. F., Sim, J. W., Kim, S. Y., Cheon, J. & Alivisatos, A. P. (2003). Surfactant-assisted elimination of a high energy facet as a means of controlling the shapes of TiO_2 nanocrystals. *Journal of the American Chemical Society*, **125** (51), 5981–15985.

Ju-Nam, Y. & Lead, J. R. (2008). Manufactured nanoparticles: an overview of their chemistry, interactions and potential environmental implications. *Science of the Total Environment*, **400**, 396-414.

Kaneko, J. & Kamio, Y. (2004). Bacterial two-component and hetero-heptameric pore-forming cytolytic toxins: structures pore-forming mechanism organization of the genes. *Bioscience, Biotechnology and Biochemistry*, **68**, 981– 1003.

Kashchiev, D. (2000). Nucleation: theory and basic applications, Butterworth-Heinemann. 540 -544.

Kataby, G., Prozorov, R. & Gedanken, A. (1999). Characterization of self assembled alcohols coatings on amorphous iron. *Nanostructured Materials,* **12**, 421–424.

Katzenell, U., Shemer, J. & Bar-Dayan, Y. (2001). Streptococcal contamination of food: an unusual cause of epidemic pharyngitis. *Epidemiology and Infection,* **127** (2), 179-184.

Kelly, K. L., Coronado, E., Zhao, L. L. & Schatz, G. C. (2003). The optical properties of metal nanoparticles: The influence of size, shape, and dielectric environment. *Journal of Physical Chemistry B*, **107**, 668 –677.

Kelsall, R. W., Hamley, I. W. & Geoghegan, M. (2005). Nanoscale Science and Technology. John Wiley and Sons Ltd. Chichester. (Pp 200- 230).

Kim, J. Y., Kim, M., Kim, H. M., Joo, J. & Choi, J. H. (2003). Electrical and optical studies of organic light emitting devices using SWCNTs-Polymer nanocomposites. *Optical Materials*, **21** (3), 147-151. Doi: 10.1016/S0925-3467(02)00127-1

Kirtikar, K. R. & Basu, B. D. (1987). *Indian medicinal plants*, 2nd Edn, **4**, International Book Distributors, Dehradun, India. 2450.

Kishore, S., Tamio, E., Sang-Geun, C., Jongryoul, K. Tae, J. P. & Reji, P. (2013). Single step synthesis and optical limiting properties of Ni–Ag and Fe–Ag bimetallic nanoparticles. *Optical Materials*, **35** (5), 860–867.

Kitchens, L., McLeod, M. C. & Roberts, C. B. (2005). Chloride ion effects on synthesis and directed assembly of copper nanoparticles in liquid and compressed alkane microemulsions. *Langmuir*, **21,** (11), 5166–5173.

Kitching, M., Ramani, M. & Marsili, E. (2014). Fungal biosynthesis of gold nanoparticles: mechanism and scale up. *Mini Review Microbial Biotechnology*. 904–917

Klaus, T., Joerger, R. Olsson, E. & Granqvist, C. G. (1999). Silver based crystalline nanoparticles, microbially fabricated. *Proceedings of the National Academy of Sciences of the United States of America*, **96** (24), 13611–13614.

Klein, L. C. (1994). Sol-gel optics: Processing and applications. Kluwer Academic Publishers. Springer-Verlag, Boston. **2**1, 115-120.

Kolhe, N. M., Nirmal, S. A. & Pal, S. C. (2008). Nonpolar compounds from *Canna indica* rhizomes. *Physics, Chemistry and Technology,* **6** (1), 141-146.

Koole, R., Groeneveld, E., Vanmaekelbergh, D., Meijerink, A. & Donegá, C. (2014). *Size effects on semiconductor nanoparticles*. Debye Institute for Nanomaterials Science, Utrecht University, Utrecht, Netherlands. 13

Kowshik, M., Ashtaputre, S. & Kharrazi, S. (2003). Extracellular synthesis of silver nanoparticles by a silver-tolerant yeast strain MKY3. *Nanotechnology*, **14** (1), 95–100.

Kreibig, U. & Vollmer, M. (1995). *Optical properties of metal clusters*. Springer Series in Materials Science, New York, Springer-Verlag. **25**, 50.

Kukushki, S. A. & Osipov, A.V. (1998). Kinetics of first-order phase transitions in the asymptotic stage. *Journal of Experimental and Theoretical Physics,* **86** (6), 1201-1208.

Kulak, A. N., Iddon, .P, Li, Y., Armes, S., Cölfen, H., Paris, O., Meldrum, F.C. (2007). Continuous structural evolution of calcium carbonate particles: a unifying model of copolymer-mediated crystallization. *Journal of American Chemical Society* **129**, 3729-3736.

Kulkarni, A. P., Srivastava, A. A., Harpale, P. M. & Zunjarrao, R. S. (2011). Plant mediated synthesis of silver nanoparticles - tapping the unexploited sources. *Journal of Natural Product Plant Resources*, **1** (4), 100-107.

Kumamoto, C. A. (2002). *Candida* biofilms, *Current Opinion in Microbiology*, **5**, (6), 608–611.

Kumar, K. & Yadav, S. K. (2013). Influence of physiochemical factors on size of gold nanoparticles synthesised using leaf extract of *Syzygium Cumini*. *Journal of Chemical Science and Technology*, **2** (1), 21-24.

Kumbhakar, P., Ray, S. S. & Stepanov, A. L. (2014). Optical properties of nanoparticles and nanocomposites. *Journal of Nanomaterials*, Volume 2014, Article ID 181365, 2 pageshttp//

Kvítek, O., Siegel, J., Hnatowicz, V. & ŠvorIík, V. (2013). Noble metal nanostructures influence of structure and environment on their optical properties. Review Article. *Journal of Nanomaterials*, Volume 2013, 8 pages Article ID 743684.

Lamaeswari, G. & Ananthi, T. (2012). TLC analysis and antibacterial activity of *canna indica* flowers. *International Journal of Pharmacy and Technology*, **4** (2), 4268-4279.

LaMer, V. K. & Dinegar, R. H. (1950). Theory, production and mechanism of formation of monodispersed hydrosols. *Journal of the American Chemical Society*, **72** (11), 4847-4854.

Lee, W.r., Kim, M. G., Choi, J.r., Park, J.I., K.o, S. J., Oh, S. J., …Cheon, J. (2005). Redox-transmetation process as a generalized synthetic strategy for core-shell magnetic nanoparticles. *Journal of American Chemical Society,* **127** (46), 16090-16097.

Lehn, J. M. & Ourisson, G. (1962). Resonance magnetique nucleaire de produits natures: Introduction general, triterpenes de la series du lupine, Les groups methyles. *Bulletin de la Société Chimique de France,* 1137 – 1142.

Lifshitz, J. M. & Slyozov, V. V. (1961). The kinetics of precipitation from supersaturated solid solutions. *Journal* of *Physics and Chemistry* of *Solids*, **19**, 35–50.

Lin, C. N., Chung, M., Gan, K. H. & Chiang, J. R. (1987). Xanthones from *Formosan gentianaceous* plants. *Phytochemistry*, **26** (8), 2381-2384.

Lindsay, J. A. & Holden, M. T. (2004). *Staphylococcus aureus*: superbug super genome? *Trends in Microbiology*, **12,** 378–385.

Link, S. & El-Sayed, M. A. (2000). Shape and size dependence of radiative, non-radiative and photothermal properties of gold nanocrystals. *International Reviews in Physical Chemistry*, **19**, 409–453.

Link, S., Wang, Z. L. & El-Sayed, M. A. (1999). Alloy formation of gold-silver nanoparticles and the dependence of the plasmon absorption on their composition. *Journal of Physica*l *Chemistry B*, **103**, 3529.

Liu, J., Anand, M. & Roberts, C. B. (2006). Synthesis and extraction of β-D-glucose stabilized Au nanoparticles processed into low-defect, wide-area thin films and ordered arrays using CO_2-expanded liquids. *Langmuir*, **22** (9), 3964–3971.

Liu, J., Sutton, J. & Roberts, C. B. (2007). Synthesis and extraction of monodisperse Sodium carboxymethylcellulose-stabilized platinum nanoparticles for the self-assembly of ordered arrays. *Journal of Physical Chemistry* C, **111** (31), 11566–11576.

Livermore, D. M. (2002). Multiple mechanisms of antimicrobial resistance in *Pseudomonas aeruginosa*: Our worst nightmare? *Clinical Infectious Diseases*, **34,** 634–640.

Lowy, F. D. (1998). *Staphylococcus aureus* infections. *The New England Journal of Medicine*, **339**, 520–532.

Lu, J., Wei, S., Peng, Y., Yu, W. & Qian, Y. (2003). Synthesis,structure, and luminescence of 2D-dilute magnetic semiconductors: Zn1−xMnxSe·0.5L (L=diamines). *Journal of Physical Chemistry B*, **107** (15), 3427–3430.

Lyczak, J. B., Cannon, C. L. & Pier, G. B. (2000) Establishment of *Pseudomonas aeruginosa* infection: lessons from a versatile opportunist. *Clinical* M*icrobiology and Infection*, **2**, 1051–1060.

Lynch, M. & Conery, J.S. *(*2003*).* The origins of genome complexity. *Science.* **302,** 1401–1404.

Maensiria, S., Laokula, P., Klinkaewnaronga, J., Phokhaa, S., Promarakc, V. & Seraphin, S. (2008). Indium oxide (In_2O_3) nanoparticles using *Aloe vera* plant extract: Synthesis and optical properties. *Journal of Optoelectronics and Advanced Materials*, **10** (3), 161 – 165.

Maier, S. A. (2007). *Plasmonics: fundamentals and applications*, Springer (1st Edition) Springer Science and Business Media. New York, U.S.A., 224.

Mandal, D., Bolander, M. E., Mukhopadhyay, D., Sarkar, G. and Mukherjee, P. (2006). The use of microorganisms for the formation of metal nanoparticles and their application. *Applied Microbiology and Biotechnology*, **69** (5), 485–492.

Manikam, V. R., Cheong, K. Y. & Razak, K. A. (2011). Chemical reduction methods for synthesizing Ag and Al nanoparticles and their respective nanoalloys. *Materials Science and Engineering* B, **176.** 187–203.

Marazzi, B., Endress, P. K., De Queiroz, L. P. & Conti, E. (2006). Phylogenetic relationships with Senna (Leguminosae, Cassiinae) based on three chloroplast DNA regions: patterns in the evolution of floral symmetry and extrafloral nectarines. *American Journal of Botany*, **93** (2), 288-303.

Marini, M., Niederhausern, S., Iseppi, R., Bondi, M., Sabia, C., Toselli, M., … Pilati, F. (2007). Antobacterial activity of plastic coated with silver-dopped organic-inorganic hybrid coatings prepared by sol-gel process. *Biomacromolecules*, **8**, 1246-1254.

Mazumder, V., Lee, Y. & Sun, S. (2010). Recent development of active nanoparticle catalyst for fuel cell reactions. *Advanced Functional Materials*, **20,** 1224.

Mazur, M. (2004). Electrochemically prepared silver nanoflakes and nanowires. *Electrochemistry Communications*, **6**, 400–403.

McCormick, P. G., Tsuzuki, T., Robinson, J. S. and Ding. (2001). Nanopowders synthesized by mechanochemical processing. *Advanced Materials*, **13,** 1008-1010.

McGraw-Hill Dictionary of Scientific & Technical Terms, 6E, McGraw-Hill Companies, Inc.

Mead, P. B. & Winn, W. C. (2000). Vaginal-rectal colonization with group A streptococci in late pregnancy. *Infectious Diseases in Obstetrics and Gynecology*, **8** (5-6), 217-219.

Meiller, T. F., Hube, B. & Schild, L. (2009). A novel immune evasion strategy of *Candida albicans*: proteolytic cleavage of a salivary antimicrobial peptide. *PLoS One*, **4** (4), Article ID e5039.

Mididea experting division extract professional (March 26, 2013), http: www.mididea.net

Miller, R. D, Prakash, S. & Prakash, L. (1984). Different effects of RAD genes of Saccharomyces cerevisiae on incisions of interstrand crosslinks and monoadducts in DNA induced by psoralen plus near UV light treatment. *Photochemistry Photobiology*, **39** (3), 349-352.

Mntungwa, N., Pullabhotla, S. R. & Revaprasadu, N. (2012). Facile synthesis of organically capped CdTe nanoparticles. *Journal of Nanoscience and Nanotechnology*, **12**, 2640-2644.

Mohanpuria, P., Rana, N. K. & Yadav, S. K. (2008). Biosynthesis of nanoparticles: technological concepts and future applications. *Journal of Nanoparticle Research*, **10** (3), 507–517.

Moon, C. Y., Dalpian, G. M., Zhang, Y., Wei, S. H., Huang, X. Y. & Li, J.(2006). Study of phase selectivity of organic-inorganic hybrid semiconductors. *Chemistry of Materials*, **18** (12), 2805–2809.

Moore, N. M. & Flaws, M. L. (2011). Antimicrobial resistance mechanisms in *Pseudomonas aeruginosa*. *Clininical Laboratory Science*, **24,** 47–51.

Morton, J. F. (1987). *Fruits of warm climates*. Florida Flair Books, Miami, 221-239.

Mourato, A., Gadanho, M., Lino, A. R. and Tenreiro, R. (2011). Biosynthesis of crystalline silver and gold nanoparticles by extremophilic yeasts. *Bioinorganic Chemistry and Applications*. Vol. 2011, Article ID 546074, 8 pages. Doi:10.1155/2011/546074

Mukherjee, P., Ahmad, A. & Mandal, D. (2001a). Fungus-mediated synthesis of silver nanoparticles and their immobilization in themycelialmatrix: a novel biological approach to nanoparticles synthesis. *Nano Letters*, **1**, (10), 515–519.

Mukherjee, P., Ahmad, A. &Mandal, D. (2001b). Bioreduction of AuCl4 − ions by the fungus, *Verticillium* sp. and surface trapping of the gold nanoparticles formed. *Angewandte Chemie— International Edition*, **40** (19), 3585–3588.

Mullin, J. W. (1997). Crystallization (3rd Edition), Butterworth- Heinemann, Boston. 358-360.

Mulvaney, P. (1996). Surface plasmon spectroscopy of nanosized metal particles. *Langmuir*, **12** (3), 788–800.

Mulvihill, M., Ling, X., Henzie, J. & Yang, P. (2009). Anisotropic etching of silver nanoparticles for plasmonic structures capable of single-particle SERS. *Journal of American Chemical Society,* **132** (1), 268–274.

Murali, S., Absar, A., Khan, I. M. & Rajiv, K. (2003). Biosynthesis of metal nanoparticles using fungi and actinomycetes. *Current Science*, **85** (2), 62–170.

Murphy, C., Sau, T., Gole, A., Orendorff, C., Gao, J., Gou, L. … Li, T. (2005). Anisotropic metal nanoparticles: synthesis, assembly, and optical applications. *Journal of Physical Chemistry B,* **109**, 13857-13870.

Murray, C. B., Kagan, C. R. & Bawendi, M. G. (2000). Synthesis and characterization of monodisperse nanocrystals and close-packed nanocrystal assemblies. *Annual Review of Materials,* **30,** 545-610.

Mythili, Gajalakshmi & Sathiavelu (2011). Pharmacological activities of *Cassytha filiformis.* A Review. *Asian Journal of Plant Science and Research,* **1** (1), 77-83.

Nadkarni, A. K. (1991). *Indian materia medica*, (3rd Edition), Bombay Popular Prakashan, Bombay, India**.** 255.

Naglik, J. R., Challacombe, S. J. & Hube, B. (2003). *Candida albicans* secreted aspartyl proteinases in virulence and pathogenesis. *Microbiology and Molecular Biology Reviews*, **67** (3), 400–428.

NCCLS, (1993) National Committee for Clinical Laboratory Standards.

Naqvi, S. Z., Kiran, U. M. & Ali, I. (2013). Combined efficacy of biologically synthesized silver nanoparticles and different antibiotics against multidrug-resistant bacteria. *International Journal of Nanomedicine*, **8**, 3187–3195.

Navrotsky, A. (2004). Energetic clues to pathways to biomineralization: Precursors, clusters, and nanoparticles. Proceedings of the National Academy of Sciences of the United States of America, **101**, 12096-12101.

Nazzaro, F., Fratianni, F., Martino, L., Coppola, R. & Feo, V. (2013). Effect of essential oils on pathogenic bacteria. *Pharmaceuticals (Based),* **6** (12), 1451-74.

Nelson, S. C. (2008). *Cassytha filiformis*. Honolulu (HI): University of Hawaii. 10 p. (Plant Disease, PD-42).

Nemade, K. R. & Waghuley, S. A. (2013). UV–VIS spectroscopic study of one pot synthesized strontium oxide quantum dots. *Results in Physics,* **3**, 52-54.

Neuwinger, H. (2000). A dictionary of plant use and application. *African Traditional Medicine*. Stuttgart: Medpharm Scientific Publication, Germany. (Pp. 29-30).

Nirmal, S. A., Shelke, S. M., Garge, P. B., Jadhav, P.R. & Dethe, A. (2007). Antinociceptiv and anthelmintic activity of *Canna indica* L. *Natural Product Research*, **21** (12), 1042-1047.

Okoro, E. C. (2007). Production of red wine from roselle (*Hibiscus sabdariffa*) and pawpaw (*Carica papaya*) using palm-wine yeast (*Saccharomyces cerevisiae*). *Nigerian Food Journal*, **25** (2), 158–164.

Oldenburg, S. J., Averitt, R. D., Westcott, S. L. & Halas, N. J. (1998). Nanoengineering of optical resonances. *Chemical Physics Letters,* **28**, 243–247.

Ostwald, W. (1879). Studien uber die Bildung und Umwandlung fester Korper. *Zeitschrift für Physikalische Chemie* (*Z Phys Chem* N F). **22**, 289-330.

Pabst, W. & Gregorova, E. (2007). Characterization of particles and particle systems. *ICT Prague,* 121-123.

Pamplin, B. R. (1975*). Crystal growth*. Pergamon Press: New York. (Pp. 131-142).

Parak, W. J., Gerion, D. T., Pellegrino, Zanchet, D., Micheel, C., Williams, S.C., …Alivisatos, A. P. (2003). Biological applications of colloidal nanocrystals. *Nanotechnology*, **14** (7), 15-27.

Parashar, U. K.& Srivastava, S. P. (2009). Bioinspired synthesis of silver nanoparticles. *Digest Journal of Nanomaterials and Biostructures*, **4** (1), 159-166.

Paskevicius, M., Webb, J., Pitt, M. P., Blach, T. P., Hauback, B. C., Gray, E., … Buckley, C.E. (2009). Mechanochemical synthesis of aluminium nanoparticles and their deuterium sorption properties to 2 kbar. *Journal of alloys and compounds*, **481** (2), 595-599.

Pedersen, K. (2006). Lecture notes to the course *Organic and Inorganic Nanostructures* Department of Physics and Nanotechnology Aalborg University.

Peng, X., Wickham, J. & Alivisatos, A. (1998). Kinetics of II-VI and III-V colloidal semiconductor nanocrystal growth: "focusing" of size distributions. *Journal of the American Chemical Society*, **120** (21), 5343–5344.

Penn, R. L. (2004). Kinetics of oriented aggregation. *Journal of Physical Chemistry B,* **108**, (34), 12707-12712.

Penn, R. L. & Banfield, J. F. (1999). Morphology development and crystal growth in nanocrystalline aggregates under hydrothermal conditions: insights from titania. *Geochimica* et *Cosmochimica Acta*, **63**, 1549-1557.

Penn, R. L. & Banfield, J. F. (1998). Imperfect oriented attachment: dislocation generation in defect-Free nanocrystals. *Science*, **281,** (5379), 969

Penn, R. L., Oskam, G., Strathmann, T. J., Searson, P. C., Stone, A. T. & Veblen, D. (2001). Epitaxial Assembly in Aged Colloids. *Journal of physical chemistry B*, **105** (11), 2177–2182.

Pfaller, M. A. & Diekema, D. J. (2007). Epidemiology of invasive candidiasis: a persistent public health problem. *Clinical Microbiology Reviews*, **20**, (1), 133–163.

Philip, D. (2010). Green synthesis of gold and silver nanoparticles using *Hibiscus rosa sinensis*. *Physica E*, **42**, 1417–1424.

Pinkas, J., Reichlova, V., Zboril, R., Moravec, Z., Bezdicka, P. & Matejkova, J. (2008). Sonochemical synthesis of amorphous nanoscopic iron(III)oxide from $Fe(acac)_3$. *Ultrasonics Sonochemistry*, **15**, 257–264.

Plata1, K., Rosato, A. E. and Węgrzyn1, G. (2009). *Staphylococcus aureus* as an infectious agent: overview of biochemistry and molecular genetics of its pathogenicity. *Acta Biological Polonical*, **56** (4), 597-612.

Pliofkhazraei, M. & Rouhaghdam, A. S. (2010). Fabrication of nanostructures by Plasma electrolysis.WILEY-VCH Verlag GmbH & Co. KGaA, Weinheim ISBN: 978-3-527-326754

Plotto, A. (2004). *Hibiscus*: post-production management for improved market access. In: Food and Agriculture Organization of the UN (FAO).

Pokropivny, V. R., Lohmus, I., Hussainova, A., Pokropivny, S. & Vlasso, V. (2007). *Introduction in nanomaterials and nanotechnology*. Tartu University Press ISBN: 978–9949–11–741–3. (Pp. 225-240).

Ponarulselvam, S., Panneerselvam, C., Murugan, K., Aarthi, N., Kalimuthu, K. & Thangamani, S. (2010). Synthesis of silver nanoparticles using leaves of *Caranthus roseuslinn* and their antiplasmodial activities. *Asian Pacific Journal* of *Tropical Medicine*, **2,** 574–580.

Poole Jr., C. P. & Owens, F. J. (2003). *Introduction to Nanotechnology*, John Wiley & Sons, Inc., New Jersey. (Pp. 328).

Pouget, E. M. (2009). The initial stages of template-controlled $CaCO_3$ formation revealed by cryo-TEM. *Science*, **323**, 1455-1458.

Pruppacher, H. R. & Klett, J. D. (1997). *Microphysics of clouds and precipitation*. Dordrecht: Kluwer Academic Publishers. (Pp. 950-954).

Puntes, V. F., Zanchet, D., Erdonmez, C. K. & Alivisatos, A. P. (2002). Synthesis of hcp-Co Nanodisks. *Journal of American Chemical Society*, **124,** (43) 12874 –12880.

Rahim, A. F., Hashim, M. R. & Ali, N. K. (2011). High sensitivity of palladium on porous silicon MSM photodetector. *Physica B: Condensed Matter*, **406** (4) 1034-1037.

Rai, M., Yadav, A. & Gade, A. (2008). CRC 675—Current trends in phytosynthesis of metal nanoparticles. *Critical Reviews in Biotechnology*, **28** (4), 277–284.

Rao, P. U. (1996). Nutrient composition and biological evaluation of mesta (*Hibiscus sabdariffa*) seeds. *Plant Foods for Human Nutrition*, **49** (1), 27–34.

Rajaram, C. V., Hudson, S. D. & Chien, L. C. (1995). Morphology of polymer-stabilized liquid crystals. *Journal of Materials Chemistry,* 7, 2300-2308.

Rajaram, C. V., Hudson, S. D. & Chien, L. C. (1998). Morphology of dia-crylate copolymer networks formed in liquid crystalline media. *Polymer*. **39**, 5315-5319.

Ramage, G., Bachmann, S., Patterson, T. F., Wickes, B. L. & Opez-Ribot, J. L. (2002). investigation of multidrug efflux pumps in relation to fluconazole resistance in *Candida albicans* biofilms. *Journal of Antimicrobial Chemotherapy*, **49** (6), 973–980.

Ramage, G., VandeWalle, K., Opez-Ribot, J. L. & Wickes, B. L. (2002). The filamentation pathway controlled by the Efg1 regulator protein is required for normal biofilm formation and development in *Candida albicans*. *FEMS Microbiology Letters*, **214** (1), 95–100.

Rasi, A. & Pour-Heidari, N. (2009). Association between plaque-type psoriasis and perianal streptococcal cellulitis and review of the literature. *Archives of Iranian Medicine,* **12** (6), 591-594.

Rauwel, P., Küünal, S., Ferdov, F. and Rauwel, E. (2015). A Review on the green synthesis of silver nanoparticles and their morphologies studied via TEM. *Advances in Materials Science and Engineering*. Article ID 682749, 9 pages,.

Raveendran, P., Fu, J. & Wallen, S. L. (2003). Completely "Green" synthesis and stabilization of metal nanoparticles. *Journal of the American Chemical Society,* **125** (46), 13940–13941.

Reddy, K. R. (1988). Folk medicine from Chittoor district Andhra Pradesh, India used in the treatment of jaundice. *International Journal of Crude Drug Research,* **26,** 137-140.

Ren, Nan, Timko & Michael P. (2001). AFLP analysis of genetic polymorphism and evolutionary relationships among cultivated and wild Nicotiana species. *Genome,* **44** (4), 559–71.

Robinson, I., Zacchini, S., Tung, L. D., Maenosono, S. & Thanh, N. T. K. (2009). Synthesis and characterization of magnetic nanoalloys from bimetallic carbonyl clusters. *Chemistry of Materials*, **21** (13), 21, 3021–3026. Doi: 10.1021/cm9008442.

Roduner, E. (2006). Nanoscopic materials: size-dependent phenomena, Cambridge, UK: RSC Publishing, 213-250.

Rossetti, R. & Brus, L. (1982). Electron-hole recombination emission as a probe of surface-chemistry in aqueous CdS colloids. *Journal of Physical Chemistry,* **86**, 4470–4472.

Roy, N. & Barik, A. (2010). Green Synthesis of Silver Nanoparticles from the unexploited weed resources. *International Journal of Nanotechnology and Applications*, **4** (2), 95-101.

Ruhnke, M. & Maschmeyer, G.(2002). Management of mycoses in patients with hematologic disease and cancer—review of the literature. *European Journal of Medical Research*, **7** (5), 227–235.

Sadikot, R.T., Blackwell, T. S., Christman, J. W. & Prince, A. S. (2005) Pathogen-host interactions in Pseudomonas aeruginosa pneumonia. *American Journal of Respiratory and Critical Care Medicine*, **171**, 1209–1223.

Samadi, N., Golkaran, D., Eslamifar, A., Jamalifar, H., Fazeli, M. R. & Mohseni, F. A. (2009). Intra/extracellular biosynthesis of silver nanoparticles by an autochthonous strain of Proteus mirabilis isolated from photographic waste. *Journal of Biomedical Nanotechnology*, **5** (3), 247–253.

Saravanan, M., Amelash, T. & Negash, L. (2014). Extracellular biosynthesis and biomedical application of silver nanoparticles synthesized from baker's yeast. *International Journal of Research in Pharmaceutical and Biomedical Sciences*, **4** (3), 822–828.

Sastri, B. N. (1962). *The Wealth of India: raw materials* CSIR, New Delhi. (Pp. 47-50).

Sathishkumar, M., Sneha, K., Won, W. S., Cho, C. W., Kim, S. & Yun, Y. S. (2009). *Cynamon zeylanicum* bark extract and powder mediated green synthesis of nanocrystalline silver particles and its bactericidal activity. *Colloids Surfaces, B:Biointerfaces*, **73,** 332- 338.

Scheffer, R. P. (1991). Role of toxins in evolution and ecology of plant pathogenic fungi. *Experientia,* **47**, 804–811.

Schelenz, S. (2008). Management of candidiasis in the intensive care unit. *Journal of Antimicrobial Chemotherapy*, **61** (1), 31–34.

Schito, G. C. (2006). The importance of the development of antibiotic resistance in *Staphylococcus aureus*. *Clinical Microbiology* and *Infection* **12 (**1), 3–8.

Schmidt, H. (2001). Nanoparticles by chemical synthesis, processing to materials and innovative applications. *Applied Organometallic Chemistry*, **15,** 331–343.

Schultz, D. A. (2003). Plasmon resonant particles for biological detection. *Current Opinion Biotechnology*, **14** (1), 13-22.

Schultz, M. J., Speelman, P., Zaat, S. A., Hack, C. E., Deventer, S. J. & Poll, T. (2000) The effect of Pseudomonas exotoxin A on cytokine production in whole blood exposed to *Pseudomonas aeruginosa*. *FEMS Immunology* and *Medical Microbiology*, **29,** 227–232.

Schulze, J. & Sonnenborn, U. (2009). Yeast in the Gut: from commensals to infectious agents. *Deutsches Arzteblatt*, **106** (52), 837–842.

Scott, R. W., Ye, H. C., Henriquez, R. R. & Crooks, R. M. (2003). Synthesis, characterization, and stability of dendrimer-encapsulated palladium nanoparticles. *Chemistry of Materials*, **15** (20), 3873-3878.

Shankar, S., Rai, A., Ahmad, A. & Sastry, M. (2004). Rapid synthesis of Au, Ag and bimetallic Au core-Ag shell nanoparticles using Neem (*Azadirachta indica)* leaf broth. *Journal* of *Colloid* and *Interface Science*., **275,** 496-502.

Shikhiev, A. S., Safarova, N. V. & Nurieva, L. A. (1987). D-mannitol from *Lawsonia inermis*. *Chemistry of Natural Compounds)*, **23** (2), 245.

Shinde, K. N. (2013). *Phosphate Phosphors for Solid-State Lighting*. Springer Series in Materials Science, **174**, 41-43.

Singaravelu, G., Arockiamary, J. S., Kumar, V. G. & Govindaraju, K. (2007). A novel extracellular synthesis of monodisperse gold nanoparticles using marine alga, *Sargassum wightii Greville*. *Colloids and Surfaces B: Biointerfaces*, **57** (1), 97–101.

Skrabalak, S., Chen, J., Sun, Y., Lu, X., Au, L., Cobley, C., …Xia, Y. (2008). Gold nanocages: synthesis, properties, and applications. *Accounts of Chemical Research*, **41** (12), 1587-95.

Slutsky, M., Staebell, J., Anderson, M., Pfaller, & Soll, D. R. (1987). White-opaque transition: a second high-frequency switching system in *Candida albicans*. *Journal of Bacteriology*, **169** (1), 189–197.

Smith, A. M., Duan, H., Rhyner, M. N., Ruan, G. & Nie, S. (2006). A systematic examination of surface coatings on the optical and chemical properties of semiconductor quantum dots. *Physical Chemistry Chemical Physics*, **8** (33), 3895-3903.

Smith, E. E., Buckley, D. G. & Wu, Z. (2006). Genetic adaptation by *Pseudomonas aeruginosa* to the airways of cystic fibrosis patients. Proceedings of the National Academy of Sciences, **103,** 8487–8492.

Sobel, J. D. (1997). Current concepts: Vaginitis. *New England Journal of Medicine*, **337** (26), 1896–1903.

Solid-State Physics. (2015). *Wikipedia, the free Encyclopedia*. Wikipedia, Accessed 11 May. 2015.http://en.wikipedia.org/w/index.php?title=Solid state_physics&oldid=661807419

Song, J. Y., Kwon E. Y. & Kim, B. S. (2010). Biological synthesis of platinum Nanoparticles using *Diopyros kaki* leaf extract. *Bioprocess and Biosystems Engineering*, **33** (1), 159-164.

Sousa, C.P. (2003). Pathogenicity mechanisms of prokaryotic cells: an evolutionary view. *Brazilian Journal of Infectious Diseases*, 7 (1), 23-31.

Speziale, P., Pietrocola, G. &Rindi, S. (2009). Structural and functional role of *Staphylococcus aureus* surface components recognizing adhesive matrix molecules of the host. *Future Microbiology*, **4** (10), 1337–1352.

Srivastava, J. & Vankar, P. S. (2010). *Canna indica* flower: New source of anthocyanins. *Plant Physiology and Biochemistry*, **48** (12), 1015-1019.

Steiner, D., Mokari, T., Banin, U. & Millo, O. (2005). Electronic structure of metal-semiconductor nanojunctions in gold CdSe nanodumbbells. *Physical Review Letters*, **95** (5), 1–4.Article ID 056805.

Sugimoto, T. (2001). *Monodispersed particles*. Institute for Advanced Materials, Tohoku University, Japan, Tokyo. 40-45.

Sugimoto, T. & Shiba, F. (2000). Spontaneous nucleation of monodisperse silver halide particles from homogeneous gelatin solution II: silver bromide. *Colloids and Surfaces A*, **164**, 205-215.

Sugimoto, T., Shiba, F., Sekiguchi, T. & Itoh, H. (2000). Spontaneous nucleation of monodisperse silver halide particles from homogeneous gelatin solution I: silver chloride. *Colloids and Surfaces A*, **164** (2), 183-203.

Swarnalathan, R., Christina, R. S. & Payas, B. (2012). Evaluation of in vitro antidiabetic activity of *Sphaeranthus amaranthoides* silver nanoparticles. *International Journal of Nanomaterials Biostructures*, **2** (3), 25–29.

Takacs, L. (1996). Multiple combustion induced by ball milling. *Applied Physics Letters*, **69**, 436-438.

Takagahara, T. & Takeda, K. (1992). Theory of the quantum confinement effect on excitons in quantum dots of indirect-gap materials. *Physica Review B,* **46** (23), 15578-15581.

Tanko, Y., Kamba, B., Saleh, M. I., Musa, K. Y. & Mohammed A. (2008). Anti-nociceptive and anti-inflammatory activities of ethanolic flower extract of *Newbouldia laevis* in mice and rats. *International Journal of Applied Research in Natural. Product,* **1**, 13–19.

Tauran, Y., Brioude, A., Coleman, A.W., Beonjoom, M. R. & Kim. (2013). Review: Molecular recognition by gold, silver and copper nanoparticles. *World Journal of Biological Chemistry,* **26** (3), 35-63.

Templeton, A. C., Pietron, J. J., Murray, R. W. & Mulvaney, P. (2000). Solvent refractive index and core charge influences on the surface plasmon absorbance of alkanethiolate monolayerprotected gold clusters. *Journal of Physical Chemistry B*, **104** (3), 564–570.

Terao, Y., Kawabata, S., Kunitomo, E., NakagawaI & Hamada, S. (2002). Novellaminin-binding proteinof Streptococcus pyogenes, Lbp, is involved in adhesion to epithelial cells. I*nfectImmun,* **70,** 993–997.

Thomas, K. G., Zajicek, J. & Kamat, P. V.(2002). Surface binding properties of tetraoctylammonium bromide-capped gold nanoparticles. *Langmuir*, **18** (9), 3722–3727.

Tian, N., Zhou, Z., Sun, S., Ding, Y. & Wang, Z. (2007). Synthesis of tetrahexahedral platinum nanocrystals with high-index facets and high electro-oxidation activity. *Science*, **316** (5825), 732-735.

Todar, K. (2002). Todar's online textbook of bacteriology, University of Wisconsin-Madison, Department of Bacteriology.

Tripathy, A., Raichur, M. A., Chandrasekaran, N., Prathna, T. C. & Mukherjee, A. (2010). Process variables in biomimetic synthesis of silver nanoparticles by aqueous extract of *Azadirachta indica* (Neem) leaves. *Journal of Nano Research,* **12** (1), 237-246.

Tsarfaty, I., Sandovsky-Losica, H., Mittelman, L., Berdicevsky, I. & Segal, E. (2000). Cellular actin is affected by interaction with *Candida albicans. FEMS Microbiology Letters* **189,** 225–232.

Tsai, P., McIntosh, J., Pearce, P., Camden, B. & Jordan, B. (2002). Anthocyanin and antioxidant capacity in Roselle (*Hibiscus Sabdariffa* L.) extract. *Food Research,* **35** (4), 351–356.

Usman, H. & Osuji, J. C. (2007). Phytochemical and in vitro antibacterial assay of the leaf extract of Newbouldia laevis. *African Journal of Traditional, Complementary and Alternative Medicines,* **4**, 476–480.

Vasudevan, T. N. & Laddha, K. S. (2003). *Herbal drug microscopy*, Yucca publishing house, Dombivli, 68-69.

Velicov, K. P., Zegers, G.E. & Blaaderem, V. (2003). Synthesis and characterization of large colloidal silver particles. *Langmuir*, **19** (4), 1384–1389.

Vigneshwaran, N., Kathe, A. A., Varadarajan, P. V., Nachane, R. P. & Balasubramanya, R. H. (2006). Biomimetics of silver nanoparticlesby white rot fungus, *Phaenerochaete chrysosporium*. *Colloids and Surfaces B: Biointerfaces*, **53** (1), 55–59.

Villanueva, F. (2010). The most successful fungus in causing dermatophytosis in humans: *Trichophyton rubrum.Microbiologics Inc.*.

Wageh, S. (2007). Raman and photoluminescence study of CdSe nanoparticles capped with a bifunctional molecule, *Physica E*, **39**. 8–14.

Wagner, C. (1961). Thoerie der altering von neiderschlagen durch umlosen. *Z Elektrochem*, **65**, 581-588.

Walker, M., Bethell, D., Schiffrin, D. J. & Whyman, R. (1994). Synthesis of thiol-derivatised gold nanoparticles in a two-phase liquid-liquid system, *Journal of the Chemical Society, Chemical Communications,* **7,** 801–802.

Wang, H. Y., Li, Y. F. & Hua, C. Z. (2007). Detection of ferulic acid based on the Plasmon resonance light scattering of silver nanoparticles, special issue on China- Japan-Korea environmental analysis. *Talanta*, **72** (5), 1698-1703.

Wang, L. & Yamauchi, Y. (2009). Block copolymer mediated synthesis of dendritic platinum nanoparticles. *Journal of American Chemical Society*, **131** (26), 9152–9153.

Wani, I. A., Khatoon, S., Ganguly, A., Ahmed, J., Ganguli, A. K. & Ahmad, T. (2010). Silver nanoparticles: Large scale solvothermal synthesis and optical properties. Materials Research Bulletin, **45**, 1033–1038.

Wanke, C. A. (2013). Pathogenic Escherichia coli.Uptodate Inc. 202-207.

Wasylnka, J. A. & Moore, M. M. (2002). Uptake of *Aspergillus fumigatus* conidia by phagocytic and nonphagocytic cells *in vitro:* quantitation using strains expressing green fluorescent protein. *Infection* and *Immunity*, **70,** 3156–3163.

Wei, G. H., Zhou, Z. & Liu, Z. (2005). A simple method for the preparation of ultrahigh sensitivity surface enhanced Raman scattering (SERS) active substrate. *Applied Surface Science*, **240** (1-4), 260-267.

Weirzman, I. & Summerbell, R.C. (1995). The dermatophytes. *Clinical Microbiology Reviews*, **8** (2), 240- 259.

Wey, S. B., Mori, M., Pfaller, M. A., Woolson, R. F. & Wenzel, R. (1998). Hospital-acquired candidemia. The attributablemortality and excess length of stay. *Archives of Internal Medicine*, **148** (12), 2642–2645.

Wiley, B. J., McLellan, S. H., Siekkinen, J. A. & Xia, Y. (2006). Manoeuvring the surface plasmon resonance of silver nanostructures through shape-controlled synthesis. *Journal of Physical Chemistry B,* **110**, 15666–15675.

Willets, K. A. & Duyne, R. P. (2007). Localized surface plasmon resonance spectroscopy and sensing. *Annual Review of Physical Chemistry*, **58**, 267-270.

Wise, F.W. (2000). Lead Salt Quantum Dots: the Limit of Strong Quantum Confinement. *Accounts of Chemical Research*, **33** (11), 773–780.

Woradulayapinij, W., Soonthornchareonnon, N. & Wiwat, C. (2005). In vitro HIV type 1reverse transcriptase inhibitory activities of Thai medicinal plants and *Canna indica L*. rhizomes. *Journal of Ethnopharmacology*, **101** (3), 84-89.

Wu, M. L. & Lai, L. B. (2004). Synthesis of Pt/Ag bimetallic nanoparticles in water-in-oil Microemulsions. *Colloids and Surfaces A*, **244** (3), 149–157.

Xia, L., Hu, X., Kang, X., Zhao, H., Sun, M. & Chen, X. (2010). A onestep facile synthesis of Ag–Ni core-shell nanoparticles in water in-oil microemulsions. *Colloids and Surfaces A,* **367**, 96–101.

Xie, X. Y., Zheng, W. J., Bai, Y. and Liu, J. (2009). Cystine modified nanosulfur and its spectral properties. *Materials Letters.* **63,** 1374-1376.

Xu, B., Jahic, M., Blomsten, G., & Enfors, S. O. (1999). Glucose overflow metabolism and mixed-acid fermentation in aerobic large-scale fed-batch processes with *Escherichia coli*. *Applied Microbiology Biotechnology*, **51,** 564–571.

Xu, H. & Suslick, K. (2010). Water soluble fluorescent silver nanoclusters. *Advanced Materials*, 22, 1078-1082.

Xu, Y., Zhu, Y., Zhao, F. & Ma, C. (2007). Electrocatalytic reductive dehalogenation of polyhalogenated phenols in aqueous solution on Ag electrodes. *Applied Catalysis A General*, **324**, 83-86.

Yadav, R. N. & Agarwala, M. (2011). Phytochemical analysis of some medicinal plants. *Journal of Phytology*, **3** (12), 2075-6240.

Yang, X., Li, Q., Wang, H., Huang, H., Lin, L., Wang, W., … Jia, L. (2010). Green synthesis of palladium nanoparticles using broth of *Cinnamomum camphora* leaf. *Journal of Nanoparticle Research,* **12,** 1589–1598.

Yeadon, M., Ghaly, Yang, J. C., Averback, R. S. & Gibson, J. M. (1998). Contact epitaxy observed in supported nanoparticles. *Applied Physics Letters*, **73**, 3208-3210.

Yoffe, A.D. (1993). Low-dimensional systems: quantum size effects and electronic properties of semiconductor microcrystallites (zero-dimensional systems) and some quasi-two-dimensional systems. *Advances in Physics,* **42** (2), 173-262.

Yongqi, F., Fengzhou, F. & Zongwei, X. (2011). Nanofabrication and characterization of Plasmonic structures. Nanofabrication, Yoshiitake Masuda. Ed. China: InTech. 244-266.

Yu, H., Chen, M., Rice, P. M., Wang, S. X., White, R. L. & Sun, S. (2005). Dumbbell-like bifunctional Au-Fe_3O_3 nanoparticles. *Nano Letters*, **5** (2), 379–382.

Zhang, Q., Liu, S. & Yu, S. (2009). Recent advances in oriented attachment growth and synthesis of functional materials: concept, evidence, mechanism, and future. *Journal of Materials Chemistry*, **19,** 191–207.

Zhang, R., Khalizov, A., Wang, L., Hu, M. & Xu, W. (2012). Nucleation and growth of nanoparticles in the atmosphere. *Chemical Reviews,* **112** (3), 1957-2011.

Zhang, Y., Dalpian, G. M. & Fluegel, B. (2006). Novel approach to tuning the physical properties of organic-inorganic hybrid semiconductors. *Physical Review Letters,* **96** (2).

Zhang, Y., Yang, D., Kong, Y., Wang, X., Pandoli, O. & Gao, G. (2010). Synergetic antibacterial effects of silver nanoparticles *Aloe vera* prepared via a green method. *Nano Biomedicine and Engineering,* **2** (4), 252-257.

Zhao, Y., Zhang, Z., Dang, H. & Liu, W. (2004). Synthesis of tin sulfide nanoparticles by a modified solution dispersion method. *Materials Science Engineering B,* **113**, 175-178.

Zheng, H., Smith, R. K., Jun, Y.w., Kisielowski, C., Dahmen, U. & Alivisatos, A. P. (2009). Observation of single colloidal platinum nanocrystal growth trajectories. *Science.* **324** (5932-5939), 1309-1312.

Zielinski, T. J. & Shalhoub, G. M. (1986*). Introduction to Franck-Condon Factors*. American Chemical Society. 1191-1192.

APPENDICES

APPENDIX I: Zones of Inhibition

Plate 4.1: Inhibition zone of Ag nanoparticles formed using *C. indica* (AAg 0.5, 1.0, 2.0 and 3.0) against *Staphylococcus aureus*

Plate 4.2: Inhibition zone of nanoparticle formed using *S. occidentalis* (BAg 0.5, 1.0, 2.0 and 3.0) against *Sreptococcus pyogenes*

Plate 4.3: Inhibition zone of Nanoparticle by *C. filiformis* (DAg 0.5, 1.0, 2.0 and 3.0) against *Escherichia coli*

Plate 4.4: Inhibition zone of Ag nanoparticle formed using the leaf extract of *C. indica* (A Ag 0.5, 1.0, 2.0 and 3.0) against *Candida albicans*

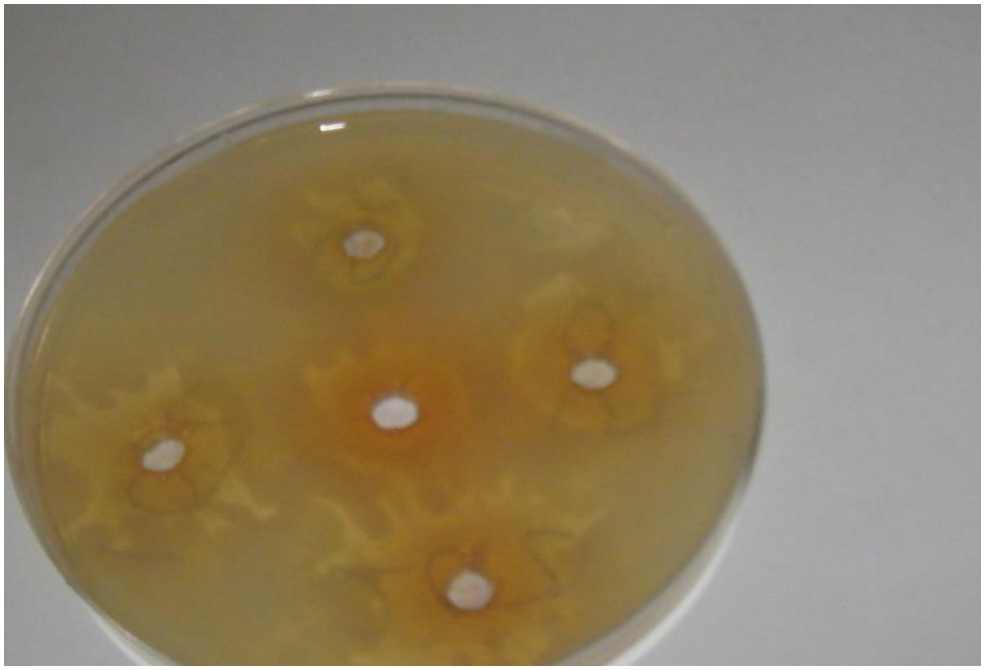

Plate 4.5: Inhibition zone of Ag-Ni bimetallic nanoparticles formed using *C. indica* leaf extracts (A1, A2, A3 and A4) against *Pseudomonas aeruginosa*

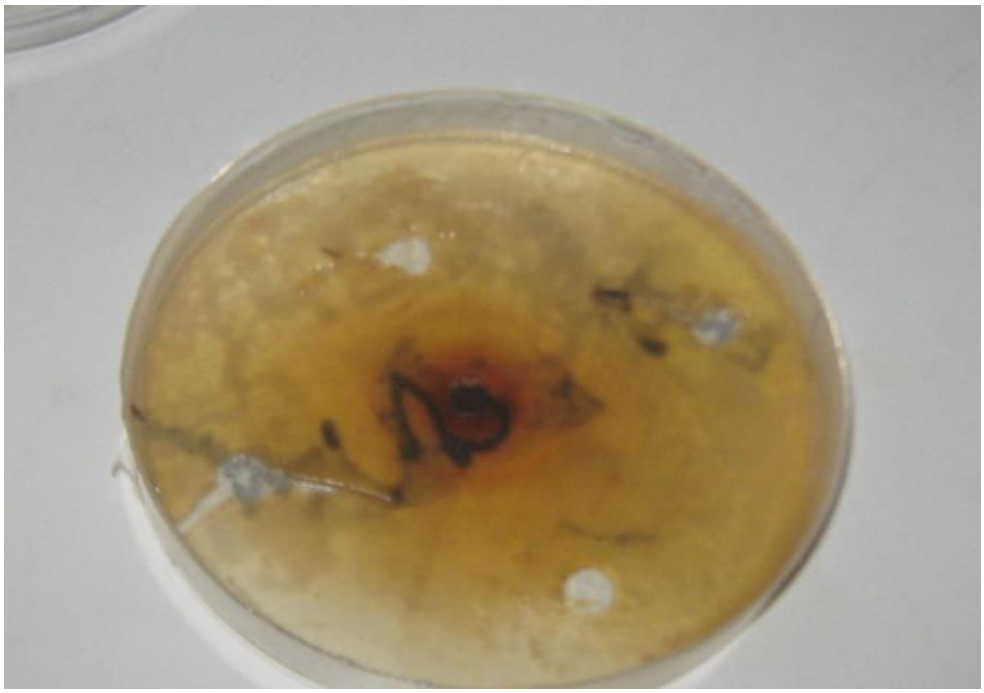

Plate 4.6: Inhibition zone of Ag-Ni nanoparticles formed using *C. indica* leaf extract (A1, A3 and A4) against *T.rubrum*

APPENDIX II: Sensitivity of Test Organisms (Agar Diffusion Test)

Nanoparticles	Organisms/Mean Zone diameter (mm) *In vitro* antibacterial activity				*In vitro* antifungal activity	
	Staphylococcus aureus	*Streptococcus pyogenes*	*Escherichia coli*	*Pseudomonas aeruginosa*	*Candida albicans*	*Trichophyton rubrum*
A Ag 0.5	7	9	7	Nil	9	Nil
A Ag 1.0	8	12	9	Nil	12	7
A Ag 2.0	10	15	13	7	13	8
A Ag 3.0	13	14	15	8	15	9
B Ag 0.5	7	8	7	Nil	8	7
B Ag 2.0	11	11	10	7.0	9	8
B Ag 3.0	12	13	12	9	11	9
C Ag 2.0	10	11	9	7	10	9
C Ag 3.0	12	13	10	9	12	10
D Ag 0.5	7	8	7	Nil	8	Nil
D Ag 1.0	8	10	8	Nil	11	7
D Ag 2.0	11	13	11	7	12	9
D Ag 3.0	13	15	12	9	14	10
Ds Ag 0.5	9	7	9	Nil	7	8
Ds Ag 1.0	12	10	11	7	9	9
DS Ag 2.0	13	12	13	8	10	11
E Ag 0.5	7	7	8	Nil	Nil	Nil
E Ag 2.0	10	9	10	Nil	8	Nil
E Ag 3.0	12	10	11	8	10	Nil

Hybrid A Ag-Ni 0.5	9	11	12	8	8	9
A Ag-Ni 1.0	12	14	10	9	10	8
A Ag-Ni 2.0	13	15	14	8	11	12
A Ag-Ni 3.0	15	16	17	9	12	16
B Ag-Ni 1.0	8	10	9	7	7	7
B Ag-Ni 2.0	10	11	14	8	9	9
D Ag-Ni 3.0	12	13	12	10	10	10
D Ag-Ni 2.0	11	10	11	12	8	7
E Ag-Ni 2.0	7	8	7	Nil	8	7
E Ag-Ni 3.0	9	10	9	7	9	8
E Ag-Co 1.0	8	8	8	7	7	8
Standard	21	18	21	20	19	18

Control-Ciprofloxacin (Bacteria) and Fluconazole (Fungi), A Ag = Silver nanoparticles of specified precursor concentration using *C. indica* leaf extract, A Ag-Ni = Silver-nickel bimetallic nanoparticles of specified precursor concentration using *C. indica* leaf extract, B Ag = Silver nanoparticles of specified precursor concentration using *S. occidentalis* leaf extract, B Ag-Ni= Silver-nickel nanoparticles of specified precursor concentration using *S. occidentalis* leaf extract, D Ag= Silver nanoparticles of specified precursor concentration using *M. charantia* leaf extract D Ag-Ni = Silver-nickel nanoparticles of specified precursor concentration using *M. charantia* leaf extract, E Ag = Silver nanoparticles of specified precursor concentration using *C. filiformis* leaf extract, E Ag-Ni = Silver nanoparticles of specified precursor concentration using *C. filiformis* leaf extract

APPENDIX III: Sensitivity Testing of Organisms with Standard Deviation In Zones of Inhibition (Agar Diffusion Test)

Nanoparticles	Organisms/Mean zone diameter (mm) ± SD					
	Staphylococcus aureus	*Streptococcus pyogenes*	*Escherichia coli*	*Pseudomonas aeruginosa*	*Candida albicans*	*Trichophyton rubrum*
A Ag 0.5	7± 0.2	9 ± 0.4	7 ± 0.1	Nil	9 ± 0.2	Nil
A Ag 1.0	8 ± 0.5	12 ± 0.8	9 ± 0.2	Nil	12 ± 0.3	7 ± 0.2
A Ag 2.0	10 ± 0.4	15 ± 0.5	13 ± 0.4	7 ± 0.2	13 ± 0.4	8 ± 0.1
A Ag 3.0	13± 1	14 ± 0.2	15 ± 0.3	8 ± 0.1	15 ±0.2	9 ± 0.1
STAT	***P > 0.05***	***P > 0.05***	***P > 0.05***	***P > 0.05***	***P > 0.05***	***P > 0.05***
B Ag 0.5	7 ± 0.8	8 ± 0.2	7 ± 0.2	Nil	8 ± 0.2	7 ± 0.1
B Ag 2.0	11 ± 1	11 ± 0.4	10 ± 0.2	7.0 ± 0.2	9 ± 0.1	8 ± 0.2
B Ag 3.0	12 ± 0.5	13 ± 0.6	12 ± 0.4	9 ± 0.1	11 ± 0.1	9 ± 0.1
STAT	***P > 0.05***	***P > 0.05***	***P > 0.05***	***P > 0.05***	***P > 0.05***	***P > 0.05***
C Ag 2.0	10 ± 0.5	11 ± 0.5	9 ± 0.2	7 ± 0.1	10 ± 0.2	9 ± 0.3
C Ag 3.0	12 ± 0.3	13 ± 0.5	10 ± 0.5	9 ± 0.1	12 ± 0.1	10 ± 0.5
STAT	***P > 0.05***	***P > 0.05***	***P > 0.05***	***P > 0.05***	***P > 0.05***	***P > 0.05***
D Ag 0.5	7± 0.5	8 ± 0.2	7 ± 0.3	Nil	8 ± 0.2	Nil
D Ag 1.0	8 ± 0.5	10 ± 0.3	8 ± 0.1	Nil	11 ± 0.1	7 ± 0.3
D Ag 2.0	11 ± 0.3	13 ± 0.4	11 ± 0.4	7 ± 0.2	12 ± 0.1	9 ± 0.1
D Ag 3.0	13 ± 0.6	15 ± 0.6	12 ±0.2	9 ± 0.3	14 ± 0.2	10 ± 0.1
STAT	***P > 0.05***	***P > 0.05***	***P > 0.05***	***P > 0.05***	***P > 0.05***	***P > 0.05***
Ds Ag 0.5	9 ± 0.5	7 ± 0.2	9 ± 0.3	Nil	7 ± 0.2	8 ± 0.3
Ds Ag1.0	12 ± 0.4	10 ± 0.2	11 ± 0.4	7 ± 0.1	9 ± 0.1	9 ± 0.1
Ds Ag 2.0	13± 0.5	12 ± 0.4	13 ± 0.2	8 ± 0.2	10 ± 0.2	11 ± 0.3
STAT	***P > 0.05***	***P > 0.05***	***P > 0.05***	***P > 0.05***	***P > 0.05***	***P > 0.05***

E Ag 0.5	7 ± 0.1	7 ± 0.1	8 ± 0.1	Nil	Nil	Nil
E Ag 2.0	10 ± 0.2	9 ± 0.2	10 ± 0.4	Nil	8 ± 0.1	Nil
E Ag 3.0	12 ± 0.1	10 ± 0.3	11 ± 0.2	8 ± 0.1	10 ± 0.2	Nil
STAT	***P > 0.05***	***P > 0.05***	***P > 0.05***	***P > 0.05***	***P > 0.05***	***P > 0.05***
A Ag-Ni 0.5	9 ± 0.2	11 ± 0.4	12 ± 0.5	8 ± 0.3	8 ± 0.1	9 ± 0.2
A Ag-Ni 1.0	12 ± 0.3	14 ± 0.6	10 ± 0.2	9 ± 0.2	10 ± 0.2	8 ± 0.1
A Ag-Ni 2.0	13 ± 0.1	15 ± 0.2	14 ± 0.4	8 ± 0.1	11± 0.2	12 ± 0.3
A Ag-Ni 3.0	15 ± 0.4	16 ± 0.6	17 ± 0.6	9 ± 0.1	12 ± 0.1	16 ± 0.2
STAT	***P > 0.05***	***P > 0.05***	***P > 0.05***	***P > 0.05***	***P > 0.05***	***P > 0.05***
B Ag-Ni 1.0	8 ± 0.1	10 ± 0.1	9 ± 0.1	7 ± 0.2	7 ± 0.2	7 ± 0.1
B Ag-Ni 2.0	10 ± 0.2	11 ± 0.2	14 ± 0.2	8 ± 0.3	9 ± 0.2	9 ± 0.2
STAT	***P > 0.05***	***P > 0.05***	***P > 0.05***	***P > 0.05***	***P > 0.05***	***P > 0.05***
D Ag-Ni 3.0	12 ± 0.1	13 ± 0.3	12 ± 0.1	10 ± 0.2	10 ± 0.4	10 ± 0.1
D Ag-Ni 2.0	11 ± 0.3	10 ± 0.2	11 ± 0.2	12 ± 0.2	8 ± 0.1	7± 0.2
STAT	***P > 0.05***	***P > 0.05***	***P > 0.05***	***P > 0.05***	***P > 0.05***	***P > 0.05***
E Ag-Ni 2.0	7 ± 0.1	8 ± 0.1	7 ± 0.1	Nil	8 ± 0.1	7 ± 0.1
E Ag-Ni 3.0	9 ± 0.1	10 ± 0.1	9 ± 0.4	7 ± 0.1	9 ± 0.1	8 ± 0.3
E Ag-Co 1.0	8 ± 0.2	8 ± 0.2	8 ± 0.6	7 ± 0.2	7 ± 0.1	8 ± 0.1
STAT	**P < 0.05**	**P < 0.05**	**P < 0.05**	**P < 0.05**	**P < 0.05**	**P < 0.05**
Control	21 ± 0.8	18 ± 0.3	21 ± 0.2	20 ± 0.4	19 ± 0.6	18 ± 0.3
STAT	***Control vs Aa, Ba, Ca, Da, Ea, A,B,C,E , F-value 21.45, P < 0.05***					

Control -Ciprofloxacin (Bacteria) and Fluconazole (Fungi), mean zone inhibition (mm) ± standard deviation of three replicates

APPENDIX IV

Minimum inhibitory concentration (MIC), mMinimum bactericidal concentration (MBC) and minimum fungicidal concentration (MFC)

	Organisms/MIC, MBC & MFC (mg/mL)					
Organisms → Nanoparticles ↓	*Staphylococcus aureus* MIC, MBC	*Streptococcus pyogenes* MIC, MBC	*Escherichia coli* MIC, MBC	*Pseudomonas aeruginosa* MIC, MBC	*Candida albicans* MIC,MFC	*Trichophyton rubrum* MIC, MFC
A Ag 0.5	100, 100	50, 100	100, 100	100, 100	50, 50	100, 100
A Ag 1.0	100, 100	25, 50	50, 100	100, 100	25, 25	100, 100
A Ag 2.0	50, 100	12.5, 25	12.5, 25	100, 100	12.5, 25	100, 100
A Ag 3.0	12.5, 25	12.5, 25	12.5, 12.5	100, 100	12.5, 12.5	50, 100
STATISTICS	***P < 0.05***	***P < 0.05***	***P < 0.05***	***P < 0.05***	***P < 0.05***	***P < 0.05***
B Ag 0.5	100, 100	100, 100	100, 100	100, 100	100, 100	100, 100
B Ag 2.0	25, 50	25, 50	25, 50	100, 100	50, 100	100, 100
B Ag 3.0	12.5, 25	12.5, 25	12.5, 25	25, 50	25, 25	50, 100
STAT	**P < 0.05**	**P < 0.05**	**P < 0.05**	**P < 0.05**	**P < 0.05**	**P < 0.05**
C Ag 2.0	50, 50	25, 25	50, 100	100, 100	25, 50	50, 100
C Ag 3.0	12.5, 25	12.5, 12.5	25, 25	50, 50	12.5, 25	25, 50
STATISTICS	***P < 0.05***	***P < 0.05***	***P < 0.05***	***P < 0.05***	***P < 0.05***	***P < 0.05***
D Ag 0.5	100, 100	100, 100	100, 100	100, 100	100, 100	100, 100
D Ag 1.0	100, 100	25, 50	100, 100	100, 100	25, 50	100, 100
D Ag 2.0	12.5, 25	12.5, 12.5	12.5, 25	100, 100	12.5, 25	50, 100
D Ag 3.0	12.5, 12.5	12.5, 12.5	12.5, 25	50, 100	12.5, 12.5	50, 50
STATISTICS	***P < 0.05***	***P < 0.05***	***P < 0.05***	***P < 0.05***	***P < 0.05***	***P < 0.05***
Ds Ag 0.5	100, 100	100, 100	50, 100	100, 100	100, 100	100,100
Ds Ag1.0	12.5, 25	25, 50	25, 50	100, 100	50, 100	50, 100
Ds	12.5, 12.5	12.5, 25	12.5, 25	50, 100	50, 50	50, 50

Ag 2.0						
STATISTICS	***P < 0.05***	***P < 0.05***	***P < 0.05***	***P < 0.05***	***P < 0.05***	***P < 0.05***
E	100, 100	100, 100	100, 100	100, 100	100, 100	100, 100
Ag 0.5						
E	25, 50	50, 50	25, 50	100, 100	50, 100	100, 100
Ag 2.0						
E	12.5, 25	25, 25	12.5, 50	100, 100	25, 25	100, 100
Ag 3.0						
STATISTICS	***P < 0.05***	***P < 0.05***	***P < 0.05***	***P < 0.05***	***P < 0.05***	***P < 0.05***
A	50, 100	25, 50	12.5, 25	100, 100	50, 100	50, 100
Ag-Ni 0.5						
A	12.5, 25	12.5, 12.5	25, 50	50, 100	25, 50	100, 100
Ag-Ni 1.0						
A	12.5, 25	12.5, 12.5	12.5, 12.5	100, 100	12.5, 25	12.5, 12.5
Ag-Ni 2.0						
A	12.5, 12.5	6.25 ,12.5	6.25, 12.5	100, 100	12.5, 25	12.5, 25
Ag-Ni 3.0						
STATISTICS	***P > 0.05***	***P > 0.05***	***P > 0.05***	***P > 0.05***	***P > 0.05***	***P > 0.05***
B	50,100	50, 100	50, 50	100, 100	100, 100	100, 100
Ag-Ni 1.0						
B	50,100	25, 50	12.5, 25	100, 100	50, 100	50, 100
Ag-Ni 2.0						
STATISTICS	***P > 0.05***	***P < 0.05***	***P < 0.05***	***P > 0.05***	***P < 0.05***	***P < 0.05***
D	25,50	12.5, 25	12.5, 12.5	25, 50	25, 50	25, 50
Ag-Ni 3.0						
D	25,50	25, 50	25, 25	12.5, 25	100, 100	100, 100
Ag-Ni 2.0						
STATISTICS	***P > 0.05***	***P < 0.05***	***P < 0.05***	***P < 0.05***	***P < 0.05***	***P < 0.05***
E	100,100	100, 100	100, 100	100, 100	100, 100	100, 100
Ag-Ni 2.0						
E	50,100	25, 50	50, 100	100, 100	50, 100	100, 100
Ag-Ni 3.0						
E	100,100	50, 100	100, 100	100, 100	100, 100	100, 100
Ag-Ni 1.0						
STATISTICS	***P <0.05***	***P < 0.05***	***P < 0.05***	***P > 0.05***	***P < 0.05***	***P > 0.05***
Control	3.13	6.25	6.25	6.25	6.25	6.25
STATISTICS	***Control vs Aa,Ba,Ca,Da,Ea,A,B,C,E , F-value 34.06, P < 0.05***					

Control- Ciprofloxacin (Bacteria) and Fluconazole (Fungi)